

AD-A064 967

TORONTO UNIV DOWNSVIEW (ONTARIO) INST FOR AEROSPACE --ETC F/G 20/4
REGIONS AND TRANSITIONS OF NONSTATIONARY OBLIQUE SHOCK-WAVE DIF--ETC(U)
AUG 78 G BEN-DOR

UNCLASSIFIED

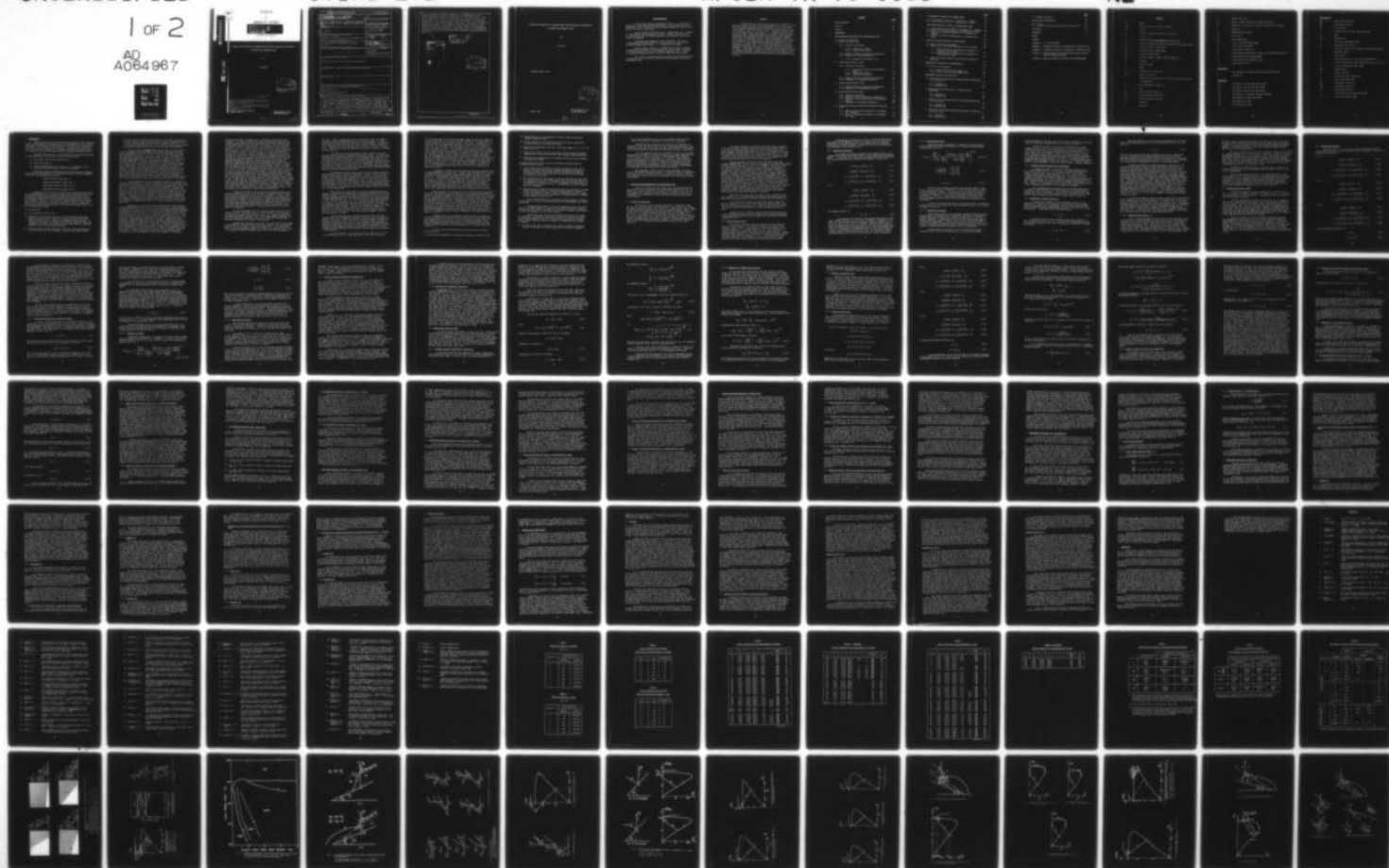
UTIAS-232

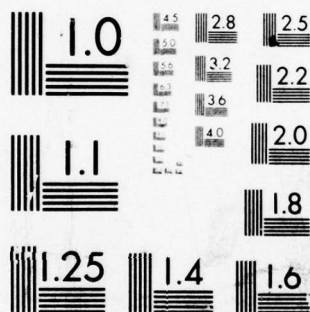
AFOSR-TR-79-0063

NL

1 of 2

AD
A064967





MICROCOPY RESOLUTION TEST CHART
NATIONAL BUREAU OF STANDARDS-1963-A

ADA064967

DDC FILE COPY



INSTITUTE

FOR

AEROSPACE STUDIES

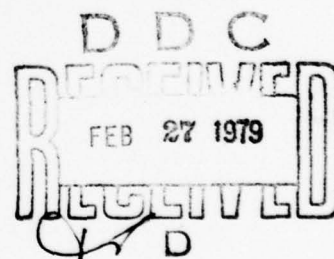
LEVEL II

UNIVERSITY OF TORONTO

REGIONS AND TRANSITIONS OF NONSTATIONARY OBLIQUE SHOCK-WAVE DIFFRACTIONS
IN PERFECT AND IMPERFECT GASES

by

G. Ben-Dor



Approved for public release;
distribution unlimited.

AIR FORCE OFFICE OF SCIENTIFIC RESEARCH (AFSC)
NOTICE OF TRANSMITTAL TO DDC

This technical report has been reviewed and is
approved for public release IAW AFR 190-12 (7b).
Distribution is unlimited.

A. D. BLOSE

Technical Information Officer
August, 1978

UTIAS Report No. 232
CN ISSN 0082-5255

70 02 16 005

19 REPORT DOCUMENTATION PAGE		READ INSTRUCTIONS BEFORE COMPLETING FORM	
1. REPORT NUMBER 18 AFOSR-TR-79-0068	2. GOVT ACCESSION NO.	3. RECIPIENT'S CATALOG NUMBER	
4. TITLE (and Subtitle) 6 REGIONS AND TRANSITIONS OF NONSTATIONARY OBLIQUE SHOCK-WAVE DIFFRACTIONS IN PERFECT AND IMPERFECT GASES.	5. TYPE OF REPORT & PERIOD COVERED INTERIM rept. 1 Feb 78 - 31 Jan 79		
7. AUTHOR(s) 10 G. Ben-Dor	6. PERFORMING ORG. REPORT NUMBER UTIAS Report No. 232		
9. PERFORMING ORGANIZATION NAME AND ADDRESS UNIVERSITY OF TORONTO INSTITUTE OF AEROSPACE STUDIES, 4925 DUFFERIN ST DOWNSVIEW, ONTARIO, CANADA, M3H 5T6	8. CONTRACT OR GRANT NUMBER(s) 15 AFOSR-77-3303		
11. CONTROLLING OFFICE NAME AND ADDRESS AIR FORCE OFFICE OF SCIENTIFIC RESEARCH/NA BLDG 410 BOLLING AIR FORCE BASE, D C 20332	10. PROGRAM ELEMENT, PROJECT, TASK AREA & WORK UNIT NUMBERS 16 2307A3 17A3 61102F		
14. MONITORING AGENCY NAME & ADDRESS (if different from Controlling Office) 14 UTIAS-232	12. REPORT DATE 11 August 1978		
	13. NUMBER OF PAGES 139 12 1570		
	15. SECURITY CLASS. (of this report) UNCLASSIFIED		
15a. DECLASSIFICATION/DOWNGRADING SCHEDULE			
16. DISTRIBUTION STATEMENT (of this Report) Approved for public release; distribution unlimited			
17. DISTRIBUTION STATEMENT (of abstract entered in Block 20, if different from Report)			
18. SUPPLEMENTARY NOTES			
19. KEY WORDS (Continue on reverse side if necessary and identify by block number) NONSTATIONARY OBLIQUE SHOCK-WAVE REFLECTIONS SHOCK-TUBE FLOWS IMPERFECT-GAS FLOWS INTERFEROMETRIC MEASUREMENTS SHOCK-WAVE DIFFRACTION $\alpha_{or} = M_{sub 5} < \alpha_{or} =$			
20. ABSTRACT (Continue on reverse side if necessary and identify by block number) The diffraction of shock waves ($2 < M_s < 8$) in perfect and imperfect nitrogen and argon by sharp compressive corners ($2^\circ < \theta_w < 60^\circ$) were investigated analytically and experimentally. It is shown that seven shock-wave diffraction domains exist in nitrogen and six in argon in the ranges $1 < M_s < 10$ and $0 < \theta_w < 90^\circ$. The domains consist of the four well-known shock wave reflections, i.e., regular reflection (RR), single-Mach (SMR), complex-Mach (CMR) and double-Mach (DMR) reflections. All the transition boundaries between \rightarrow next page			

DD FORM 1 JAN 73 1473

$0 \text{ deg} < \alpha_{or} = \theta_{\text{shock sub w}} < \alpha_{or} = 40 \text{ deg}$ 920 2 deg $\alpha_{or} = \theta_{\text{shock sub w}} < \alpha_{or} = 60 \text{ deg}$ UNCLASSIFIED

these regions were established analytically and substantiated by the present experimental results as well as the data from other sources. Over 100 experiments were conducted in the UTIAS 10 x 18 cm Hypervelocity Shock Tube equipped with a 23-cm dia field of view Mach-Zehnder interferometer equipped with a dual-frequency laser light source. It is shown that real-gas effects have a significant influence on the size of the regions and their transition boundaries. Some comparison between steady and nonstationary reflections are made and discussed. Isopycnics (lines of constant density) as well as density distributions along the wedge surface are presented for the various diffraction processes and their differences and similarities are discussed.

LEVEL II

ASSESSMENT for	
DTIS	White Section <input checked="" type="checkbox"/>
DDC	Dark Section <input type="checkbox"/>
UNANNOUNCED	<input type="checkbox"/>
JUSTIFICATION	
BY	
REVISIONS/REV. DATE	
REV. DATE	
A	

DDC
RECEIVED
FEB 27 1979
D

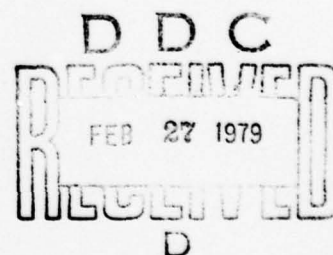
UNCLASSIFIED

REGIONS AND TRANSITIONS OF NONSTATIONARY OBLIQUE SHOCK-WAVE DIFFRACTIONS
IN PERFECT AND IMPERFECT GASES

by

G. Ben-Dor

Submitted August, 1978



August, 1978

UTIAS Report No. 232
CN ISSN 0082-5255

79 02 16 005

Acknowledgements

I should like to express my gratitude to Prof. I. I. Glass for the opportunity to work with him and learn from him. His invaluable guidance, supervision, advice, interest and understanding throughout the course of this project are very much appreciated.

Sincere thanks are offered to Prof. S. Molder and Dr. H. G. Hornung for their helpful and stimulating discussions. Thanks are extended to Mr. B. T. Whitten for many interesting discussions and invaluable assistance in computer programming.

I appreciate the suggestions received from Prof. C. K. Law in re-initiating and extending his M.A.Sc. Thesis research at UTIAS and the clarifying communications from Dr. L. F. Henderson on his papers.

Finally I wish to thank Mr. L. Buchanan for his help in carrying out some of the experiments and proofreading the present report, the staff of the UTIAS machine shop for their technical assistance, Mrs. L. Quintero for drawing the figures and Mrs. W. Dillon for typing the final report.

This work was supported financially by the National Research Council of Canada and the U.S. Air Force Office of Scientific Research under grant USAF-AFOSR 77-3303.

Abstract

The diffraction of shock waves ($2 \leq M_s \leq 8$) in perfect and imperfect nitrogen and argon by sharp compressive corners ($2^\circ \leq \theta_w \leq 60^\circ$) were investigated analytically and experimentally. It is shown that seven shock-wave diffraction domains exist in nitrogen and six in argon in the ranges $1 \leq M_s \leq 10$ and $0 \leq \theta_w \leq 90^\circ$. The domains consist of the four well-known shock wave reflections, i.e., regular reflection (RR), single-Mach (SMR), complex-Mach (CMR) and double-Mach (DMR) reflections. All the transition boundaries between these regions were established analytically and substantiated by the present experimental results as well as the data from other sources. Over 100 experiments were conducted in the UTIAS 10 x 18 cm Hypervelocity Shock Tube equipped with a 23-cm dia field of view Mach-Zehnder interferometer equipped with a dual-frequency laser light source. It is shown that real-gas effects have a significant influence on the size of the regions and their transition boundaries. Some comparison between steady and nonstationary reflections are made and discussed. Isopycnics (lines of constant density) as well as density distributions along the wedge surface are presented for the various diffraction processes and their differences and similarities are discussed.

CONTENTS

	<u>Page</u>
Acknowledgements	ii
Abstract	iii
Notation	vii
1. INTRODUCTION	1
2. OBLIQUE SHOCK-WAVE REFLECTION IN NONSTATIONARY FLOWS	7
2.1 Reasons for Reflection	7
2.2 Regular Reflection (RR)	8
2.2.1 Analytical Formulation	9
2.2.1.1 Perfect-Gas Solution	10
2.2.1.2 Imperfect-Gas Solution	10
2.2.2 Graphical Solution (Shock-Polar Presentation)	11
2.2.3 Termination of Regular Reflection	11
2.2.3.1 Change-Over Mach Number - M_{Oc}	12
2.3 Single-Mach Reflection (SMR)	13
2.3.1 Analytical Formulation	14
2.3.1.1 Prediction of Triple Point Trajectory Angle - χ	15
2.3.1.2 Perfect-Gas Solution	16
2.3.1.3 Imperfect-Gas Solution	17
2.3.2 Graphical Solution (Shock-Polar Presentation)	18
2.3.3 Termination of Single-Mach Reflection	19
2.4 Complex-Mach Reflection (CMR)	19
2.4.1 Graphical Solution (Shock-Polar Presentation)	19
2.4.2 Termination of Complex-Mach-Reflection	22
2.5 Double-Mach Reflection (DMR)	23
2.5.1 Analytical Formulation	23
2.5.2 Graphical Solution (Shock-Polar Presentation)	26
2.5.3 Prediction of the Second Triple-Point-Trajectory Angle χ'	28
2.5.4 Termination of Double-Mach Reflection	28
2.6 Nonstationary-Oblique Shock-Wave Reflection in (M_s , θ_w')-Plane	28
2.6.1 Regions and Transition Boundaries in a Diatomic Gas - Nitrogen	30
2.6.2 Regions of Transition Boundaries in a Monatomic Gas - Argon	30

	<u>Page</u>
3. FLOW-DEFLECTION PROCESS OVER A WEDGE CORNER	31
3.1 Flow-Deflection Process in a Diatomic Gas - Nitrogen	32
3.2 Flow-Deflection Process in a Monatomic Gas - Argon	32
4. SHOCK-WAVE-DIFFRACTION PROCESS IN NONSTATIONARY FLOWS	32
4.1 Triple-Point-Trajectory Angle in a Diatomic Gas - Nitrogen	33
4.2 Triple-Point-Trajectory Angle in a Monatomic Gas - Argon	34
4.3 Domains of Shock-Wave Diffractions in a Diatomic Gas - Nitrogen	35
4.4 Domains of Shock-Wave Diffractions in a Monatomic Gas - Argon	35
5. OBLIQUE SHOCK-WAVE REFLECTION IN STEADY FLOWS	36
5.1 Types of Reflection Obtainable	36
5.2 Steady Oblique Shock-Wave Reflection in (M_0, ϕ_0) -Plane	37
5.2.1 Steady Flow Regions and Transition Boundaries in a Diatomic Gas - Nitrogen	37
5.2.2 Steady Flow Regions and Transition Boundaries in a Monatomic Gas - Argon	37
5.3 Comparison Between Steady and Nonstationary Shock-Wave Reflection	37
6. EXPERIMENTAL TECHNIQUES AND INSTRUMENTATION	39
6.1 Accuracy of Measurements	40
6.1.1 Incident Shock Wave Mach Number - M_s	40
6.1.2 Initial Pressure P_0 and Temperature T_0	41
7. EXPERIMENTAL RESULTS AND DISCUSSIONS	41
7.1 Verification of Nonstationary Oblique Shock-Wave Reflection in (M_s, θ_w) -Plane	42
7.1.1 Diatomic Gas	42
7.1.2 Monatomic Gas	43
7.2 Triple-Point-Trajectory Angle - χ Comparison With Experiments	43
7.2.1 Diatomic Gas	44
7.2.2 Monatomic Gas	44
7.3 Verification of Nonstationary Oblique Shock-Wave Reflection in (M_s, θ_w) -Plane	45
7.3.1 Diatomic Gas	45
7.3.2 Monatomic Gas	45
7.4 Verification of Nonstationary Oblique Shock-Wave Diffraction in (M_s, θ_w) -Plane	46
7.4.1 Diatomic Gas	46
7.4.2 Monatomic Gas	46

	<u>Page</u>
7.5 Summary Discussions	47
8. DENSITY-FIELD INVESTIGATION	48
8.1 Nitrogen	49
8.2 Comparison With Some Numerical Data and Discussions	51
9. CONCLUSIONS	55
REFERENCES	57
TABLES	
FIGURES	
APPENDIX A - (P, θ)-SHOCK POLARS	
APPENDIX B - ANALYTICAL SOLUTION OF THE EQUATIONS OF MOTION FOR RR	
APPENDIX C - ANALYTICAL SOLUTION OF THE EQUATIONS OF MOTION FOR SMR	
APPENDIX D - RELATIVE MOTION OF THE SECOND TRIPLE POINT (OR KINK) WRT THE FIRST TRIPLE POINT	
APPENDIX E - METHOD OF REDUCING ISOPYCNICS FROM INTERFEROGRAMS	

Notation

Ar	argon
E(a)	absolute error in measuring quantity a
He	helium
h_i	specific enthalpy of the flow in region (i)
L	$= L_i/L_s$
L_i	distance between first and second triple points
L_s	distance travelled by incident shock wave from the wedge corner
M_i	flow Mach number in region (i)
M_s	incident shock wave Mach number
M_{oc}	change over Mach number
M_2^*	flow Mach number in region (2) for a DMR to form
N_2	nitrogen
n	isopycnic number
O_2	oxygen
P_i	flow pressure in region (i)
P(T)	partition function
r	distance along wedge surface or shock tube wall measured from the wedge corner
T_i	flow temperature in region (i)
t	time
U_i	flow velocity in region (i)
U_s	incident shock wave velocity
\bar{V}_{ij}	velocity vector (i) wrt (j)
x	coordinate
y	coordinate

γ	specific heat ratio
Δt	time for incident shock wave to travel distance L_s
θ_i	deflection of flow from its original direction while entering region (i)
θ_m	maximum-deflection angle
θ_s	sonic angle
θ_w	actual wedge angle
θ'_w	$= \theta_w + \chi$, effective wedge angle
μ	$= \sin^{-1}(1/M)$, Mach angle
ρ_i	flow density in region (i)
ϕ_i	incident angle between flow in region (i) and oblique shock wave
χ	first triple-point-trajectory angle
χ'	second triple-point-trajectory angle
ω	angle between I and R

Superscripts

'	flow properties as measured from the second triple point
*	see Fig. 50

Subscripts

(o)	flow ahead of I for RR, SMR, CMR and DMR
(1)	flow behind I for RR, SMR, CMR and DMR
(2)	flow behind R for RR, SMR, CMR and DMR
(2')	flow behind I in laboratory frame of reference
(3)	flow behind M for SMR, CMR and DMR
(4)	flow behind M_1 for DMR
(5)	flow behind R_1 for DMR

Abbreviations

CMR	complex-Mach reflection
DMR	double-Mach reflection
FD	flow deflection
I	incident shock wave in RR, SMR, CMR and DMR
K	kink
LHS	left-hand side
M	Mach stem in SMR, CMR and DMR
M_1	second Mach stem in DMR
P	reflection point in RR or location of M along the wedge in SMR, CMR and DMR
Q	wedge corner
R	reflected shock wave in RR, SMR, CMR and DMR wrt T
R'	reflected shock wave in CMR and DMR with respect to K or T_1
R_1	second reflected shock wave in DMR
RHS	right-hand side
RR	regular reflection
S	slipstream in SMR, CMR and DMR
S_1	second slipstream in DMR
SD	shock (wave) diffraction
SMR	single-Mach reflection
SR	shock (wave) reflection
T	first triple point in SMR, CMR and DMR
T_1	second triple point in DMR

1. INTRODUCTION

When a planar moving incident shock wave encounters a sharp compressive corner in a shock tube, two processes take place simultaneously. The incident shock wave is reflected by the wedge surface, whereas the induced nonstationary flow behind it is deflected by the wedge corner. Throughout this report the first process will be referred to as shock-wave reflection (SR), the second as flow deflection (FD) and the overall phenomena as shock-wave diffraction (SD).

Shock-wave diffraction, i.e., the combination of shock-wave reflection and flow deflection, for a given gas, depends on three factors:

- (1) Mach number of the incident shock wave M_s .
- (2) Corner wedge angle θ_w .
- (3) Initial thermodynamic state of the gas, i.e., temperature T_0 and pressure P_0 (for a perfect gas this is not required).

Since the nonuniform terminology of the various reflection processes used in the literature tends to be confusing the following terms are suggested and will be used throughout this report:

Regular reflection (RR), Fig. 1a

Single-Mach reflection (SMR), Fig. 1b

Complex-Mach reflection (CMR), Fig. 1c

Double-Mach reflection (DMR), Fig. 1d

Although RR and SMR were first noticed by the distinguished physicist and philosopher Mach (Ref. 1) as early as 1878, almost no work was done in this field until the 1940's, when Neumann reinitiated the problem (Refs. 2 and 4). An intensive investigation at Princeton University under the supervision of Prof. Bleakney finally led to the discovery of CMR by Smith (Ref. 6) and DMR by White (Refs. 17 and 18). Once these four different types of reflection were found it became necessary to establish the transition criteria between them. The transition problem from RR to SMR was first studied by Neumann (Refs. 2 and 4) who assumed the following:

- (1) A perfect gas.
- (2) Two-dimensional inviscid flows.
- (3) When there are two possible solutions (the so-called weak and strong families of shock waves for producing a required deflection) the weak-shock solution will occur. This is an experimental fact, which was verified in the study of two-dimensional supersonic wedge flows (Ref. 28). Although an explanation of minimum entropy for weaker shocks is sometimes advanced it has not been proven analytically.
- (4) The flow problem is pseudo-stationary. This arose from the observation that any point on the wave configuration having a plane radius vector \bar{r}

with the corner as origin was transformed to a new point $\bar{c}r$, where c is a scalar constant. This means that instead of three independent variables x , y and t the phenomenon was describable in terms of x/t and y/t , i.e., x and y may be measured relative to any point moving with constant velocity with respect to the corner; in other words, the flow is self-similar.

Using the above assumptions Neumann argued (Refs. 2 and 4) that in an RR the streamline deflection angle θ_2 through the reflected shock wave is equal in magnitude but opposite in sign to the deflection angle θ_1 through the incident shock wave, i.e., $\theta_1 + \theta_2 = 0$ (Fig. 7). This is violated when the wedge angle θ_w decreases to the point where it forces θ_1 to exceed in magnitude the maximum deflection angle θ_{2m} . This criterion will be referred to as the "detachment" criterion. The detachment criterion can best be illustrated by using the pressure-deflection (P, θ)-shock polars. Consider Fig. 2a where the I and R-polars represent the incident and reflected shock waves, respectively. Since the net deflection through an RR is zero the solution is at the point where the R-polar intersects the P/P_0 -axis, i.e., state (2') on R_{III} . As the wedge angle θ_w decreases the R-polar moves away from the P/P_0 -axis until it becomes tangent to it [Fig. 2a, state (2') on R_{IV}]. Upon further decrease in θ_w the R-polar will not intersect the P/P_0 -axis any more and an RR is not possible. Consequently, the detachment criterion is represented by the R_{IV} shock polar. (Note that the term detachment comes from steady flows where the oblique shock detaches at this angle.)

Some disagreement between the detachment criterion and experiments were found by Smith (Ref. 6). In his experiments RR persisted beyond the limit determined by the detachment criterion. Bleakney and his students (Refs. 9, 10, 13, 15, 17, 18, 20, 22, 23) tried to resolve the disagreement found by Smith (Ref. 6). Unfortunately however, they were unable to do so. Kawamura and Saito (Ref. 24) who also tried to resolve this problem by making use of shock polars discovered that the point of tangency between the R-polar and the P/P_0 -axis (i.e., R_{IV} , Fig. 2a) can lie outside or inside the I-polar depending on whether or not the value of M_0 is greater or less than a certain change-over value M_{0c} . Unlike the case of a diatomic gas where different values of M_{0c} are reported by different investigators (Refs. 24, 60 and 81), only one value is reported for a monatomic gas (Ref. 81). All these values are for perfect gases only.

Henderson and Lozzi (Ref. 60) investigated the $RR \rightarrow SMR$ -transition problem experimentally in a wind tunnel and in a shock tube. They introduced an alternative criterion which has the property that the system always remained in mechanical equilibrium (i.e., no pressure discontinuities) during transition. Consider Fig. 2a and note that, once RR terminates and SMR forms, the solution moves from the point where the R-polar intersects the P -axis (state 2' on R_{IV}) to the point where the I and R-polars intersect (states 2 and 3 on R_{IV}). Consequently, a sharp pressure change (from $P_{2'}$ to P_2) is associated with this transition, if the detachment criterion is accepted. Henderson and Lozzi argue (Ref. 60) that "a system which develops a pressure discontinuity during transition cannot be in mechanical equilibrium". Furthermore they say that, "If a pressure discontinuity occurs during transition then an unsteady wave of finite amplitude or a finite amplitude band of waves will be generated in the flow. These would be expansion [waves] for $RR \rightarrow SMR$ and compression [waves] for $SMR \rightarrow RR$." However, since these waves have not been observed, they discarded (Ref. 60) the detachment criterion and suggested an alternative

criterion that enables the system to be in mechanical equilibrium during transition. In order to maintain the system in mechanical equilibrium, the transition should take place at the point where the R-polar intersects the I-polar (SMR solution) on the P/P_0 -axis (RR solution). This is illustrated by states (2) and (3) on the R_{ii} polar. The formulation of this criterion yields $\theta_1 + \theta_2 = \theta_3 = 0$ and it will be referred to as the "mechanical-equilibrium" criterion. Consider polar R_{iii} (Fig. 2a) and note that according to the detachment criterion an RR takes place at (2') since the termination case R_{iv} was not reached. However, according to the mechanical-equilibrium criterion, RR cannot occur, since the termination criterion given by R_{ii} was exceeded. It is worth noting that the area of disagreement in the (M_s, θ_w) -plane between these two different criteria (Fig. 2b) is very large. The mechanical-equilibrium criterion, rather than reducing the previously-mentioned disagreement between theory and experiment found by Smith (Ref. 6), where RR occurred even below the line of the detachment criterion in shock-tube experiments at low incident shock wave Mach numbers, made it even worse, for their line lies above the detachment-criterion line for all $M_s > 1.68$ ($M_0 = 2.23$, $\phi_0 = 41.20$). Nevertheless, Henderson and Lozzi should be credited for their new physical approach to the problem. It is worth noting that in an experiment where the wedge angle θ_w is changed gradually perhaps one might obtain two different criteria for $RR \rightarrow SMR$ and $SMR \rightarrow RR$ transitions. Consider Fig. 2a and note that if one starts with a given SMR at states (2) and (3) on R_{iv} and the wedge angle is increased slowly, it is possible that states a (SMR), b (SMR), c (SMR \rightarrow RR) and d (RR) might be encountered, and hence the transition would follow the mechanical-equilibrium criterion. However, if one started with a given RR state (2) on R_i and then decreased θ_w gradually, it is possible that the sequence of events might be: states d (RR), c (RR), e (RR), f (RR) and a (SMR). This sequence of events follows the detachment criterion. Such experiments have not been made to date and need further study.

During their attempt to substantiate their mechanical-equilibrium criterion, Henderson and Lozzi (Ref. 60) found a "remarkable anomaly" between their results from wind-tunnel and shock-tube experiments. In their shock-tube results RR continued to exist below the detachment and mechanical-equilibrium transition boundary lines (Fig. 2b) in a region where the perfect-gas theory had no RR solution. They resolved the anomaly by advancing that those RR-configurations found below their mechanical-equilibrium transition line were really undeveloped DMR-configurations in which all shock waves, slip-streams and triple points typical of a well-developed DMR were too close together to be observed.

Hornung and Kychakoff (Ref. 65) initiated another criterion for the termination of RR. They argued that in order for an SMR to form, a length scale must be available at the reflection point, i.e., pressure signals must be communicated to the reflection point. This single argument eventually led them to two different termination lines for RR, depending on whether the flow under consideration is steady or nonstationary.

Consider the nonstationary RR in Fig. 2c (i) and note that the length l_w can affect the reflection point P only when a subsonic flow is established between Q and P (in a frame of reference attached to P). In a steady flow (Fig. 2c, ii) the geometrical length l_w can affect the reflection point P only if a propagation path exists between point Q and point P via the expansion

wave at Q' . This is possible only if the flow between P and Q' is subsonic. According to Hornung and Kychakoff (Ref. 65) this could happen if an SMR existed since the flow behind the Mach stem is always subsonic. Consequently, they argued that transition takes place the very first time when an SMR can occur. Consider Fig. 2a and note that this corresponds to states (2) and (3) on R_{ij} . That also represents the mechanical-equilibrium criterion of Henderson and Lozzi (Ref. 60).

Consequently, Hornung and Kychakoff's sonic criterion led to two different transition lines in steady and nonstationary flows. In steady flows the transition satisfies the mechanical-equilibrium criterion, while for nonstationary flows their analysis led to a new transition line, which will be referred to as the "sonic" criterion. Note that if the sonic-transition line was drawn in Fig. 2b, it would coincide with the detachment criterion-transition line since it lies below it only at very low incident shock waves (Ref. 74). Consequently it could not be drawn on Fig. 2b. Note that Hornung and Kychakoff (Ref. 65) claim to have experimental data obtained in both shock-tube and wind-tunnel flows which verify their criterion.

The transition boundary lines in Fig. 2b were calculated using the steady-flow theory for regular and single-Mach reflection. This is justified by the fourth assumption discussed previously. In 1951 Jones, Martin and Thornhill (Ref. 16) used this assumption to transform the equations of motion so that instead of three independent variables x, y, t only two x/t and y/t were sufficient to describe the phenomenon. Their analysis was later verified experimentally by Parks (Ref. 19). However, since in the nonstationary case the shock waves are usually curved, the results from the steady-state analysis are correct only in the vicinity of the reflection point for RR and the triple point in SMR, CMR and DMR.

Skews (Refs. 57 and 58) tried to resolve the disagreement between analysis and experiment by arguing that the boundary conditions for RR and SMR should be relaxed. In the case of SMR he assumed that the pressure and flow deflection immediately behind the reflected shock wave R need not be the same as those behind the Mach stem. Consequently he defined two relaxed variables $F = (P_2 - P_0)/(P_3 - P_0)$ and $\epsilon = \theta_2 - \theta_3$. (Note that in the usual SMR theory $F = 1$ and $\epsilon = 0$.) He supported this new approach by the fact that some investigators claimed that the slipstream was not a surface of discontinuity but a shear-flow mixing region. However, since excellent agreement was found between the classical (without relaxed boundary conditions) theory and experiment for the angles between the various shock waves and slipstream (Refs. 6, 10, 13, 15, 18 and 43), one cannot justify the need to relax the boundary conditions for SMR.

In the RR-analysis (Ref. 58) Skews relaxed the usual boundary condition that the flow immediately behind the reflected shock is uniform and parallel to the wall. Instead, he defined a relaxation angle ϵ between the flow direction and the wall. (Note $\epsilon = 0$ is the usual boundary condition.) Although his numerical results were in better agreement with experiments one must bear in mind that his analysis was based mainly on mathematical concepts. Unlike the foregoing SMR-case physical considerations impose the boundary condition that the supersonic flow behind the reflected shock wave is parallel to the rigid wall.

Once RR terminates, three different types of reflection can occur in nonstationary flows, i.e., SMR, CMR and DMR. White (Ref. 17) was the

first to notice that when the flow Mach number behind the reflected shock wave R, becomes supersonic in a frame of reference attached to the triple point a "kink" K forms in R and the transition SMR \rightarrow CMR occurs. A mechanism for the transition was later suggested by Gvozdeva et al (Ref. 45) and Henderson and Lozzi (Ref. 60). Henderson and Lozzi suggested that a "band of compression waves" must exist in a CMR. These compression waves then converge to a shock wave to form DMR when $M_2 > 1$. Unfortunately, their suggestion was not substantiated analytically or experimentally. In addition the precise value of M_2 for the termination of CMR and the formation of DMR was not established either. The correct gasdynamic criterion for the termination of CMR and formation of DMR was established during the present study. It will be shown in Section 2.4.2 that the flow behind the reflected shock wave must be supersonic with respect to the kink of a CMR in order for a DMR to form. Consequently, the CMR \rightarrow DMR transition occurs at $M_2 = 1$. It was found further that $M_2 = 1$ corresponds to $M_2 \approx 1.3$ (M_2 measured wrt the first triple point) and hence Gvozdeva et al (Ref. 45) and Henderson and Lozzi (Ref. 60) were correct in predicting the transition at $M_2 > 1$.

An attempt to establish some transition-boundary lines experimentally was made by Bazhenova et al (Ref. 62). However, their experiments did not cover a significant range of incident shock wave Mach number (M_s) and corner wedge angle (θ_w). Their experimental boundaries for SMR, CMR and DMR are limited to $M_s < 4.5$. Unfortunately, experiments made by other researchers also did not cover a wide range of interest. Smith (Ref. 6), Kawamura and Saito (Ref. 24) and White's (Ref. 17, 18) experimental data covered only the range $1 < M_s < 2.75$, while Henderson and Lozzi's (Ref. 60) experiments were centred around the RR-termination criterion line. Law and Glass (Ref. 51) were the first to extend the range of incident shock Mach number up to $M_s \leq 8$, but their corner wedge-angle range at the lower end was limited ($25^\circ \leq \theta_w \leq 60^\circ$).

Figure 3 which is a reproduction of Fig. 5 from the paper by Bazhenova et al (Ref. 62) summarizes all the theoretical and experimental knowledge (excluding the mechanical equilibrium criterion for the termination of RR, discussed earlier) concerning the regions and boundaries of regular, single-Mach, complex-Mach and double-Mach reflections available when the present study started. Only the termination criterion of RR is calculated theoretically for both perfect and imperfect gases (lines 1 and 2, respectively). Although the SMR boundary line is also calculated, line 5 (for a perfect gas only) it does not start or terminate at any other boundary line and hence does not enclose any region. The imperfect boundary lines between SMR, CMR and DMR (lines 3 and 4) were all obtained experimentally and they do not encompass any closed region either. There is no information about the types of reflections for wedge angles in the range $0 < \theta_w < 20^\circ$.

Although most of the investigators were interested in finding the correct transition criteria from one type of reflection to another there were some attempts (Refs. 5, 15, 61, 63, 64) to solve the entire flow field for a given reflection utilizing various analytical or numerical methods. Unfortunately the numerical results suffer from a lack of agreement for the same initial conditions depending on the technique used for a solution (Refs. 61, 63 and 73).

In view of the above literature survey, the present research was directed towards:

- (1) Resolving the disagreements concerning the termination criterion of RR.

- (2) Establishing the correct termination criterion of CMR and hence the formation criterion of DMR.
- (3) Defining domains and transition boundaries of the various reflections in order that they can be predicted a priori.
- (4) Extending the experimental data over a much wider range, i.e., $0 < \theta_w < 60^\circ$ and $1 < M_s < 10$.
- (5) Comparing the existing numerical predictions of the isopycnic (constant-density lines) in the flow field with those obtained interferometrically.
- (6) Resolving and clarifying areas of disagreement existing in the literature concerning this problem.

To achieve these goals it was decided to approach the problem using the following physical concepts:

- (1) It was assumed that the physical processes are governed by the usual equations of conservation of mass, momentum and energy, as written for oblique shock waves. The pressure and flow directions were taken as invariant across shear layers, and very near the wall flow was assumed to be parallel to the wall.
- (2) The shock-reflection process depends on the flow-deflection process behind it. Consequently, the interaction between these two processes should be investigated and understood. Note that this approach was initiated by Law (Ref. 48) and Law and Glass (Ref. 51). Unfortunately, it was not adopted by other investigators.
- (3) Real-gas effects strongly influence the location of the transition boundary lines in the (M_s, θ_w) -plane. Consequently, they should be included in solving the equations of motion. This is substantiated by lines 1 and 2 of Fig. 3 that illustrate the significance of real-gas effects in shifting the RR-transition boundary line.

Due to the difficulties in solving the nonlinear equations of motion it was decided to restrict the imperfect-gas model to thermodynamic and chemical equilibrium.

The imperfect-gas model in this report takes into account the excitation of the internal degrees of freedom such as rotation-vibration coupling, vibration and dissociation in nitrogen, and electronic excitation and ionization in argon (see Appendix A in Ref. 48 for details).

Note that the flow usually passes through two shock waves (incident and reflected). Consequently, even if the incident shock wave is very weak the temperature behind the reflected shock wave can be such that the contribution of the vibrational degree of freedom in a diatomic gas can no longer be neglected.

- (4) The CMR and SMR should be treated from a frame of reference attached to the kink of the CMR or the second triple point of the DMR. Therefore,

the correct transformation of the frame of reference from the first triple point should be investigated, understood and formulated.

During the present study all the criteria for the formation and termination of RR, SMR, CMR and DMR have been established analytically. Consequently, the (M_s, θ_w') and the (M_s, θ_w) -planes were divided into the domains of the different types of reflection and diffraction processes, respectively.

Over 100 experiments have been performed in the 10 cm x 18 cm UTIAS Hypervelocity Shock Tube in nitrogen and argon, at an initial temperature of nearly 300 K and a pressure of 15 torr. The shock-Mach-number range was $2 \leq M_s \leq 8$ over a series of wedge angles $2^\circ \leq \theta_w \leq 60^\circ$. Dual-wavelength laser interferograms were obtained by using a 23-cm dia field of view Mach-Zehnder interferometer. For each and every type of diffraction the shock shapes and density field (isopycnics) as well as the density distribution along the wedge surface were deduced from the corresponding interferograms, and comparisons were made with existing numerical analyses.

The experimental results from the present experiments and other sources substantiate the present analysis. In addition areas of disagreement which existed in the literature have been clarified and resolved. Finally, some comparisons between steady and nonstationary shock reflections were made and discussed.

2. OBLIQUE SHOCK-WAVE REFLECTION IN NONSTATIONARY FLOWS

Since the incident shock wave moves with a constant velocity, the entire problem can be considered from a pseudo-stationary point of view, by attaching a frame of reference to any point on the incident shock wave. The above suggests that instead of three independent variables x , y and t the phenomenon is now describable in terms of x/t and y/t and the flow problem is self-similar.

2.1 Reasons for Reflection

Consider now a planar incident shock wave I, having Mach number M_s (Fig. 4a), colliding with a sharp compressive corner of angle θ_w . Denote the states ahead of and behind it by (0) and (1), respectively. Attach a frame of reference to the reflection point P where I meets the wedge surface. The flow in state (0) moving parallel to the wedge surface approaches I with a velocity $U_0 = U_s \csc \phi_0$ or a Mach number $M_0 = M_s \csc \phi_0$, where $\phi_0 = 90^\circ - \theta_w$ is the incident angle. While passing through I the flow is deflected towards the wedge surface by an angle θ_1 from its original direction, and its dynamic and thermodynamic properties are changed. The deflection causes the flow in state (1) to approach the wedge surface obliquely at an angle θ_1 (Fig. 4a).

From simple gasdynamic considerations this situation is analogous to the case of having a steady flow (P_1 , T_1 and M_1) over a wedge θ_1 (Fig. 5). It is well known that depending on M_1 this flow can negotiate the corner either through a subsonic turning (Fig. 5a) if $M_1 < 1$, or through a bow shock wave, straight and attached (Fig. 5b), curved and attached (Fig. 5c) or curved and detached (Fig. 5d) depending on θ_1 (perfect gas), when the flow is supersonic $M_1 > 1$ (see Appendix A for further details). For an imperfect gas the initial temperature T_1 and pressure P_1 are also important.

Applying the above steady flow results, the pseudo-stationary situation suggests that if $M_1 > 1$ the flow can negotiate the wedge surface either through an attached (to point P) shock wave (straight or curved, Fig. 6b and 6c, respectively) which will result in an RR, or through a detached shock wave that will result in a reflection through a three-shock confluence configuration rather than two (Fig. 6d). In the case of $M_1 < 1$ the analogy suggests that the flow adjusts its direction through a subsonic turning (Fig. 6a). However, it has been found experimentally throughout this study that in the nonstationary case SMR occurs even for combinations of M_s and θ_w for which $M_1 < 1$ wrt point P. We suggest that the reflection (when $M_1 < 1$ arises from the interaction between the incident shock wave and the bow shock generated by the wedge (Fig. 4b). Let the frame of reference be attached to point T, where these two shock waves meet. State (2) results from state (1) on passing through a bow shock wave R. Consequently $P_2 > P_1$ and $P_2/P_0 > P_1/P_0$. To satisfy the last condition the portion of the incident shock wave I that lies below T (dashed line TP) must move forward from P to M in order to become more normal to the oncoming relative flow, forming a Mach stem TM, triple point T and slipstream S (omitted for clarity).

The triple point trajectory path angle χ plays a significant role when it makes $\theta_w = \theta_w + \chi$ large enough such that M_1 will always be greater than unity wrt triple point T (a necessary condition for the existence of R).

Note that when the induced flow behind the incident shock wave becomes subsonic ($M_2' < 1$), and no shock waves arise from the corner, since the flow can turn subsonically (Fig. 5a), neither the first reason, Fig. 4a (the only one quoted in the literature), nor the one added here, Fig. 4b, apply.

Perhaps the most significant conclusion from the above discussion is that shock-wave reflection in the nonstationary case depends additionally on the flow-deflection process over the wedge corner, and cannot be treated independently of it.

2.2 Regular Reflection (RR)

The regular reflection shock-wave configuration (two-shock confluence) is shown in Fig. 7. The frame of reference is attached to the reflection point P and it is moving parallel to the wedge surface with the constant velocity $U_0 = U_s \csc \phi_0$, where $\phi_0 = 90^\circ - \theta_w$ is the angle of incidence between the incident shock wave I and the oncoming flow U_0 . Upon passing through I the flow (U_0) is deflected by an angle θ_1 from its original direction. This deflected supersonic flow U_1 is then redeflected by the reflected shock wave R, by an angle $\theta_2 = -\theta_1$, so that the flow is again parallel to the wedge surface, meeting the required boundary condition.

It has already been mentioned (Section 2.1) that the flow behind R (U_2) could be either supersonic ($M_2 > 1$) or subsonic ($M_2 < 1$) wrt point P. Consequently, two different types of RR are possible since the reflected shock wave can be either straight or curved (Figs. 6b and 6c, respectively) in the vicinity of the reflection point P.

2.2.1 Analytical Formulation

In the frame of reference attached to the reflection point P, the incident and reflected shock waves (I and R) can be treated using steady-flow theory. Considering I and R separately and making use of the oblique shock wave relations the equations of motion for the regular reflection are:

For I:

$$\rho_0 \tan \phi_0 = \rho_1 \tan(\phi_0 - \theta_1) \quad (2.1)$$

$$\rho_0 U_0 \sin \phi_0 = \rho_1 U_1 \sin(\phi_0 - \theta_1) \quad (2.2)$$

$$P_0 + \rho_0 U_0^2 \sin^2 \phi_0 = P_1 + \rho_1 U_1^2 \sin^2(\phi_0 - \theta_1) \quad (2.3)$$

$$h_0 + \frac{1}{2} U_0^2 \sin^2 \phi_0 = h_1 + \frac{1}{2} U_1^2 \sin^2(\phi_0 - \theta_1) \quad (2.4)$$

For R:

$$\rho_1 \tan \phi_1 = \rho_2 \tan(\phi_1 - \theta_2) \quad (2.5)$$

$$\rho_1 U_1 \sin \phi_1 = \rho_2 U_2 \sin(\phi_1 - \theta_2) \quad (2.6)$$

$$P_1 + \rho_1 U_1^2 \sin^2 \phi_1 = P_2 + \rho_2 U_2^2 \sin^2(\phi_1 - \theta_2) \quad (2.7)$$

$$h_1 + \frac{1}{2} U_1^2 \sin^2 \phi_1 = h_2 + \frac{1}{2} U_2^2 \sin^2(\phi_1 - \theta_2) \quad (2.8)$$

The boundary condition is:

$$\theta_2 = -\theta_1 \quad (2.9)$$

If equilibrium is assumed, two thermodynamic properties are sufficient to define a state, e.g., $\rho = \rho(P, T)$, $h = h(P, T)$. Consequently, the above nine equations have thirteen independent variables, namely: $P_0, P_1, P_2, T_0, T_1, T_2, U_0, U_1, U_2, \phi_0, \phi_1, \theta_1$ and θ_2 . Thus, if four of them are known, the remaining nine can be calculated. The four known parameters are usually the flow pressure and temperature ahead of the incident shock wave P_0 and T_0 , respectively, the flow velocity $U_0 = U_s \sec \theta_w$ and its angle of incidence with the primary shock wave $\phi_0 = 90^\circ - \theta_w$. Note that in shock tube experiments P_0, T_0, M_s and θ_w are the known or measured parameters.

2.2.1.1 Perfect-Gas Solution

When the gas under consideration is assumed to be calorically and thermally perfect the above nine equations can be reduced to the following four equations (Ref. 31):

$$\tan \theta_{1,2} = \frac{\frac{P_{1,2}}{P_{0,1}} - 1}{1 + \gamma \frac{M_{0,1}^2}{2} - \frac{P_{1,2}}{P_{0,1}}} \left[\frac{\frac{2\gamma}{\gamma+1} M_{0,1}^2 + \frac{\gamma-1}{\gamma+1} - \frac{P_{1,2}}{P_{0,1}}}{\frac{\gamma-1}{\gamma+1} + \frac{P_{1,2}}{P_{0,1}}} \right]^{1/2} \quad (2.10, 11)$$

$$\frac{1 + \frac{\gamma-1}{2} M_0^2}{1 + \frac{\gamma-1}{2} M_1^2} = \frac{\frac{\gamma+1}{\gamma-1} + \frac{P_1}{P_0}}{\frac{\gamma+1}{\gamma-1} + \frac{P_0}{P_1}} \quad (2.12)$$

$$\theta_1 + \theta_2 = 0 \quad (2.13)$$

The above set of equations involves seven unknowns, namely: γ , M_0 , M_1 , θ_1 , θ_2 , P_1/P_0 and P_2/P_1 . Consequently, in order to solve this set, three of the variables must be known. If γ , M_0 , P_1/P_0 are selected, the rest can be easily calculated, since the solution now involves solving one equation at a time with one unknown, i.e., θ_1 is calculated from Eq. 2.10, then M_1 and θ_2 from Eqs. 2.12 and 2.13, respectively, and finally P_2/P_1 from Eq. 2.11. This also suggests that Eqs. 2.10 to 2.13 are reducible to one equation with one unknown.

It should be mentioned that for this case (perfect gas), the equations of motion (Eqs. 2.1 to 2.9) have been reduced by Henderson (Ref. 31) to a single polynomial of order six.

2.2.1.2 Imperfect-Gas Solution

When real-gas effects such as vibration, vibration-rotation coupling and dissociation in diatomic gases or electronic excitation and ionization in monatomic gases are considered, the equations of motion (Eqs. 2.1 to 2.9) cannot be simplified. Consequently, one has to solve nine nonlinear algebraic equations with nine unknowns. However, since the nine equations of motion consist of two similar sets of four equations each (2.1 to 2.4 and 2.5 to 2.8), a method was developed in which each set is treated independently. The final solution is obtained when the last equation (Eq. 2.9) is satisfied.

Consider the first set (Eqs. 2.1 to 2.4) which involves eight variables P_0 , T_0 , U_0 and ϕ_0 on the LHS and P_1 , T_1 , U_1 and θ_1 on the RHS.

Since the variables on the LHS consist of the initial conditions and hence are known, the RHS can be calculated and P_1 , T_1 , U_1 and θ_1 are found.

The second set (Eqs. 2.5 to 2.8) which again consist of eight variables P_1 , T_1 , U_1 and ϕ_1 on the LHS and P_2 , T_2 , U_2 and θ_2 on the RHS is slightly different since not all the parameters on the LHS are known. Only P_1 , T_1 and U_1 which were obtained from the solution of the first set are known, while ϕ_1 is still unknown. However, if we guess a value of ϕ_1 , the second set becomes exactly the same as the first one and the four parameters on the RHS (P_2 , T_2 , U_2 and θ_2) can be calculated. The correct value of ϕ_1 must satisfy the boundary condition, i.e., Eq. 2.9. The Newton-Raphson method ensures a rapid convergence to the correct value of ϕ_1 . A computer program (based on the above method), as well as a typical output is given in Appendix B.

2.2.2 Graphical Solution (Shock-Polar Presentation)

A graphical solution of an RR can be obtained by making use of (P, θ)-shock polars (Ref. 27). Consider Fig. 8 in which the I-polar corresponds to P_0 , T_0 and $M_0 = M_g \sec \theta_w$. State (1) behind I can be easily obtained from the known incident angle $\phi_0 = 90^\circ - \theta_w$. Once state (1) is determined the shock polar that corresponds to P_1 , T_1 and M_1 , i.e., the R-polar, can be drawn. The solution, state (2), is at the point where the net deflection equals zero ($\theta = 0$), i.e., where the R-polar intersects the P/ P_0 -axis. Figure 8 reveals that theoretically two solutions are possible, (2) and (2'). However (2') corresponds to the so-called strong solution and is discarded on physical grounds that it is not observed in practice.

It is worthwhile mentioning again that the reflected shock wave R is straight (in the vicinity of the reflection point P) if the solution on the R-polar lies in the interval $\theta - \theta_{sp}$ (see Fig. 9a) whereas for the small interval $\theta_{sm} - \theta_{mp}$ a curved reflected shock wave is obtained (Fig. 9b). An RR with a curved reflected shock wave can be seen in Fig. 20 of Ref. 23.

2.2.3 Termination of Regular Reflection

As noted earlier (Section 1) three different criteria for the termination of RR exist in the literature. The first one is due to Neumann (Ref. 2) and is known as the "detachment" criterion, which states that RR terminates when the R-polar becomes tangent to the P-axis on the (P, θ)-plane (Fig. 2a, R_{1v}). Analytically this can be expressed as:

$$\theta_1 + \theta_{2m} = 0 \quad (2.14)$$

The second criterion, the "mechanical equilibrium" criterion, is due to Henderson and Lozzi (Ref. 60). It states that RR terminates when the I and R-polars intersect on the P axis (Fig. 2a, R_{1i}). Analytically it assumes the relation:

$$\theta_1 + \theta_2 = \theta_3 = 0 \quad (2.15)$$

The third criterion is due to Hornung and Kychakoff (Ref. 65) which states that RR terminates when the R-polar intersects the P-axis at its sonic point, i.e.,

$$\theta_1 + \theta_{2s} = 0 \quad (2.16)$$

Since the sonic point and the point of maximum deflection are usually very close, it is impractical to distinguish between this criterion and the detachment criterion, and hence only the first two criteria will be considered here. One should note that the third criterion, the so-called sonic criterion, lies slightly below the detachment criterion at very low Mach numbers.

Hornung and Kychakoff who suggested the third criterion (Eq. 2.16) found that two different criteria for the terminations of RR exist, one for steady flow and one for nonstationary flow. They claim that their recent finding was substantiated by their experiments in both a wind tunnel and a shock tube. Their data for nonstationary flows (Refs. 65 and 74) do not agree with the "mechanical-equilibrium" criterion. One should also keep in mind that Henderson and Lozzi's experimental data revealed a "remarkable anomaly" between the results obtained in steady and nonstationary (or pseudo-stationary) flows, where RR was obtained in a region where the "perfect-gas theory" (for both criteria) has no RR solution. Henderson and Lozzi (Ref. 60) resolved this disagreement for their shock-tube data by arguing that the RR-like configurations were really undeveloped DMR-configurations, where both the triple points as well as the slipstreams and the shock waves typical of a well-developed DMR were too small to be observed. (They estimate the primary and secondary confluences as being 0.1 mm apart.) A few experiments conducted in the present work in order to verify their argument, using an optical magnification of 5.4 for $M_s \approx 4.7$, $\theta_w = 60^\circ$ and a wedge 8.5 cm long, failed to show any sign of a DMR.

In all the experiments claimed by Henderson and Lozzi to be undeveloped DMR-configurations, the reflected shock wave R is straight near the reflection point. This indicates that the flow behind R is supersonic ($M_2 > 1$) and hence parallel to the wall. However a DMR should produce subsonic flow. Consequently, all the available evidence favours Hornung and Kychakoff's (Ref. 65) conclusion that the "mechanical equilibrium" criterion established by Henderson and Lozzi (Ref. 60) is inapplicable to nonstationary flows. Therefore, the detachment criterion, i.e., the case where the R-polar becomes tangent to the P-axis, Eq. 2.14 is the correct criterion for the termination of RR.

2.2.3.1 Change-Over Mach Number - M_{Oc}

It was noted that Kawamura and Saito (Ref. 24) were the first to show that the point of tangency between the R-polar and the P-axis (the termination criterion of RR) can lie inside or outside the I-polar (Figs. 10a and 10b, respectively) depending on whether the value of M_0 is less or greater than a certain change-over value - M_{Oc} . Unfortunately, their value for $M_{Oc} = 3.203$ ($\gamma=1.4$) does not match their other variables $P_0/P_1 = 0.433$ and $\phi_0 = 41.5^\circ$ which result in $M_{Oc} = 2.198$. Henderson and Lozzi (Ref. 60) pointed out that a misprint occurred and that it should read $M_{Oc} = 2.203$, which is in good agreement with

the above values. Unfortunately, Henderson and Lozzi (Ref. 60) who quoted the value $M_{OC} = 2.23$ in the text of their paper used the number 2.40 in the caption of their Fig. 3, thereby adding to the confusion caused by Kawamura and Saito's misprint. A different value, $M_{OC} = 2.202$, was recently calculated by Molder (Ref. 81) for a perfect diatomic gas.

The value calculated here yields $M_{OC} = 2.190$ ($M_S = 1.450$, and $\theta'_w = 48.55^\circ$) for a perfect diatomic gas ($\gamma = 1.4$) and $M_{OC} = 2.185$ ($M_S = 1.449$ and $\theta'_w = 48.46^\circ$) for imperfect nitrogen at $P_0 = 15$ torr and $T_0 = 300$ K. The significance of real-gas effects (vibration and vibration-rotation coupling) even at this low Mach number ($M_S \approx 1.45$) is clear, albeit small. In the case of a perfect monatomic gas ($\gamma = 5/3$) the value calculated by Molder (Ref. 81) is 2.470 and our calculated value of M_{OC} is 2.453 ($M_S = 1.540$ and $\theta'_w = 51.13^\circ$). The present value applies to imperfect argon at $P_0 = 15$ torr and $T_0 = 300$ K.

The shock-polar combinations that correspond to M_{OC} for perfect and imperfect nitrogen and argon (or any monatomic gas) are shown in Figs. 11a, 11b and 11c, respectively.

When RR terminates the reflection can be achieved only by a three-shock confluence, i.e., a triple point (T). In nonstationary flows three types of reflection can occur depending on the flow Mach number behind the reflected shock wave R. One more difference between these three types of reflection and RR lies in the fact that they all make the flow near the wedge surface (behind the Mach stem) subsonic ($M_3 < 1$), while in the case of an RR the flow near the wall (behind the reflection point) is usually supersonic.

2.3 Single-Mach Reflection (SMR)

When the flow behind the reflected shock wave R is subsonic, i.e., $M_2 < 1$, in a frame of reference attached to the triple point T, it can negotiate the wedge surface by turning subsonically. Consequently, there is no physical need for additional shock waves.

The wave configuration of an SMR is shown in Fig. 12. The frame of reference is attached to the triple point T and it moves along a straight line (the triple point trajectory at an angle χ) with a constant velocity $U_0 = U_s \operatorname{cosec} \phi_0$ where $\phi_0 = 90^\circ - \theta'_w$ ($\theta'_w = \theta_w + \chi$) is the angle of incidence between the incident shock wave I and the oncoming flow and χ is the angle between the triple point trajectory and the wedge surface. Throughout this report θ'_w will be referred to as the effective wedge angle, whereas θ_w is the actual wedge angle. The Mach stem M lies ahead of the incident shock wave I. It is normal to the wedge surface but not necessarily straight.

The flow in state (0) can reach the region bounded by R and M by passing through two shock waves I and R or only one shock wave M depending upon whether it is above or below the triple point trajectory. However, gas-dynamic considerations imply that the gas must be compressed to the same pressure, and must move in the same direction on either side of the slipstream. Consequently, all other thermodynamic properties such as entropy, density, temperature, etc., are different giving rise to a slipstream S. It divides the two regions of equal pressure and flow direction, but different thermodynamic states.

2.3.1 Analytical Formulation

The shock waves I, R and M are again treated separately, using the oblique-shock-wave relations across each one of them. Consequently, the equations of motion for an SMR are:

For I:

$$\rho_0 \tan \phi_0 = \rho_1 \tan(\phi_0 - \theta_1) \quad (2.17)$$

$$\rho_0 U_0 \sin \phi_0 = \rho_1 U_1 \sin(\phi_0 - \theta_1) \quad (2.18)$$

$$P_0 + \rho_0 U_0^2 \sin^2 \phi_0 = P_1 + \rho_1 U_1^2 \sin^2(\phi_0 - \theta_1) \quad (2.19)$$

$$h_0 + \frac{1}{2} U_0^2 \sin^2 \phi_0 = h_1 + \frac{1}{2} U_1^2 \sin^2(\phi_0 - \theta_1) \quad (2.20)$$

For R:

$$\rho_1 \tan \phi_1 = \rho_2 \tan(\phi_1 - \theta_2) \quad (2.21)$$

$$\rho_1 U_1 \sin \phi_1 = \rho_2 U_2 \sin(\phi_1 - \theta_2) \quad (2.22)$$

$$P_1 + \rho_1 U_1^2 \sin^2 \phi_1 = P_2 + \rho_2 U_2^2 \sin^2(\phi_1 - \theta_2) \quad (2.23)$$

$$h_1 + \frac{1}{2} U_1^2 \sin^2 \phi_1 = h_2 + \frac{1}{2} U_2^2 \sin^2(\phi_1 - \theta_2) \quad (2.24)$$

For M:

$$\rho_0 \tan \phi_3 = \rho_3 \tan(\phi_3 - \theta_3) \quad (2.25)$$

$$\rho_0 U_0 \sin \phi_3 = \rho_3 U_3 \sin(\phi_3 - \theta_3) \quad (2.26)$$

$$P_0 + \rho_0 U_0^2 \sin^2 \phi_3 = P_3 + \rho_3 U_3^2 \sin^2(\phi_3 - \theta_3) \quad (2.27)$$

$$h_0 + \frac{1}{2} U_0^2 \sin^2 \phi_3 = h_3 + \frac{1}{2} U_3^2 \sin^2(\phi_3 - \theta_3) \quad (2.28)$$

where the boundary conditions are:

$$P_2 = P_3 \quad (2.29)$$

$$\theta_3 = \theta_1 + \theta_2 \quad (2.30)$$

It will be shown in Section 2.3.2, using the (P, θ) -plane, that two combinations (families) of SMR are possible, the usual one, in which the reflected shock wave R redeflects the flow so that $\theta_3 = \theta_1 - \theta_2$ and one where the flow is being further deflected while passing through R, i.e., $\theta_3 = \theta_1 + \theta_2$. For $M_0 < 1.55$ in nitrogen (or $M_0 < 1.74$ in argon) only the latter occurs, and hence the plus sign (+) should be used in Eq. 2.30. In the range $1.55 < M_0 < M_{0c}$ in nitrogen (or $1.74 < M_0 < M_{0c}$ in argon) both combinations are possible. For $M_0 > M_{0c}$ only the first combination occurs and hence the minus sign (-) should be used in Eq. 2.30. (Note M_{0c} was introduced in Section 2.2.3.1, where the corresponding value for argon or nitrogen can be found.)

The above fourteen equations have eighteen independent variables, namely $P_0, P_1, P_2, P_3, T_0, T_1, T_2, T_3, U_0, U_1, U_2, U_3, \phi_0, \phi_1, \phi_3, \theta_1, \theta_2$ and θ_3 . Consequently, if four of the eighteen parameters are known the remaining fourteen can be calculated. The four chosen parameters are again the flow pressure P_0 and temperature T_0 ahead of the incident shock wave, the flow velocity $U_0 = U_s \sec \theta_w'$ and the angle of incidence between it and the incident shock wave I, $\phi_0 = 90^\circ - \theta_w'$. Unfortunately, unlike the case of RR, the initial conditions in shock tube experiments, namely P_0, T_0, M_s and θ_w are not sufficient to define these four chosen parameters, since $\theta_w' = \theta_w + \chi$ involves one more parameter χ , which is not known before a photograph of the wave configuration is obtained.

One way of overcoming the problem was suggested by Law and Glass (Ref. 51) who developed a graphical method to obtain $\chi = \chi(P_0, T_0, M_s, \theta_w)$. Their graphical method was in good agreement with experiments (in oxygen) only in the range $25^\circ \leq \theta_w \leq 45^\circ$. However, the present analytical formulation of their graphical method gives better agreement (in nitrogen), over a greater range, i.e., $5^\circ \leq \theta_w \leq 45^\circ$. For the range $\theta_w < 5^\circ$ a new method is suggested (to be discussed subsequently).

2.3.1.1 Prediction of Triple Point Trajectory Angle - χ

As noted, a fairly good method for predicting the values of χ in the range $25^\circ \leq \theta_w \leq 45^\circ$ was developed by Law and Glass (Refs. 48 and 51), based on the experimental observation that, except for very strong shock-wave diffractions, the Mach stem M is only slightly curved. Consequently, they assumed a straight Mach stem normal to the wedge surface, and introduced an additional independent geometrical relation (Fig. 12):

$$\phi_3 = 90^\circ - \chi \quad (2.31)$$

This additional equation together with the fourteen equations of motion (Eqs. 2.17 to 2.30) can now be used to find expressions of the form:

$$\chi = \chi(P_0, T_0, M_s, \theta_w) \quad (2.32)$$

This is done by keeping P_0, T_0 and M_0 constants and changing ϕ_0 [$\phi_0 = 90^\circ - (\theta_w + \chi)$] in small steps, and then finally solving graphically for each set of P_0, T_0, M_0 and ϕ_0 the equations of motion (Eqs. 2.17 to 2.30). Once these

equations are solved χ is calculated from Eq. 2.31 and M_s from the relation $M_s = M_0 \sin \phi_0$. Consequently, for a given value of M_0 , each value of $\theta_w + \chi$ ($90^\circ - \phi_0$) corresponds to a value of M_s and χ . Repeating the above with different values of M_0 but still maintaining the same pressure and temperature (P_0 and T_0) will produce a set of points (M_s, χ) for each ($\theta_w + \chi$). Thus χ vs M_s can be plotted for constant ($\theta_w + \chi$). Using these curves χ can be determined for any M_s and θ_w at a given P_0 and T_0 .

Law and Glass (Ref. 51) found that this method is in good agreement with experimental results only in the range $25^\circ \leq \theta_w \leq 45^\circ$; consequently they suggested that an alternative method should be developed for smaller wedge angles.

An alternative method for very small wedge angles $\theta_w \leq 4^\circ$ is suggested in the following. This method is again based on an experimental fact, i.e., the fact that at small wedge angles an SMR occurs even though the flow behind the incident shock wave I is subsonic ($M_1 < 1$) wrt the reflection point P (Fig. 4a). It has been discussed previously that the triple-point-trajectory angle plays a significant role (at these small wedge angles) when it makes the effective wedge angle $\theta'_w = \theta_w + \chi$ large enough so that M_1 will always be greater than unity wrt the triple point T (Fig. 4b). Consequently, one can easily find a relation of the form $\theta'_w|_{M_1=1} = \theta'_w(M_s, P_0, T_0)$ for which the flow behind the incident shock wave is exactly sonic, i.e., $M_1 = 1$. Once this relation is derived, χ can be found from:

$$\chi = \theta'_w|_{M_1=1} - \theta_w \quad (2.33)$$

It will be shown in Section 7.2 that for very small wedge angles the value of χ predicted by Eq. 2.33 is in better agreement with experimental results than the one obtained by Law and Glass (Eq. 2.32).

Note that although P_0 and T_0 do not appear explicitly in Eq. 2.33 as they do in Eq. 2.32, the first term on the RHS of Eq. 2.33 depends on the initial pressure and temperature and hence both methods of predicting χ have in general the form $\chi = \chi(P_0, T_0, M_s, \theta_w)$.

2.3.1.2 Perfect-Gas Solution

A significant simplification is obtained when the gas under consideration is assumed to be calorically and thermally perfect. The fourteen equations of motion (Eqs. 2.17 to 2.30) are then reduced to the following six equations (Ref. 31):

$$\tan \theta_{1,2,3} = \frac{\frac{P_{1,2,3}}{P_{0,1,0}} - 1}{1 + \gamma M_{0,1,0}^2 - \frac{P_{1,2,3}}{P_{0,1,0}}} \left[\frac{\frac{2\gamma}{\gamma+1} M_{0,1,0}^2 - \frac{\gamma-1}{\gamma+1} - \frac{P_{1,2,3}}{P_{0,1,0}}}{\frac{\gamma-1}{\gamma+1} + \frac{P_{1,2,3}}{P_{0,1,0}}} \right]^{1/2} \quad (2.34, 35, 36)$$

$$\frac{1 + \frac{\gamma - 1}{2} M_0^2}{1 + \frac{\gamma - 1}{2} M_1^2} = \frac{\frac{\gamma + 1}{\gamma - 1} + \frac{P_1}{P_0}}{\frac{\gamma + 1}{\gamma - 1} + \frac{P_0}{P_1}} \quad (2.37)$$

$$\theta_3 = \theta_2 + \theta_1 \quad (2.38)$$

$$\frac{P_3}{P_0} = \frac{P_1}{P_0} \frac{P_2}{P_1} \quad (2.39)$$

This set of six equations involves nine variables, namely, γ , M_0 , M_1 , θ_1 , θ_2 , θ_3 , P_1/P_0 , P_2/P_0 and P_3/P_0 . Consequently, three variables must be defined for a solution. If γ , M_0 and P_1/P_0 are selected, θ_1 and M_1 can be immediately calculated from Eqs. 2.34 and 2.37, respectively, and the number of equations to be solved is reduced to four.

A further simplification was made by Henderson who reduced this system of equations of motion to a single polynomial of degree ten, with the pressure ratio P_3/P_0 as the polynomial variable. The polynomial coefficients were taken to be functions of γ , M_0 and P_1/P_0 . A detailed description is given in Ref. 31. Note that a polynomial of degree ten yields ten mathematical roots. Henderson shows, however, that from simple physical consideration and the possibility of double roots, seven of the ten roots can be discarded. A detailed discussion of the possible roots can be found in Refs. 31 and 48.

2.3.1.3 Imperfect-Gas Solution

When real-gas effects are considered the equations of motion (Eqs. 2.17 to 2.30) cannot be simplified. Consequently, the fourteen nonlinear algebraic equations must be solved. A method of solution, very much the same to the one utilized for RR (Section 2.2.1.2) was developed and solved for the first time.

Note that Eqs. 2.17 to 2.30 consist of three similar sets of four equations each (2.17 to 2.20, 2.21 to 2.24 and 2.25 to 2.28) which are treated separately. The final solution is obtained when Eqs. 2.29 and 2.30 are satisfied. The first set (Eqs. 2.17 to 2.20) involves the following eight variables: P_0 , T_0 , U_0 and ϕ_0 on the LHS and P_1 , T_1 , U_1 and θ_1 on the RHS. Since all variables on the LHS consist of initial conditions and are known, the RHS can be solved and P_1 , T_1 , U_1 and θ_1 obtained.

The second set (Eqs. 2.21 to 2.24) consists again of eight variables: P_1 , T_1 , U_1 and ϕ_1 on the LHS and P_2 , T_2 , U_2 and θ_2 on the RHS; thus by assuming a value of ϕ_1 the LHS becomes known (P_1 , T_1 and U_1 were calculated in the first set) and the RHS can be solved to give P_2 , T_2 , U_2 and θ_2 . The third set (Eqs. 2.25 to 2.28) also consists of eight variables: P_0 , T_0 , U_0 and ϕ_3 on the LHS and P_3 , T_3 , U_3 and θ_3 on the RHS. It is solved in the same fashion as the second set, i.e., assume a value of ϕ_3 so that the LHS becomes known (P_0 , T_0 and U_0 are the initial conditions) and then solve for P_3 , T_3 , U_3 and θ_3 . The

correctly assumed values of ϕ_1 and ϕ_3 are those which will result in values of P_2 , P_3 , θ_1 , θ_2 and θ_3 that will satisfy the boundary conditions, i.e., Eqs. 2.29 and 2.30. Fast convergence is assured by using the Newton-Raphson method. A computer program (based on the above method) as well as a typical output is given in Appendix C.

2.3.2 Graphical Solution (Shock-Polar Presentation)

An SMR in the (P, θ) -plane is shown in Fig. 13. The R-polar does not intersect the P/P_0 -axis, and hence an RR is not possible. State (2) behind the reflected shock wave R, and state (3) behind the Mach stem M, in the vicinity of the triple point T, are at the point where the R-polar intersects the I-polar [state (2) on the R-polar and state (3) on the I-polar], since it satisfies the equations of motion (Eqs. 2.17 to 2.28) as well as the boundary conditions (Eqs. 2.29 and 2.30), i.e., $\theta_3 = \theta_1 - \theta_2$ and $P_3 = P_2$. Note that since the Mach stem is not straight it corresponds to a small portion of I rather than single point (3), see Law and Glass (Ref. 51) for details.

It was stated earlier that a necessary condition for an SMR to exist (once RR is terminated) is that the flow behind the reflected wave R (Fig. 12) is subsonic ($M_2 < 1$) wrt the triple point T. This means that the subsonic portion of R-polar (i.e., the one above the sonic point S_R) intersects with the I-polar. One should note that if the intersection was on the supersonic portion of R (i.e., below S_R) the flow behind it would be supersonic ($M_2 > 1$) and since $\theta_2 \neq 0$ an additional deflecting mechanism would be needed to turn away this supersonic flow from the wedge surface, or make it subsonic before colliding with it.

When $M_0 < M_{0c}$, i.e., when the R-polar becomes tangent to the P/P_0 -axis inside the I-polar (Fig. 10a), the termination of RR will always be followed by an SMR. In this case, the R-polar will intersect the I-polar at a point above its point of maximum deflection, i.e., on the strong-shock family portion. In this range ($M_0 < M_{0c}$) the I and R-polars can take on two basically different combinations. In one of them the solution in the (P, θ) -plane (Fig. 14a) indicates that the flow is ~~redeflected~~ by R so that $\theta_3 = \theta_2 < \theta_1$, while the other combination (Fig. 14b) gives $\theta_3 = \theta_2 > \theta_1$ and hence the flow is being further deflected by R. The present modification of Eq. 2.30 (the boundary condition for the equations of motion) that was presented earlier was made for this reason.

The limiting condition between these two cases is the combination where $\theta_3 = \theta_2 = \theta_1$ (Fig. 14c), for which there is no deflection through R (in the vicinity of the triple point T), i.e., R is normal to the streamlines. The analysis suggests, furthermore, that for $M_0 \leq 1.55$ in nitrogen and $M_0 \leq 1.74$ in argon, only the second combination of the I and R-polars (the one in which $\theta_3 = \theta_2 > \theta_1$) occurs, while for $1.55 < M_0 \leq M_{0c}$ in nitrogen, and $1.74 < M_0 \leq M_{0c}$ in argon, both combinations are possible.

When $M_0 > M_{0c}$ (i.e., the R-polar becomes tangent to the P-axis outside the I-polar, Fig. 10b) two interesting cases exist. In one of them $M_{0c} < M_0 < 2.40$, 2.41 and 2.69 for perfect nitrogen, imperfect nitrogen and argon, respectively, the R-polar intersects the I-polar in the portion between its sonic point S_R and its point of maximum deflection, m_R (Fig. 15), which corresponds to the subsonic portion, and hence $M_2 < 1$ and an SMR will still occur.

For higher values of M_0 , the termination of RR will result in $M_2 > 1$ and hence an SMR is not possible. However, if θ'_w (or θ_w) is decreased and M_0 kept constant the R-polar moves away from the P-axis, and a situation is reached in which once again the R-polar intersects the I-polar at its sonic point s (Fig. 16, R_{ii}). Upon a further decrease of θ_w , the R-polar intersects the I-polar below its sonic point (Fig. 16, R_{iii}) and hence again an SMR is obtained. Thus one can conclude that any value of M_0 can be matched with a corresponding value of ϕ_0 [$\phi_0 = 90^\circ - (\theta_w + \chi)$] for which $M_2 = 1$. The significance of this family of SMR-solutions lies in the experimental fact that it corresponds to an SMR in which the slipstream is curled back, perhaps owing to the extremely high flow deflections involved. (For example, on Figs. 10a and 10b, $\theta_1 \approx 1^\circ$ and 5° , respectively, while in Fig. 16, $\theta_1 > 25^\circ$).

2.3.3 Termination of Single-Mach Reflection

As described earlier, the SMR can be viewed as a reflection process through a three-shock-confluence (I, R and M), by which the flow behind R is made subsonic ($M_2 < 1$), wrt the triple point T, and hence can negotiate the solid surface. However, when the Mach number of the incident shock wave is increased, the flow Mach number behind the reflected shock wave R is also increased, and finally it exceeds the value of one. Consequently, an SMR is no longer sufficient, since again we have a supersonic flow ($M_2 > 1$) directed towards a solid surface ($\theta_2 \neq 0$ always). On the (P, θ)-plane this means that the intersection point between the I and R-polars lies on the supersonic part of the R-polar (Fig. 16, R_i). Physically, this supersonic flow will have to be made either parallel to the solid surface or become subsonic before it reaches the wall by means of a shock wave (or a compression wave) so that it can negotiate the solid surface subsonically. In practice the second process occurs and a CMR forms, where the flow Mach number behind the reflected shock wave is reduced by passing through a compression wave. At higher values of M_2 this compression wave becomes a shock wave and CMR terminates. Henderson and Lozzi (Ref. 60) were the first to suggest this sequence of events, i.e., a band of compression waves which can converge to form a shock wave. The existence of this compression wave was first verified experimentally during this study. The reflection associated with the compression wave is a CMR while the one associated with the shock wave is a DMR.

2.4 Complex-Mach Reflection (CMR)

The CMR shock-wave configuration is shown in Fig. 17. Unlike the case of an SMR where the reflected shock wave R has continuous (smooth) curvature until it finally terminates at the surface, here the curvature reverses discontinuously. (In some CMR only a smooth reversal of curvature takes place.) As a result a kink forms in the reflected shock wave. R is straight between the triple point T and the kink K, but the remaining portion curves continuously until it terminates at the wall. It will be shown that a compression wave is located at the kink. When it converges to form a shock wave in DMR, the kink becomes the second triple point.

2.4.1 Graphical Solution (Shock-Polar Presentation)

As mentioned previously, the existence of a band of compression waves suggested by Henderson and Lozzi (Ref. 60) was verified experimentally during the present study. In order to solve the problem analytically or

graphically it is assumed that this compression wave exists between the kink K (Fig. 17) of the reflected wave R and the slipstream S. Consequently, the flow from region (2) is compressed (by passing through this compression wave) to a new higher-pressure state (region 5). Furthermore, we impose the boundary condition that the pressure and flow direction in states (4) and (5) are equal, and hence they correspond to a single point in the (P, θ) -plane.

The solution is no longer as simple as in the RR or SMR case, since the kink and its vicinity should be treated from a frame of reference attached to the kink. Thus the solution must be done in two steps: first, when the frame of reference is attached to the triple point T, and then when it is attached to the kink. Consequently, the relative motion of the kink wrt the triple point should be known (see Appendix D).

Figure 18 represents the graphical solution of a CMR. States (0), (1), (2) and (3) are found in the same way as for an SMR (see Section 2.3.2), and states (1'), (2') and (3') are found in the same way as for a DMR (see subsequent discussion in Section 2.5.2).

Once state (2') is found, the (P, θ) -curve of the compression wave should be drawn from (2'). Unfortunately, real-gas effects prevent derivation of an explicit algebraic formula of the (P, θ) -curve of a compression wave. In order to overcome this difficulty, assume that the compression process is perfect (reasonable for such a weak compression) and make use of the Prandtl-Meyer function, $-\theta + \text{const} = \nu(M)$, where θ is the deflection angle measured wrt the direction of a given flow with Mach number M , and $\nu(M)$ is the Prandtl-Meyer function (Ref. 27).

Let any point inside the compression be denoted by i so that:

$$-\theta_i + \text{const} = \nu(M_i) \quad (2.40)$$

where:

$$\nu(M) = \sqrt{\alpha} \tan^{-1} \sqrt{\alpha(M^2 - 1)} - \tan^{-1} \sqrt{M^2 - 1} \quad (2.41)$$

Equation 2.40 holds also in state (2'), Fig. 18, and hence:

$$-\theta'_2 + \text{const} = \nu(M'_2)$$

Defining $\theta'_2 = 0$ results in:

$$\text{const} = \nu(M'_2) \quad (2.42)$$

Inserting Eq. 2.42 into Eq. 2.40 gives:

$$\theta_i = \nu(M'_2) - \nu(M_i) \quad (2.43)$$

The isentropic relations

$$\frac{P_0}{P_1} = \left[1 + \frac{\gamma-1}{2} M_1^2 \right]^{\frac{\gamma}{\gamma-1}}$$

$$\frac{P_0}{P_2} = \left[1 + \frac{\gamma-1}{2} (M_2')^2 \right]^{\frac{\gamma}{\gamma-1}}$$

are employed to obtain:

$$\frac{P_1}{P_2} = \left[\frac{1 + \frac{\gamma-1}{2} (M_2')^2}{1 + \frac{\gamma-1}{2} M_1^2} \right]^{\frac{\gamma}{\gamma-1}}$$

(Note that $P_2 = P_2'$.) Rearrangement of the above equations results in:

$$M_1^2 = \left[\frac{2}{\gamma-1} + (M_2')^2 \right] \left[\frac{P_2}{P_1} \right]^{\frac{\gamma-1}{\gamma}} - \frac{2}{\gamma-1} \quad (2.44)$$

Inserting Eq. 2.44 into Eq. 2.43 yields a relation of the form:

$$\theta_1 = v(M_2') - f(M_2', P_2, P_1) \quad (2.45)$$

where

$$v(M_2') = \sqrt{\alpha} \tan^{-1} \sqrt{\alpha[(M_2')^2 - 1]} - \tan^{-1} \sqrt{(M_2')^2 - 1}$$

and

$$f(M_2', P_2, P_1) = \sqrt{\alpha} \tan^{-1} \sqrt{\alpha \left\{ \left[\frac{2}{\gamma-1} + (M_2')^2 \right] \left[\frac{P_2}{P_1} \right]^{\frac{\gamma-1}{\gamma}} - \alpha \right\}} \\ - \tan^{-1} \sqrt{\left[\frac{2}{\gamma-1} + (M_2')^2 \right] \left[\frac{P_2}{P_1} \right]^{\frac{\gamma-1}{\gamma}} - \alpha}$$

Since M_2' and P_2 are known [state (2') was already found], Eq. 2.45 represents the (P, θ) -relation across a perfect compression wave.

Once this curve is drawn from state (2'), states (4) and (5) are obtained at the point where this curve intersects the R'-polar. State (4) is on the R'-polar while state (5) is on the compression wave polar.

Note that since the compression wave under consideration is weak it can be replaced by a weak shock wave. For this case, the CMR graphical solution becomes the same as the DMR graphical solution that is given in Section 2.5.2.

2.4.2 Termination of Complex-Mach-Reflection

It has been found in the present study that when the flow Mach number, M_2' , behind the reflected shock wave R becomes supersonic in a frame of reference attached to the kink K (Fig. 17), then CMR terminates resulting in DMR (Fig. 19). The kink K becomes the second triple point T_1 . The portion of the reflected shock wave R, between T and T_1 , is straight. The two triple points and their flow and wave systems are shown in Fig. 20. In the following the appropriate expression for M_2' , i.e., the flow Mach number behind the reflected shock wave in a frame of reference attached to the kink is developed.

Consider Fig. 21 in which the kink K (or the second triple point T_1) moves with the velocity V_{T_1T} (or V_{KT}) wrt the first triple point T. The flow velocity behind the reflected shock wave R, $V_{2T} \equiv U_2$ is directed along a line that is inclined with an angle $\phi_1 - \theta_2$ to the direction of motion of the kink. Consequently, using simple vector analysis and the (x, y)-coordinate system shown in Fig. 21,

$$V_{2T_1}^x = V_{2T} \cos(\phi_1 - \theta_2) - V_{T_1T}$$

$$V_{2T_1}^y = V_{2T} \sin(\phi_1 - \theta_2)$$

where $V_{2T_1}^x$ and $V_{2T_1}^y$ are the x and y components of the velocity of the flow behind R wrt the kink K or the second triple point T_1 . Thus the absolute flow velocity wrt K becomes:

$$|V_{2T_1}| = [V_{2T}^2 + V_{T_1T}^2 - 2V_{2T}V_{T_1T} \cos(\phi_1 - \theta_2)]^{1/2}$$

Rearranging the above expression results in:

$$V_{2T_1} = V_{2T} \left[1 + \left(\frac{V_{T_1T}}{V_{2T}} \right)^2 - 2 \left(\frac{V_{T_1T}}{V_{2T}} \right) \cos(\phi_1 - \theta_2) \right]^{1/2}$$

and in terms of Mach numbers one obtains:

$$M_2' = M_2 \left[1 + \left(\frac{V_{T_1T}}{V_{2T}} \right)^2 - 2 \left(\frac{V_{T_1T}}{V_{2T}} \right) \cos(\phi_1 - \theta_2) \right]^{1/2} \quad (2.46)$$

The velocity of the second triple point T_1 wrt the first triple point T, developed in Appendix D, is given by:

$$V_{T_1T} = \frac{\rho_0}{\rho_1} \operatorname{cosec}(\phi_1 + \phi_0 - \theta_1) U_s \quad (2.47)$$

Note that the above expression for V_{T_1T} (see Appendix D for details) is based on an analytical method for predicting the location of the kink originally

suggested by Law and Glass (Refs. 48, 51). Their method was found to be in very good agreement with experiments only in the range $\theta_w \leq 40^\circ$, while for the range $\theta_w > 40^\circ$ the agreement became progressively worse (Ref. 46).

2.5 Double-Mach Reflection (DMR)

When the flow Mach number M_2' behind the reflected shock wave R (in a frame of reference attached to the second triple point T_1) exceeds the value of one, a shock wave is formed at the kink of the CMR, and consequently a DMR is obtained. The shock wave configuration of a DMR is shown in Fig. 19. The additional shock wave R_1 results in a second triple point T_1 , and a second slipstream S_1 , since the flow behind T_1 is obtained from state (1) by passing through either one shock wave (M_1) or two shock waves (R and R_1). The first triple point trajectory angle is again χ while the second triple point trajectory angle is χ' .

States (1), (2) and (3) can be found by solving Eqs. 2.17 to 2.30. It is worth mentioning that the major assumption behind Eqs. 2.17 to 2.30 is that states (0), (1), (2) and (3) are uniform. Consequently, one can conclude that they describe the first triple point of a DMR better than that of an SMR since in a DMR state (2) is supersonic and it is obtained from state (1) through a straight shock wave (R). Recall that in the case of an SMR, R is curved and hence the flow behind it is not uniform. Note that Eqs. 2.17 to 2.30 are applicable only in the vicinity of the triple point with a confluence of curved shock waves, and further away from it when the shock waves are straight.

2.5.1 Analytical Formulation

The analytical formulation is based on the similarity between the flow fields associated with the first and second triple points. Consider Figs. 20a and 20b, which describe the flow fields in the vicinity of T and T_1 respectively. Let the notation $a \equiv b$ mean that symbol 'b' in Fig. 20b is equivalent (analogous) to symbol 'a' in Fig. 20a; thus one can write:

$$\begin{aligned} \text{state (1)} &\equiv \text{state (0)}, \text{state (2)} \equiv \text{state (1)}, \text{state (5)} \equiv \text{state (2)}, \\ \text{state (4)} &\equiv \text{state (3)}; \end{aligned}$$

$$R \equiv I, R_1 \equiv R, M_1 \equiv M, S_1 \equiv S;$$

$$U_1' \equiv U_0, U_2' \equiv U_1, U_5' \equiv U_2, U_4' \equiv U_3;$$

$$\theta_2' \equiv \theta_1, \theta_5' \equiv \theta_2, \theta_4' \equiv \theta_3;$$

and finally,

$$\phi_1' \equiv \phi_0, \phi_2' \equiv \phi_1 \text{ and } \phi_4' \equiv \phi_3.$$

Applying this analogy to Eqs. 2.17 to 2.30 will result in the equations of motion for the second triple point.

For R:

$$\rho_1 \tan \phi'_1 = \rho_2 \tan(\phi'_1 - \theta'_2) \quad (2.48)$$

$$\rho_1 U'_1 \sin \phi'_1 = \rho_2 U'_2 \sin(\phi'_1 - \theta'_2) \quad (2.49)$$

$$P_1 + \rho_1 U'^2_1 \sin^2 \phi'_1 = P_2 + \rho_2 U'^2_2 \sin^2(\phi'_1 - \theta'_2) \quad (2.50)$$

$$h_1 + \frac{1}{2} U'^2_1 \sin^2 \phi'_1 = h_2 + \frac{1}{2} U'^2_2 \sin^2(\phi'_1 - \theta'_2) \quad (2.51)$$

For R₁:

$$\rho_2 \tan \phi'_2 = \rho_5 \tan(\phi'_2 - \theta'_5) \quad (2.52)$$

$$\rho_2 U'_2 \sin \phi'_2 = \rho_5 U'_5 \sin(\phi'_2 - \theta'_5) \quad (2.53)$$

$$P_2 + \rho_2 U'^2_2 \sin^2 \phi'_2 = P_5 + \rho_5 U'^2_5 \sin^2(\phi'_2 - \theta'_5) \quad (2.54)$$

$$h_2 + \frac{1}{2} U'^2_2 \sin^2 \phi'_2 = h_5 + \frac{1}{2} U'^2_5 \sin^2(\phi'_2 - \theta'_5) \quad (2.55)$$

For M₁:

$$\rho_1 \tan \phi'_4 = \rho_4 \tan(\phi'_4 - \theta'_4) \quad (2.56)$$

$$\rho_1 U'_1 \sin \phi'_4 = \rho_4 U'_4 \sin(\phi'_4 - \theta'_4) \quad (2.57)$$

$$P_1 + \rho_1 U'^2_1 \sin^2 \phi'_4 = P_4 + \rho_4 U'^2_4 \sin^2(\phi'_4 - \theta'_4) \quad (2.58)$$

$$h_1 + \frac{1}{2} U'^2_1 \sin^2 \phi'_4 = h_4 + \frac{1}{2} U'^2_4 \sin^2(\phi'_4 - \theta'_4) \quad (2.59)$$

And finally the boundary conditions are:

$$P_5 = P_4 \quad (2.60)$$

$$\theta'_4 = \theta'_2 + \theta'_5 \quad (2.61)$$

Since thermodynamic properties do not depend on the frame of reference of the solution $\rho'_1 = \rho_1$, $\rho'_2 = \rho_2$, etc, and hence the prime was omitted from the thermodynamic variables in the above equations.

It has been shown in Section 2.3.1.3 that once P_0 , T_0 , U_0 and ϕ_0 are known, Eqs. 2.17 to 2.30 can be solved. Thus, in order to solve Eqs. 2.48 to 2.61, P_1 , T_1 , U_1' and ϕ_1' should be defined. In the following expressions for U_1' and ϕ_1' are developed. (Note that P_1 and T_1 are known from the solution of Eqs. 2.17 to 2.30).

Consider Fig. 21 in which the second triple point T_1 moves along the x-axis (defined by the direction of the reflected shock R) with the velocity $V_{T_1 T}$ wrt the first triple point T. Simple vector analysis yields that:

$$V_{1T_1}^x = V_{1T} \cos \phi_1 - V_{T_1 T}$$

$$V_{1T_1}^y = V_{1T} \sin \phi_1$$

where $V_{1T_1}^x$ and $V_{1T_1}^y$ are the x and y components of the velocity of the flow in state (1) wrt the second triple point T_1 , i.e., the x and y components of U_1' . The value of U_1' then becomes:

$$U_1' = (U_1^2 + V_{T_1 T}^2 - 2U_1 V_{T_1 T} \cos \phi_1)^{1/2}$$

whereas the value of ϕ_1' is:

$$\phi_1' = \tan^{-1} \left(\frac{U_1 \sin \phi_1}{U_1 \cos \phi_1 - V_{T_1 T}} \right)$$

Inserting the value of $V_{T_1 T}$ (Eq. D.3 in Appendix D) into the above two equations results in:

$$U_1' = (U_1^2 + L^2 U_s^2 - 2L U_1 U_s \cos \phi_1)^{1/2} \quad (2.62)$$

$$\phi_1' = \tan^{-1} \left(\frac{U_1 \sin \phi_1}{U_1 \cos \phi_1 - L U_s} \right) \quad (2.63)$$

where $L = L_1/L_s$ and L_1 and L_s , defined in Fig. D.1a, should be measured from an actual interferogram.

It is mentioned in Appendix D that Law and Glass (Ref. 51) developed an analytical method to predict L in the range $\theta_w \leq 40^\circ$ (Eq. D.12). Using their method one obtains:

$$L = \frac{\rho_0}{\rho_1} \operatorname{cosec}(\phi_1 + \phi_0 - \theta_1) \quad (2.64)$$

Thus for the range $\theta_w \leq 40^\circ$ Eqs. 2.62 and 2.63 reduce to:

$$U_1' = \left[U_1^2 + \left(\frac{\rho_o}{\rho_1} \right)^2 U_s^2 \operatorname{cosec}^2(\phi_1 + \phi_o - \theta_1) - 2U_1 U_s \left(\frac{\rho_o}{\rho_1} \right) \operatorname{cosec}(\phi_1 + \phi_o - \theta_1) \cos \phi_1 \right]^{1/2}$$

$$\phi_1' = \tan^{-1} \left[\frac{U_1 \sin \phi_1}{U_1 \cos \phi_1 - \frac{\rho_o}{\rho_1} U_s \operatorname{cosec}(\phi_1 + \phi_o - \theta_1)} \right]$$

A further simplification can be made using Eq. 2.18 and the relation $U_s = U_o \sin \phi_o$ that together result in

$$\frac{\rho_o}{\rho_1} U_s = U_1 \sin(\phi_o - \theta_1)$$

Inserting this relation into the above expressions for U_1' and ϕ_1' results in

$$U_1' = U_1 \left[1 + \frac{\sin^2(\phi_o - \theta_1)}{\sin^2(\phi_1 + \phi_o - \theta_1)} - 2 \frac{\sin(\phi_o - \theta_1) \cos \phi_1}{\sin(\phi_1 + \phi_o - \theta_1)} \right]^{1/2} \quad (2.65)$$

$$\phi_1' = \tan^{-1} \left[\frac{\sin \phi_1}{\cos \phi_1 - \sin(\phi_o - \theta_1) \operatorname{cosec}(\phi_1 + \phi_o - \theta_1)} \right] \quad (2.66)$$

Using trigonometric functions Eq. 2.66 can be finally reduced to

$$\phi_1' = \phi_1 + \phi_o - \theta_1 \quad (2.67)$$

Since all the variables in Eqs. 2.66 and 2.67 are known once Eqs. 2.17 to 2.30 are solved, the 4 required parameters, P_1 , T_1 , U_1' and ϕ_1' , for solving Eqs. 2.48 to 2.61 are analytically determined. It will be shown later that in spite of the limitation on the wedge angle ($\theta_w \leq 40^\circ$) that was introduced by the use of Eq. 2.64 in the foregoing development, Eqs. 2.66 and 2.67 can almost always be used since the DMR domain is centred in this angular range..

2.5.2 Graphical Solution (Shock-Polar Presentation)

The graphical solution of DMR is akin to CMR described in Section 2.4.1. The solution is again done in two steps, first with the frame of reference attached to the triple point T and then when it is attached to the second triple point T_1 . The relative-motion relations of the second triple point T_1 wrt the first triple point T are given in Appendix D. Once they are

known the solution is as follows. First attach the frame of reference to the triple point T and draw the I and R-polars (Fig. 22a) in the same way as described in Section 2.3.2. States (2) and (3) are at the point where the I and R-polars intersect. Note that the flow directions in states (0), (1), (2) and (3) are all measured wrt the first triple point trajectory, i.e., $\theta_0 = 0$, since the flow in state (0) moves parallel to the first triple point trajectory. Consider now Fig. 22b in which θ and θ' are the angles corresponding to the same direction measured in two different frames of reference T and T_1 , respectively. Simple geometrical consideration yields:

$$\theta = \theta' + (\chi' - \chi) \quad (2.68)$$

or alternatively:

$$\theta = \theta' + (\phi_0 - \phi'_0) \quad (2.69)$$

where $\phi_0 = 90^\circ - \theta_w - \chi$ and $\phi'_0 = 90^\circ - \theta_w - \chi'$ (ϕ'_0 is given by Eq. D.14). Rearranging Eq. 2.69 results in:

$$\theta' = \theta - (\phi_0 - \phi'_0) \quad (2.70)$$

Consequently, state (1) in a frame of reference attached to T_1 is at $\theta'_1 = \theta_1 - (\phi_0 - \phi'_0)$ and $P'_1 = P_1$ (no change in thermodynamic properties by changing a frame of reference). Once state (1') is known, the R'-polar (i.e., the R-polar in a frame of reference attached to T_1) that corresponds to M'_1 (Eq. 2.65), $P'_1 = P_1$ and $T'_1 = T_1$ is constructed. States (2') and (3') are at the point where a constant pressure line drawn from states (2) and (3) intersects the R'-polar. Once state (2') is known the R_1 -polar (M'_2 , $P'_2 = P_2$ and $T'_2 = T_2$) is drawn. States (4) and (5) (Fig. 19) are at the point where the R_1 -polar intersects the R'-polar. The initial conditions for the case illustrated in Fig. 22a are $M_s = 3.681$, $\theta_w = 40^\circ$, $\chi = 4.8^\circ$, $P_0 = 15.3$ torr and $T_0 = 297.4$ K. Consequently the corresponding values for the I polar are $M_0 = 5.189$, $P_0 = 15.3$ torr and $T_0 = 297.4$ K. The first triple-point solution results in $M_1 = 1.984$, $P_1 = 239.6$ torr, $T_1 = 1062.2$ K, $P_2 = 474.2$ torr, $T_2 = 1302.9$ K, $\theta_1 = 32.26^\circ$ and $\phi_1 = 43.10^\circ$. Therefore the R-polar that corresponds to M_1 , P_1 and T_1 is drawn from a point $\theta = \theta_1$ on the I polar. Using the above listed values and Eq. D.14 results in $\phi'_0 = 42.6^\circ$ and hence (1') is shifted by 2.6° ($\phi_0 - \phi'_0$) from state (1) along a constant pressure line. With the help of Eq. 2.65 and the above values one finds that $M'_1 = 0.8237 \times M_1 = 1.634$ and the R'-polar that corresponds to M'_1 , P_1 and T_1 is drawn from state (1'). States (2') and (3') are at the point where a constant pressure line drawn from (2) and (3) intersects the R'-polar, i.e., $P'_2 = P_2 = 474.2$ torr. The present solution from the R'-polar yields $P'_2 = 474.2$ torr, $T'_2 = 1269.6^\circ$, $M'_2 = 1.125$. Consequently a polar corresponding to these values was drawn from states (2') and (3') to obtain states (4') and (5') or (4) and (5) at the intersection of this polar with the R'-polar. Note that although $T'_2 \neq T_2$ probably due to the use of Eq. 2.64, the relative error is only 2.55%.

2.5.3 Prediction of the Second Triple-Point-Trajectory Angle χ'

The second triple-point-trajectory angle χ' can be expressed by using Fig. D.1a as follows:

$$\chi' = 90^\circ - \theta_w - \phi'_0 \quad (2.71)$$

Inserting the value of ϕ'_0 (Eq. D.14) into Eq. 2.71 results in:

$$\chi' = 90^\circ - \theta_w - \tan^{-1} \left[\frac{1 - \frac{\rho_0}{\rho_1}}{\cot \phi_0 - \frac{\rho_0}{\rho_1} \cot(\phi_1 + \phi_0 - \theta_1)} \right] \quad (2.72)$$

Thus for a set of given initial conditions P_0 , T_0 , M_s and θ_w the value of χ (the first triple-point-trajectory angle) can be calculated using the appropriate method (given in Section 2.3.1.1). Once χ is known, ϕ_1 , θ_1 and ρ_1 can be found by solving Eqs. 2.17 to 2.30. (Note that $\phi_0 = 90^\circ - \theta_w - \chi$ and $M_0 = M_s \csc \phi_0$), and consequently χ' can be calculated from Eq. 2.72.

It should be mentioned again that although this method of predicting χ' is limited to $\theta_w \leq 40^\circ$ (see Appendix D for details) it can be used here since the DMR-domain exists mainly in this range (see subsequent discussions). Recall that Appendix D was developed in general for the kink K of a CMR as well as the second triple point T_1 of a DMR. Consequently this method of predicting χ' is applicable also for a CMR for which χ' is defined as the kink trajectory angle.

2.5.4 Termination of Double-Mach Reflection

Following the gasdynamic reasons for the formation of the kink in a CMR (i.e., termination of SMR) where the flow in state (2) behind R (Fig. 12) became supersonic wrt T, and then the formation of DMR (i.e., termination of CMR) when the flow in state (2) became supersonic wrt K (Fig. 17), one might assume that if the flow Mach number in state (4) behind M_1 exceeds the value of unity wrt the second triple point T_1 (Fig. 19) a new kink will form on M_1 and DMR will terminate. If the flow in state (4) becomes supersonic wrt this new kink a triple-Mach reflection (TMR) can form.

In order to verify the above hypothesis, reflections must be obtained using very strong incident shock waves as well as long compression models in order to allow the shock wave configuration to develop to a significant size.

Unfortunately, experiments with high Mach numbers ($M_s > 8$) involve the risk of damaging the interferometric-quality windows. Consequently it was not possible to verify the existence of TMR in the present facility.

2.6 Nonstationary-Oblique Shock-Wave Reflection in (M_s, θ'_w) -Plane

The formation and termination criteria for RR, SMR, CMR and DMR having been established can be shown on the (M_s, θ'_w) -plane to give the domains

of the different reflection processes and their boundaries. A necessary condition for a reflection to occur is that the flow behind the incident shock wave I must be supersonic ($M_1 > 1$) wrt the reflection point P (in the case of RR) or the triple point T (for the other reflections) (Figs. 4a and 4b, respectively). Thus the (M_s, θ_w') -plane [(M_0, ϕ_0) -plane] can be divided into two major domains. One of them corresponds to $M_1 < 1$, where shock-wave reflection is not possible and the other corresponds to $M_1 > 1$ where shock reflections occur. This region of shock-wave reflection is then divided into four domains corresponding to the four reflection processes, i.e., RR, SMR, CMR and DMR.

The criterion for predicting the termination of RR makes use of the boundary condition that the flow downstream of the reflection point (Fig. 7) must be parallel to the wall, i.e., $\theta_2 + \theta_1 = 0$ (Eq. 2.9). When this condition is violated (i.e., ϕ_0 increases to a point where θ_1 exceeds the detachment angle (θ_{2m}) in state (1) (Fig. 7), RR terminates. Therefore, the termination criterion is:

$$\theta_1 + \theta_{2m} = 0 \quad (2.73)$$

When RR terminates, 3 different types of reflection, i.e., SMR, CMR and DMR, can occur depending on the Mach number of the flow behind the reflected shock wave R. As long as the flow behind R is subsonic wrt the first triple point T, an SMR occurs. When this flow becomes supersonic wrt T, SMR terminates and a CMR forms. Consequently, the termination criterion for SMR and the formation criterion for CMR is:

$$M_2 = 1 \quad (2.74)$$

CMR terminates when the flow behind R becomes supersonic wrt the kink K. Therefore the termination criterion for CMR and the formation criterion for DMR is:

$$M'_2 = 1 \quad (2.75)$$

It is worthwhile mentioning that the line $M'_2 = 1$ corresponds approximately to $M_2 = 1.30$ in both nitrogen and argon. Alternatively one may use the following empirical criteria for the existence of SMR, CMR and DMR in nitrogen and argon. SMR occurs only if:

$$M_2 < 1 \quad (2.76)$$

A CMR takes place when:

$$1 < M_2 < 1.3 \quad (2.77)$$

A DMR results for all

$$M_2 > 1.3 \quad (2.78)$$

In the following the domains of RR, SMR, CMR and DMR in the (M_s, θ_w') -plane are given. Note that $\theta_w' = \theta_w + \chi$ in the domains of SMR, CMR and DMR

while in the RR domain $\theta'_w = \theta_w$ since $\chi = 0$ by definition. Note also that since $M_0 = M_s \sec \theta'_w$ and $\phi_0 = 90^\circ - \theta'_w$ one might assume that the reflection domains apply to steady flows as well. However, it will be shown later that in a steady flow CMR and DMR cannot occur due to geometrical limitation, and that the termination criterion of RR is different to that described by Eq. 2.73. Therefore the following domains are for nonstationary flows only.

2.6.1 Regions and Transition Boundaries in a Diatomic Gas-Nitrogen

The domains of RR, SMR, CMR, DMR and NR and the boundaries between them in the (M_s, θ'_w) -plane for nitrogen are shown in Fig. 23. The dashed boundary lines are for a perfect gas ($\gamma = 1.4$) while the solid lines account for real-gas effects (vibration, rotation-vibration coupling and dissociation) with four different initial pressures: $P_0 = 1, 10, 100$ and 1000 torr and a constant initial temperature $T_0 = 300$. It can be seen that the imperfect-gas boundary lines start to diverge from those of a perfect gas at very low incident shock wave Mach numbers owing to temperature-dependent vibrational excitation. At higher values of M_s each boundary line splits and diverges according to its initial pressure as a result of dissociation. At still higher shock Mach numbers electronic excitation and ionization would play a similar role. Under such conditions the sharp boundary lines which exist for a perfect gas between the domains of the different types of reflection are replaced by a multiplicity of lines depending on the initial pressure. For example, one should expect an RR for $M_s = 10$ and $\theta'_w = 45^\circ$ when the initial pressure is 1000 torr or more and a DMR when $P_0 = 100$ torr or less. As M_s approaches unity the line $\theta_1 + \theta_{2m}$ approaches the line $M_1 = 1.00$. These two lines are coincident at the origin $M_s = 1, \theta'_w = 0$.

It can be seen from Fig. 23 that if the shock Mach number M_s is fixed while varying the effective wedge angle θ'_w (i.e., the actual wedge angle θ_w), then different domains of reflection are encountered. This figure clears up some problems and disagreements between various investigators who reported different sequences of events as one passed through a range of wedge angles θ_w for a fixed M_s . They were unaware of the domains and boundaries presented in Fig. 23. The different sequences of events (and experimental and numerical investigations) are summarized as follows: $1.00 < M_s < 1.60$ (see point a) $RR \rightarrow SMR$ (Bleakney and Taub, Ref. 10), $1.60 < M_s < 2.69$ (see point b), $RR \rightarrow CMR \rightarrow SMR$ (Smith, Ref. 6), for $M_s > 2.69$, $RR \rightarrow DMR \rightarrow CMR \rightarrow SMR$ (Kutler et al, Ref. 63, and Shankar et al, Ref. 64). RR and SMR can occur with a proper choice of θ'_w (or θ_w) for any incident shock wave Mach number M_s , while the other reflections are limited to defined values of M_s , e.g., CMR occurs only for $M_s > 1.60$ (see point a) and DMR only for $M_s > 2.69$ (see point b).

2.6.2 Regions of Transition Boundaries in a Monatomic Gas-Argon

The domains of RR, SMR, CMR, DMR and NR, and the boundaries between them in the (M_s, θ'_w) -plane for argon are shown in Fig. 24. The dashed boundary lines are for a perfect gas ($\gamma = 5/3$) while the solid lines account for real-gas effects (electronic excitation and ionization) with four different initial pressures: $P_0 = 1, 10, 100$ and 1000 torr and a constant initial temperature $T_0 = 300$ K.

Unlike a diatomic gas (Fig. 23) the imperfect-gas boundary lines start to diverge from those of a perfect gas only at relatively high incident

shock wave Mach numbers. Therefore, the perfect-gas theory is adequate in the range $M_s < 5.36$ for $P_0 \geq 1$ torr, $T_0 = 300$ K (the point where the RR imperfect-gas boundary lines start to diverge). It should be noted, however, that as the initial pressure (P_0) decreases the corresponding imperfect-gas boundary line splits at a lower value of M_s . For example, the imperfect-gas boundary lines for the termination of SMR ($M_2 = 1$) split at $M_s = 7.62, 8.15, 8.50$ and 8.77 for $P_0 = 1, 10, 100$ and 1000 torr, respectively. Therefore, the sharp boundary lines which exist for a perfect gas between domains of different reflections are replaced by a multiplicity of lines depending on the initial pressure (when the temperature is fixed). Consequently, one can expect an SMR for $M_s = 10$ and $\theta_w = 30^\circ$ when $P_0 > 100$ torr and a CMR when $P_0 < 100$ torr.

It can again be seen from Fig. 24 that if the incident shock wave Mach number is fixed while varying the effective wedge angle θ_w' (or θ_w), different domains of reflections are encountered. The different sequences of events are: $1.00 < M_s < 1.85$, RR \rightarrow SMR (point a), $1.85 < M_s < 3.17$, RR \rightarrow CMR \rightarrow SMR (point b), for $M_s > 3.17$, RR \rightarrow DMR \rightarrow CMR \rightarrow SMR. RR and SMR can occur with a proper choice of θ_w (or θ_w') for any incident shock wave Mach number M_s , while the other reflections are limited to definite values of M_s , e.g., CMR can occur only for $M_s > 1.85$ (point a) and DMR only for $M_s > 3.17$ (point b).

3. FLOW DEFLECTION PROCESS OVER A WEDGE CORNER

It has been mentioned earlier (Section 2.1) that the diffraction process in nonstationary flows also depends on the flow-deflection process of the flow induced by the incident shock wave over the corner.

Consider a planar shock wave propagating in a shock tube and denote the state behind it as (2'). For any given set of initial conditions (P_0, T_0) and incident shock wave Mach number M_s , the induced flow Mach number M_2' , as well as the pressure and temperature (P_2' and T_2') can be calculated. Consequently, the corresponding sonic deflection angle θ_{s2}' , and the angle of maximum deflection (detachment angle) θ_{m2}' , can be determined.

Thus the (M_s, θ_w)-plane is now divided into two main regions; one corresponds to $M_2' < 1$, where the induced flow is subsonic and hence turns over the corner subsonically (Fig. 5a), and the other corresponding to $M_2' > 1$ where the flow is supersonic. The latter region is subdivided into three regions of different flow deflection processes (Ref. 36);

- (1) $0 < \theta_w < \theta_{s2}'$, for deflection through a straight and attached oblique shock wave (Fig. 5b).
- (2) $\theta_{s2}' < \theta_w < \theta_{m2}'$, for deflection through a curved and attached shock wave (Fig. 5c).
- (3) $\theta_w > \theta_{m2}'$, where the deflection is through a curved and detached shock wave (Fig. 5d).

Since the maximum separation between θ_{m2}' and θ_{s2}' is usually very small (for nitrogen at $P_0 = 15$ torr and $T_0 = 300$ K, $\theta_{m2}' - \theta_{s2}' = 0.63^\circ$) only two regions $0 < \theta_w < \theta_{m2}'$, where the shock wave is attached, and $\theta_w > \theta_{m2}'$, where the shock wave is detached, need be considered for practical purposes.

3.1 Flow Deflection Process in a Diatomic Gas - Nitrogen

The above-mentioned regions of different types of deflection processes for nitrogen are shown in the (M_s, θ_w) -plane in Fig. 25. The dashed line is for a perfect gas ($\gamma = 1.4$), while the solid lines are for imperfect nitrogen with different initial pressures ($P_0 = 1, 10, 100$ and 1000 torr) and fixed initial temperature ($T_0 = 300$ K). One should note that the line $M_2' = 1$ corresponds to $M_s = 2.068$ (for a perfect gas) and 2.055 when vibrational energy is included. Since the difference between these two values of M_s is too small to be plotted, only one line is shown. It can be seen from Fig. 25 that the deflection process depends strongly on real-gas effects (i.e., initial pressure P_0 for a given temperature T_0). For $M_s = 10$ and $\theta_w = 35^\circ$ the flow will negotiate the corner through a detached shock wave if $P_0 \leq 1$ torr or through an attached shock wave if $P_0 \geq 10$ torr.

Since the imperfect-gas boundary line diverges from the perfect gas even at the lowest value of M_s one must conclude that the perfect-gas theory is not adequate and imperfect-gas theory should be used.

3.2 Flow Deflection Process in a Monatomic Gas - Argon

The regions of different types of reflection processes for argon in the (M_s, θ_w) -plane are shown in Fig. 26. Again the dashed line is for a perfect gas ($\gamma = 5/3$) while the solid lines are for imperfect argon with different initial pressures ($P_0 = 1, 10, 100$ and 1000 torr) and a constant initial temperature ($T_0 = 300$ K).

Unlike the case of a diatomic gas (see Fig. 25) the imperfect-gas boundary lines start to diverge from the perfect-gas lines at quite high values of M_s (i.e., $M_s = 7.36$) and consequently the perfect-gas theory is adequate in the range $M_s \leq 7.36$. It is worthwhile mentioning that the line $M_2' = 1$ corresponds to $M_s = 2.758$ for both perfect and imperfect gases.

The dependence of the deflection process on real-gas effects (at high values of M_s) is again clearly seen (Fig. 26). For $M_s = 10$ and $\theta_w = 10^\circ$ the flow will negotiate the corner through an attached shock wave if $P_0 \leq 10$ torr or through a detached shock wave if $P_0 \geq 100$ torr. Note that unlike a diatomic gas (Fig. 25) the region that corresponds to a deflection with the aid of an attached shock wave is very small compared to the regions of detached shock wave and subsonic turning. Therefore, in general (unless the wedge angles are very small and the initial pressures very low), only two flow deflection processes will be observed, i.e., a subsonic turning over the corner or a turn with the aid of a detached shock wave.

4. SHOCK-WAVE DIFFRACTION PROCESS IN NONSTATIONARY FLOWS

The two independent phenomena discussed in the previous chapters, i.e., shock reflection (Section 2) and flow deflection (Section 3) interact and give rise to the overall shock-wave diffraction phenomenon. To show this process the figures corresponding to shock-wave reflection (Figs. 23 and 24 for nitrogen and argon, respectively) and the figures for flow deflection (Fig. 25 for nitrogen and Fig. 26 for argon) are superimposed. However, the vertical axis of Figs. 23 and 24 and that of Figs. 25 and 26 are different.

In Figs. 23 and 24 the vertical axis is θ'_w while in Figs. 25 and 26 it is θ_w . The effective wedge angle θ'_w equals θ_w (the actual wedge angle) in the RR-regime and $\theta_w + \chi$ elsewhere. Thus, the triple point trajectory angle χ should be subtracted from the appropriate curves of Figs. 23 and 24 prior to any superposition.

The interaction between the shock-wave reflection phenomenon and the induced-flow deflection process causes the reflected shock wave R to curl back towards the model and terminates at the wedge corner on the shock-tube wall. Since the shock-wave configuration is growing with time, the point where R terminates at the shock-tube wall moves towards the oncoming shock-induced flow, therefore increasing the oncoming relative flow Mach number. Consequently, the subsonic turning region shown in Figs. 25 and 26 cannot be established in nonstationary flows. At the limiting case of a degenerated incident shock wave ($M_s = 1$) the reflected shock wave becomes a Mach wave. Therefore, as there are four reflection processes (RR, SMR, CMR and DMR) and two deflection processes (an attached or detached shock wave), a maximum of eight different shock-diffraction systems are possible.

In Section 2.3.1.1 two methods of predicting χ were suggested. The first one is due to Law and Glass (Ref. 51), where straight Mach stem (normal to the wedge surface) is assumed, and the second, developed here, makes use of the experimental fact that shock-wave reflections occur even at very low wedge angles when the flow Mach number behind the incident shock wave I (Fig. 4b) is much smaller than unity ($M_1 < 1$) wrt the reflection point. The methods were discussed in detail in Section 2.3.1.1. Consequently only the results, i.e., $\chi = \chi(\theta_w, M_s, P_0, T_0)$ for nitrogen and argon will be presented in the following.

4.1 Triple-Point-Trajectory Angle in a Diatomic Gas - Nitrogen

The present analytical extension of the graphical method by Law and Glass (Ref. 51) for predicting the triple-point-trajectory angle χ was applied to obtain Figs. 27 to 31.

The triple point trajectory angles χ as a function of the incident shock wave Mach number M_s with the effective wedge angle θ'_w as a parameter for a constant P_0 and T_0 shown in Fig. 27. The dashed lines are for a perfect gas ($\gamma = 1.4$) while the solid lines are for an imperfect gas. Since the perfect-gas model results in no reflection for $\theta'_w = 22.2^\circ$ (see Fig. 23) only a solid line (i.e., imperfect gas) is shown for this effective wedge angle. It can be seen that the perfect gas result yields values of χ greater than for an imperfect gas. At low Mach numbers the imperfect-gas lines approach those of a perfect gas. At higher Mach numbers and lower θ'_w the dependence of χ upon M_s becomes stronger for an imperfect gas due to dissociation. However, for a perfect gas χ is almost independent of M_s . (Note that at higher M_s the dashed lines level out.)

At $\theta'_w = 40^\circ$, the perfect gas gives an almost constant value of χ throughout the entire region of M_s . In other words, one might conclude that a wedge angle exists for which χ is independent of M_s (a constant). This fact is more clearly illustrated in Fig. 28 showing the variation of χ with θ_w for a given M_s . Only 3 lines ($M_s = 4, 7$ and 10) are drawn for clarity. Note that all 3 lines intersect practically at one point ($\theta_w \approx 35.05^\circ$, $\chi \approx 6.45$ and $\theta'_w = 41.50^\circ$). A reproduction of Fig. 28 for imperfect nitrogen is shown in Fig. 29; again only 3 curves are given ($M_s = 4, 7$ and 10). The lines corresponding to $M_s = 4$ and 7 intersect at $\theta_w = 45.38^\circ$ and $\chi = 3.30^\circ$ (i.e., $\theta'_w = 48.68^\circ$). A comparison between

imperfect and perfect gas results is shown in Fig. 30. Only the lines that correspond to $M_s = 10$ are shown. It can be clearly seen that the value of χ predicted using a perfect gas is greater than for an imperfect gas.

The dependence of χ on M_s and θ_w is shown in Fig. 31. The dashed lines are again for a perfect gas ($\gamma = 1.4$) while the solid lines are for imperfect nitrogen. It can again be seen that the perfect gas values of χ are higher than those predicted by the imperfect gas theory. The discrepancy between the two values (i.e., perfect and imperfect nitrogen) increases as M_s increases and θ_w decreases. Again the perfect gas lines level out at high Mach numbers and χ is almost independent of M_s or $\chi = \chi(\theta_w)$ only.

Law and Glass developed this method of predicting χ and found that it agrees with experiments only in the range $25^\circ \leq \theta_w \leq 45^\circ$ (Ref. 51). It will be shown later that during the present research their method was found to be in good agreement with experiments in a much larger range of wedge angles $5^\circ \leq \theta_w < 45^\circ$. This, we believe, is due to the fact that they solved Eqs. 2.17 to 2.31 graphically, while during the present study an analytical solution was obtained. Their graphical solution was rechecked and verified. Since their method was found to be good in the range $5^\circ \leq \theta_w \leq 45^\circ$ an alternative method was developed for the range $\theta_w < 5^\circ$ which was described in detail in Section 2.3.1.1. The results are as follows.

Figure 32 represents the variation of the triple point trajectory angle χ with the incident shock Mach number M_s and the actual wedge angle θ_w , as a parameter, for very small wedge angles ($\theta_w < 5^\circ$). Note that although Fig. 32 is based only on the experimental fact that SMR occurs even for very low wedge angles (i.e., χ should be large enough to keep θ_w' above the line $M_1 = 1$ of Fig. 23; recall that $\chi = \theta_w' - \theta_w$), it resembles the characteristics of Fig. 31, for small wedge angles $5^\circ \leq \theta_w \leq 20^\circ$; that results from physical considerations. In both figures χ is a decreasing function with increasing M_s and θ_w and while, for the imperfect gas model, the dependence of χ upon M_s is prominent as M_s increases due to dissociation, the perfect gas lines (dashed) level out so that χ becomes nearly independent of M_s , i.e., $\chi = \chi(\theta_w)$ only (Figs. 31 and 32).

4.2 Triple-Point-Trajectory Angle in a Monatomic Gas - Argon

The dependence of χ on M_s for fixed θ_w' is shown in Fig. 33. The solid lines for imperfect argon in ionizational equilibrium start to diverge from the perfect-gas lines $\gamma = 5/3$ (dashed) slightly above $M_s = 7$. Consequently, in the range $1 \leq M_s \leq 7$ the perfect-gas solution is adequate.

The perfect-gas lines level out as M_s increases making χ independent of M_s on $\chi = \chi(\theta_w')$ only. This can be more clearly seen in Fig. 34, in which χ is plotted against θ_w for fixed values of M_s . For clarity only 3 lines are drawn ($M_s = 4, 5$ and 10). All the lines intersect practically at one point, $\theta_w = 29.87^\circ$, $\chi = 10.22^\circ$ (i.e., $\theta_w' = 40.09^\circ$). This value differs very slightly from the corresponding value of a diatomic gas found earlier ($\theta_w' = 41.50^\circ$).

A similar plot for imperfect argon is given in Fig. 35. Again only 3 lines ($M_s = 4, 7$ and 10) are shown. Only two lines, those corresponding to $M_s = 4$ and 7 intersect (at $\theta_w = 32.72^\circ$, $\chi = 8.83^\circ$, $\theta_w' = 41.55^\circ$). Therefore a wedge angle θ_w does not exist for which χ is completely independent of M_s . A comparison between perfect and imperfect argon is shown in Fig. 36. It can be clearly seen that the value of χ predicted by perfect-gas theory is larger than the one for imperfect argon.

The dependence of χ on M_s for given θ_w is shown in Fig. 37. Again the imperfect argon (solid line) starts to diverge from the perfect gas values $\gamma = 5/3$ (dashed lines) only for $M_s > 7$. Therefore the perfect gas values are adequate in the range $1 < M_s \leq 7$. The perfect-gas lines level out as M_s increases, giving $\chi = \chi(\theta_w)$ only. However, electronic excitation and ionization start when $M_s > 7$ and the dependence of χ upon M_s increases for imperfect argon.

The previous method for very low wedge angles was also used for argon to obtain Fig. 38. The solid lines are for imperfect argon in ionization equilibrium while the dashed lines are for a perfect monatomic gas. It can again be seen that for $M_s > 2$, χ is a decreasing function of M_s and θ_w , while for imperfect argon the dependence on M_s becomes strong at $M_s \geq 7$ when ionization starts. The perfect-gas lines (Fig. 38, dashed lines) level out and χ becomes independent of M_s or $\chi = \chi(\theta_w)$. This type of behaviour is similar to the results that were obtained using the method of Law and Glass (Ref. 51) as shown in Fig. 37.

4.3 Domains of Shock-Wave Diffractions in a Diatomic Gas - Nitrogen

Figures 23 (with χ subtracted) and 25 were superimposed to obtain Fig. 39. Only the boundary line corresponding to $P_0 = 15$ torr is reproduced. Out of a maximum of eight possible shock-wave diffractions only seven are obtained in the range $1 \leq M_s \leq 10$. The unobtainable diffraction is an RR with an attached shock wave at the wedge corner. Note that if the lines $\theta_1 + \theta_{2m} = 0$ and the attached/detached lines are extrapolated beyond $M_s = 10$ they might intersect, and hence an RR with an attached shock wave could be obtained. The seven different shock wave diffractions in the range $1 < M_s < 10$ appear in Fig. 39 and are listed in Table 1. They consist of an RR with a detached shock wave (region 1), SMR having a detached or attached shock wave (regions 2 and 3, respectively); CMR with deflection through a detached or attached shock wave (regions 4 and 5, respectively); and finally DMR with a detached or an attached shock wave (regions 6 and 7, respectively).

4.4 Domains of Shock-Wave Diffractions in a Monatomic Gas - Argon

Figures 24 (with χ subtracted) and 26 were superimposed to obtain Fig. 40. Only the lines corresponding to $P_0 = 15$ torr are reproduced. In the range $1 \leq M_s \leq 10$ this time only six diffractions out of a maximum of eight are possible. The two unobtainable diffractions are an RR and a DMR with an attached shock wave at the corner. However, if the lines $\theta_1 + \theta_{2m} = 0$, $M_2 = 1.00$ and the attached/detached line ($\theta_w = \theta_{m2}$) are extrapolated beyond $M_s = 10$, the two former lines might intersect the latter one, resulting in the missing two diffractions. The six different shock-wave diffractions in the range $1 \leq M_s \leq 10$ are RR with a detached shock wave (region 1); SMR with a detached or an attached shock wave (regions 2 and 3, respectively); CMR with a detached or an attached shock wave (regions 4 and 5, respectively); and DMR with a detached shock wave (region 6). The six different diffractions are shown in Fig. 40 and listed in Table 2.

5. OBLIQUE SHOCK-WAVE REFLECTION IN STEADY FLOWS

Prior to the present study it was accepted among most researchers that the shock wave reflection phenomenon in the nonstationary case is equivalent to the reflection process in steady flows, once a frame of reference is attached to the triple point in SMR or the reflection point in RR (Fig. 41). However, since several differences have already been pointed out throughout this report it is of interest to summarize the phenomenon in steady flow as well as to compare the steady and nonstationary shock-wave reflections. Note that one cannot use the term "diffraction" in steady flows as only reflection takes place.

When a steady supersonic flow encounters a wedge with an angle θ_1 (Fig. 42) it will be deflected by an oblique shock wave I through an angle θ_1 to become parallel to the deflecting surface. The angle of incidence ϕ_0 as well as all the thermodynamic and dynamic properties of state (1) behind the oblique shock wave I are defined by P_0 , T_0 , M_0 and θ_1 . If the flow behind the oblique shock wave I is supersonic ($M_1 > 1$) a reflected shock wave occurs to turn it away from and make it parallel to the wall. It is an experimental fact that the weak solution is the one that occurs. Consequently M_1 will be greater than unity.

If the value of θ_1 (see Fig. 42) is smaller than the maximum deflection angle θ_{2m} of the flow in state (1) an RR occurs (Fig. 43a), while for $\theta_1 > \theta_{2m}$ an RR is not possible and an SMR occurs (Fig. 43b). It is not assumed that this is the transition criterion from RR to SMR. Note that an RR or an SMR can also be obtained other than from a rigid wall by the intersection of two oblique shock waves (generated by two wedges in a steady supersonic flow) as shown in Figs. 44a and 44b. Actual interferograms of RR and SMR in a supersonic wind tunnel are shown in Figs. 45a and 45b (standard interferogram) and Figs. 46a and 46b (infinite fringe interferogram). (We are indebted to Dr. H. G. Hornung of the Australian National University for supplying us with these interferograms; see Ref. 77.)

It was noted in Section 2.2.3 that the termination criterion for RR in steady flows is different from a nonstationary flow (Refs. 65 and 74). While in nonstationary flows, the "detachment" criterion or the "sonic" criterion (Eqs. 2.14 and 2.16, respectively) is used (Fig. 2a, R_{iv}). In steady flow, Hornung and Kychakoff (Ref. 65) verified Henderson and Lozzi's (Ref. 60) "mechanical-equilibrium" criterion, described by Eq. 2.15 (Fig. 2a, R_{ii}). It should be noted, however, that Hornung and Kychakoff's general criterion for the transition $RR \rightarrow SMR$ includes both specific criteria of steady and nonstationary flows.

5.1 Types of Reflection Obtainable

It is an experimental fact that only SMR and RR have been obtained in steady-flow wind-tunnel experiments. It is suggested that the reason lies in the experimental set-up used to obtain oblique shock-wave reflections in steady-flow experiments. Recall that the reason for the termination of SMR and formation of CMR and later DMR in the nonstationary case is that the flow behind the reflected shock wave R becomes supersonic wrt the triple point T ($M_2 > 1$) while it is directed towards the wedge surface (see discussion in Section 2.4). In the steady case, the flow in state (2) is always interrupted

by either an expansion wave or a reflected shock wave (Figs. 47a and 47b, respectively), which arises from the wedge used to generate the incident oblique shock wave I. Thus the flow in state (2) behind the reflected shock wave is prevented from reaching the wedge surface again. Therefore the need to turn this flow away from the wall is eliminated. Consequently, in steady flows unlike nonstationary flows it is possible to have SMR with supersonic flow behind the reflected wave.

5.2 Steady Oblique Shock Wave Reflection in (M_0, ϕ_0) -Plane

In steady flows the parameters M_s and θ_w which were used for nonstationary flows cease to be significant. Instead the flow Mach number in state (0), M_0 and the flow incidence angle ϕ_0 to the oblique shock wave I are used. Consequently the reflection phenomenon is described in the (M_0, ϕ_0) -plane.

5.2.1 Steady Flow Regions and Transition Boundaries in a Diatomic Gas - Nitrogen

The domains of different types of oblique shock wave reflection in nitrogen are shown in Fig. 48. The solid boundary lines account for real-gas effects, while the dashed lines are for a perfect diatomic gas ($\gamma = 1.4$).

The (M_0, ϕ_0) -plane is divided into 3 domains of RR, SMR and NR. The significance of real-gas effects on shifting the boundary lines can be clearly seen. The perfect-gas theory can be used only in the narrow range $1 < M_0 < 2.22$. At $M_0 = 2.22$ the imperfect-gas lines start to diverge from the perfect-gas line due to vibrational excitation. At higher Mach numbers ($M_0 > 8.6$) the imperfect-gas line splits into a multiplicity of lines for different initial pressures at constant temperature due to dissociation. At even higher Mach numbers electronic excitation and ionization would play a similar role. When M_0 approaches unity the line $\theta_1 \neq \theta_2 = \theta_3 = 0$ approaches the line $M_1 = 1.00$. These two lines are coincident at $M_0 = 1$ and $\phi_0 = 90^\circ$.

5.2.2 Steady Flow Regions and Transition Boundaries in a Monatomic Gas - Argon

The domains of SMR, RR and NR for argon are shown in Fig. 49. The solid lines are again for imperfect argon while the dashed lines are for a perfect monatomic gas ($\gamma = 5/3$).

Unlike the case of a diatomic gas where the perfect-gas theory was adequate only for very small values of M_0 ($M_0 < 2.22$, Fig. 48), here (Fig. 49) it can be used over a much wider range, $1.00 < M_0 < 8.95$. At $M_0 = 8.95$ the imperfect-gas boundary line splits with initial pressure (at constant temperature) due to electronic excitation and ionization. Consequently one can expect an SMR when $M_0 = 16$, $\phi_0 = 30^\circ$ and $P_0 \geq 10$ torr, while an RR will be obtained if $P_0 \leq 1$ torr.

5.3 Comparison Between Steady and Nonstationary Shock Wave Reflection

It has already been mentioned that in spite of the similarity between shock-wave reflection in steady and nonstationary flows, several differences exist between them. Therefore it is worthwhile to summarize these differences. The first and most important difference lies in the fact that the shock-wave-reflection process in the nonstationary case always interacts with the flow deflection process over the corner, while in steady flows only reflection occurs.

Consequently, unlike that in steady flow, an NR domain exists in the (M_0, ϕ_0) -plane (Figs. 48 and 49); in the nonstationary case, there is no actual NR domain (Figs. 39 and 40) in the (M_s, θ_w) -plane. Recall that in the nonstationary case, a reflection occurs even when the flow behind the incident shock wave I becomes subsonic wrt point P (Fig. 4a) due to the interaction with the flow-deflection process (Fig. 4b). In the steady flow case only one reason exists for shock-wave reflection, i.e., a need to turn the supersonic flow moving towards a solid surface (Fig. 42). In the nonstationary case there are two reasons. The first is analogous to the steady case and holds for $M_1 > 1$ (Fig. 4a), while the other applies to $M_1 < 1$ (Fig. 4b). Note that in steady flows $M_1 < 1$ yields no reflection (NR). A more detailed discussion of these two reasons is given in Section 2.1.

In Section 2.2.3 it was noted that the termination criteria of RR are different for steady and nonstationary flows. In nonstationary flows either the "detachment" criterion (Eq. 2.14) established by Neumann (Refs. 2, 4) or the "sonic" criterion (Eq. 2.16) established by Hornung and Kychakoff (Ref. 65) holds, while in steady flow the "mechanical-equilibrium" criterion (Eq. 2.15), established by Henderson and Lozzi (Ref. 60) and Hornung and Kychakoff (Ref. 65), applies.

Once RR is terminated three different types of reflection can occur in nonstationary flows, i.e., SMR, CMR and DMR. In steady flows, however, CMR and DMR cannot occur due to the geometrical limitations used to obtain the reflection (see discussion in Section 5.1) and hence only an SMR is possible. It should be noted, however, that while in steady flow one can have an SMR with supersonic flow behind the reflected shock wave, in nonstationary flows SMR is terminated when the flow behind the reflected wave becomes supersonic.

The interaction between the shock-wave-reflection process and the flow-deflection process in nonstationary flow results in a three-shock confluence where the reflected wave R, Mach stem M and slipstream S are usually curved (not in the vicinity of the triple point where they are all straight, see Ref. 53). In steady flow, these shock waves and slipstream are usually straight, and hence the flow regions bounded by them are much more uniform than those in the nonstationary case. One should note that in steady flow the slipstream never curls back, a typical property of nonstationary reflections.

Due to the fact that the incident shock wave in nonstationary reflections always moves into a quiescent flow, the reflection point (Fig. 4a) is always independent of the boundary-layer growing behind it. However, in steady flow the boundary-layer effects depend on the geometrical set-up used to obtain the reflection. A severe boundary-layer interaction is eliminated if the intersection of shock waves is used to obtain the reflection (Figs. 44a and 44b).

The triple-point trajectory angle χ has no physical meaning in steady flows, where the configuration is fixed wrt time, i.e., does not grow linearly with time. However, in steady flow the length of the Mach stem can be regarded as a similarity parameter. So far a theory for predicting the length of the Mach stem has not been published. The equations of motion (Eqs. 2.17 to 2.30) are all satisfied if one moves the triple point to any point along the

incident shock wave (Fig. 50) and draws the corresponding reflected shock wave R^* , Mach stem M^* and slipstream S^* . However, repeated experiments for the same initial conditions and geometrical configurations provide identical shock-wave configurations. This suggests that the factors governing the reflection process in steady flow are related to the waves emanating from the wedge (Figs. 47a and 47b). It should be noted here that Molder (Ref. 76) developed a theory for the reflection of curved shock waves in steady flows, using the assumption of constant curvature, by which the length of the Mach stem can be determined analytically. However, his theory fails to predict the length of the Mach stem in the case of the reflection of straight shock waves. (Owing to the lack of experimental data on the reflection of curved shock waves, Molder's analysis remains unsubstantiated.)

The incident shock wave was observed to be accelerating somewhat when it passed over the compression model in the test section. A constant-velocity shock wave was measured when the model was removed. The reason for this acceleration is not known. Although this acceleration is usually very small it might have an influence on the reflection process. Consequently Eqs. 2.1 to 2.9 for an RR and Eqs. 2.17 to 2.30 for the triple point T describe the reflection phenomenon in steady flows better than they do in nonstationary flows, where the flow Mach number M_0 ahead of the incident shock wave [state (0)] changes slightly as the incident shock wave accelerates, i.e., M_s increases.

6. EXPERIMENTAL TECHNIQUES AND INSTRUMENTATION

The UTIAS 10 cm x 18 cm Hypervelocity Shock Tube (Ref. 32) was used to generate the incident shock waves. An updated and detailed description of the entire facility, its performance maintenance and operational techniques is reported in Ref. 71. Therefore in the following only a brief discussion is given.

The cold runs were used to generate the shock waves in the range $2 < M_s \leq 8$ of the present study. The initial conditions, i.e., the pressure ratio across the mylar diaphragm and the driver gas combinations used to obtain different incident shock waves into nitrogen and argon are given in Tables 3 and 4, respectively. The shock wave Mach numbers, M_s , given in Tables 3 and 4 represent the average values obtained throughout the present study. Consequently, the initial conditions listed in Tables 3 and 4 will produce, in general, shock waves in the range $M_s \pm 0.1$ of the predicted value. The initial pressures P_0 in the range $5.00 \leq P_0 < 65.00$ torr were monitored with two Wallace and Tiernan type FA 160 (0-50 torr and 0-200 torr) dial gauges. A more accurate measurement of P_0 was made using an oil manometer (0.2-40 torr).

The nonstationary process was recorded using a 23-cm dia field of view Mach-Zehnder interferometer (Refs 21, 71). The light source was a giant-pulse ruby laser (Ref 71). Simultaneous dual-frequency interferograms were taken at 6943Å and 3471.5Å, respectively. Kodak, Royal X Pan (1250 ASA), 10 x 13 cm (4 x 5 inch) plate film was used to record the interferograms.

A schematic instrumentation diagram of the equipment used throughout the present study is shown in Fig. 51. When the shock-wave arrives at station D, time-counters 1, 2, 3, 4 and 5 are triggered simultaneously. (Note that these 5 counters are connected to a common external 1-megacycle oscillator, and hence have a uniform time base of 1-microsecond resolution.) These 5

counters then stopped in succession as the shock wave passed subsequent detectors at stations F, G, H, I and J. An additional counter (No. 7) was used between stations I and J to indicate the time taken for the shock wave to travel past the test section. Since the shock wave velocity changes somewhat due to the convergence of the cross section caused by the model (Refs. 39 and 46), the measurement of counter No. 7 was used only as a monitor of the shock location.

The control of the laser light source operation is also included in Fig. 51. The laser flashlamp capacitor bank was usually triggered by the shock arrival at station F, suitably delayed in a Tetronix type 555 oscilloscope to get 900 μ sec of energy pumping by the time the Pockels-cell shutter opened. The Pockels cell Q-switch was always triggered from station I, delayed correctly in a pulser delay unit to take the interferograms at a desired time (or location of the shock wave wrt station I).

To monitor the actual flashlamp pumping time in each experiment, synchronization pulses from both the flashlamp capacitor bank and the Pockels-cell pulser unit were used to start and stop, respectively, a UTIAS microsecond counter (Fig. 51, Counter No. 6).

As an additional check on shock-tube performance in each experiment, a Kistler type 601-B, piezo-electric pressure transducer was used to monitor the pressure variation with time behind the incident shock wave. The transducer output was taken directly to a charge amplifier (Kistler, Model 504) with a final signal displacement on the designated oscilloscope (Fig. 51).

6.1 Accuracy of Measurements

A detailed description of the absolute errors associated with the various measurements involved in the operation of the shock tube facility is given in Ref. 71. Consequently, only a brief summary follows.

6.1.1 Incident Shock Wave Mach Number - M_s

The maximum possible relative error in calculating the incident shock wave Mach number was (Ref. 71):

$$\frac{E(M_s)}{M_s} = (1.15 M_s + 10.18) \times 10^{-3} \quad \text{for nitrogen} \quad (6.1)$$

$$\frac{E(M_s)}{M_s} = (1.05 \times M_s + 10.18) \times 10^{-3} \quad \text{for argon} \quad (6.2)$$

Consequently, in the range of incident shock wave Mach numbers used in the present study, $2 < M_s \leq 8$, $E(M_s) = 0.02$ for both nitrogen and argon at the lower end ($M_s = 2$) while for $M_s = 8$, $E(M_s) = 0.16$ and 0.15 for nitrogen and argon, respectively. Equations 6.1 and 6.2 are shown in Fig. 52a. It can be seen that the relative error $E(M_s)/M_s$ increases linearly as M_s increases. Consequently the absolute error $E(M_s)$ is proportional to M_s^2 .

6.1.2 Initial Pressure P_0 and Temperature T_0

Initial pressures in the range $5 \leq P_0 \leq 40$ were measured with an oil manometer. The pressure P_0 is calculated from (Ref. 71):

$$P_0 = \frac{\rho_{\text{oil}} H(\text{mm})}{13.5951} \quad (6.3)$$

where H is the oil-height difference in mm as measured in the manometer, and ρ_{oil} is the density of the oil and it is given by:

$$\rho_{\text{oil}} = 1.0690 + 9.5 \times 10^{-4} (25-T) \quad (6.4)$$

~~T , the oil temperature,~~ was assumed to be equal to the laboratory temperature measured near the manometer ($T = T_L$). The absolute error associated with the initial pressures is then (Ref. 71):

$$E(P_0) = [1.4 \times 10^{-5} H(\text{mm}) + 7.86 \times 10^{-2}] \text{ torr} \quad (6.5)$$

Consequently, the maximum possible errors associated with lowest (5 torr) and highest (37 torr) pressures that were measured with the oil manometer are 0.08 torr and 0.09 torr, respectively.

Pressures in the range $P_0 \geq 40$ torr were measured with a Wallace and Tiernan type FA 160 (0-200 torr) within an accuracy of ± 0.2 torr and hence the maximum possible error was $E(P_0) = 0.4$ torr. A plot of the absolute error involved in the pressure measurements in the present study $5 \leq P_0 \leq 65$ is given in Fig. 52b.

The initial temperature T_0 was measured to an accuracy of $\pm 0.1^\circ$ with a standard mercury bulb thermometer inserted in a 5 cm deep, 6 mm dia oil-filled port in the upper wall of the shock tube. Consequently, an error $E(T_0) = 0.2^\circ$ was associated with all temperature readings.

7. EXPERIMENTAL RESULTS AND DISCUSSIONS

The above discussed facility was used to obtain and record non-stationary oblique shock-wave diffraction in nitrogen and argon. Fifty-eight successful experiments were made in nitrogen, with 9 different compression corners (wedges) having $\theta_w = 2^\circ, 5^\circ, 10^\circ, 20^\circ, 26.56^\circ, 30^\circ, 40^\circ, 50^\circ$ and 60° . In the case of argon 48 successful experiments were performed with 7 different wedge angles, $\theta_w = 2^\circ, 10^\circ, 20^\circ, 30^\circ, 40^\circ, 50^\circ$ and 60° . All angles had an accuracy of $\pm 0.016^\circ$.

Unfortunately, due to mechanical limitations wedge angles lower than 2° could not be machined. Wedge angles greater than 60° were not of interest as they would have resulted in RR, thereby not adding any important data. The incident shock wave Mach numbers M_s , wedge angle θ_w and initial pressures and

and temperatures (P_0 and T_0) associated with each experiment are listed in Table 5 for nitrogen and Table 6 for argon. These tables also include the experimental values of the primary and secondary triple point trajectory angles χ and χ' as well as the type of reflection obtained with the initial conditions. Note that χ' is listed also for CMR; it is omitted, however, for CMR where the location of the kink is not sufficiently clear. Since the location of the kink in a CMR is not as well defined as the location of the second triple point in a DMR, the accuracy of measuring χ' in a CMR is smaller than in a DMR. Consequently, the absolute errors are $E(\chi') = 1^\circ$ for CMR and $E(\chi') = 0.5^\circ$ for DMR. (The errors associated in measuring M_s , P_0 and T_0 are discussed in Chapter 6.)

Owing to the size of the present report, most of the interferograms have been omitted. However, as they are important as a data bank that might be helpful in the future to various researchers, all the actual interferograms of the nonstationary oblique shock wave reflections that were obtained throughout the present study (see Tables 5 and 6 for details) are given in Ref. 72. In all, 106 experiments were conducted.

7.1 Verification of Nonstationary Oblique Shock-Wave Reflection in (M_s , θ'_w)-Plane

In the present analysis the two different phenomena of shock-wave reflection by the wedge surface and the induced-flow deflection over the wedge corner were treated independently (in Chapters 2 and 3, respectively). In this manner Figs. 23 (nitrogen) and 24 (argon) were produced for reflection and Figs. 25 (nitrogen) and 26 (argon) for flow deflection. A superposition of these figures (Chapter 4) produced the overall phenomena of oblique shock-wave diffractions shown in Figs. 39 and 40 for nitrogen and argon, respectively. Recall that the appropriate value of χ was subtracted from Figs. 23 and 24 in order to superimpose them with Figs. 25 and 26.

In the following, the present analysis of nonstationary reflection of oblique shock waves is compared with experiments. Figures 53 and 54 are reproductions of Figs. 23 and 24 with $P_0 = 15$ torr only, for clarity. Note that although most of the present experiments were made with $P_0 \sim 15$ torr, those corresponding to low Mach numbers ($M_s \approx 2$ in nitrogen and argon) and high Mach numbers ($M_s \geq 6.79$ in nitrogen and $M_s \geq 7.53$ in argon) were obtained with slightly different initial pressures (see Tables 5 and 6 for details). However, Figs. 23 and 24 indicate that the initial pressure becomes significant for the boundary lines $M_1 = 1.00$, $M_2 = 1.00$ and $M_2' = 1.00$ (Fig. 23) at $M_s = 7.56$, 7.51 and 7.47, respectively, and for the boundary lines $M_1 = 1.00$, $M_2 = 1.00$ and $M_2' = 1.00$ (Fig. 24) at $M_s = 7.72$, 7.65 and 7.32, respectively. These high values of M_s were about the highest used throughout the present study. For the boundary line $\theta_1 + \theta_{2m} = 0$ of Figs. 23 and 24 the initial pressure becomes significant at $M_s = 6.05$ and 5.56, respectively. However, in the neighbourhood of these boundary lines the experiments did not go up to $M_s \sim 8$, since in similar experiments that were conducted in the past with the same facility the high-quality optical windows were burned (Ref. 43).

7.1.1 Diatomic Gas

The experimental data of Smith (Ref. 6) for $M_s = 1.25$, 1.51, 2.10 and 2.40, and White (Ref. 17) in air, Law and Glass (Ref. 51) in oxygen, and our data in nitrogen are all added to Fig. 53 (a reproduction of Fig. 23 for $P_0 = 15$ torr) in order to check the present analysis for nonstationary

oblique shock-wave reflection in diatomic gases. [Note that the term reflection is used here as the results are plotted in the pseudo-steady plane (M_s, θ_w).] Two points from Smith's experimental data that are reported to be RR lie slightly below their analytical terminating boundary line. We believe that this slight disagreement is probably due to Smith's use of air (the lines in Fig. 53 are for nitrogen). The presence of 20% oxygen in air would cause the boundary line to be lower than that of nitrogen, since the oxygen becomes vibrationally excited at a lower temperature, and hence the line would start shifting downwards at a lower Mach number.

Shock-wave reflection configurations reported by Smith (Ref. 6) to be SMR in the range $2.10 < M_s \leq 2.42$ appear to lie in the region that corresponds to CMR (Fig. 53). However, a careful check of Smith's report reveals that he observed that, "for strong shocks (his strongest shock was $M_s = 2.42$) a reversal of curvature (in the reflected shock wave) develops", and furthermore "the portion of the reflected shock near the triple point that appears to be straight". This we believe corresponds to CMR. It is clear that although he had noticed a CMR-configuration, he referred to it as an SMR rather than propose a new type of reflection, since these two configurations, except for the kink in R, are quite similar in appearance. When White (Ref. 17) discovered DMR in 1951, the importance of CMR was recognized as a different type of reflection. However, in White's report CMR is still considered as SMR. Note that one experimental point of White (Ref. 17), $M_s = 2.3$, $\theta_w = 39.2^\circ$ in the region where Smith (Ref. 6) reported SMR, resulted in a CMR; this verifies the previous remark that those experiments by Smith are CMR and not SMR. Excellent agreement can be seen with all the other boundary lines since all the experimental points lie in their predicted regions.

7.1.2 Monatomic Gas

The present experimental results (Table 6) in argon as well as some data from Law and Glass (Ref. 51) in argon and helium are all shown in Fig. 54 (a reproduction of Fig. 24, for $P_0 = 15$ torr).

One experiment reported by Law and Glass as CMR lies inside the DMR regime ($M_s = 7.66$, $\theta_w' \approx 45^\circ$). However this experimental point is surrounded by DMR points that were obtained during the present study. It might be that the initial directions of the fringes chosen by Law and Glass (different from ours) was such that the R_1 -shock wave (Fig. 19) of a DMR could not be seen clearly. Note that Bazhenova et al (Ref. 62) also reported DMR in argon, in the region where Law and Glass did not notice it.

Out of all our experimental points, only one ($M_s = 4.44$, $\theta_w' = 45.5^\circ$) that corresponds to a DMR lies outside its predicted region, in the CMR domain. This we believe is due to the use of Eq. 2.47 in calculating the CMR/DMR boundary line. Recall that Eq. 2.47 was found by Law and Glass (Refs. 48 and 51) and Bazhenova et al (Ref. 46) to be in good agreement with experiments only in the range $\theta_w \leq 40^\circ$ while for the range $\theta_w > 40^\circ$ the agreement becomes progressively worse. Note that aside from this slight disagreement all the other experimental points lie inside their predicted regions.

7.2 Triple Point Trajectory Angle - χ Comparison With Experiments

In order to superimpose the shock-reflection process (Figs. 23 for nitrogen and 24 for argon) with the flow-deflection process (Figs. 25

and 26 for nitrogen and argon, respectively) the value of χ was subtracted from the corresponding boundary lines of Figs. 23 and 24. Two different methods for the prediction of χ were discussed in Section 2.3.1.1. The first, due to Law and Glass (Ref. 51), was found by them to be in good agreement with experiments (in oxygen) only in the range $25^\circ \leq \theta_w \leq 45^\circ$.

The other, developed here, is for very small wedge angles, $\theta_w < 5^\circ$. These two methods were applied to nitrogen and argon (Sections 4.1 and 4.2, respectively) to obtain Figs. 31 and 32 for nitrogen, and Figs. 37 and 38 for argon. In the following, these two methods are checked against the experimental results in nitrogen and oxygen.

7.2.1 Diatomic Gas

The present data (Table 5) were added to Fig. 55 (a reproduction of Fig. 31), in order to test the present analytical version of the graphical method by Law and Glass (Ref. 51) for predicting χ in nitrogen. It is seen that the agreement with experiments for wedge angles in the range $5^\circ \leq \theta_w \leq 40^\circ$ is reasonably good. Most of the experimental points in this range lie within $\pm 0.5^\circ$ from their predicted values. However, for $\theta_w < 5^\circ$ the agreement becomes progressively worse as θ_w decreases. Note that while Law and Glass (Ref. 51), who developed this method of predicting χ , found it to be good only in the range $25^\circ < \theta_w < 45^\circ$ (in oxygen), it is seen that good agreement actually exists over a much wider range $5^\circ \leq \theta_w \leq 45^\circ$. This is probably due to the fact that they solved Eqs. 2.17 to 2.31 graphically, whereas the present solution is analytical. During the present study their graphical solution was checked for nitrogen. It was found to exhibit the same characteristics as their graphical solution for oxygen. Note that for $\theta_w < 40^\circ$ the actual values of χ are greater than those predicted. In this range all the data points fall between the predicted perfect and imperfect gas models.

The experimental data for 2° and 5° wedge angles (Table 5) are shown in Fig. 56 (a reproduction of Fig. 32) in order to check the present method for predicting χ for low wedge angles. It can be seen that for a 5° wedge the present analytical version of the graphical method of Law and Glass (Ref. 51) is actually in better agreement with experimental results than the present method for small wedge angles. For $\theta_w \leq 4^\circ$ the present method is in good agreement with experiments.

It should be noted that it is very difficult to predict the value of χ , using the analytical version of the method of Law and Glass for very small wedge angles ($\theta_w < 5^\circ$) owing to severe convergence problems as θ_w becomes small. The graphical solution is possible, however, accuracy is very low and the error at even greater wedge angles ($5^\circ < \theta_w < 20^\circ$) becomes significant (Ref. 51). Consequently this is the only existing method of predicting χ at low wedge angles ($\theta_w < 5^\circ$).

7.2.2 Monatomic Gas

The data from Table 6 for $\theta_w = 10^\circ, 20^\circ, 30^\circ, 40^\circ$ and 50° is shown in Fig. 57 (a reproduction of Fig. 37) in order to test the present analytical method (based on Law and Glass, Ref. 51) for predicting χ against experiments for argon. Very good agreement can be seen with the wedge angles $20^\circ, 30^\circ$ and 40° while for 10° and 50° the actual value of χ is smaller than the predicted one by more than 1° (the error bar). For these two wedge angles the agreement is fairly good for small values of M_s ($M_s < 3$ for $\theta_w = 50^\circ$ and $M_s < 5$ for $\theta_w = 10^\circ$) and becomes progressively worse as M_s increases.

The data points for $\theta_w = 2^\circ$ (Table 6) are shown in Fig. 58 (a reproduction of Fig. 38 for $\theta_w = 2^\circ$). The agreement is fairly good for low and high Mach numbers while in the range $3 \leq M_s \leq 6$ it is not so good. Here as well, owing to convergence problems, it was not possible to get a prediction of χ using our analytical version of the method of Law and Glass (Ref. 51) for $\theta_w = 2^\circ$.

7.3 Verification of Nonstationary Oblique Shock Wave Reflections in (M_s, θ_w) -Plane

Figures 53 (nitrogen) and 54 (argon) correspond to nonstationary oblique shock wave reflection in the (M_s, θ'_w) -plane. However, while the exact value of the effective wedge angle θ'_w can be measured only after an actual experiment is recorded, the actual wedge angle θ_w is a given parameter. Consequently, it is of interest to obtain the reflection phenomena in the (M_s, θ_w) -plane rather than the (M_s, θ'_w) -plane. This is done by subtracting the appropriate value of χ (Figs. 31 and 32 for nitrogen, and Figs. 37 and 38 for argon) from the vertical axis of Figs. 53 and 54 (nitrogen and argon, respectively).

The line $\theta_1 + \theta_{2m}$ (Figs. 53 and 54) represents the boundary of the RR process. Consequently, the actual value of χ above (and on) this line is zero. Therefore it does not change throughout the transformation. Recall that the present method for predicting χ for very small wedge angles (Section 2.3.1.1) is based on the experimental fact that in the nonstationary case, the incident shock wave always reflects. Following this method (Eq. 2.33) one can immediately see that the transformation $\theta'_w \rightarrow \theta_w$ eliminate the lines $M_1 = 1.00$ of Figs. 53 and 54. In other words, on the lines $M_1 = 1.00$ (Figs. 53 and 54), $\theta'_w = \chi$ and since $\theta'_w = \theta_w + \chi$ by definition the transformation $\theta'_w \rightarrow \theta_w$ yields that the lines $M_1 = 1.00$ coincide with the lines $\theta_w = 0$. Consequently only the lines $M_2 = 1.00$ and $M'_2 = 1.00$ of Figs. 53 and 54 need be transformed.

7.3.1 Diatomic Gas

The data from Smith (Ref. 6), White (Ref. 17) and Bazhenova et al (Ref. 55) in air, Law and Glass (Ref. 51) in oxygen, Bazhenova et al (Ref. 55) and the present in nitrogen are all shown in a combined plot on Fig. 59 (obtained from Fig. 53 by subtracting χ) in order to verify the present analysis of nonstationary oblique shock-wave reflection in the (M_s, θ_w) -plane for diatomic gases.

Two experiments (present one and one from Law and Glass) with $\theta_w = 40^\circ$ and $M_s = 2.00$ and 2.56 , respectively, in the region where Smith (Ref. 6) reported SMR results in CMR, and verifies our previous remarks that those experiments by Smith are CMR and not SMR. Many more data points from White (Ref. 17) could have been used. However, since they all fall in their predicted regions, they were omitted for clarity. It can be concluded from this figure that our analysis of the nonstationary oblique shock-wave reflection in the (M_s, θ_w) -plane for a diatomic gas is substantiated.

7.3.2 Monatomic Gas

The data of Law and Glass (Ref. 51) in helium, Bazhenova et al (Ref. 55), Law and Glass (Ref. 51) and the present experiments in argon

appear in Fig. 60 (obtained from Fig. 54 by subtracting χ) in order to check the present analysis for nonstationary oblique shock-wave reflection in a monatomic gas on the (M_s, θ_w) -plane. Very good agreement was obtained with the calculated regions and their boundary lines. All the experimental points lying outside their predicted regions are discussed in Section 7.1.2. It can be concluded that the present analysis for nonstationary reflection of oblique shock-waves in a monatomic gas is substantiated.

7.4 Verification of Nonstationary Oblique Shock-Wave Diffraction in (M_s, θ_w) -Plane

Figures 61 and 62 are reproductions of Figs. 39 and 40 for nitrogen and argon respectively. Unfortunately, not all the data shown in Figs. 53, 54, 59 and 60 could be used since information concerning the flow deflection process is usually not reported [e.g., Bazhenova et al (Ref. 55), where in all the recorded pictures the wedge corner is not in the field of view]. Consequently, the present data in nitrogen and argon as well as a few data points from different sources are shown in Figs. 61 and 62, that test the present analysis of nonstationary oblique shock-wave diffraction (shock reflection and flow deflection) in the (M_s, θ_w) -plane.

7.4.1 Diatomic Gas

Our experimental data points from Table 5 in nitrogen and White's (Ref. 17) in air are shown in Fig. 61 (a reproduction of Fig. 39). It is seen that all the data points fall inside their predicted region. Therefore, our analysis of the shock-wave diffraction in nonstationary diatomic gases is substantiated, and the seven different types of diffractions listed in Table 1 are all valid.

It is worthwhile to refer the reader to White's report (Ref. 17) where excellent examples of shock-wave diffractions with degenerated reflected shock waves are given (Figs. 34, 38 and 42 of Ref. 17). Note that White was able to obtain very weak incident shock waves ($M_s = 1.010, 1.047$ and 1.022 for these figures) for which the reflected shock wave vanishes as it degenerates into a Mach wave. For further details see Section 8.

7.4.2 Monatomic Gas

Our data from Table 6 in argon are all shown in Fig. 62 (a reproduction of Fig. 40). All experimental points (except the one at $M_s = 4.44, \theta_w = 40^\circ$ which have already been discussed) lie inside these predicted regions. Consequently, one can conclude that the present analysis for nonstationary oblique shock-wave diffraction in a monatomic gas is substantiated. Unfortunately, out of the six different diffractions predicted by the present analysis (Table 2) only five were observed experimentally. The remainder, a CMR with an attached shock wave at the wedge corner (region 5, Figs. 40 and 62), was not observed since its domain starts at $M_s = 9.4$ and lies beyond the practical possibilities of incident shock waves ($M_s \approx 8$) without damaging the interferometric quality windows of the test section. However, in light of Fig. 62 and the verification of 5 regions out of the 6 listed in Table 2, one can conclude that the present analysis for the diffraction of oblique shock waves in nonstationary monatomic flows is substantiated and that six different types of shock-wave diffraction exist in the range $1 \leq M_s \leq 10$.

7.5 Summary Discussions

The present experiments and analyses have verified the regions and boundaries of nonstationary reflection of oblique shock waves in the (M_S, θ_w') and (M_S, θ_w) -planes as well as those of nonstationary diffraction of oblique shock waves in the (M_S, θ_w) -plane for diatomic and monatomic gases.

It is worthwhile to refer again to Fig. 3 which shows all the information concerning these domains and transition boundaries of nonstationary oblique shock-wave reflection in the (M_S, θ_w) -plane that was known prior to the present research. A detailed description of Fig. 3 is given in Section 1, and hence only a brief comparison follows. While Fig. 59 covers a wide range of wedge angles $0 \leq \theta_w \leq 90^\circ$ and shock Mach numbers $1 \leq M_S \leq 10$, Fig. 3 is limited to $20^\circ \leq \theta_w \leq 60^\circ$ (the region $60^\circ \leq \theta_w < 90^\circ$ corresponding to RR was probably not drawn since it does not contain any significant information) and $1 \leq M_S \leq 9$. However, although the upper limit in Fig. 3 is $M_S = 9$, only line 1 extends all over the entire range. Lines 2, 3, 4 and 5 terminate at $M_S = 8.00, 4.75, 3.50$, and 2.75 , respectively. In Fig. 59 all lines extend over the entire range, up to $M_S = 10$. However, although Fig. 59 was limited to $M_S = 10$ (due to the fact that it was decided to make experiments only up to $M_S = 8$, in order not to damage the high quality test section windows) the present analyses apply for $M_S > 10$ as well. Unlike the case of Fig. 3 the analytically-obtained boundary lines are for a perfect gas while those accounting for real-gas effects are all experimental, all the boundary lines in Fig. 59 were obtained analytically, either by solving Eqs. 2.1 to 2.9 for an RR or Eqs. 2.17 to 2.30 for the triple point with and without real-gas effects. It is probably the first time that an analytical solution was obtained for Eqs. 2.17 to 2.30 with real-gas effects.

The contributions of the present study to knowledge concerning the reflection of oblique shock waves in the (M_S, θ_w) or (M_S, ϕ_0) -planes are summarized in Tables 7 and 8. While RR and SMR were discovered one hundred years ago (1878) by Ernst Mach, it is only about 35 years since CMR was first noticed by Smith (1945) and DMR discovered by White (1951). The formation criterion of RR in both steady and nonstationary flows was established by Neumann (1943), as well as its termination criterion in nonstationary flows (1943). More recently Henderson and Lozzi (1975) suggested a new criterion for the termination of RR that was found (Ref. 65) to be correct only in steady flows. However, Hornung and Kychakoff (1975) established a more general criterion for the termination of RR resulting in the sonic-criterion (slightly below Neumann's criterion) for nonstationary flows, and Henderson and Lozzi's criterion for steady flows. Henderson and Lozzi (1975) were the first to suggest that the termination of SMR is followed by a CMR, and later when M_2 increases a DMR is formed. However, the exact criterion for the termination of CMR, and hence the formation of DMR, was established only in the present analytical study and verified by experiments.

Table 8 summarizes by whom and when the boundary lines between domains of different types of oblique shock-wave reflection were calculated. For a perfect monatomic gas the boundary line between RR and SMR, CMR or DMR was calculated by Law (1970) and all the other boundary lines for both perfect and imperfect gases were calculated in the present study. In the case of a diatomic gas, the perfect gas boundary lines RR/SMR, CMR or DMR, SMR/CMR and CMR/DMR were calculated by Neumann (1943), Bazhenova et al (1976) and Ben-Dor (present), respectively. (Note that since Neumann worked in low Mach numbers, in his case

the termination of RR was followed by an SMR, however, his criterion of the termination of RR is good also for higher values of M_s where RR is followed by a CMR or DMR.) All the boundaries corresponding to an imperfect gas, i.e., RR/SMR, CMR or DMR, SMR/CMR and CMR/DMR were calculated in the present study.

8. DENSITY-FIELD INVESTIGATION

The experimental facility and instrumentation discussed in Chapter 6 were used to obtain interferograms of nonstationary oblique shock-wave reflections. Lines of constant density (isopycnics) were obtained from them using a method developed by Whitten (Ref. 75). A detailed description of this very precise data-evaluation technique is given in Refs. 71 and 75. Therefore, only a brief description will be given for obtaining the isopycnics (see Appendix E for details).

Very good agreement with sophisticated numerical analyses were obtained previously, using the identical equipment and evaluation techniques, in studies such as ionizing shock-wave structure (Refs. 68 and 69), flat-plate and sidewall boundary layers (Refs. 70 and 75) where boundary layer refraction errors are more significant than in the present study. Consequently, one can conclude that the refraction errors from sidewall boundary layers had a negligible effect.

The errors associated with the present experimental and evaluation techniques are discussed in detail in Ref. 71. However, since the number of fringes inside the shock-diffraction region was small, a more conservative estimation was made of the absolute error in measuring fringe shifts. The error is taken as $E(s) = 0.1$ rather than the already conservative estimation used by Whitten and Ben-Dor (Ref. 71), i.e., 0.05. Consequently, the absolute errors associated with the densities as measured from the interferograms are:

$$E(\Delta\rho) = 4.292 \times 10^{-6} \frac{g}{cm^3} \quad \text{for argon} \quad (8.1)$$

$$E(\Delta\rho) = 2.097 \times 10^{-6} \frac{g}{cm^3} \quad \text{for nitrogen} \quad (8.2)$$

Since the values of the isopycnics were all normalized wrt the flow density ahead of the incident shock wave ρ_0 , the relative error $\Delta\rho/\rho_0$ is used throughout the present report.

During the last few years various investigators (Refs. 61, 63 and 64) tried to develop computer codes for predicting the density field associated with RR and SMR. No such data exist for CMR and DMR. A detailed comparison between their numerically predicted density fields and the present results is given in Ref. 73 and briefly discussed in Section 8.2. The comparison reveals that all numerical methods provide reasonable prediction of the wave systems and their shock shapes for the cases that were compared. However, they predict rather poor values and locations of the more sensitive indicators of the flow isopycnics. Consequently the various codes (Refs. 61, 63 and 64) require a reassessment and perhaps a new approach in the light of the disagreement with the present detailed and very accurate interferometric data. Undoubtedly,

numerical codes will evolve in the future that will reliably predict such complex flow in imperfect gases. No doubt the present data will provide a solid base for future comparison.

8.1 Nitrogen

The seven shock wave diffraction domains corresponding to regions 1 to 7 of Fig. 39 are shown in the interferograms 63a to 63g, respectively. The density distribution (ρ/ρ_0) in the flow fields, in terms of isopycnics (n) associated with each diffraction process, are shown in Figs. 64a to 64g. The density profiles along the wedge and the shock-tube wall appear in Figs. 65a to 65g. In the following, a general description is given of each diffraction as well as their similarities and differences.

Figures 63a, 63b, 63c and 63f which correspond to flow deflections through detached shock waves (regions 1, 2, 4 and 6 of Fig. 39), shock wave bifurcation and boundary layer roll-up are clearly seen. In order to have a closer look at the shock wave bifurcation four experiments with $M_s = 4.64$, 4.59, 4.60 and 4.72 and $\theta_w = 40^\circ$ were made. The process was recorded 26, 126, 226 and 326 μsec after the incident shock wave passed the centre of the test section. The four corresponding interferograms are shown in Figs. 66a to 66d, respectively. Figure 66a reveals, as expected, a DMR with a detached bifurcated shock wave. In Figs. 66b to 66d the incident shock wave is already outside of the field of view; however, the bifurcation process is seen to be growing with time. Figures 66b and 66c, for example, show very clearly a bifurcated shock and a slipstream, i.e., a three-shock confluence or a triple point. Note the clear compression at the wedge corner and expansion wave as the wedge becomes flat giving rise to a corner-expansion flow. In Fig. 66d the reflected shock wave R is seen reflecting from the upper wall of the shock tube. Unfortunately, the upper wall is not in the field of view; however, it looks like the reflected wave R reflected through a single-Mach reflection and that a Mach stem joins it to the upper wall.

It is worthwhile mentioning that White in his pioneering work (Ref. 17) was able to produce some very weak incident shock waves. He evaluated his interferograms on shock-wave diffractions at very low M_s . Figures 67a and 67b are reproductions of two of his original figures (Figs. 34 and 46 of Ref. 17). The initial conditions for these two pictures are $M_s = 1.010$, $\theta_w = 5.7^\circ$ (SMR) and $M_s = 1.018$, $\theta_w = 30^\circ$ (RR), respectively. For these low values of M_s the reflected shock wave degenerates to a Mach wave and the flow turns over the wedge subsonically. Note that for these two examples from White (Ref. 17) the induced flow Mach number M_2' is 0.017 and 0.029, respectively.

When the flow deflection over the corner is achieved through an attached or detached shock wave there is a sharp density jump at b point (Fig. 65). In the case of an attached shock wave at the corner (Figs. 63c, 63e and 63g) the highest density along the wall is measured immediately behind the attached shock wave, i.e., at the corner (point b, Figs. 65c, 65e and 65g) while in the case of a detached shock wave (Figs. 63b, 63d, and 63g) the highest density may or may not be (Figs. 65a and 65d) behind this shock wave or at the corner. It can occur near the slipstream (Fig. 65b) or near the corner (Fig. 65d).

The existence of a compression wave at the kink K of a CMR can be clearly seen in Figs. 65d and 64e where the isopycnics converge. The corresponding compression strengths (density ratios) are approximately 6.880/6.447

and 8.778/8.127 or 1.067 and 1.080, respectively. For the compressions of 1.067 and 1.080 an increasingly clearer kink can be seen (Figs. 63d and 63e). The equivalent perfect shock wave Mach numbers that would give the same compressions are 1.040 and 1.048, respectively. The calculated flow Mach numbers behind the reflected wave M_2 in the vicinity of the triple point T are 1.251 and 1.319, respectively. Once a DMR is formed ($M_2 > 1$) the isopycnics do not converge any more (Figs. 64f and 64g) and the compression wave is replaced by a shock wave.

In the cases of SMR (Figs. 64b and 64c) the convergence of the isopycnics corresponds to a weak expansion wave rather than a compression wave (follow the isopycnic numbers). The strengths of those expansion waves are: 3.747/3.868 and 5.53/6.11 or 0.969 and 0.905, respectively. The case with an attached shock wave has the strongest expansion. This is also true for CMR (Figs. 64c and 64e). Figures 65a to 65g show that the density along the wedge surface always increases as one moves from the Mach stem towards the point where the slipstream disappears into the boundary layer. Consequently the flow behind the Mach stem is being further compressed.

Although the density flow field associated with the various shock wave diffractions differ greatly, nevertheless they do have some similarities. For example, in the case of an attached shock wave, Figs. 64c - SMR and 64e - CMR, the isopycnics tend to run perpendicular to the reflected shock wave. In the case of DMR (Figs. 64f and 64g) a "corridor" is formed for the second slipstream. In Fig. 63g the second slipstream is not visible, probably because the change in the density is not sufficiently large to establish a noticeable fringe shift. However, the "corridor" is clearly seen in Fig. 64g and consequently a thin dashed line has been drawn in Fig. 65g to indicate the possible location of the second slipstream.

The density at any point (x,y) of Figs. 64a to 64g can be calculated either by interpolating between or by extrapolating beyond the isopycnic in the vicinity of that point. However, since the density difference between the isopycnics is quite small, any region between them can be assumed to have a uniform average value. For a region where the density change was not sufficiently large to plot isopycnics it can be assumed as uniform with the indicated density number. For example, region n = 6 bounded by R, R_1 and S in Fig. 64g is assumed with $\rho = 8.87\rho_0$. The relative error $\Delta\rho/\rho_0$ given in each figure (Figs. 64a to 64g) was obtained from Eq. 8.2 simply by dividing with the corresponding value of ρ_0 . The error is fixed for a particular experiment. It can be as high as 37.6% for $P_0 \approx 5$ torr (Fig. 64g) and as low as 5.2% for $P_0 \approx 37$ torr (Fig. 64b). Note that the position of a point on any isopycnic was drawn within an accuracy of ± 1 mm.

8.2 Comparison With Some Numerical Data and Discussions

The different compared cases and their initial conditions are shown in Table 9. Although we have tried to perform our new experiments using exactly the same initial conditions as those chosen by Schneyer and Kutler and Shankar for their numerical analyses, it was experimentally convenient to use nitrogen at different initial pressures. However, owing to the fact that nitrogen and oxygen can be treated as a perfect gas at a shock Mach number $M_s = 2.00$, the change in the initial pressure was not significant. Furthermore, since the value of the flow isopycnics were normalized by the initial density ahead of

the incident shock wave any correctly-computed and actual isopycnic shapes and values must be the same. However, for strong shock waves real gas effects are important and must be taken into account, for RR at $M_s = 4.68$ and $P_o = 15.31$ torr.

It can be seen from Table 9 that three different cases were compared. Case 1 results in an RR with a weak incident shock wave ($M_s = 2.0$) and it was numerically solved by Schneyer and Kutler and Shankar. Case 2 is again an RR but with a stronger incident shock wave ($M_s = 4.71$) and it was analyzed by Kutler and Shankar. Case 3, an SMR, was solved by Schneyer using two different computer codes, the two-dimensional Eulerian code THOR, a revised version of the HELP (Ref. 78) code, and the two-dimensional Lagrangian code CRAM, based on Wilkins' formulation (Ref. 79). In Kutler and Shankar the two-dimensional time-dependent Euler equations were solved. The hyperbolic partial-differential equations were transformed to introduce self-similarity and the distance between the corner and the incident shock wave was used for normalization. The self-similar transformation reduces these equations from an unsteady to a quasi-steady set of mixed elliptic-hyperbolic equations. Then the equations were made totally hyperbolic by reintroducing a time-like term. The final set of equations were written in a "strong conservation law form" and solved using MacCormack's (Ref. 80) second-order finite-difference algorithm.

Comparison With Case 1

The shape of the isopycnics obtained numerically by Schneyer, Kutler and Shankar and in the present experiments are shown in Figs. 68a, 68b and 68c, respectively. The contour number and the corresponding density ratio are tabulated in Figs. 68a and 68c. Unfortunately we were unable to obtain the contour numbers from Kutler and Shankar (Ref. 63) for Fig. 68b. It is worth noting that the measured density ratios immediately behind the incident and reflected shock waves always agree well with theory. It can be seen immediately that the actual shapes of the isopycnics obtained experimentally appear similar to those predicted by Kutler and Shankar. However, the results from Schneyer do not represent the physical flow. One could discard the isopycnics shown by Schneyer using the following argument. Schneyer's isopycnics (even if their lines were taken to represent the shock as a result of artificial viscosity smearing) have the same value over the entire length of the reflected shock R. This means that the density jump across R is constant everywhere. However, since the angle of incidence between the flow entering R (in a frame of reference attached to the reflection point P) decreases as R moves away from P, the strength of R should increase to maintain a constant density jump. This contradicts both theory and experiment where the shock-wave strength along R decreases as the distance from the reflection point increases, as shown in Fig. 68c. Consequently, the density ratios in the vicinity of Q in Fig. 68a are much larger compared with the actual result (Fig. 68c). However, just the range of density given by Schneyer (Fig. 68a) approximates the measured range (Fig. 68c). Unfortunately only a qualitative comparison can be made with the results of Kutler and Shankar since their values corresponding to the various isopycnics were not given on the figures in Ref. 63, and were unavailable from private communications.

A comparison between the actual shock-wave configuration and the shapes predicted by Schneyer and Kutler and Shankar is shown in Fig. 68d. Since several isopycnics of Schneyer represent shock waves as a result of artificial viscosity, the two extreme contours were reproduced in Fig. 68d. The distance

between the incident shock wave and the corner is normalized for all shapes. It can be clearly seen from Fig. 68d that the predicted shapes do not differ too much from the actual shock-wave configuration. It is worth mentioning that Kutler and Shankar predict their numerically-obtained configuration to be slightly larger than the actual one. However, their explanation that this is due to viscous or real-gas effects is reasonable for the latter. It can be shown analytically that vibrational excitation will reduce the angle between the reflected shock wave and the wedge and hence will result in a smaller configuration. The angle between R and the wedge surface at the reflection point is 16.34° for a perfect gas and 16.04° when real-gas effects are considered. Note that although Schneyer and Kutler and Shankar used two different computational methods which disagree in the prediction of the entire density field, they nevertheless agree in the shock shapes and systems. One can only conclude that the isopycnics are much more sensitive indicators of the accuracy of the physical flow modelled by a specific numerical technique.

Comparison of Case 2

The general shapes of the isopycnics predicted by Kutler and Shankar (Fig. 69a) do not agree with the actual ones (Fig. 64a). Their predicted shapes for this case of RR are almost the same as those discussed previously (Fig. 68b) while our results are very different (Fig. 68c). The disagreement between the actual and numerical isopycnics may arise from the fact that Kutler and Shankar assume a perfect gas. However, for $M_s = 4.71$, $P_0 = 15$ torr, $T_0 = 298$ K, real-gas effects cannot be neglected as the vibrational contribution is significant (e.g., $\rho_2/\rho_0 = 14.53$ for a perfect gas and 17.75 for an imperfect gas). Although this will change the absolute numerical values of the isopycnics it might also affect their shapes.

Although Kutler and Shankar did not report the values of the various isopycnics on their reproduced Fig. 69a, we deduced representative values from their density distribution along the wall shown in Fig. 69b. The range of their densities is lower than the present owing to their assumption of a perfect gas. Note that the strength of the reflected shock wave R decreases from the reflection point to the shock-tube wall in agreement with experiment (Fig. 64a). The numerically calculated density distribution along the wall surface predicted by Kutler and Shankar as well as the measured values close to the wall above the thin boundary layer are shown in Figs. 69b and 65a, respectively. The fact that the actual density values are higher than those predicted by Kutler and Shankar again arises from their perfect-gas assumption. For their case of $M_s = 4.71$ the perfect-gas value $\rho_2/\rho_0 = 14.53$, while for the present case the measured value of $\rho_2/\rho_0 = 16.77$, and it lies between the perfect and imperfect equilibrium values of 14.48 and 17.65, respectively.

The vortical singularity predicted by Kutler and Shankar (V, Fig. 69a) or point d (Fig. 69b) cannot be seen in the interferogram. Therefore the curve from b to f (Fig. 65a), unlike the curve in Fig. 69b, has no discontinuity. If one existed it would be smeared out by the boundary layer. Both curves consist of a sharp density jump $\rho_{20}(f - f)$ at the reflection point followed by a uniform-density region (which is longer in Fig. 69b) terminated by an expansion. At the detached shock-wave position b another sharp rise takes place (the rise is greater in Fig. 69b). The fringe pattern due to the shock-boundary-layer interaction at the corner was too complex to analyse. Therefore the density ratio was extrapolated to the location of the detached shock wave near the corner.

The actual shock wave configuration and the one predicted by Kutler and Shankar are shown in Fig. 69c. This figure agrees with their statement that "the experimental shock location would fall inside the numerical solution". As mentioned earlier, the reason for this lies in real-gas effects rather than viscous effects suggested by Kutler and Shankar. The angle between the reflected shock wave R and the wedge surface for a perfect gas is 14.80° and 12.45° for a real gas. Consequently the actual shape is smaller than the one obtained from a perfect-gas model.

Comparison With Case 3

The shapes of the isopycnics obtained numerically by Schneyer (Ref. 61) using the Lagrangian and Eulerian computer codes as well as those obtained experimentally are shown in Figs. 70a, 70b and 70c, respectively. It is evident that the Lagrangian and Eulerian results differ quite considerably from each other and from the actual isopycnics. The numerical configurations suffer from the same artificially viscous spreading of the incident and reflected shock waves. The isopycnics maintaining the same values along R imply a physically unrealistic reflected shock wave of increasing strength as it moves away from the triple point T. Spurious isopycnics ($n = 4$ and 5 , Fig. 70a) appear from the Lagrangian code in the middle of the reflected wave R. There are no density contours generated in the important region between the Mach stem M and the slipstream S. The Eulerian contours fail to predict the existence of a slipstream altogether (Fig. 70b). If a line is drawn at the estimated location of the slipstream, it intersects the isopycnics implying that the densities on both sides of the slipstream are equal in violation of the physical condition that the slipstream divides two thermodynamic regions of different densities, even if not large. Schneyer (Ref. 61) attributes the appearance of the spurious expansion and shock waves in the middle of R in the Lagrangian results to an inexact choice of the initial velocity profile. He explains the disappearance of the slipstream (in the Eulerian result) as being "washed out" by the "effective [artificial] viscosity".

The actual shape of the isopycnics (Fig. 70c) show very clearly that the densities on both sides of the slipstream are different. The densities behind the reflected shock wave are higher than those behind the Mach stem, as expected from gasdynamic considerations. The approximate density ratio across the slipstream is 1.12 ($3.67/3.27$ near the triple point) shows that it is indeed a weak discontinuity. The analytical density ratio across the slipstream in the vicinity of the triple point is 1.10. A qualitative comparison between the shapes of the actual isopycnics and those of Schneyer indeed show poor agreement. However, as in the previous case only the range of density values approximate those obtained experimentally.

A comparison between the normalized predicted shock shapes and the actual wave configuration is shown in Fig. 70d. The Lagrangian wave system is somewhat larger than the Eulerian. The actual shock wave system lies close to or inside the Eulerian shape boundaries. The slipstream predicted by the Lagrangian code agrees reasonably well with experiment. It is worth repeating that also in this case the Lagrangian and Eulerian codes predict the actual wave system quite well. However, the isopycnic fields and the varying strength of the reflected wave are poorly represented.

It can be summarized that the present experiments show that all numerical methods provide reasonable predictions of the wave systems and their

shapes for the two analysed cases of RR and SMR. No numerical data exist for the cases of CMR and DMR. The numerical codes predict rather poor values and locations for the more sensitive indicators of the flow properties, namely the isopycnics. Of the various numerical analyses produced so far, the one of Kutler and Shankar (Ref. 63) and Shankar, Kutler and Anderson (Ref. 64) are superior. Even their codes require a reassessment and perhaps a new approach in the light of the disagreement with the detailed and very accurate interferometric data presented here.

Undoubtedly, numerical codes will evolve in the future that will reliably predict not only RR and SMR but also CMR and DMR in real gases. The present interferometric data of all these cases should provide a solid base for comparison. In the meantime, those laboratories that have shock tubes equipped with interferometers will benefit from experiments in nonstationary flows in order to check their numerical analyses.

9. CONCLUSIONS

The criteria for the formation and termination of RR, SMR, CMR and DMR, their domains and transition boundaries in both nitrogen and argon, in the (M_s, θ_w') -plane for nonstationary flows and in the (M_0, ϕ_0) -plane for steady flows have been established analytically and verified experimentally.

The equations of motion for RR and SMR in a perfect and an imperfect gas (nitrogen in dissociation equilibrium and argon in ionization equilibrium) have been solved, and the significance of real-gas effects on shifting the boundary lines between the domains of different reflections was shown for the first time.

Analytical methods for predicting the values of χ and χ' were developed, and consequently the reflection process was transformed from the (M_s, θ_w') -plane to the more physical (M_s, θ_w) -plane. The reflection phenomenon in the (M_s, θ_w) -plane was then superimposed with the flow deflection process in the (M_s, θ_w) -plane to yield the overall shock-wave-diffraction phenomenon. It is shown that the range $1 \leq M_s \leq 10$ seven different types of diffraction are possible in nitrogen and six in argon depending on the incident shock wave Mach number M_s , the wedge angle θ_w , and the initial pressure P_0 and temperature T_0 . The present analyses were all substantiated by over 120 interferometric experiments conducted in the UTIAS 10 cm x 18 cm Hypervelocity Shock Tube, as well as many other data in nitrogen, oxygen and air for a diatomic gas and argon and helium for a monatomic gas obtained from other sources. This has brought new order and understanding of the various results from different researchers.

One significant problem remains, namely a more accurate analytical method for calculating the triple-point trajectory angle χ than the one developed earlier by Law and Glass (Ref. 61) using a graphical technique and presently by using a more accurate analytical method.

The density fields of the different diffraction processes have been deduced from the corresponding interferograms, and compared with available numerical predictions.

The very comprehensive isopycnic data are the first since the early pioneering work of White (Refs. 17 and 18) who first noticed the four types of reflection. The results provide an important base for testing available and future computational codes describing such complex flows. Although the numerical methods can satisfactorily predict the gross features of the wave system and shock shapes for regular and single-Mach reflections, they are as yet unsatisfactory for predicting the isopycnics of the flow (Ref. 73). No computational data presently exist for complex and double-Mach reflections. Undoubtedly, such codes will evolve in the near future.

REFERENCES

1. Mach, E. Akad. Wiss. Wien 77, II, 1228 (1878).
2. von Neumann, J. "Oblique Reflection of Shocks", Explosive Research Report No.12, Navy Dept., Bureau of Ordnance, Re2C, Washington, D. C. (1943).
3. Seeger, R. J.
Polachek, H. "Regular Reflection of Shocks in Ideal Gases". Explosive Research Report No.13, Navy Dept., Bureau of Ordnance, Re2C, Washington, D. C. (1943).
4. von Neumann, J. "Refraction, Intersection and Reflection of Shock Waves", NAVORD Report 203-45, Navy Dept. Bureau of Ordnance, Washington, D. C. (1945).
5. Bargmann, V. "On Nearly Glancing Reflection of Shocks", Applied Math. Panel Report No. 108.2R National Research Defence Committee (1945).
6. Smith, L. G. "Photographic Investigation of the Reflection of Plane Shocks in Air", OSRD Report No. 6271, or NORC Report No. A-350 (1945).
7. Lean, G. H. "Report on Further Experiments on the Reflection on Inclined Shock Waves", National Physical Laboratory, London (1946).
8. Pack, D. C. "The Condition for Detachment of the Shock Wave from a Wedge in Supersonic Stream", Proceedings of the Cambridge Philosophical Society Vol. 44 Pt 2, Printed in Great Britain (1947).
9. Taub, A. H. "Refraction of Plane Shock Waves", Rev. Mod. Phys. V. 21, p. 51 (1947).
10. Bleakney, W.
Taub, A. H. "Interaction of Shock Waves", Rev. Mod. Phys. V. 21, p. 584 (1949).
11. Lighthill, M. J. "On the Diffraction of Blast I", Proc. Roy. Soc., V 198, p. 454 (1949).
12. Lighthill, M. J. "On the Diffraction of Blast II", Proc. Roy. Soc., V 200, p. 554 (1950).
13. Fletcher, C. H. "The Mach Reflection of Weak Shock Waves", Tech. Report II-4, Dept. of Phys., Princeton Univ. (1950).
14. Ting, L.
Ludloff, H. F. "Aerodynamics of Blasts", J. Aero. Sci., V. 18, p. 139 (1951).

15. Fletcher, C. H.
Taub, A. H. "The Mach Reflection of Shock Waves at Nearly Glancing Incidence", Rev. Mod. Phys., V. 23, p. 271 (1951).
16. Jones, D. M.
Martin, P. M.
Thornhill, C. K. "A Note on the Pseudo-Stationary Flow Behind a Strong Shock Diffracted or Reflected at a Corner", Proc. Roy. Soc. Sec. A, V. 205, p. 238 (1951).
17. White, D. R. "An Experimental Survey of the Mach Reflection of Shock Waves", Tech. Report II-10, Dept. of Phys., Princeton Univ. (1951).
18. White, D. R. "An Experimental Survey of the Mach Reflection of Shock Waves", 2nd Midwestern Conference on Fluid Mech. (1952).
19. Parks, E. K. "Supersonic Flow in a Shock Tube of Divergent Cross Section", UTIAS Report No. 18 (1952).
20. Jhan, R. G. "The Refraction of Shock Waves at a Gaseous Interface. I. Regular Reflection of Weak Shocks", Tech. Report II-16, Dept. of Phys., Princeton Univ. (1954).
21. Hall, J. G. "The Design and Performance of a 9 inch Plate Mach-Zehnder Interferometer", UTIAS Report No. 27, (1954).
22. Jahn, R. G. "The Refraction of Shock Waves at a Gaseous Interface II. Regular Reflection of Strong Shocks", Tech. Report II-18, Dept. of Phys., Princeton Univ. (1955).
23. Jahn, R. G. "The Refraction of Shock Waves at a Gaseous Interface III-Irregular Reflection", Tech. Report II-19, Dept. of Phys., Princeton Univ. (1956).
24. Kawamura, R.
Saito, H. "Reflection of Shock Waves - I, Pseudo-Stationary Case", Journal of the Phys. Soc. of Japan, V. 11, No. 5, p 584 (1956).
25. Jahn, R. G. "Transonic Process in Shock Wave Interactions", J. Fluid Mech., V. 2, p. 33 (1956).
26. Clutterham, D. R.
Taub, A. H. "Numerical Results on the Shock Configuration in Mach Reflection", Proc. 6th Symp. in Applied Math., p. 45, American Math. Soc., New York (1956).
27. Liepmann, H. W.
Roshko, A. "Elements of Gasdynamics", John Wiley and Sons, New York (1957).
28. Molder, S. "Head on Interaction of Oblique Shock Waves", UTIAS Tech. Note 38 (1960).
29. Pach, D. C. "The Reflexion and Diffraction of Shock Waves", J. Fluid Mech., V. 18, Pt. 4, p. 549 (1964).
30. Molder, S. "Shock Reflection and Interaction at Hypersonic Speeds", J. of Aircraft and Rockets, p. 688 (1964).

31. Henderson, L. F. "On the Confluence of Three Shock Waves in a Perfect Gas", Aero. Quarterly V. XV, p. 181 (1964).
32. Boyer, A. G. "Design, Instrumentation and Performance of the UTIAS 4 in x 7 in Hypersonic Shock Tube", UTIAS Report No. 99 (1964).
33. Henderson, L. F. "The Refraction of a Plane Shock Wave at a Gas Interface", J. Fluid Mechanics V. 26, Pt. 3, p. 607 (1966).
34. Skews, B. W. "Shock Wave Diffraction, a Review", Dept. of Mech. Eng. Report No. 32, Univ. of Witwatersrand, Johannesburg (1966).
35. Skews, B. W. "Profiles of Diffracting Shock Waves (an analysis based on Whitham's theory)", Dept. of Mech. Eng. Report No. 35, Univ. of Witwatersrand, Johannesburg (1966).
36. Shapiro, A. M. "The Dynamic and Thermodynamics of Compressible Fluid Flow", the Ronald Press Co., New York (1954).
37. Henderson, L. F.
McPherson, A. K. "On the Refraction of a Plane Shock Wave at a Mach Number Interface", Dept. of Mech. Eng., Univ. of Sydney (1966).
38. Gvozdeva, L. G.
Predvoditeleva,
O. A. "Experimental Investigation of Mach Reflection of Shock Waves With Velocities of 1000-3000 m/sec in Carbon Dioxide Gas, Nitrogen and Air", Soviet Physics, Doklady, V. 10, No. 8 (1966)
39. Russel, D. A. "Shock Wave Strengthening by Area Convergence", J. Fluid Mech., V. 27, Pt. 2, p. 305 (1967).
40. Henderson, L. F. "The Reflection of a Shock Wave at a Rigid Wall in the Presence of a Boundary Layer", J. Fluid Mech., V. 30, Pt. 4, p. 699 (1967).
41. Skews, B. W. "The Shape of Diffracting Shock Waves", Dept. of Mech. Eng. Report No. 41, Univ. of Witwatersrand, Johannesburg (1967).
42. Skews, B. W. "The Perturbed Region Behind a Diffracting Shock Wave", Dept. of Mech. Eng. Report No. 44, Univ. of Witwatersrand, Johannesburg (1967).
43. Weynants, R. R. "An Experimental Investigation of Shock Wave Diffraction over Compression and Expansion Corners", UTIAS Tech. Note No. 126 (1968).
44. Merritt, D. L. "Mach Reflection on a Cone", AIAA Jour. V. 6, No. 6 (1968).
45. Gvozdeva, L. G.
et al "Mach Reflection of Shock Waves in Real Gases", Astronautica Acta, V. 14, p. 503 (1969).

46. Higashimo, F. "Real Gas Effects on Converging Shock Waves", *Astronautica Acta*, V. 15, p. 523 (1970).
47. Gvozdeva, L. G. et al "Pressure and Temperature at the Wedge Surface for Mach Reflection of Strong Shock Waves", *Astronautica Acta*, V. 15 p. 503 (1970).
48. Law, C. K. "Diffraction of Strong Shock Waves by a Sharp Compressive Corner", UTIAS Tech. Note No. 150 (1970).
49. Hanson, R. K. "Shock Wave Reflection in a Relaxing Gas", *J. Fluid Mech.*, V. 45, Pt. 4, p. 721 (1971)
50. Skews, B. W. "Shock - Shock Reflection", *CASI Transactions*, V. 4, No. 1 (1971).
51. Law, C. K.
Glass, I. I. "Diffraction of Strong Shock Waves by a Sharp Compressive Corner", *CASI Transactions*, V. 4, No. 1 (1971).
52. Skews, B. W. "The Flow in the Vicinity of a Three Shock Intersection", *CASI Transactions*, V. 4, No. 2 (1971).
53. Molder, S. "Reflection of Curved Shock Waves in Steady Supersonic Flow", *CASI Transactions*, V. 4, No. 2 (1971).
54. Lozzi, A. "Double Mach Reflection of Shock Waves", M.Sc. Report, The Univ. of Sydney, Sydney, New South Wales, Australia (1971).
55. Bazhenova, T.V. et al "Pressure and Temperature Change on the Wall Surface in Steady Shock Wave Diffraction", *Astronautica Acta*, V. 17 p. 659 (1972).
56. Skews, B. W. "The Shape of a Shock in Regular Reflection from a Wedge", *CASI Transactions*, V. 5, No. 1 (1972).
57. Skews, B. W. "The Effect of a Angular Slipstream on Mach Reflection", McMaster Univ., Hamilton, Ontario, Canada (1972).
58. Skews, B. W. "The Deflection Boundary Condition in the Regular Reflection of Shock Waves", McMaster Univ., Hamilton, Ontario, Canada (1972).
59. Molder, S. "Polar Streamline Direction at the Triple Point of a Mach Interaction of Shock Waves", *CASI Transactions*, V. 5, No. 2 (1972).
60. Henderson, L. F.
Lozzi, A. "Experiments on Transition of Mach Reflection", *J. Fluid Mech.*, V. 68, Pt. 1, p. 139 (1975).
61. Schneyer, G. P. "Numerical Simulation of Regular and Mach Reflection", *The Phys. of Fluids*, V. 18, No. 9 (1975).
62. Bazhenova, T.V. et al "Regions of Various Forms of Mach Reflection and its Transition to Regular Reflection", *Astronautica Acta*, V. 3, p. 131 (1976).

63. Kutler, P.
Shankar, V. "Diffraction of a Shock Wave by a Compression Corner - Part I: Regular Reflection", AIAA Journal, V. 5, No. 2 (1977).
64. Shankar, V.
Kutler, P.
Anderson, D. "Diffraction of a Shock Wave by a Compression Corner - Part II: Single Mach Reflection", AIAA Journal, V. 16, No. 1 (1977). See also AIAA 15th Aerospace Sciences Meeting, paper No. 77-89 (1977).
65. Hornung, H. G.
Kychakoff, G. "Transition from Regular to Mach Reflection of Shock Waves in Relaxing Gases", Proc. of the 11th International Shock Tube Symposium, Univ. of Washington, Seattle (1977).
66. Heilig, W. H. "A Result Concerning the Transition From Regular Reflection to Mach Reflection of Strong Shock Waves", Proc. of the 11th International Shock Tube Symposium, Univ. of Washington, Seattle (1977).
67. Tang, F. C. "Effects of Impurities on Shock Wave Stability and Structure in Ionizing Monatomic Gases", UTIAS Tech. Note No. 212 (1977).
68. Glass, I. I.
Liu, W. S.
Tang, F. C. "Effects of Hydrogen Impurity on Shock Structure and Stability in Ionizing Monatomic Gases, Part 2: Krypton", Canadian J. of Phys., V. 55, No. 14, (1977).
69. Glass, I. I.
Liu, W. S. "Effects of Hydrogen Impurities on Shock Structure and Stability in Ionizing Monatomic Gases, Part 1: Argon", J. Fluid Mech., V. 84, Pt. 1, p. 55 (1978).
70. Liu, W. S.
Whitten, B. T.
Glass, I. I. "Ionizing Boundary Layers: 1. Quasi-Steady Flat-Plate Laminar Boundary-Layer Flows", J. of Fluid Mech. (To be published 1978).
71. Whitten, B. T.
Ben-Dor, G. "Experimental Techniques and Interferometric-Evaluation Methods for the UTIAS 10 cm x 18 cm Hypervelocity Shock Tube", UTIAS Tech. Note (to be published).
72. Ben-Dor, G. "Nonstationary Oblique Shock Wave Diffractions in Nitrogen and Argon - Experimental Results", UTIAS Tech. Note (to be published).
73. Ben-Dor, G.
Glass, I. I. "Nonstationary Oblique Shock Wave Reflections. Actual Isopycnics and Some Numerical Experiments", AIAA Journal (to be published, 1978).
74. Hornung, H. G.
Oertel, H., Jr.
Sandeman, R. J. "Transition to Mach Reflection of Shock Waves in Steady and Pseudosteady Flow With and Without Relaxation", Dept. of Phys., Australian National University, Canberra, Australia. (1978).
75. Whitten, B. T. "An Interferometric Investigation of Quasi-Steady Shock-Induced Boundary Layers in Partially Ionized Argon", UTIAS Report (To be published).

76. Molder, S. Private Communication.
77. Hornung, H. G. Private Communication.
78. Hageman, L. J.
Walsh, J. M. "HELP, a Multi-Material Eulerian Program for Compressible Fluid and Elastic-Plastic Flows in Two Space Dimensions and Time", Ballistic Research Laboratories, BRL Contract Report No. 39 (1971).
79. Wilkins, M. L. "Method in Computational Physics", edited by B. Alder, S. Fernbach and M. Rotenberg (Academic Press, New York), V. 3 (1964).
80. MacCormack, R. W. "The Effect of Viscosity in Hypervelocity Impact Cratering", AIAA Paper 69-354 (1969).
81. Molder, S. "Particular Conditions for the Termination of Regular Reflection of Shock Waves", CASI Trans. (to be published, 1969).
82. Ben-Dor, G.
Glass, I. I. "Domains and Boundaries of Nonstationary Oblique Shock-Wave Reflections: I. Diatomic Gas", Jour. Fluid Mechanics (to be published, 1979).
83. Ben-Dor, G.
Glass, I. I. "Domains and Boundaries of Nonstationary Oblique Shock-Wave Reflections: II. Monatomic Gas" (to be published).

Table 1

Diffraction Regions in Nitrogen

(Fig. 39)

Region No.	Shock Diffraction	
	Shock Reflection	Flow Deflection
1	RR	Detached
2	SMR	Detached
3	SMR	Attached
4	CMR	Detached
5	CMR	Attached
6	DMR	Detached
7	DMR	Attached

Table 2

Diffraction Regions in Argon

(Fig. 40)

Region No.	Shock Diffraction	
	Shock Reflection	Flow Deflection
1	RR	Detached
2	SMR	Detached
3	SMR	Attached
4	CMR	Detached
5	CMR	Attached
6	DMR	Detached

Table 3

Initial Conditions for Obtaining
Various Shock Wave Mach Numbers - Nitrogen

M_s	P_{41}	Driving Gas
2.0	110	CO ₂
3.7	220	He
4.8	690	He
6.2	800	He
7.0	1550	H ₂
7.8	3320	H ₂

Table 4

Initial Conditions for Obtaining
Various Shock Wave Mach Numbers - Argon

M_s	P_{41}	Driving Gas
2.0	60	CO ₂
3.0	70	He
4.4	350	He
5.2	800	He
6.1	520	H ₂
6.9	1000	H ₂
7.9	1900	H ₂

Table 5

Initial Conditions for the Experiments in Nitrogen

θ_w	M_s	P_o	T_o	χ	χ'	Reflec- tion	Exp.
2	1.95	52.50	297.2	26.0		SMR	70
2	1.89	53.50	297.3	26.5		SMR	71
2	1.85	52.50	297.4	26.5		SMR	72
2	3.84	15.19	297.4	23.5		SMR	73
2	4.15	15.17	297.3	23.0		SMR	74
5	3.75	15.25	295.9	20.5		SMR	37
5	4.71	15.81	295.2	20.0		SMR	31
5	5.85	15.18	297.0	19.5		SMR	33
5	6.01	15.19	295.8	18.5		SMR	34
5	6.86	10.00	295.6	18.0		SMR	35
5	7.51	5.17	296.0	17.5		SMR	36
10	2.01	50.00	295.8	19.0		SMR	39
10	2.37	35.44	297.7	18.5		SMR	88
10	2.61	37.00	297.8	18.0		SMR	90
10	2.82	30.34	297.6	18.0		SMR	89
10	3.62	15.23	295.4	16.5		SMR	40
10	4.59	15.16	298.5	16.2		SMR	5
10	4.72	15.00	295.0	16.0		SMR	41
10	5.92	15.27	295.0	15.5		SMR	42
10	6.79	10.21	295.2	15.0		SMR	43
10	7.58	5.13	294.8	14.5		SMR	44
20	1.93	51.00	297.2	12.5		SMR	50
20	3.74	15.31	297.4	12.0		CMR	49
20	4.81	15.29	296.6	11.5	15.5	CMR	48
20	6.27	15.33	296.0	11.2	14.5	CMR	47
20	6.87	10.12	295.8	11.0	14.0	CMR	46
20	7.71	5.06	296.0	10.0	11.5	CMR	45
26.56	2.01	50.00	296.6	9.2		SMR	26
26.56	8.06	5.10	298.2	9.0	9.9	DMR	102
30	1.97	51.00	297.4	8.5		SMR	51
30	3.68	15.27	297.3	8.0	10.0	CMR	52
30	4.68	15.28	297.4	7.8	9.5	DMR	53
30	5.93	15.22	297.4	7.7	10.0	DMR	54
30	6.96	10.11	297.4	7.6	9.8	DMR	55
30	7.97	4.99	297.4	7.4	9.0	DMR	56

Continued.....

Table 5 - Continued

Initial Conditions for the Experiments in Nitrogen

θ_w	M_s	P_o	T_o	χ	χ'	Reflec- tion	Exp.
40	2.02	50.00	297.3	4.0		CMR	63
40	3.69	15.34	297.4	4.8	7.0	DMR	62
40	4.59	15.64	298.2			DMR	9
40	4.60	15.15	298.4			DMR	10
40	4.64	15.29	297.2	5.0	6.2	DMR	6
40	4.72	15.31	296.4			DMR	7
40	4.75	15.30	297.4	5.2	6.2	DMR	61
40	4.98	5.13	296.9	5.2	6.8	DMR	5
40	6.17	15.34	297.4	4.2	6.0	DMR	60
40	6.97	10.28	297.3	3.8	5.5	DMR	59
40	7.78	5.00	297.3	3.5	4.0	DMR	57
40	7.95	5.01	298.5	3.8	4.0	DMR	58
50	2.07	50.00	299.6			RR	127
50	3.69	15.27	298.9			RR	126
50	4.78	15.24	298.4			RR	125
50	6.22	15.29	299.6			RR	124
50	7.29	10.22	299.1			RR	123
60	1.96	65.00	299.0			RR	130
60	2.03	59.00	299.2			RR	128
60	3.84	17.18	299.0			RR	129
60	4.68	15.31	298.1			RR	18
60	4.76	15.26	298.4			RR	131
63.43	2.01	50.00	296.8			RR	25

Table 6

Initial Conditions for the Experiments in Argon

θ_w	M_s	P_o	T_o	χ	χ'	Reflec- tion	Exp.
2	2.03	50.00	297.4	28.5		SMR	84
2	3.02	20.29	297.8	28.0		SMR	83
2	4.39	15.00	297.4	27.5		SMR	75
2	5.19	15.30	297.2	27.0		SMR	78
2	5.33	5.04	297.3				76
2	5.42	5.08	297.3				77
2	6.13	15.33	296.0			SMR	80
2	6.47	15.32	295.4	26.0		SMR	81
2	7.77	9.80	297.6	25.0		SMR	82
10	2.01	50.00	298.6	21.0		SMR	85
10	2.96	20.28	299.0	20.0		SMR	86
10	4.39	15.32	297.0	19.5		SMR	87
10	5.22	15.22	298.4	19.2		SMR	91
10	6.06	15.24	299.0	18.5		SMR	92
10	6.47	15.27	299.0	18.5		SMR	93
10	7.88	9.96	298.6	17.5		SMR	94
20	2.00	50.00	298.4	15.0		SMR	101
20	2.82	20.32	299.0	14.5		SMR	100
20	4.40	15.26	299.0	14.0		CMR	99
20	5.20	15.22	299.0	14.0	17.0	CMR	98
20	6.04	15.27	297.2	13.7	17.5	CMR	97
20	6.84	15.22	298.4	14.0	18.0	CMR	96
20	7.76	9.84	299.0	14.0	17.5	CMR	95
30	2.03	50.00	299.6	9.5		SMR	103
30	2.89	20.24	299.2	9.5	12.0	CMR	104
30	4.51	15.25	299.0	10.0	13.0	CMR	105
30	5.29	15.21	299.4	10.0	12.5	CMR	106
30	6.36	15.27	299.4	10.2	13.0	CMR	107
30	6.96	15.00	295.4	10.0	13.0	CMR	109
30	8.01	9.80	299.5	10.0	13.0	CMR	108
40	2.05	50.00	297.8	6.0	11.0	CMR	116
40	3.11	20.34	299.8	5.5	10.0	CMR	115
40	4.44	15.00	299.1	5.5	10.0	DMR	114
40	5.28	15.29	297.9	5.5	10.0	DMR	113
40	6.12	15.32	297.6	5.7	10.0	DMR	112
40	6.81	15.23	298.8	5.7	9.5	DMR	111
40	7.53	9.87	297.0	5.5	9.5	DMR	110
50	2.04	50.00	298.2	1.0		CMR	117
50	2.96	20.50	298.4	1.5	4.0	DMR	118
50	4.40	15.30	299.2	2.0	4.0	DMR	119
50	5.27	15.32	298.2	1.5	4.0	DMR	120
50	6.27	15.34	299.4	1.4	4.0	DMR	121
50	7.03	15.29	299.4	1.3	3.5	DMR	122

Continued.....

Table 6 - Continued

Initial Conditions for the Experiments in Argon

θ_w	M_s	P_o	T_o	χ	χ'	Reflec- tion	Exp.
60	2.03	50.00	301.0			RR	132
60	2.03	50.00	299.2			RR	134
60	3.03	20.00	299.5			RR	133
60	4.50	16.16	299.8			RR	135
60	5.24	15.30	299.2			RR	136

Table 7

Discovery of Four Types of Oblique-Shock-Wave Reflections

	Discovered by	Suggestion of Criterion for	
		Formation	Termination
RR	Mach Ref. 1 1878	Neumann Ref. 2 1943	Hornung et al Ref. 65 1976 *
SMR	Mach Ref. 1 1878	Hornung et al Ref. 65 1976 *	White Ref. 17 1951
** CMR	Smith Ref. 6 1945	White Ref. 17 1951	Ben-Dor Present 1978
** DMR	White Ref. 17 1951	Ben-Dor Present 1978	***

* The termination criterion of RR and formation criterion of SMR for non-stationary flows were established by Neumann (1943) and for steady flows by Henderson and Lozzi (1975). However, Hornung and Kychakoff established a more general criterion which holds for both steady and nonstationary flows.

** Recall that CMR and DMR do not exist in steady flows.

*** For the time being DMR may not terminate. However, it is possible that for very high values of M_s , the flow Mach number in state (5), see Fig. 19, will become so high that a shock wave will be needed to prevent it from colliding with the wall. Under these circumstances DMR will terminate, and a triple-Mach reflection (TMR) might be formed.

Table 8

Discovery of Analytical Boundaries

for Four Types of Oblique-Shock-Wave Reflection

Calculation of Boundary Lines Between Reflection Domains				
	Monatomic Gas		Diatomic Gas	
	Perfect	Imperfect	Perfect	Imperfect
RR / SMR CMR DMR *	Law Ref. 48 1970	Ben-Dor Present 1978	Neumann Ref. 2 1943	Ben-Dor Present 1978
DMR/CMR	Ben-Dor Present 1978	Ben-Dor Present 1978	Ben-Dor Present 1978	Ben-Dor Present 1978
CMR/SMR	Ben-Dor Present 1978	Ben-Dor Present 1978	Bazhenova et al Ref. 55 1976	Ben-Dor Present 1978

* Recall that the termination of RR can result in either an SMR, CMR or DMR depending on the value of M_s (see Figs. 39 and 40 for details).

Table 9

The Compared Reflection Cases and Their Initial Conditions

Type	Case	Initial* Conditions	Imperfect Gas	Perfect Gas		
			Present Experiment	Schneyer		Kutler & Shankar
				Eulerian	Lagrangian	
REGULAR REFLECTION	1	Gas	N ₂	$\gamma=1.40$		$\gamma=1.40$
		θ_w°	63.43	63.43		63.41
		M _s	2.01	2.00		2.00
		P _o (torr)	50.00	760		760
		T _o (K)	298.6			
		$\rho_o(\text{g/cm}^3)$	7.57×10^{-5}	10^{-3}		10^{-3}
	2	Gas	N ₂			O ₂
		θ_w°	60.00			60
		M _s	4.68			4.71
		P _o (torr)	15.31			15
		T _o (K)	298.1			298.6
		$\rho_o(\text{g/cm}^3)$	2.31×10^{-5}			2.50×10^{-5}
SINGLE-MACH REFLECTION	3	Gas	N ₂	$\gamma=1.40$	$\gamma=1.40$	
		θ_w°	26.56	26.56	26.56	
		M _s	2.01	2.00	2.00	
		P _o (torr)	50.00			
		T _o (K)	296.6			
		$\rho_o(\text{g/cm}^3)$	7.57×10^{-5}	10^{-3}	10^{-3}	

* Initial conditions are for the quiescent gas ahead of the incident shock wave.

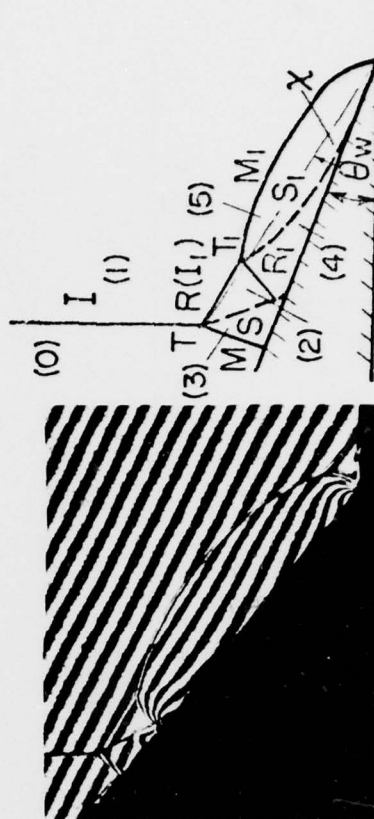
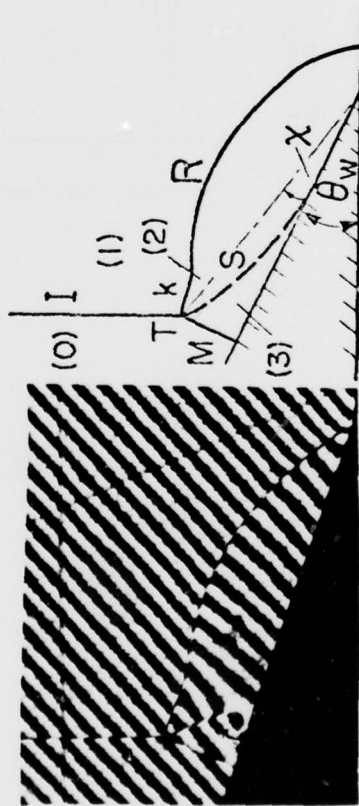
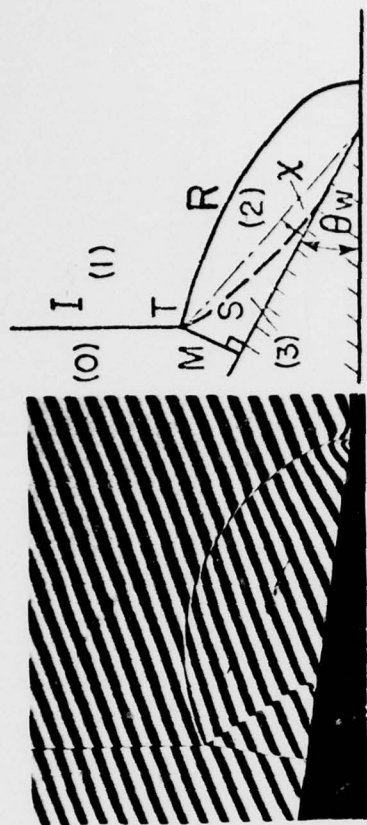
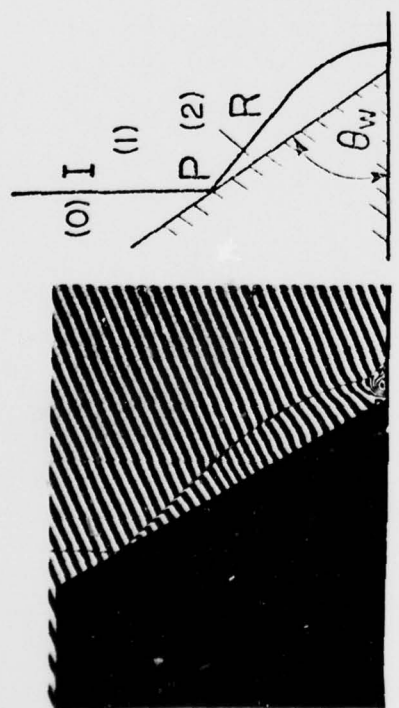


FIG. 1 ILLUSTRATION OF FOUR POSSIBLE OBLIQUE SHOCK-WAVE REFLECTIONS IN NITROGEN

- (a) REGULAR REFLECTION (RR), $\theta_w = 60^\circ$, $M_s = 4.68$.
- (b) SINGLE-MACH REFLECTION (SMR), $\theta_w = 10^\circ$, $M_s = 2.61$.
- (c) COMPLEX-MACH REFLECTION (CMR), $\theta_w = 20^\circ$, $M_s = 6.90$.
- (d) DOUBLE-MACH REFLECTION (DMR), $\theta_w = 40^\circ$, $M_s = 3.76$.

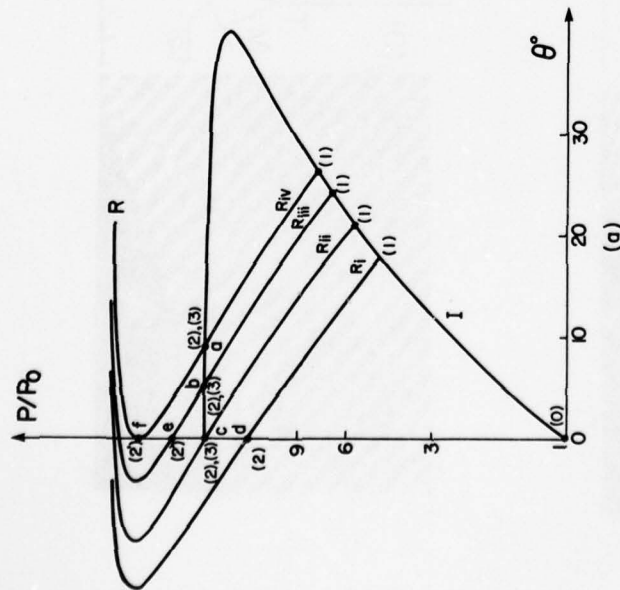


FIG. 2a. INCIDENT (I) AND REFLECTED (R) SHOCK POLAR COMBINATION ILLUSTRATING DIFFERENT TERMINATION CRITERIA FOR REGULAR REFLECTION (RR). IMPERFECT NITROGEN $M_0 = 4.00$, $P_0 = 15$ TORR, $T_0 = 300$ K.

(i) $\theta_1^* = 50.06^\circ$, $M_1 = 2.00$

(ii) "mechanical-equilibrium" criterion, $\theta_1^* = 56.42^\circ$, $M_1 = 2.21$

(iii) $\theta_1^* = 52.66^\circ$, $M_1 = 2.43$

(iv) "detachment" criterion, $\theta_1^* = 49.99^\circ$, $M_1 = 2.57$.

Note all polars are accurately drawn to scale for given conditions.

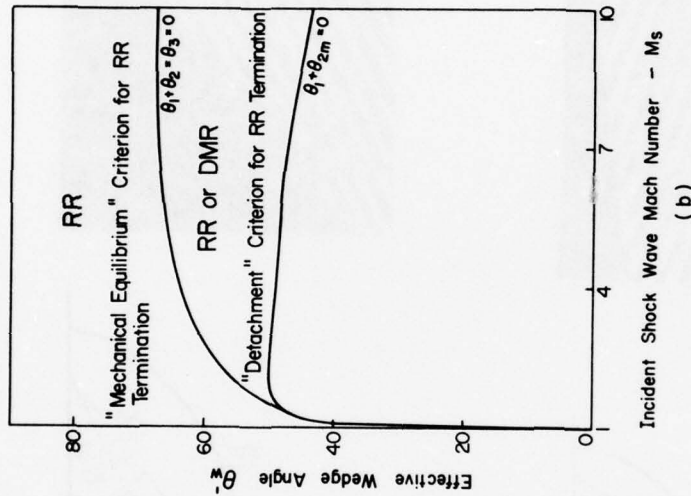


FIG. 2(b). COMPARISON BETWEEN THE "DETACHMENT" AND THE "MECHANICAL-EQUILIBRIUM" CRITERIA FOR RR-TERMINATION IN THE (M_1, θ_1^*) -PLANE, IMPERFECT NITROGEN $P_0 = 15$ TORR, $T_0 = 300$ K.

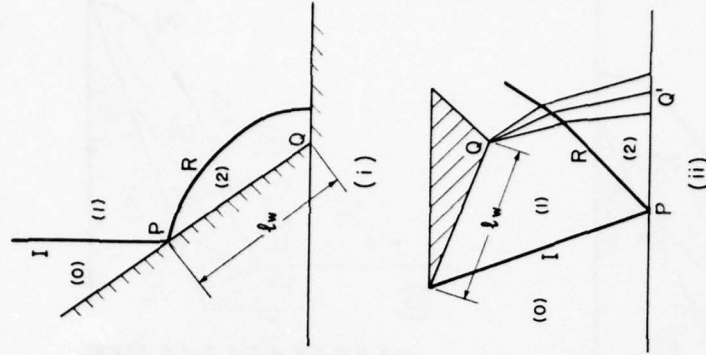


FIG. 2(c). COMMUNICATION OF A SCALE LENGTH TO THE REFLECTION POINT.

(i) - Nonstationary Flow

(ii) - Steady Flow

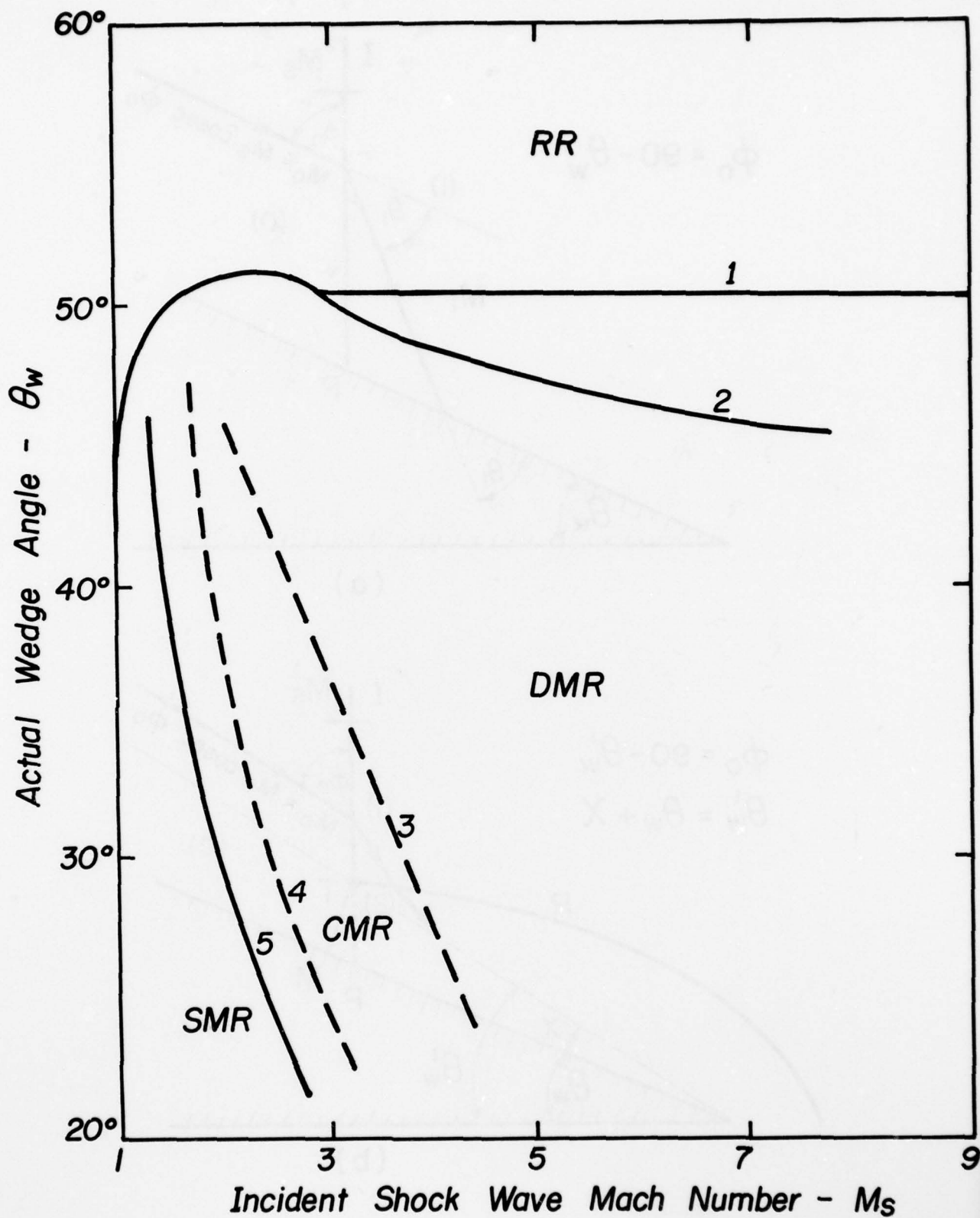


FIG. 3. DOMAINS AND BOUNDARIES OF SHOCK WAVE REFLECTION IN (M_s, θ_w) -PLANE (ENLARGE REPRODUCTION OF FIG. 5, REF. 62). SOLID LINES ARE ANALYTICAL, DASHED LINES ARE EXPERIMENTAL.

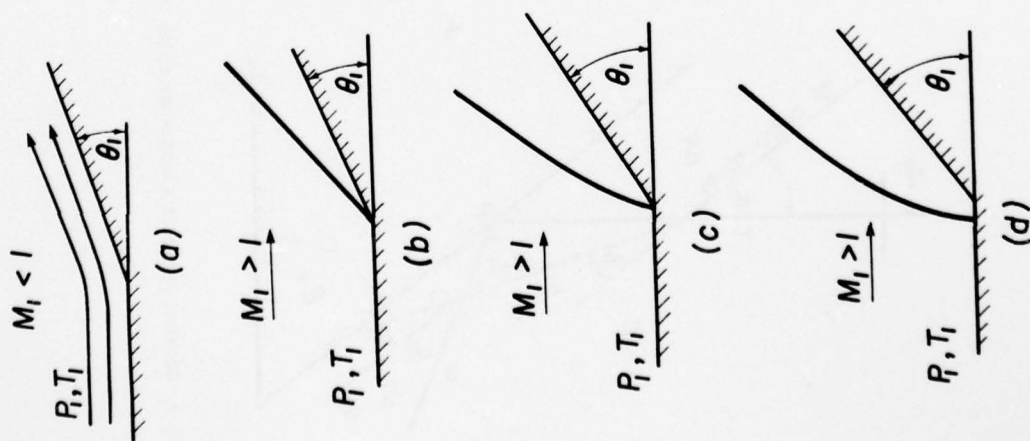


FIG. 5. FLOW OVER WEDGE IN STEADY FLOW
 (a) $M_1 < 1$, subsonic tuning
 (b) $M_1 > 1$, $0 < \theta < \theta^*$ straight attached bow shock
 (c) $M_1 > 1$, $\theta < \theta^* < \theta_m$ curved attached bow shock
 (d) $M_1 > 1$, $\theta_m^* < \theta < 90^\circ$ curved detached bow shock

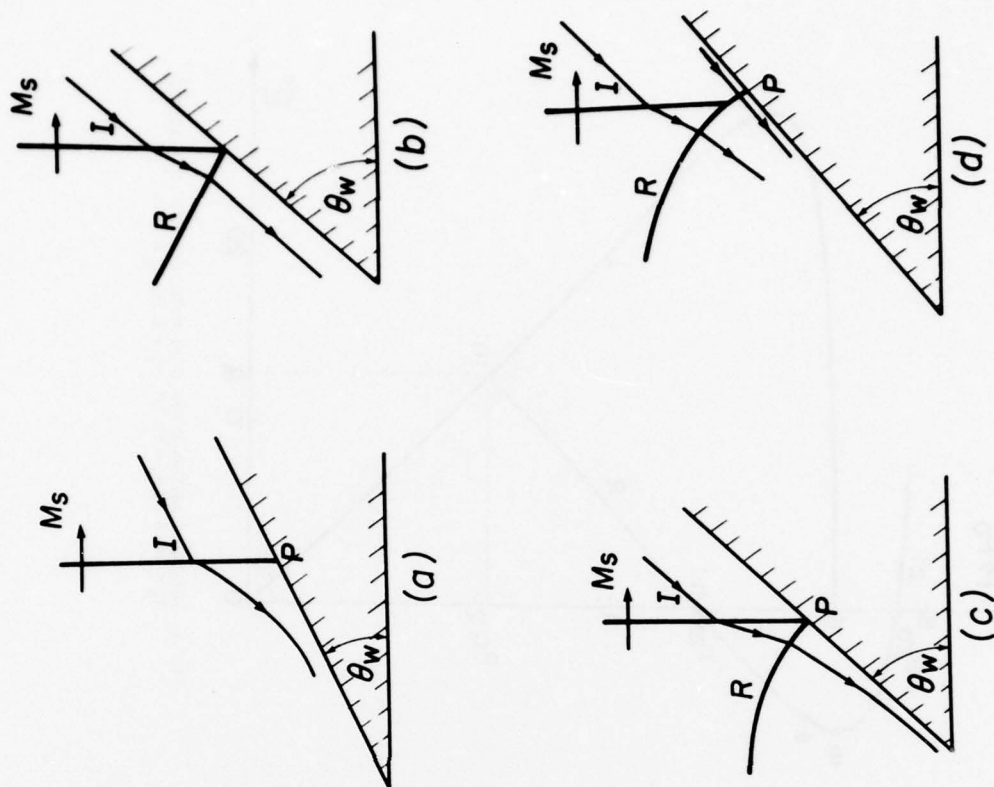


FIG. 6. THE NONSTATIONARY ANALOGY OF FIG. 5(a) to (d), RESPECTIVELY.

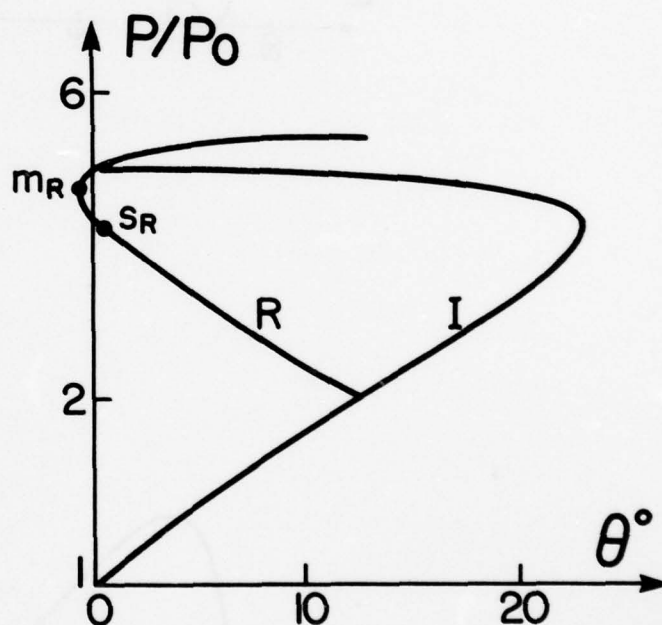
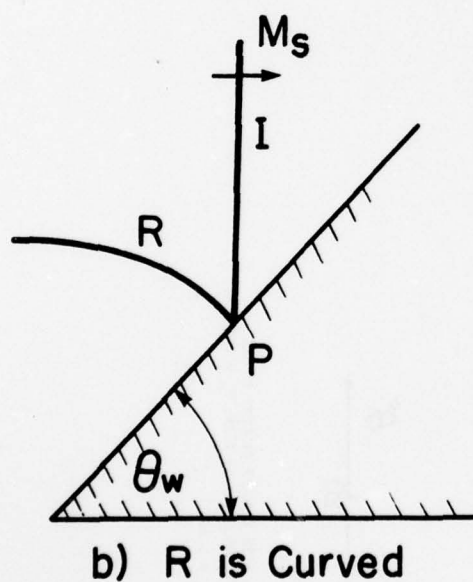
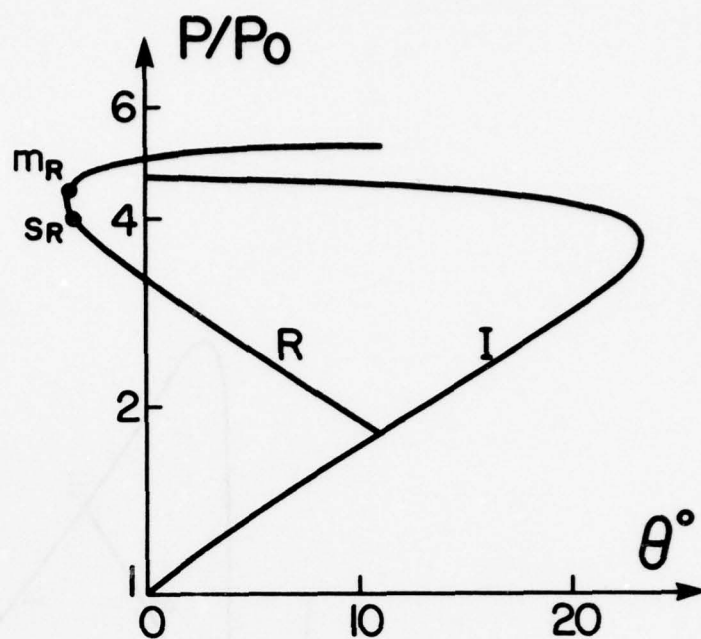
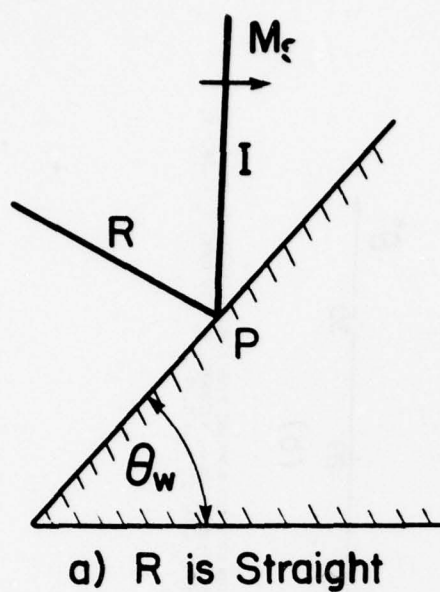


FIG. 9. REGULAR REFLECTION PROCESS AT POINT P, NITROGEN, $P_0 = 15$ TORR, $T_0 = 298.6$ K, $M_0 = 2.00$.
 (a) $\theta_w = 49.59^\circ$, $M_s = 1.30$
 (b) $\theta_w = 47.46^\circ$, $M_s^S = 1.35$

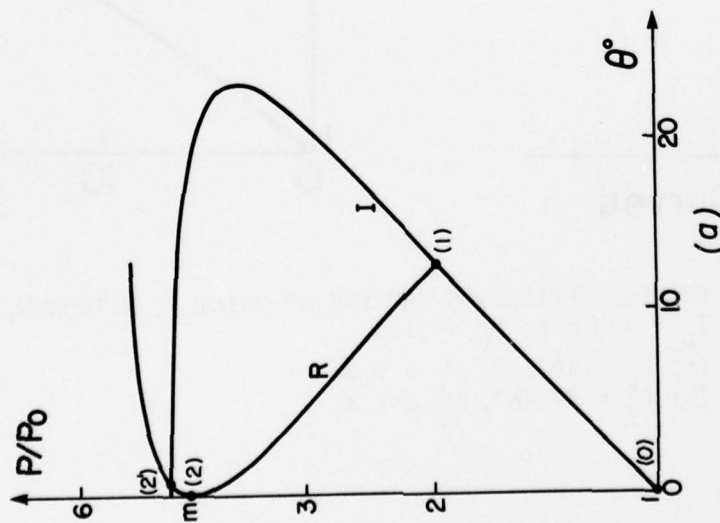


FIG. 10(a) COMBINATION OF I AND R-POLARS WITH R-POLAR TANGENT TO THE P/P₀-AXIS INSIDE I-POLAR, NITROGEN, P₀ = 15 TORR, T₀ = 298.6 K, M₀ = 2.00, $\theta_w = 47.32^\circ$, M_s = 1.36.

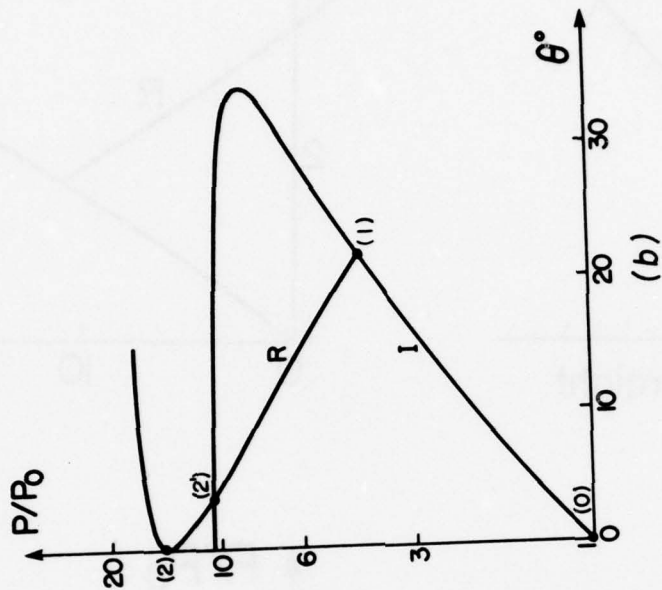


FIG. 10(b) COMBINATION OF I AND R-POLARS WITH R-POLAR TANGENT TO THE P/P₀-AXIS OUTSIDE I-POLAR, NITROGEN, P₀ = 15 TORR, T₀ = 298.6 K, M₀ = 3.00, $\theta_w = 50.01^\circ$, M_s = 1.93

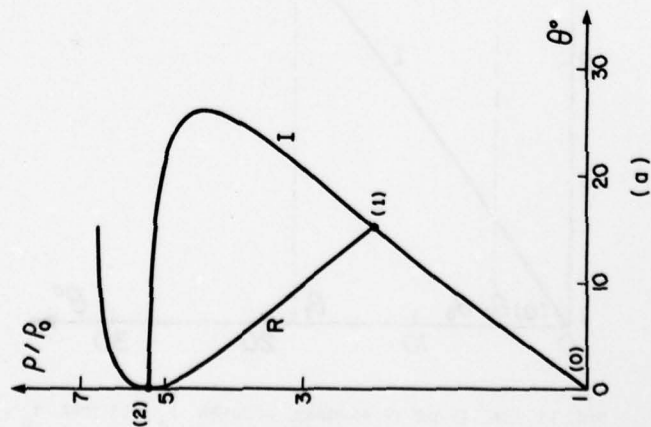


FIG. 11(a) I AND R-POLAR COMBINATION FOR CHANGE OVER MACH NUMBER M_{0c} .
 $\gamma = 1.400$, $M_{0c} = 2.190$, $M_0 = 1.450$, $\theta_w = 48.55^\circ$.

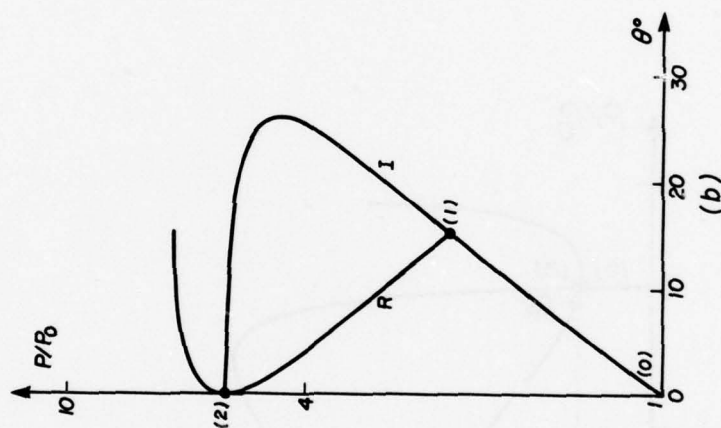


FIG. 11(b) I AND R-POLAR COMBINATION FOR CHANGE OVER MACH NUMBER M_{0c} .
 IMPURE NITROGEN, $M_{0c} = 2.185$, $M_0 = 1.449$, $\theta_w = 48.46^\circ$,
 $P_0 = 15$ TORR, $T_0 = 300^\circ K$.

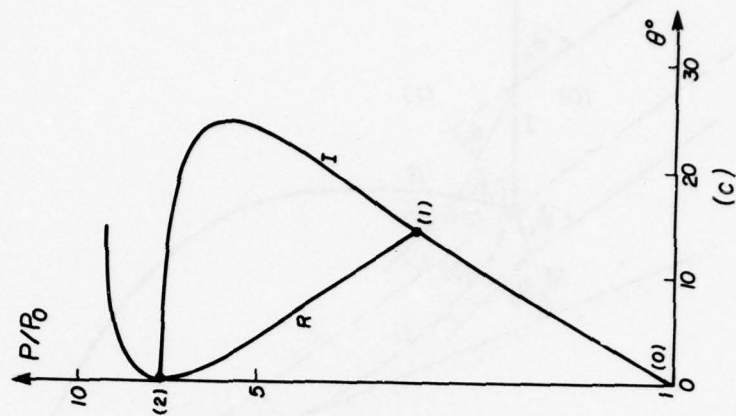


FIG. 11(c) I AND R-POLAR COMBINATION FOR CHANGE OVER MACH NUMBER M_{0c} .
 $\gamma = 1.667$, $M_{0c} = 2.453$, $M_0 = 1.540$, $\theta_w = 51.13^\circ$.

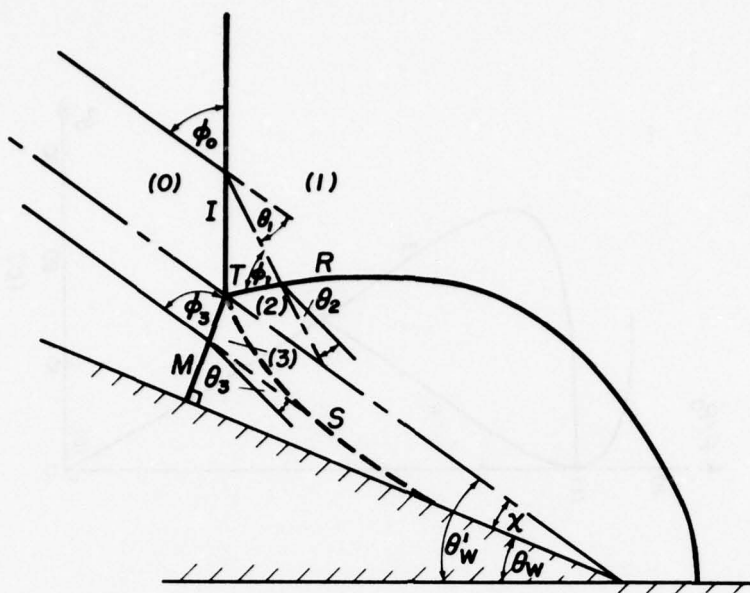


FIG. 12. SCHEMATIC DIAGRAM OF A SINGLE-MACH REFLECTION (SMR).

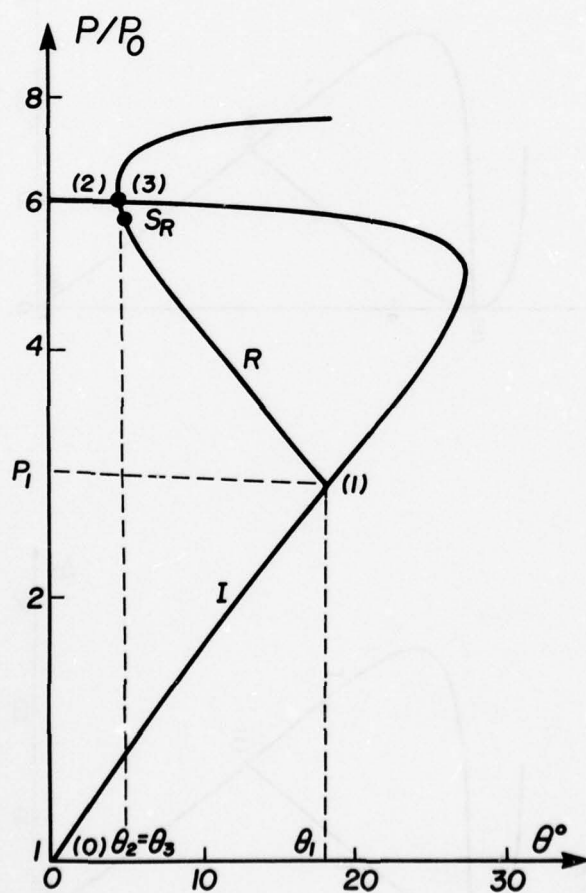


FIG. 13. SMR IN THE (P, θ) -PLANE, NITROGEN. $P_0 = 15$ TORR. $T_0 = 300$ K, $M_s = 1.59$, $\theta'_w = 46.27^\circ$, $M_0 = 2.30$.

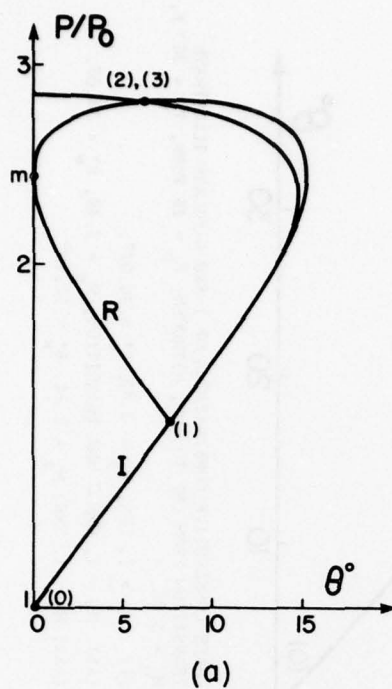


FIG. 14(a) SMR SOLUTION IN THE (P, θ) -PLANE WHEN $\theta_3 = \theta_2 < \theta_1$, $\gamma = 1.40$, $M_0 = 1.60$, $\theta'_w = 42.12^\circ$, $M_s = 1.18$.

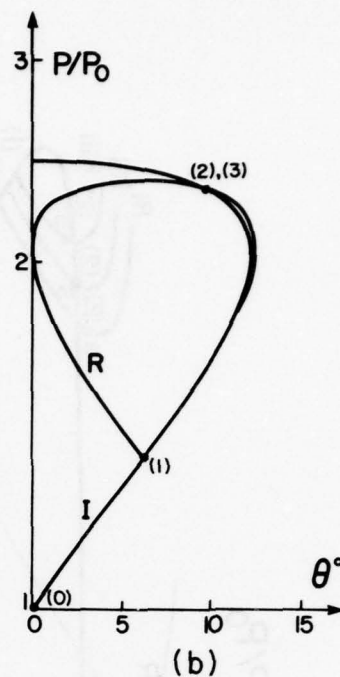


FIG. 14(b) SMR SOLUTION IN THE (P, θ) -PLANE WHEN $\theta_3 = \theta_2 > \theta_1$, $\gamma = 1.40$, $M_0 = 1.50$, $\theta'_w = 40.33^\circ$, $M_s = 1.14$.

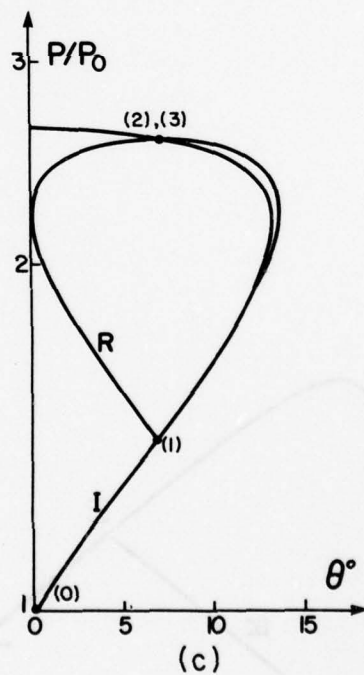


FIG. 14(c) SMR SOLUTION IN THE (P, θ) -PLANE WHEN $\theta_3 = \theta_2 = \theta_1$, $\gamma = 1.40$, $M_0 = 1.55$, $\theta'_w = 48.50^\circ$, $M_s = 1.03$.

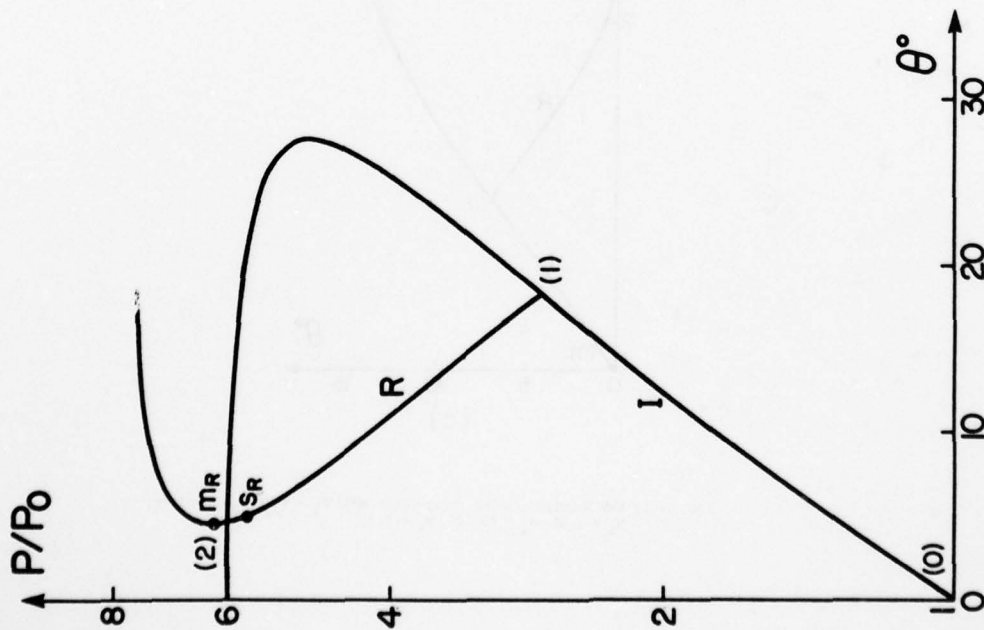


FIG. 15. I AND R-POLAR COMBINATION FOR $2.23 < M_0 < 2.40$, $\gamma = 1.40$, $M_0 = 2.30$, $\theta'_w = 46.27^\circ$, $M_s = 1.59$.

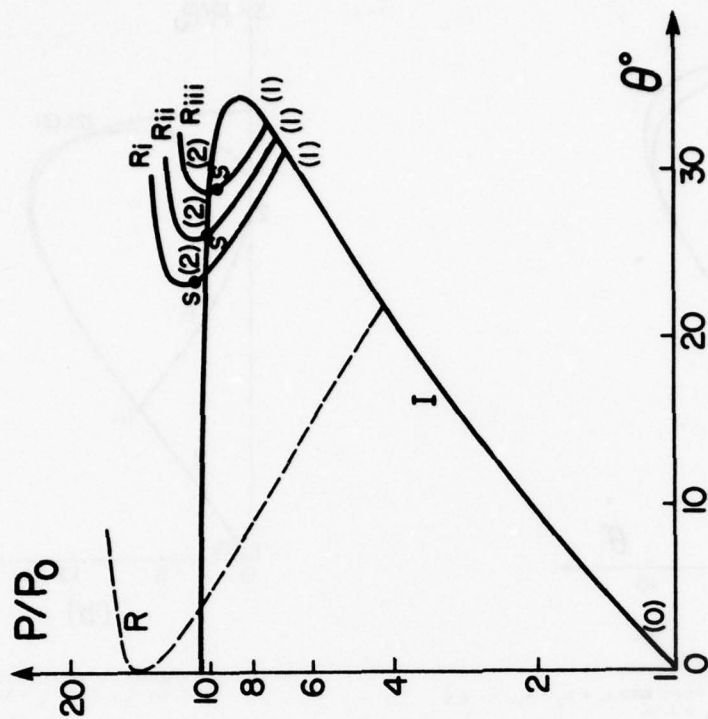


FIG. 16. THREE CONSECUTIVE COMBINATIONS OF I AND R-POLARS ILLUSTRATE TRANSITION FROM CMR TO SMR, NITROGEN, $P_0 = 15$ TORR, $T_0 = 300$ K, $M_0 = 3.00$.

(i) $M_2 > 1$, CMR, $M_s = 2.43$, $\theta'_w = 36.02^\circ$.

(ii) $M_2 = 1$, CMR \rightleftharpoons SMR TRANSITION, $M_s = 2.49$, $\theta'_w = 34.07^\circ$.

(iii) $M_2 < 1$, SMR, $M_s = 2.54$, $\theta'_w = 32.10^\circ$.

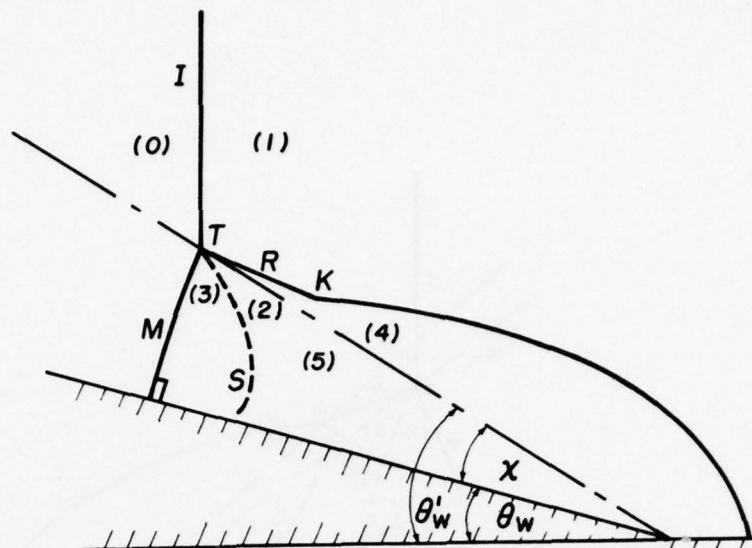
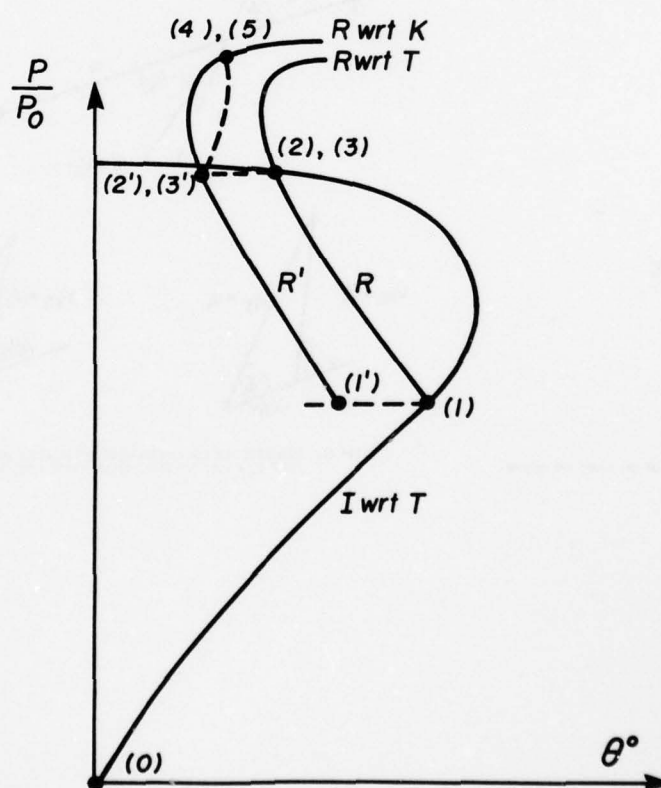


FIG. 17. SCHEMATIC DIAGRAM OF A COMPLEX-MACH REFLECTION (CMR).

FIG. 18. CMR IN THE (P, θ) -PLANE.

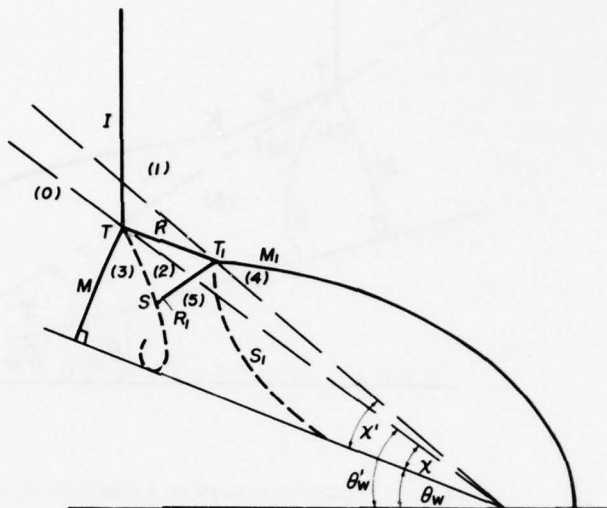


FIG. 19. SCHEMATIC DIAGRAM OF A DOUBLE-MACH REFLECTION (DMR).

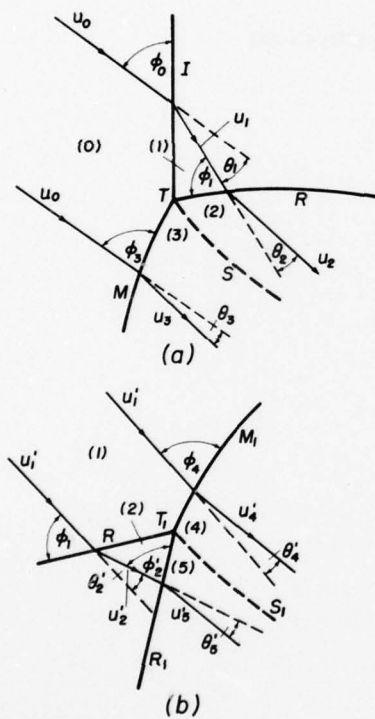


FIG. 20. THE ANALOGY BETWEEN THE WAVE SYSTEM OF THE FIRST AND SECOND TRIPLE POINTS (T AND T₁) OF A DMR.

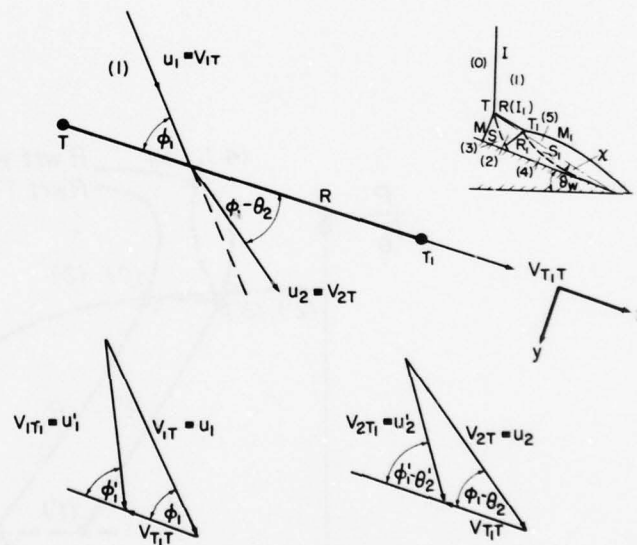


FIG. 21. SCHEMATIC DIAGRAM ILLUSTRATING THE RELATIVE MOTION OF THE SECOND TRIPLE POINT T₁ w.r.t. THE FIRST TRIPLE POINT T AND SOME VELOCITY TRANSFORMATIONS.

AD-A064 967

TORONTO UNIV DOWNSVIEW (ONTARIO) INST FOR AEROSPACE --ETC F/G 20/4
REGIONS AND TRANSITIONS OF NONSTATIONARY OBLIQUE SHOCK-WAVE DIF--ETC(U)
AUG 78 G BEN-DOR

AFOSR-77-3303

UNCLASSIFIED

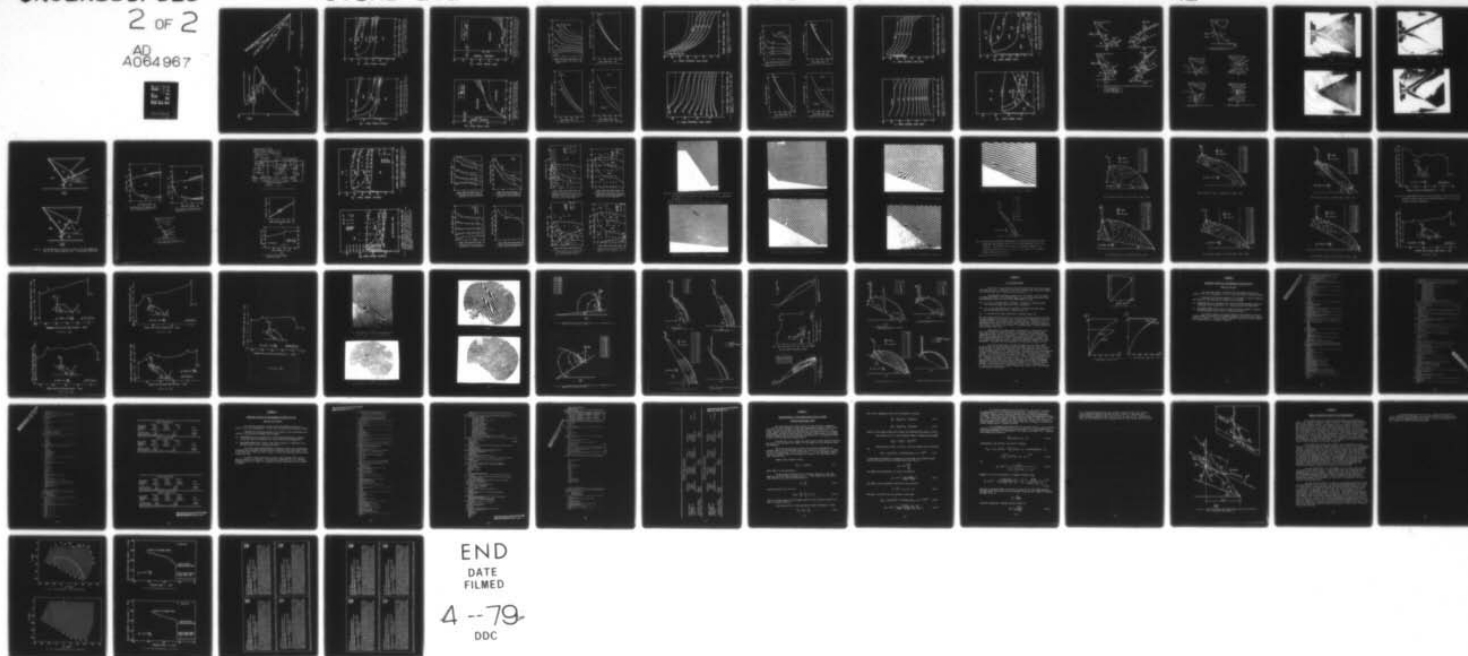
UTIAS-232

AFOSR-TR-79-0063

NL

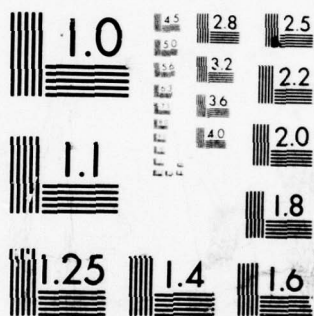
2 OF 2

AD
A064967



END
DATE
FILMED

4 --79
DDC



MICROCOPY RESOLUTION TEST CHART
NATIONAL BUREAU OF STANDARDS-1963-A

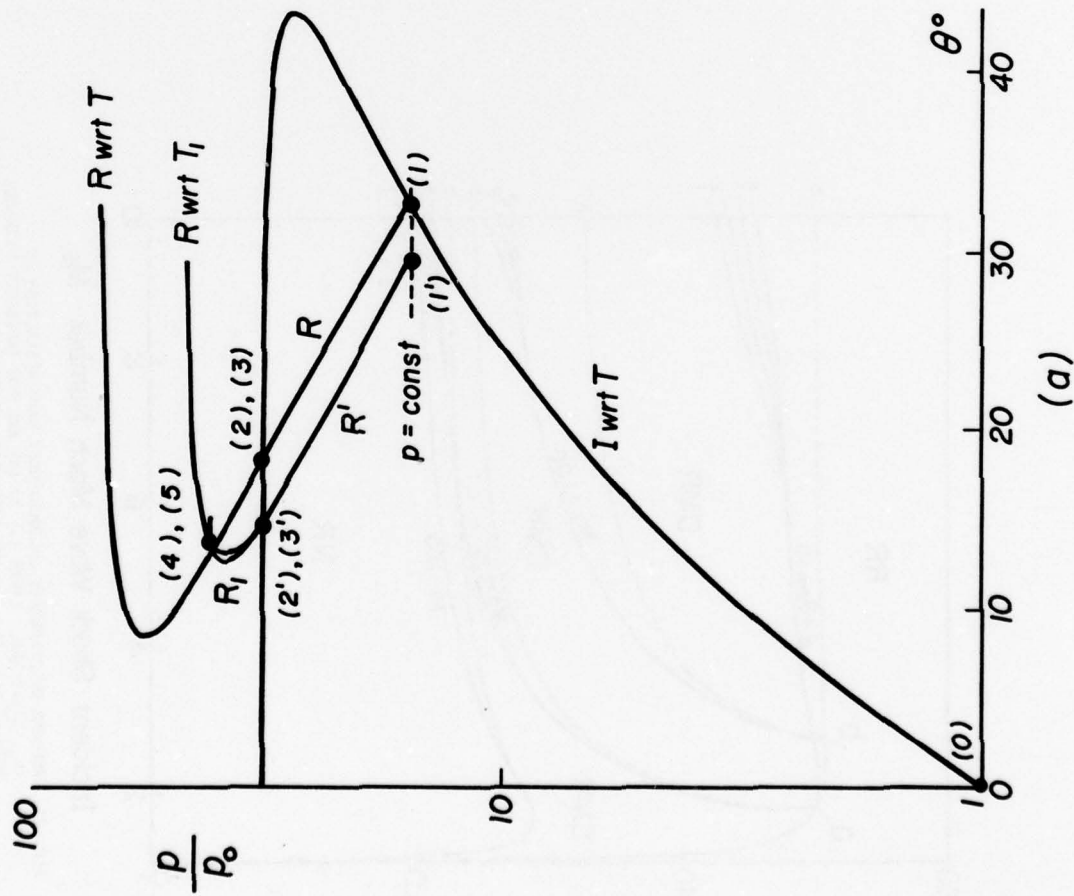


FIG. 22(a) DMR IN THE (P, θ) -PLANE, $M = 3.68$, $\theta_w = 40^\circ$, $\chi = 4.8^\circ$
 $P_0 = 15$ TORR, $T_0 = 297.4$ K.

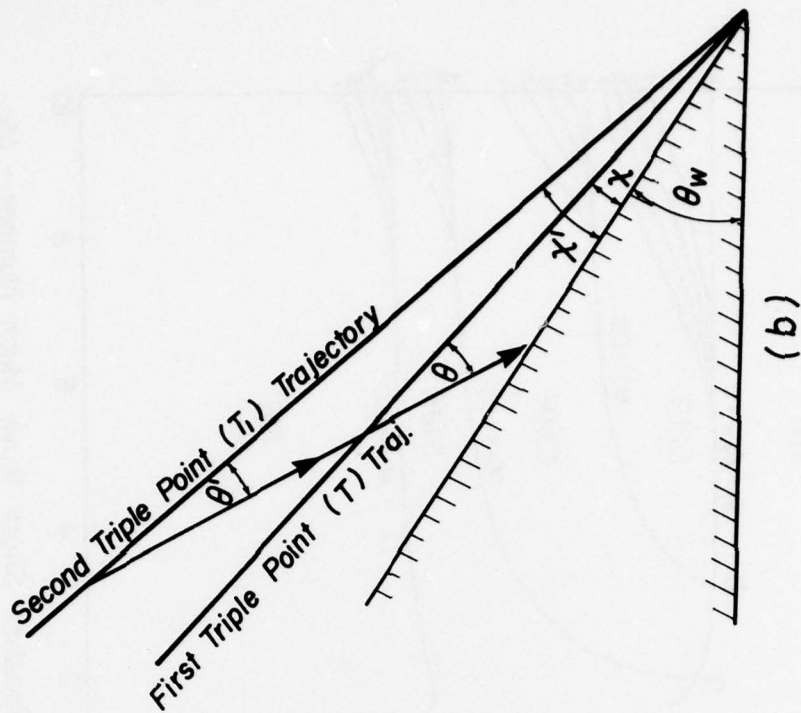


FIG. 22(b). SCHEMATIC DIAGRAM SHOWING THE ROTATION INVOLVED IN MOVING THE FRAME OF REFERENCE FROM T TO T_1 .

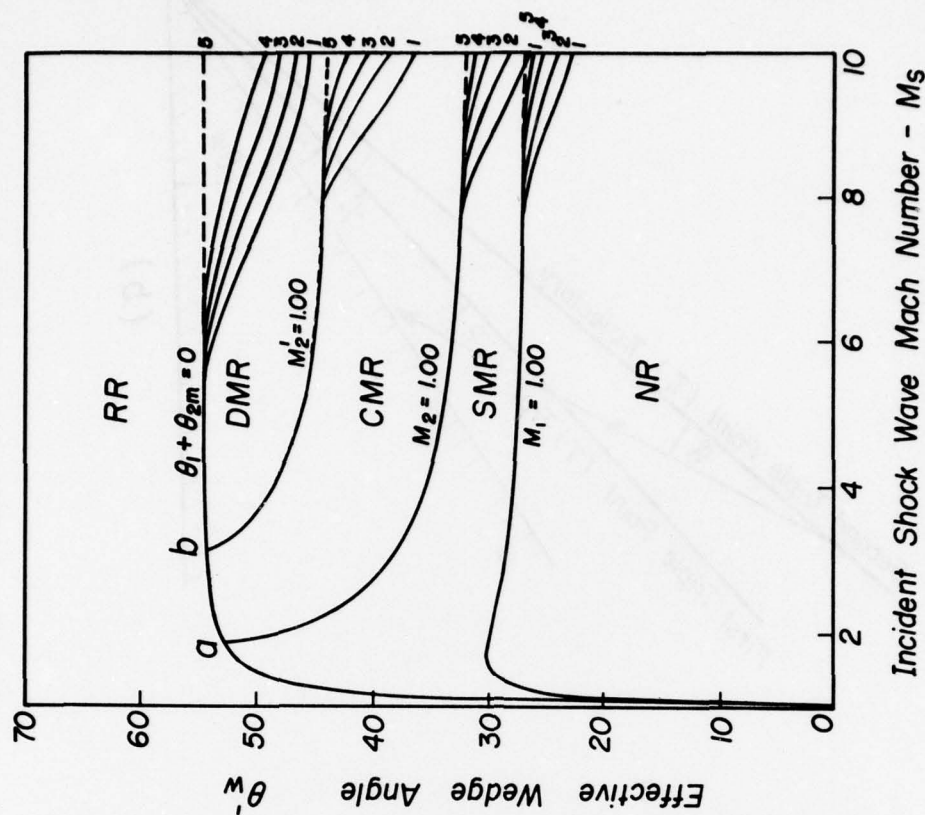


FIG. 24. REGIONS OF DIFFERENT OBLIQUE-SHOCK-WAVE REFLECTIONS IN (M_s, θ'_w) -PLANE. LINES (1) TO (4) ARE FOR IMPERFECT ARGON WITH $p_{01} = 1, 10, 100$ AND 1000 TORR, RESPECTIVELY, AND $T_{01} = 300$ K. LINE (5), DASHED, IS FOR A PERFECT MONATOMIC GAS $\gamma = 5/3$.

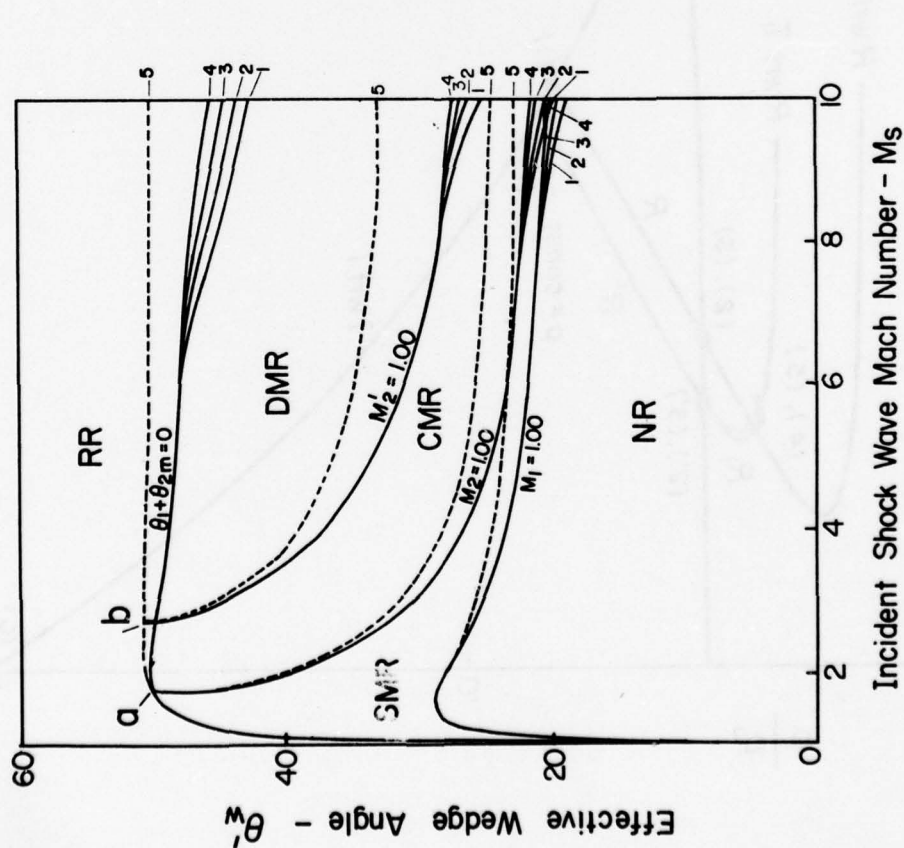


FIG. 23. REGIONS OF DIFFERENT OBLIQUE-SHOCK-WAVE REFLECTION IN (M_s, θ'_w) -PLANE. LINES (1) TO (4) ARE FOR IMPERFECT NITROGEN WITH $p_{01} = 1, 10, 100$ AND 1000 TORR, RESPECTIVELY, AND $T_{01} = 300$ K. LINE (5), DASHED, IS FOR A PERFECT DIATOMIC GAS $\gamma = 1.40$.

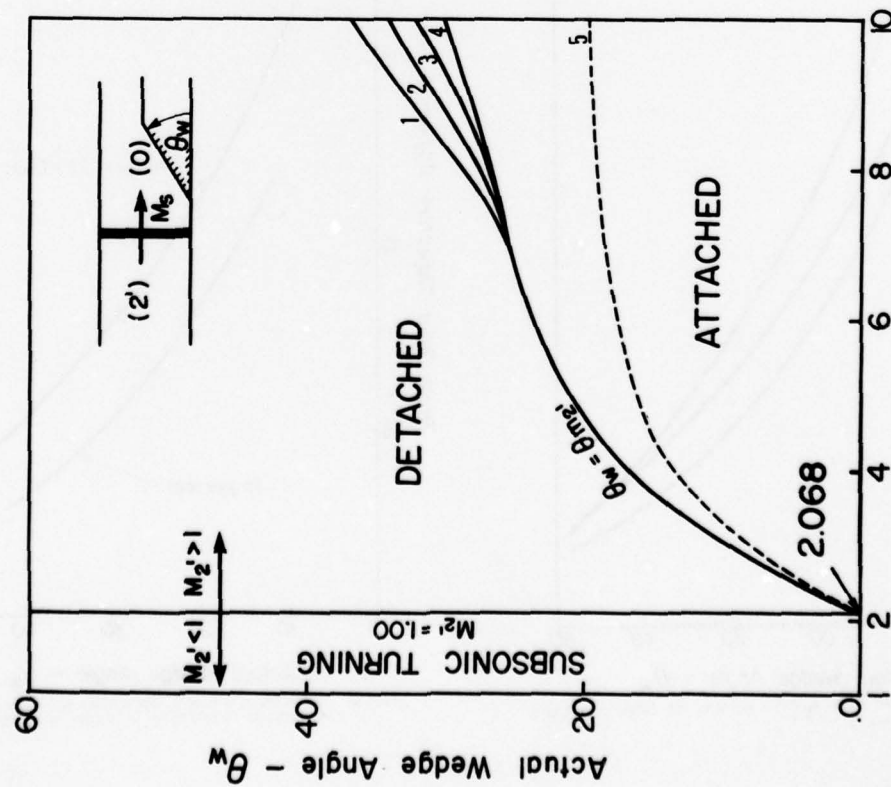


FIG. 25. DEFLECTION OF THE SHOCK-INDUCED QUASI-STEADY FLOW ($2'$) AS A FUNCTION OF M_s AND θ_w . LINES (1) TO (4) ARE FOR IMPERFECT NITROGEN WITH $P_0 = 1, 10, 100$ AND 1000 TORR, RESPECTIVELY, AND $T_0 = 300$ K. LINE (5), DASHED, IS FOR A PERFECT DIATOMIC GAS $\gamma = 1.40$.

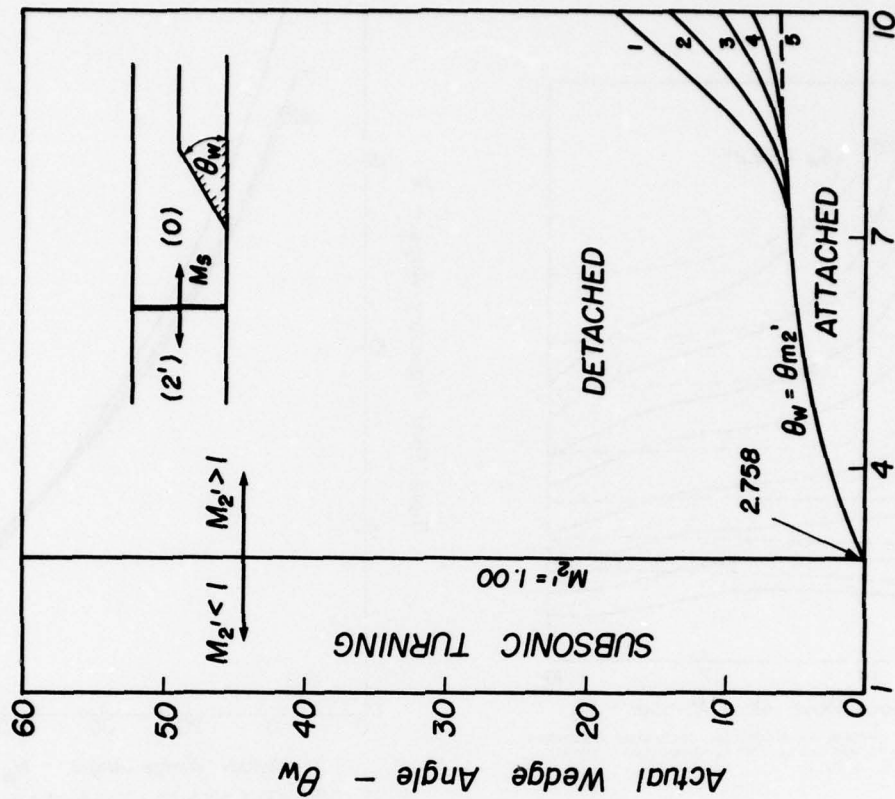


FIG. 26. DEFLECTION PROCESSES OF THE SHOCK-INDUCED QUASI-STEADY FLOW ($2'$) AS A FUNCTION OF M_s AND θ_w . LINES (1) TO (4) ARE FOR IMPERFECT ARGON WITH $P_0 = 1, 10, 100$ AND 1000 TORR, RESPECTIVELY, AND $T_0 = 300$ K. LINE (5), DASHED, IS FOR A PERFECT MONATOMIC GAS $\gamma = 5/3$.

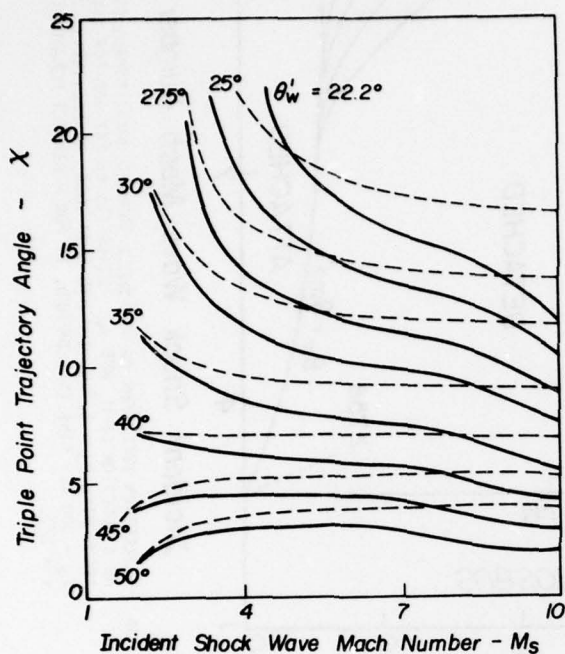


FIG. 27. VARIATION OF χ WITH M_s FOR A GIVEN θ_w' . SOLID LINES - IMPERFECT NITROGEN $P_0 = 15$ TORR AND $T_0 = 300$ K, DASHED LINES - PERFECT DIATOMIC GAS $\gamma = 1.40$.

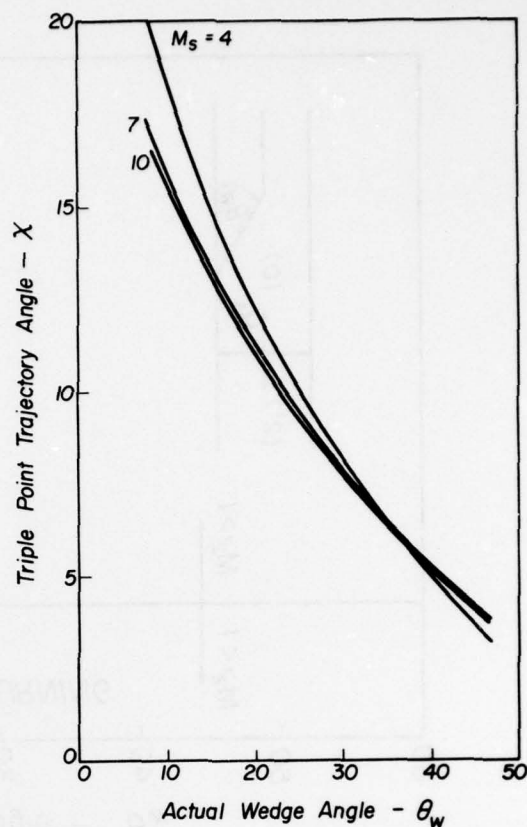


FIG. 28. VARIATION OF χ WITH θ_w FOR A GIVEN M_s FOR A PERFECT DIATOMIC GAS $\gamma = 1.40$.

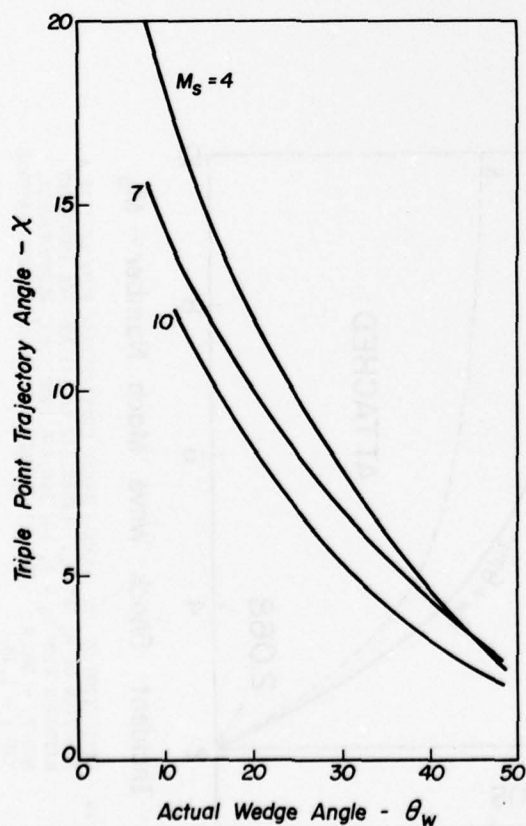


FIG. 29. VARIATION OF χ WITH θ_w FOR A GIVEN M_s FOR IMPERFECT NITROGEN $P_0 = 15$ TORR, $T_0 = 300$ K.

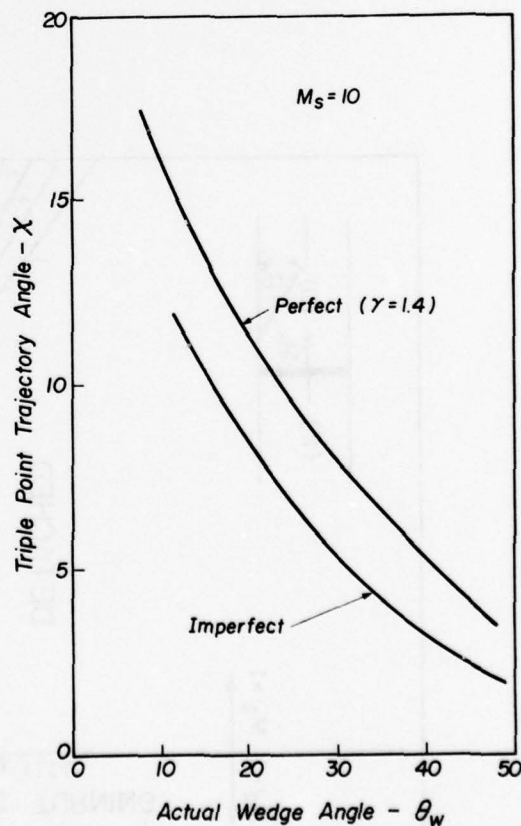


FIG. 30. VARIATION OF χ WITH θ_w FOR A GIVEN M_s . COMPARISON BETWEEN PERFECT AND IMPERFECT ($P_0 = 15$ TORR, $T_0 = 300$ K) NITROGEN.

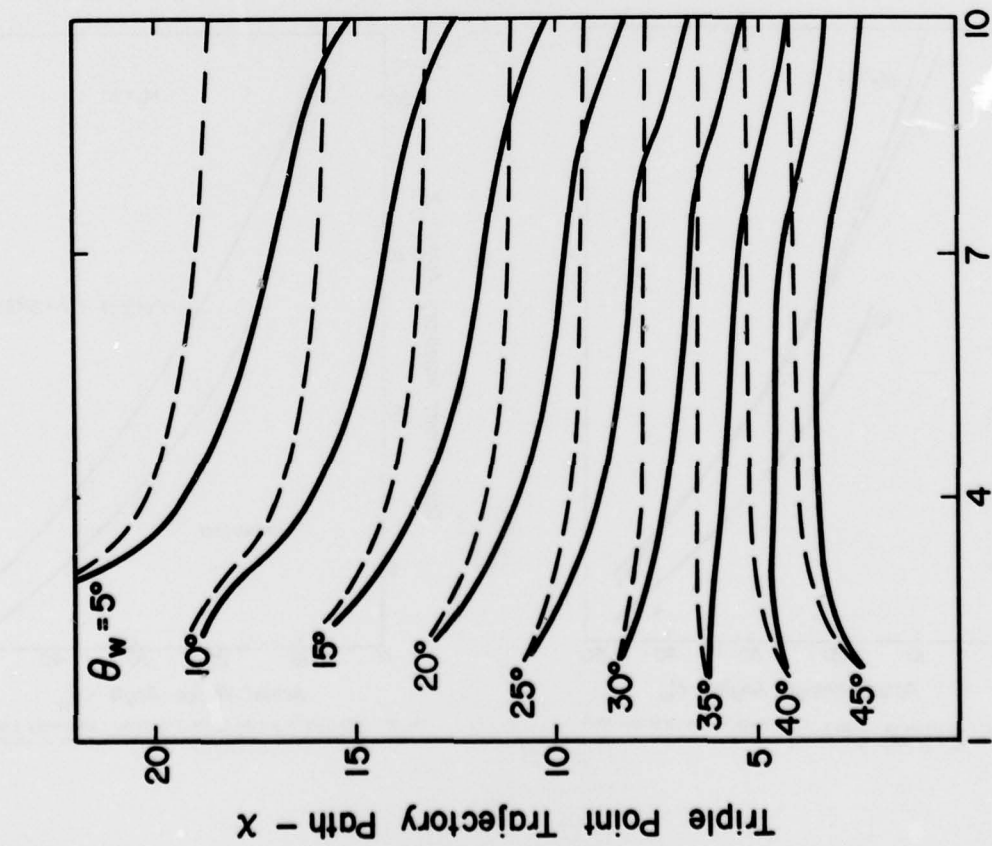


FIG. 31. VARIATION OF X WITH M_s FOR GIVEN θ_w . SOLID LINES - IMPERFECT NITROGEN $P_0 = 15$ TORR AND $T_0 = 300$ K, DASH LINES - PERFECT DIATOMIC GAS $\gamma = 1.40$.

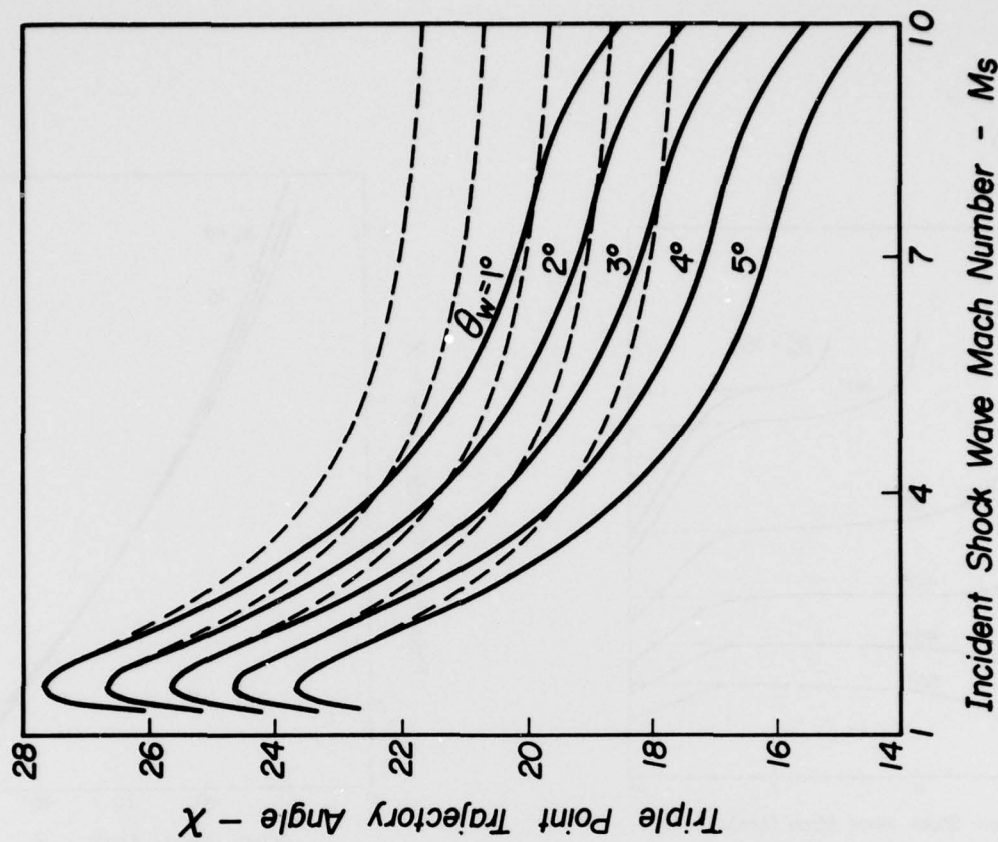


FIG. 32. VARIATION OF X WITH M_s FOR A GIVEN θ_w . SOLID LINES - IMPERFECT NITROGEN $P_0 = 15$ TORR AND $T_0 = 300$ K, DASH LINES - PERFECT DIATOMIC GAS $\gamma = 1.40$.

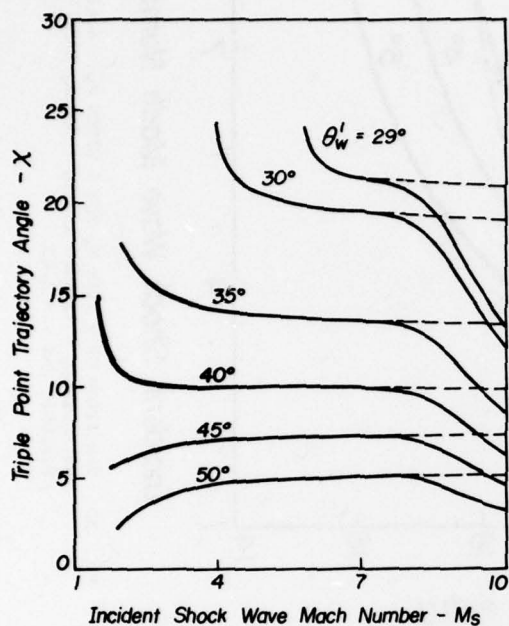


FIG. 33. VARIATION OF x WITH M_s FOR A GIVEN θ_w^l . SOLID LINES - IMPERFECT ARGON $P_0 = 15$ TORR AND $T_0 = 300$ K, DASHED LINES - PERFECT MONATOMIC GAS $\gamma = 5/3$.

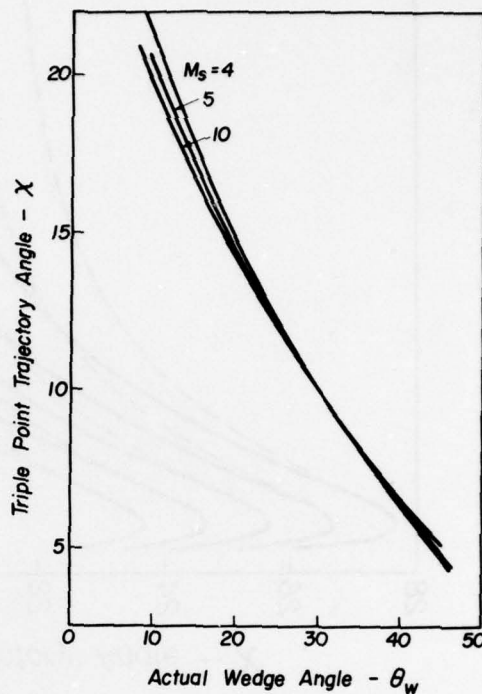


FIG. 34. VARIATION OF x WITH θ_w FOR A GIVEN M_s FOR A PERFECT MONATOMIC GAS $\gamma = 5/3$.

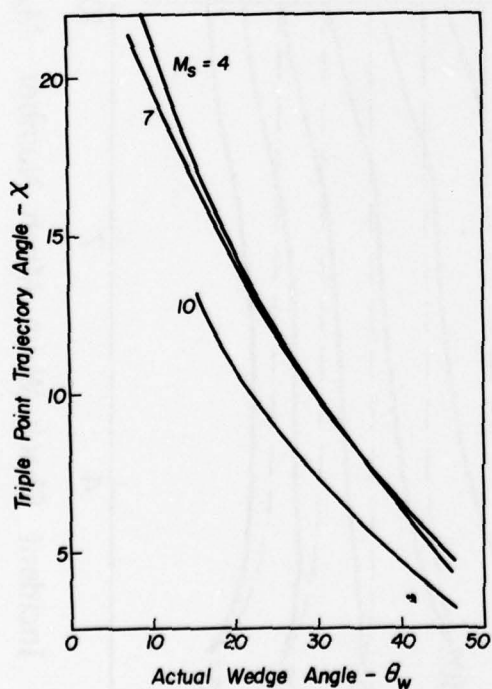


FIG. 35. VARIATION OF x WITH θ_w FOR A GIVEN M_s FOR IMPERFECT ARGON $P_0 = 15$ TORR, $T_0 = 300$ K.

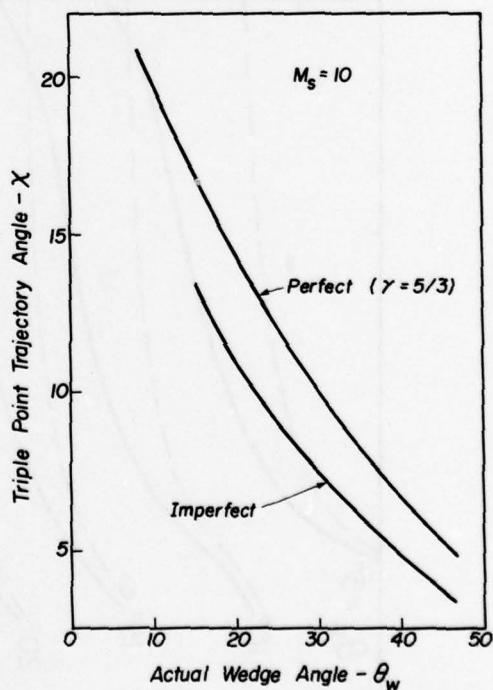


FIG. 36. VARIATION OF x WITH θ_w FOR A GIVEN M_s , COMPARISON BETWEEN PERFECT AND IMPERFECT ($P_0 = 15$ TORR, $T_0 = 300$ K) ARGON.

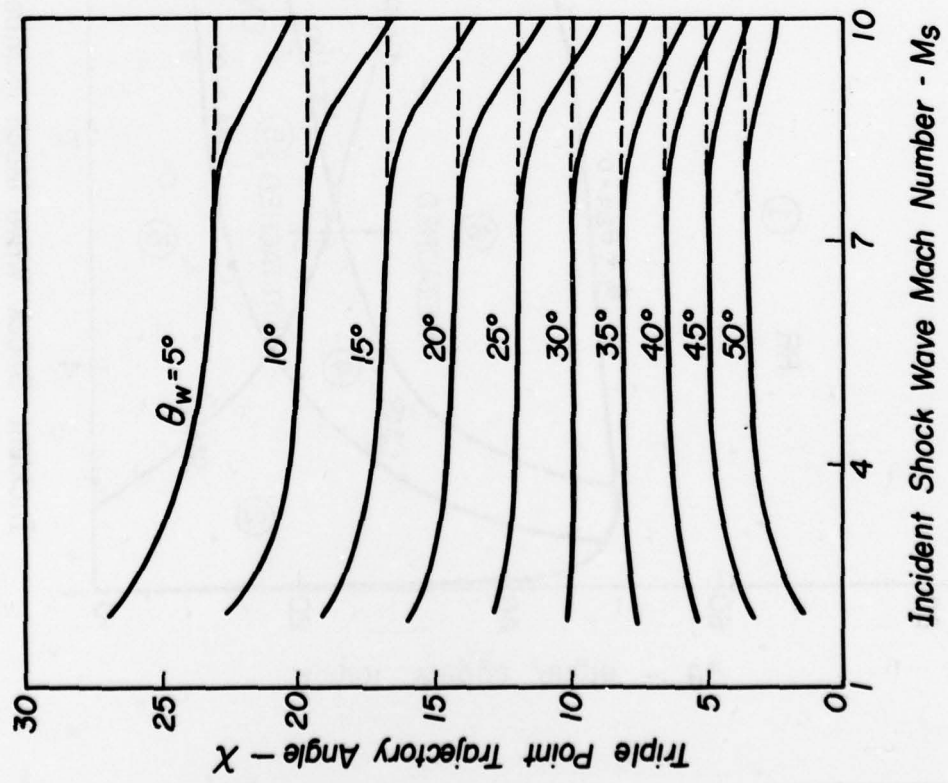


FIG. 37. VARIATION OF χ WITH M_s FOR A GIVEN θ_w . SOLID LINES - IMPERFECT ARGON $P_0 = 15$ TORR AND $T_0 = 300$ K, DASHED LINES - PERFECT MONATOMIC GAS $\gamma = 5/3$.

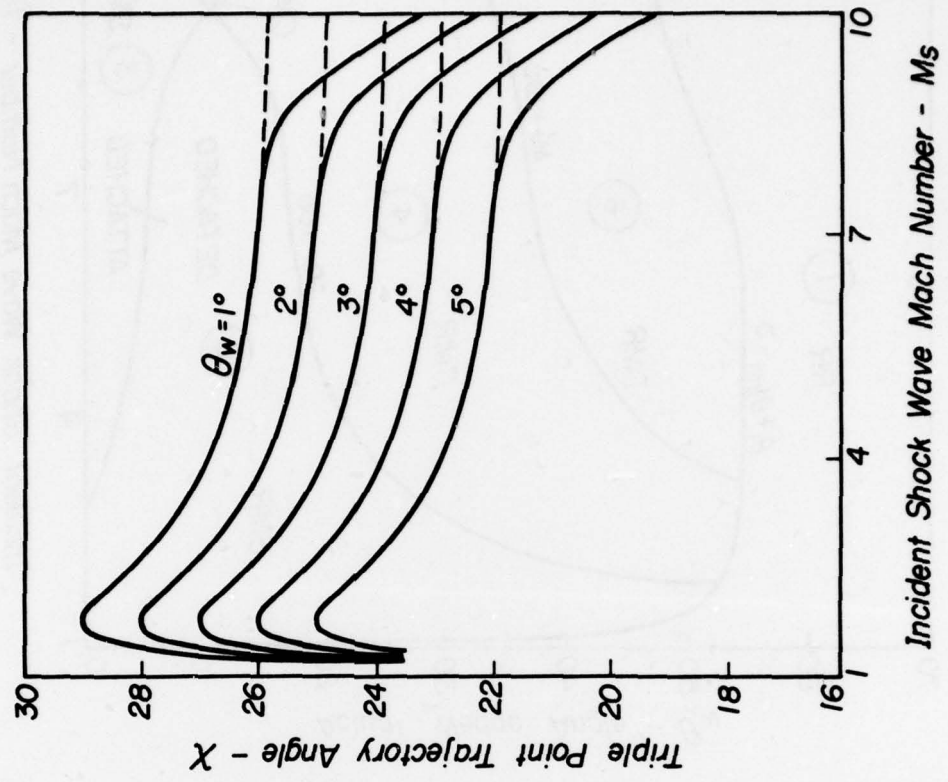


FIG. 38. VARIATION OF χ WITH M_s FOR A GIVEN θ_w . SOLID LINES - IMPERFECT ARGON $P_0 = 15$ TORR AND $T_0 = 300$ K, DASHED LINES - PERFECT MONATOMIC GAS $\gamma = 5/3$.

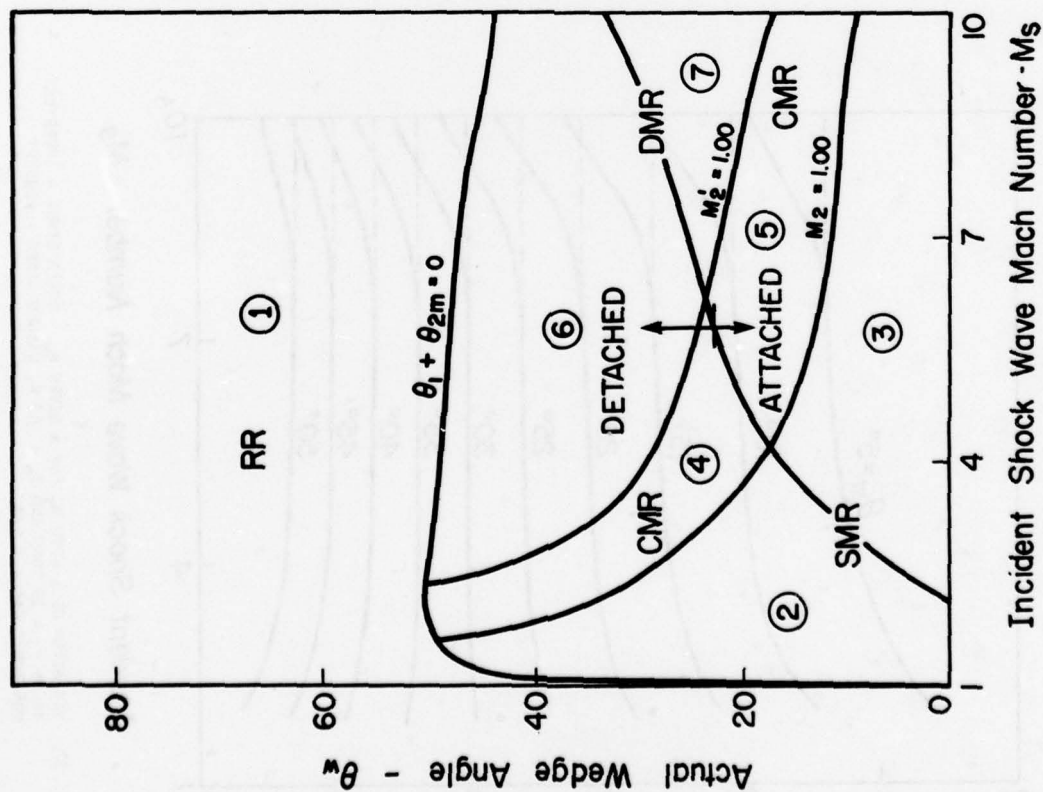


FIG. 39. TEN DOMAINS AND THEIR TRANSITION BOUNDARIES OF NONSTATIONARY SHOCK-WAVE DIFFRACTIONS IN (M_s, θ_w) -PLANE. IMPERFECT ARGON: $P_0 = 15$ TORR, $T_0 = 300$ K (see Table 1).

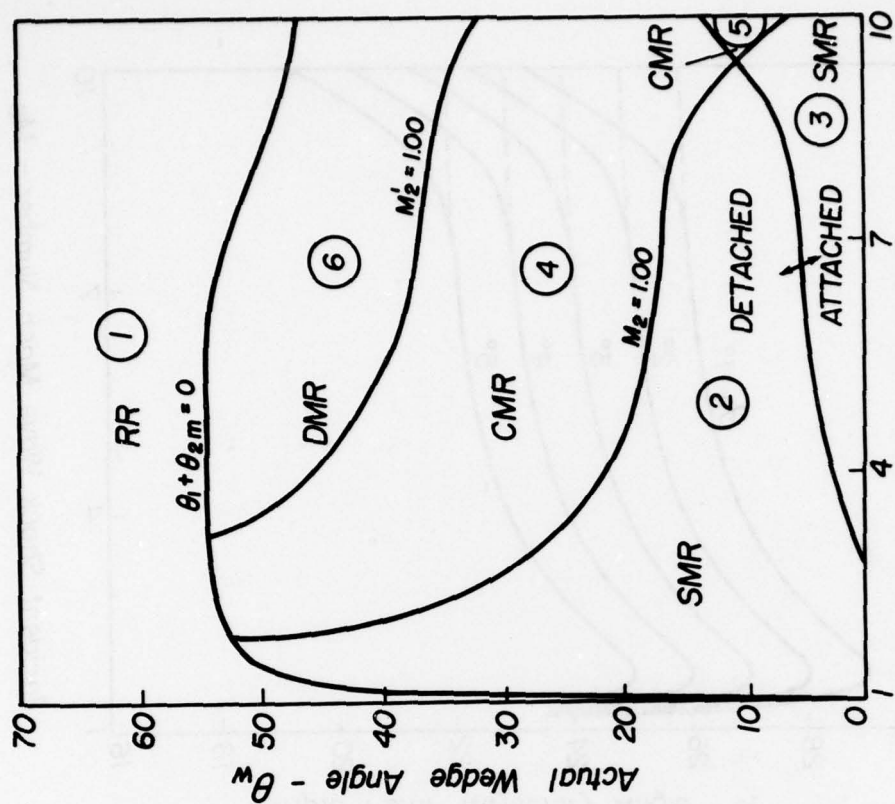


FIG. 40. NINE DOMAINS AND THEIR TRANSITION BOUNDARIES OF NONSTATIONARY SHOCK-WAVE DIFFRACTIONS IN (M_s, θ_w) -PLANE. IMPERFECT ARGON: $P_0 = 15$ TORR, $T_0 = 300$ K (see Table 2).

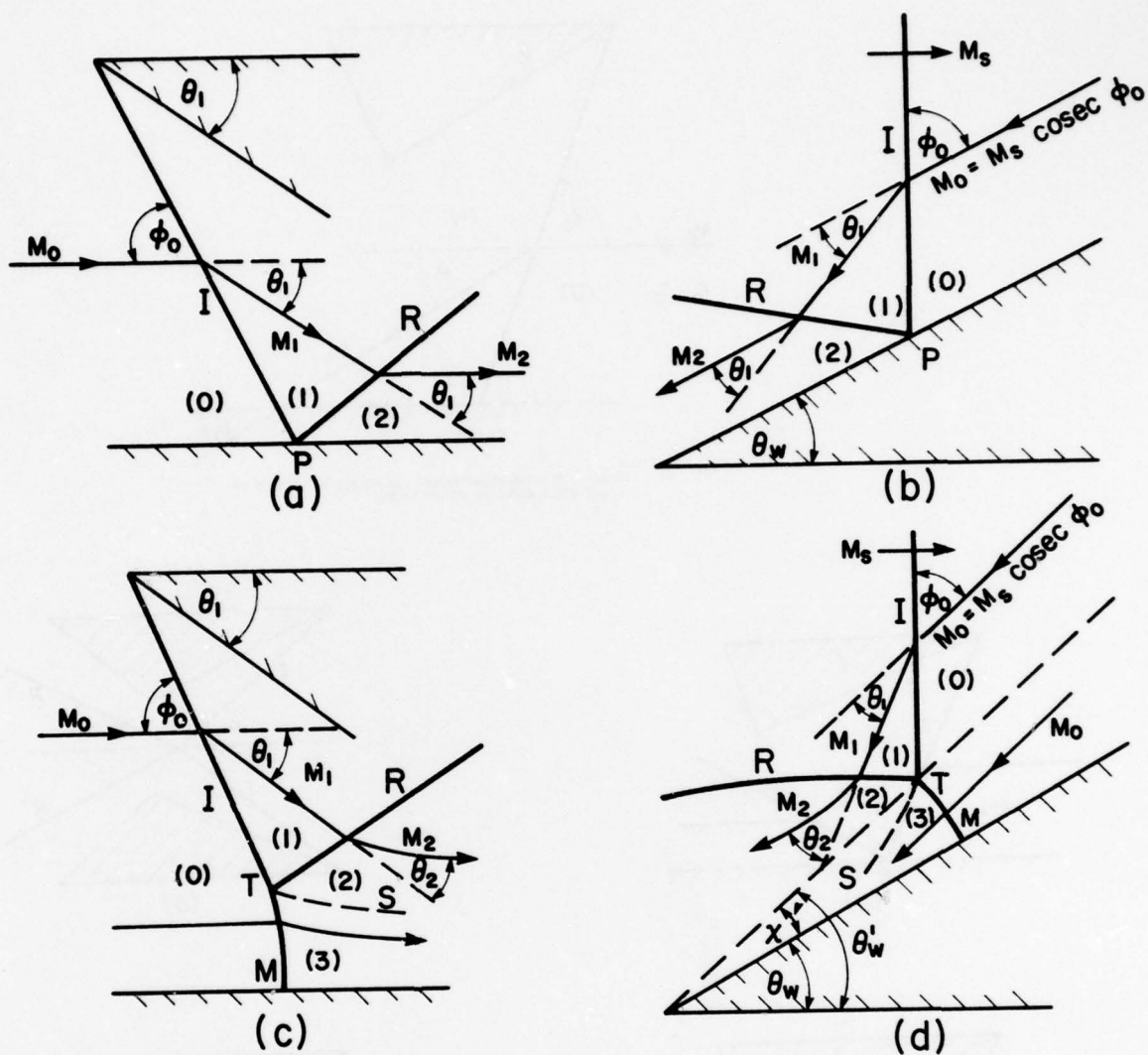


FIG. 41. EQUIVALENT OBLIQUE SHOCK-WAVE REFLECTIONS IN STEADY AND NONSTATIONARY FLOWS.

- (a) RR IN STEADY FLOW
- (b) RR IN NONSTATIONARY FLOW
- (c) SMR IN STEADY FLOW
- (d) SMR IN NONSTATIONARY FLOW

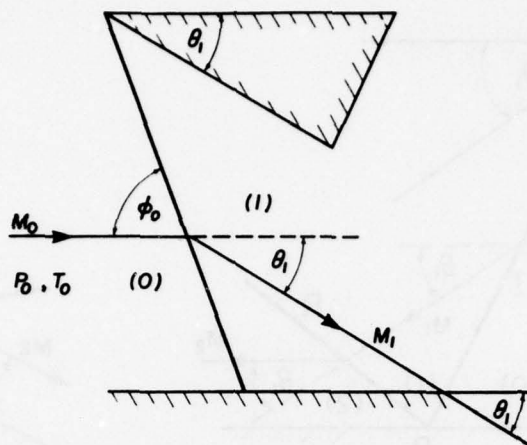


FIG. 42. SCHEMATIC DIAGRAM ILLUSTRATING REASON FOR REFLECTION OF OBLIQUE SHOCK-WAVES IN STEADY FLOWS.

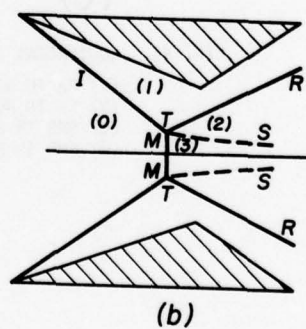
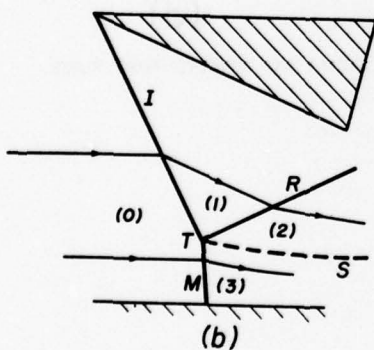
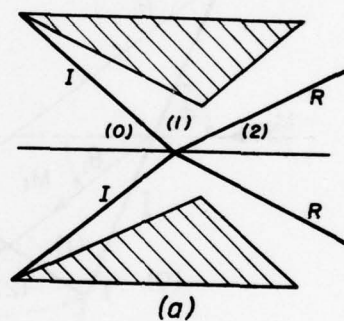
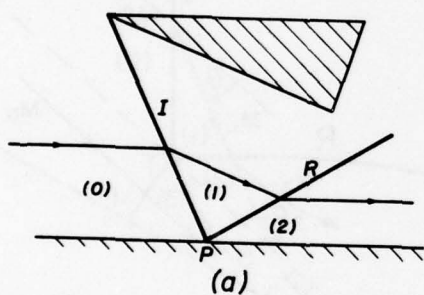
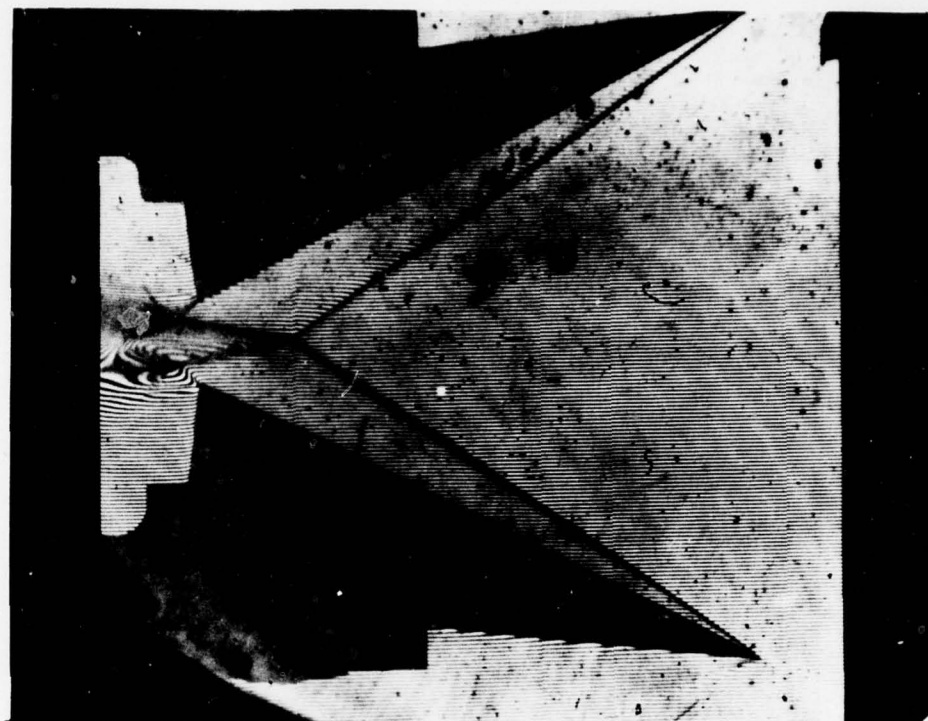


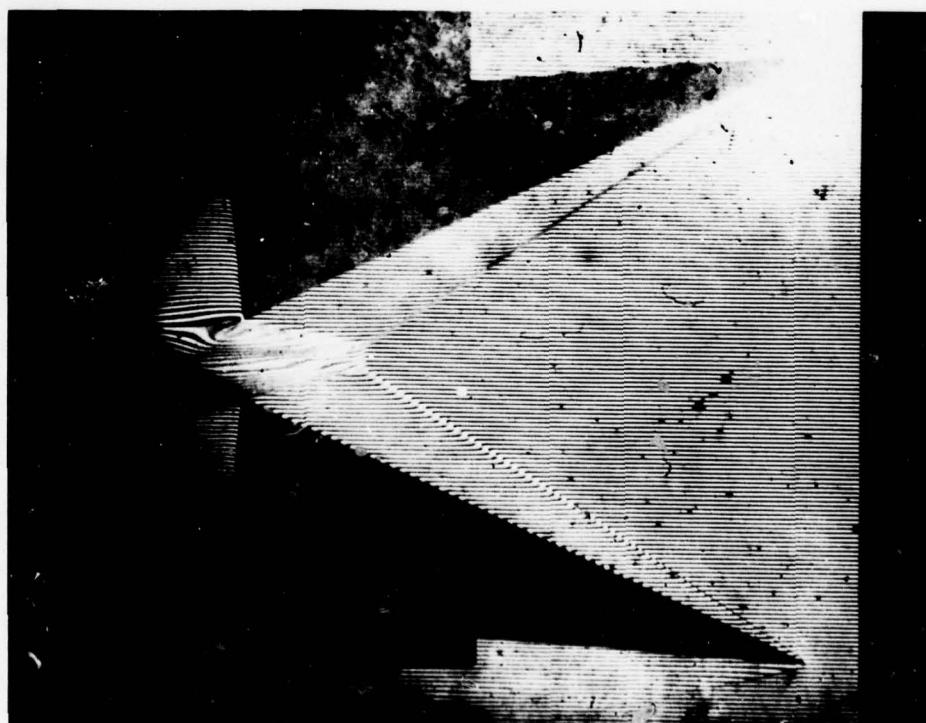
FIG. 43. DIFFERENT TYPES OF OBLIQUE SHOCK-WAVE REFLECTION IN STEADY FLOWS: (a) RR; (b) SMR.

FIG. 44. ILLUSTRATION OF BOUNDARY LAYER FREE REFLECTIONS IN A STEADY FLOW. (a) RR. (b) SMR.



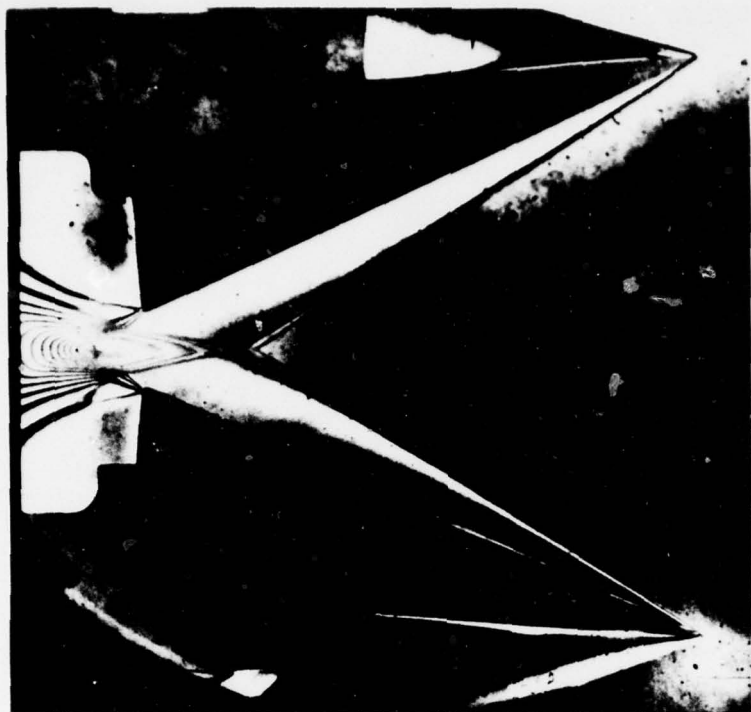
(a)

FIG. 45(a). RR USING SET-UP SHOWN IN FIG. 44(a), STANDARD INTERFEROGRAM (REF. 77).



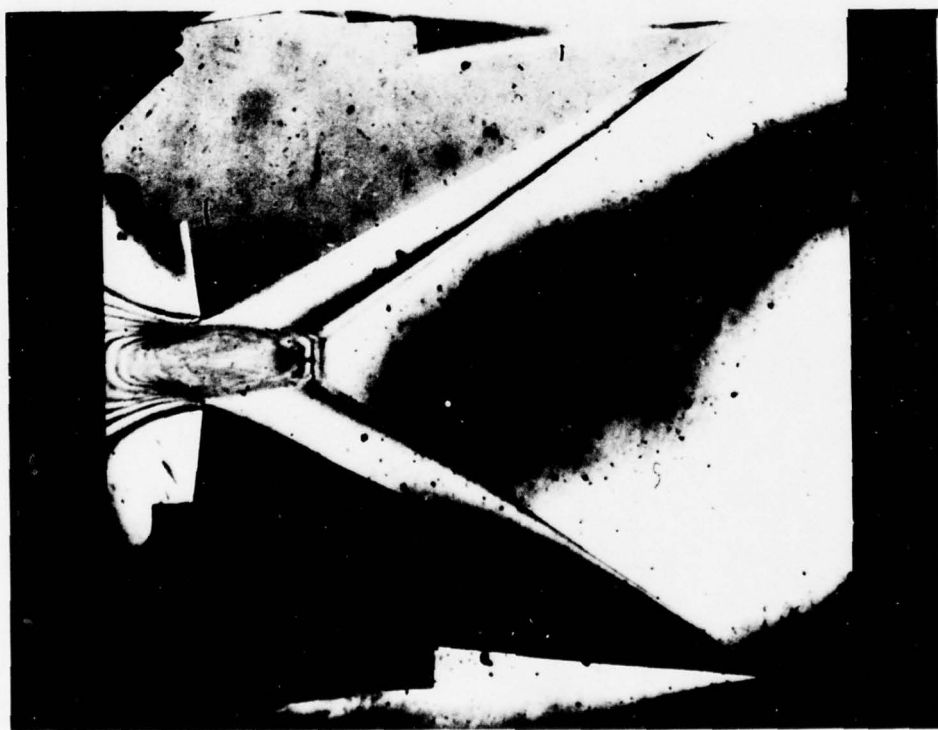
(b)

FIG. 45(b). SMR USING SET-UP SHOWN IN FIG. 44(b) STANDARD INTERFEROGRAM (REF. 77).



(a)

FIG. 46(a). RR USING SET-UP SHOWN IN FIG. 44(a), INFINITE-FRINGE INTERFEROGRAM (REF. 77).



(b)

FIG. 46(b). SMR USING SET-UP SHOWN IN FIG. 44(b), INFINITE FRINGE INTERFEROGRAM (REF. 77).

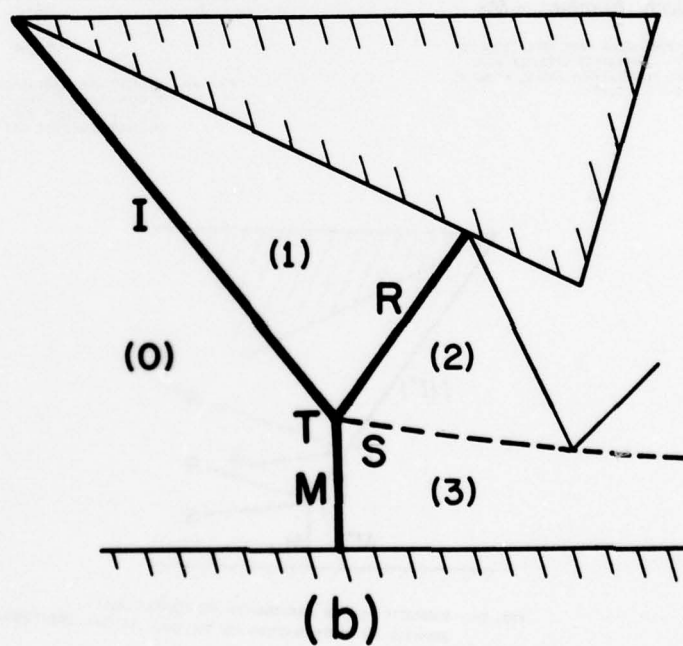
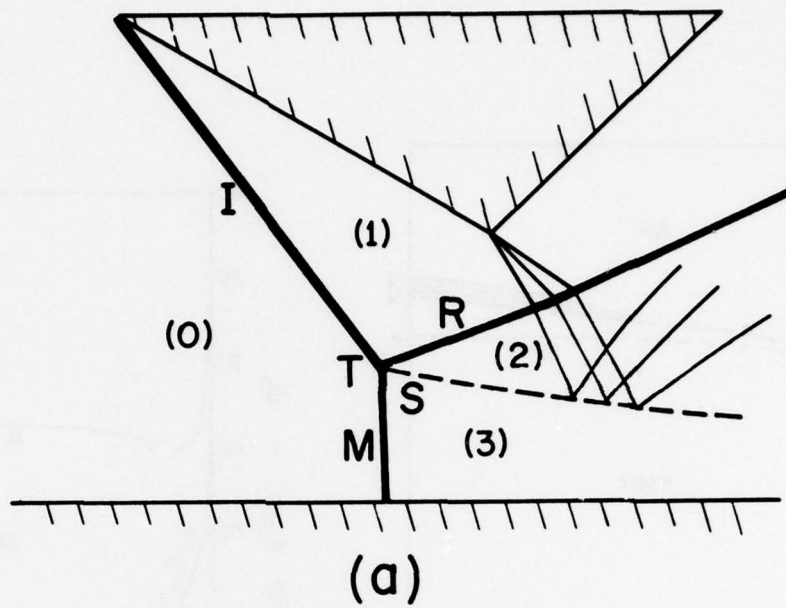


FIG. 47. THE INTERRUPTION OF THE FLOW IN STATE (2) BY THE GEOMETRICAL SET-UP. (a) Corner expansion wave. (b) Reflected shock wave.

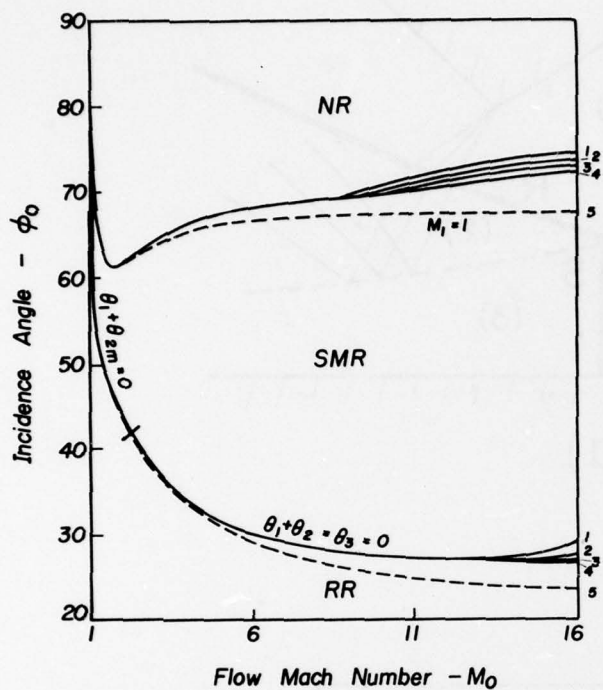


FIG. 48. DOMAINS AND BOUNDARIES OF OBLIQUE SHOCK-WAVE REFLECTION IN STEADY FLOW. LINES (1) TO (4) - IMPERFECT NITROGEN WITH $P_0 = 1, 10, 100$ AND 1000 TORR, RESPECTIVELY AND $T_0 = 300$ K. LINE (5) - PERFECT DIATOMIC GAS $\gamma = 1.40$

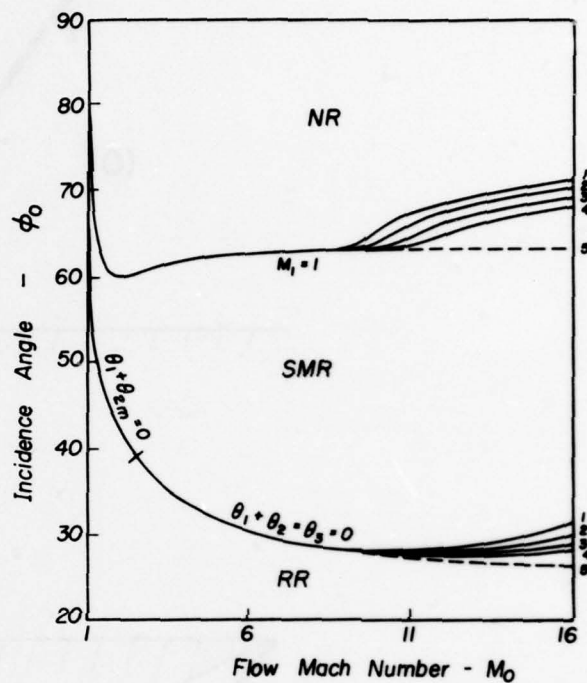


FIG. 49. DOMAINS AND BOUNDARIES OF OBLIQUE SHOCK-WAVE REFLECTION IN STEADY FLOW. LINES (1) TO (4) - IMPERFECT ARGON WITH $P_0 = 1, 10, 100$ AND 1000 TORR, RESPECTIVELY AND $T_0 = 300$ K. LINE (5) - PERFECT MONATOMIC GAS $\gamma = 5/3$

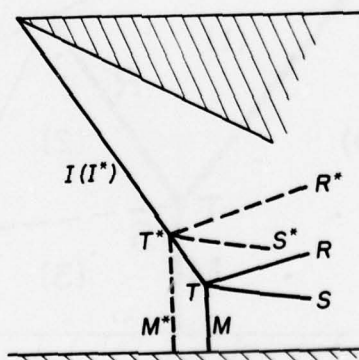


FIG. 50. SCHEMATIC DIAGRAM ILLUSTRATING TWO THEORETICALLY POSSIBLE SMR CONFIGURATIONS FOR THE SAME INITIAL CONDITIONS.

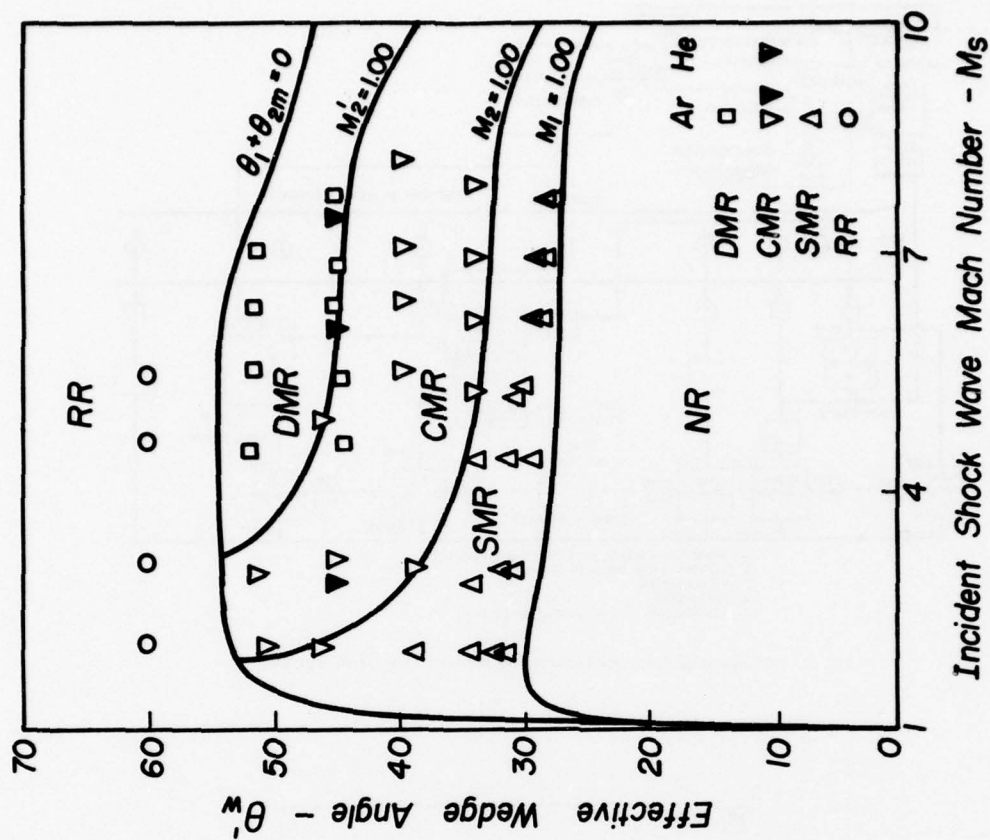


FIG. 54. EXPERIMENTAL VERIFICATION OF OBLIQUE SHOCK-WAVE REFLECTION ANALYSIS IN THE (M_s, θ_w') -PLANE. IMPERFECT ARGON, $P_0 = 15$ TORR, $T_0 = 300$ K. EXPERIMENTAL DATA: ARGON - LAW AND GLASS ∇ (Ref. 51), PRESENT $\square \nabla \Delta \circ$; HELIUM - LAW ∇ (Ref. 48).

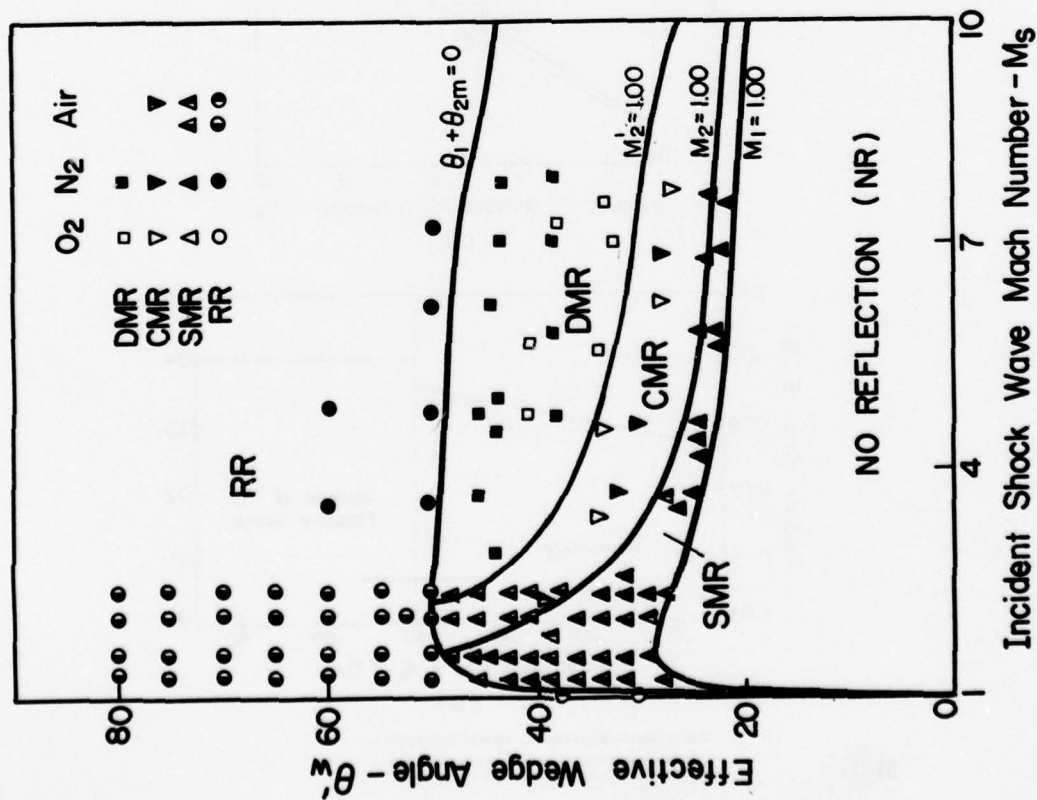


FIG. 53. EXPERIMENTAL VERIFICATION OF OBLIQUE SHOCK-WAVE REFLECTION ANALYSIS IN THE (M_s, θ_w') -PLANE. IMPERFECT NITROGEN, $P_0 = 15$ TORR, $T_0 = 300$ K. EXPERIMENTAL DATA: AIR - SMITH $\Delta \bullet$ (Ref. 6), WHITE $\nabla \Delta \bullet$ (Ref. 17); OXYGEN - LAW AND GLASS $\square \nabla \Delta \circ$; NITROGEN - PRESENT $\square \nabla \Delta \bullet$. NOTE THE TERM REFLECTION RATHER THAN DIFFRACTION IS USED SINCE THE RESULTS ARE PLOTTED IN (M_s, θ_w') PLANE.

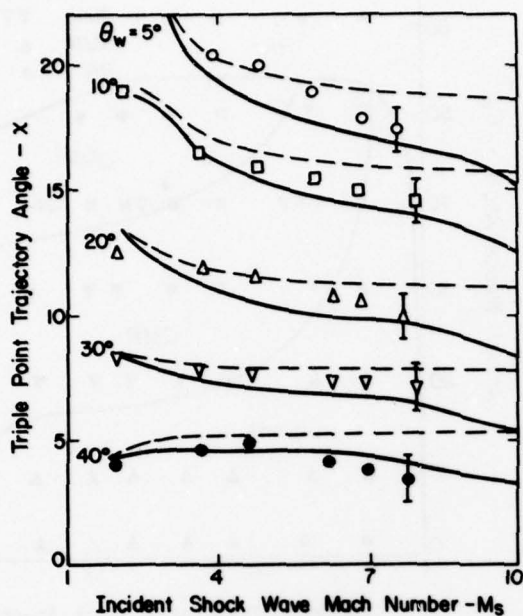


FIG. 55. VARIATION OF X WITH M_s FOR A GIVEN θ_w AND COMPARISON WITH PRESENT EXPERIMENTS. SOLID LINES - IMPERFECT NITROGEN, $P_0 = 15$ TORR, $T_0 = 300$ K. DASHED LINES - PERFECT DIATOMIC GAS $\gamma = 1.40$.

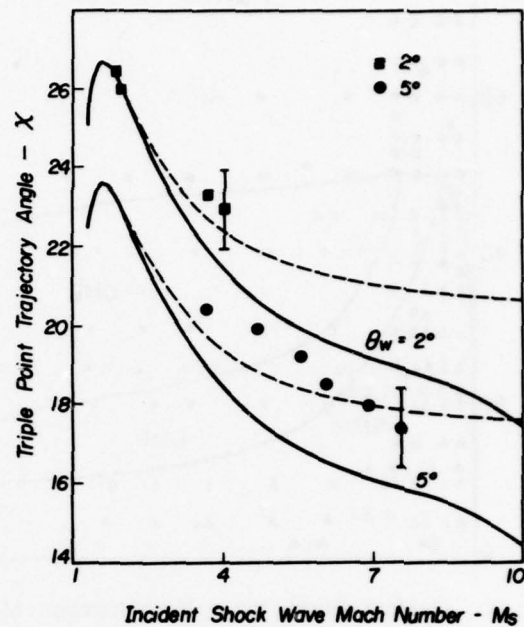


FIG. 56. VARIATION OF X WITH M_s FOR SMALL θ_w AND COMPARISON WITH PRESENT EXPERIMENTS. SOLID LINES - IMPERFECT NITROGEN, $P_0 = 15$ TORR, $T_0 = 300$ K. DASHED LINES - PERFECT DIATOMIC GAS $\gamma = 1.40$.

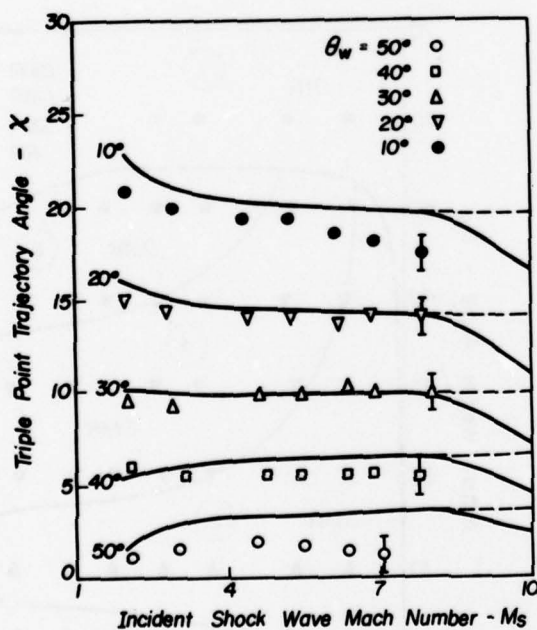


FIG. 57. VARIATION OF X WITH M_s FOR A GIVEN θ_w AND COMPARISON WITH PRESENT EXPERIMENTS. SOLID LINES - IMPERFECT ARGON, $P_0 = 15$ TORR, $T_0 = 300$ K. DASHED LINES - PERFECT MONATOMIC GAS $\gamma = 5/3$.

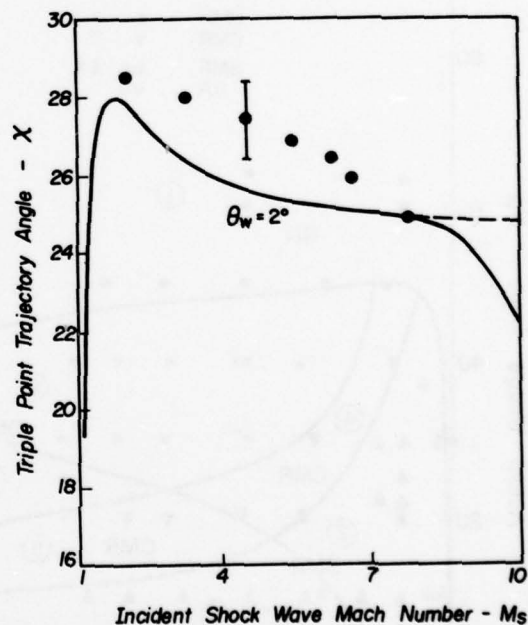


FIG. 58. VARIATION OF X WITH M_s FOR SMALL θ_w AND COMPARISON WITH PRESENT EXPERIMENTS. SOLID LINES - IMPERFECT ARGON, $P_0 = 15$ TORR, $T_0 = 300$ K. DASHED LINES - PERFECT MONATOMIC GAS $\gamma = 5/3$.

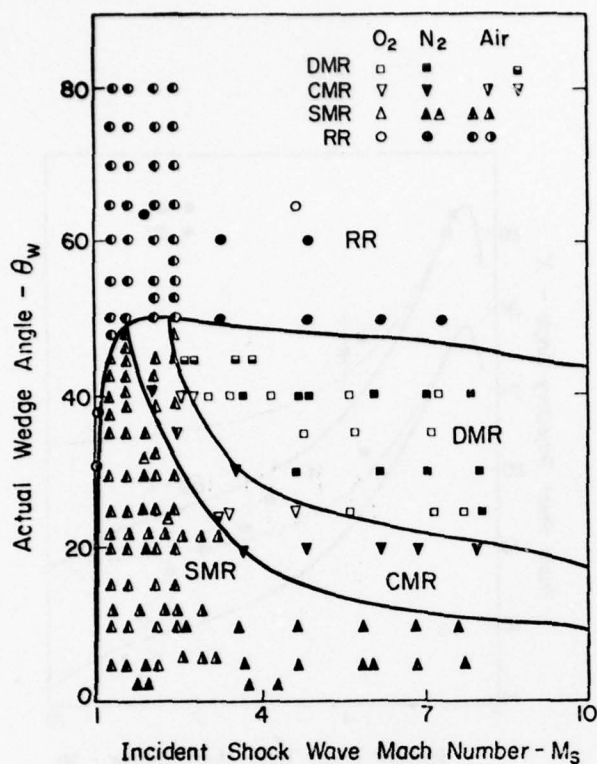


FIG. 59. EXPERIMENTAL VERIFICATION OF ANALYSIS OF OBLIQUE SHOCK-WAVE REFLECTION IN (M_s, θ_w) -PLANE FOR DIATOMIC GAS. LINES ARE FOR IMPERFECT NITROGEN, $P_0 = 15$ TORR, $T_0 = 300$ K. EXPERIMENTAL DATA: AIR - SMITH Δ (REF. 6), WHITE ∇ (REF. 17), BEZHENOVA ET AL \square (REF. 62); OXYGEN - LAW AND GLASS \square (REF. 51); NITROGEN - BEZHENOVA ET AL Δ (REF. 62) AND PRESENT \blacksquare .

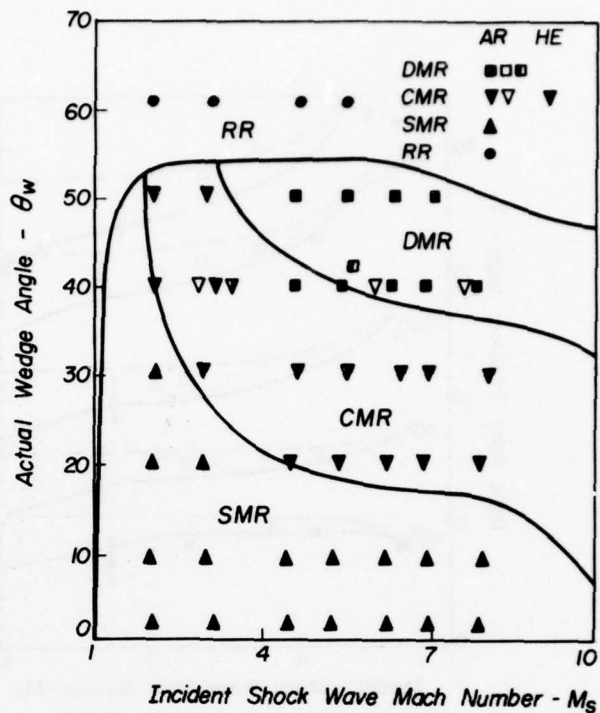


FIG. 60. EXPERIMENTAL VERIFICATION OF ANALYSIS OF OBLIQUE SHOCK-WAVE REFLECTION IN (M_s, θ_w) -PLANE FOR MONATOMIC GAS. LINES ARE FOR IMPERFECT ARGON, $P_0 = 15$ TORR, $T_0 = 300$ K. EXPERIMENTAL DATA: HELIUM - LAW ∇ (REF. 48); ARGON - LAW AND GLASS ∇ (REF. 51), BAZHENOVA ET AL \square (REF. 62) AND PRESENT \blacksquare .

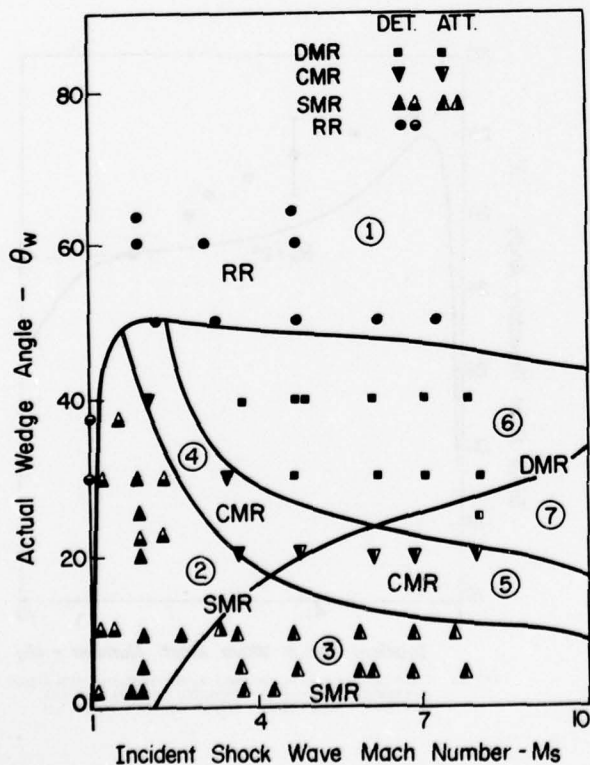


FIG. 61. EXPERIMENTAL VERIFICATION OF ANALYSIS OF TEN DOMAINS AND THEIR TRANSITION BOUNDARIES OF NONSTATIONARY OBLIQUE SHOCK-WAVE DIFFRACTION. EXPERIMENTAL DATA: AIR - WHITE \square (REF. 17); NITROGEN - PRESENT \blacksquare (REF. 62). LINES ARE FOR IMPERFECT NITROGEN, $P_0 = 15$ TORR, $T_0 = 300$ K.

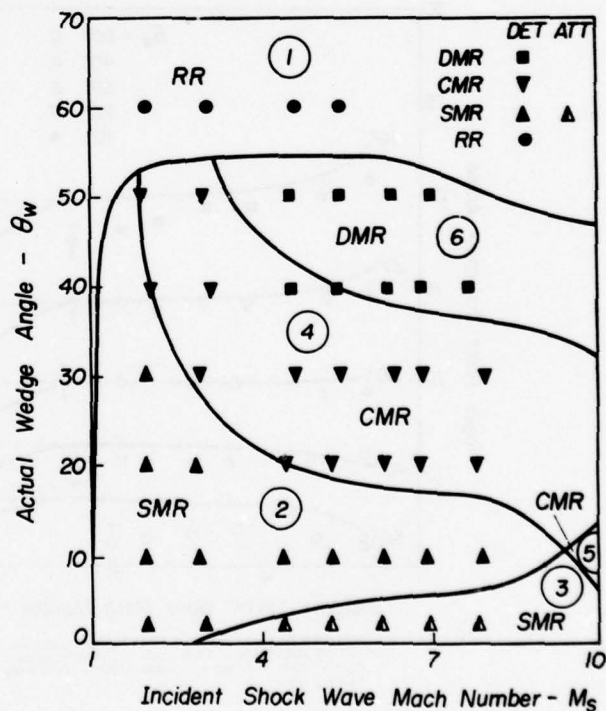
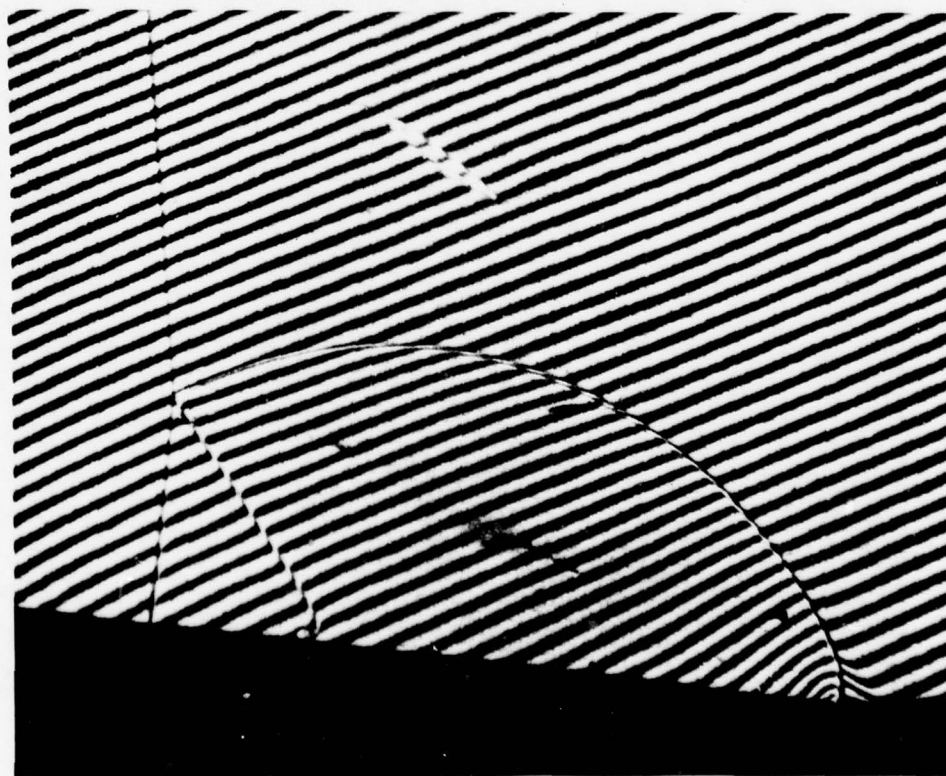


FIG. 62. EXPERIMENTAL VERIFICATION OF NINE DOMAINS AND THEIR TRANSITION BOUNDARIES OF NONSTATIONARY OBLIQUE SHOCK-WAVE DIFFRACTION. EXPERIMENTAL DATA: ARGON - \square (REF. 62) AND PRESENT \blacksquare . LINES ARE FOR IMPERFECT ARGON $P_0 = 15$ TORR, $T_0 = 300$ K.

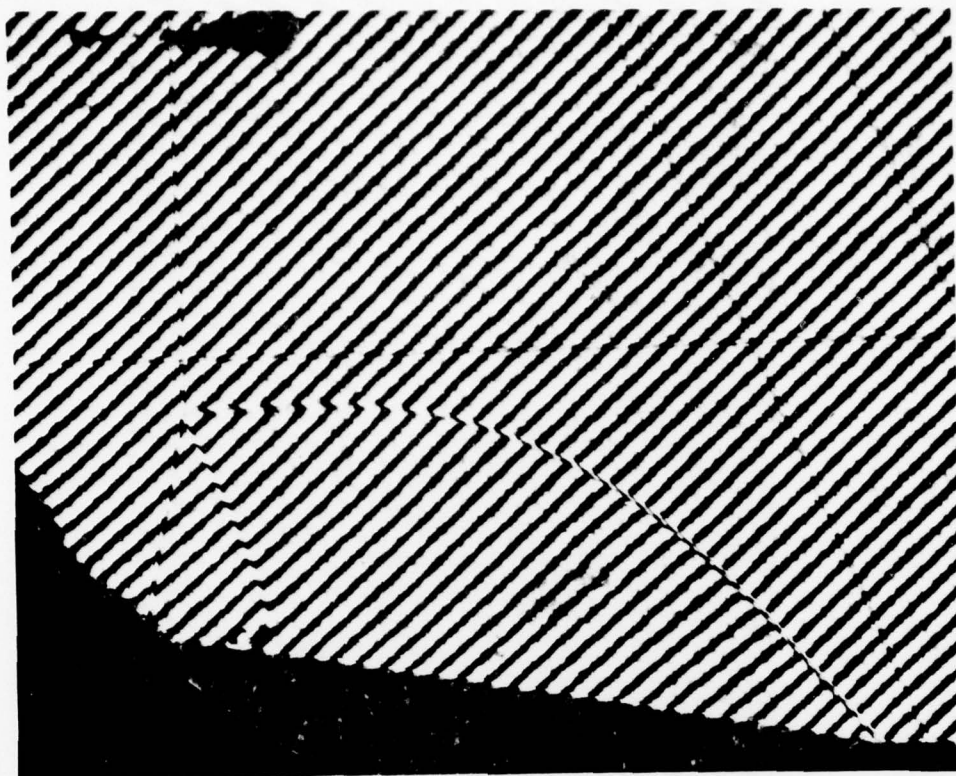


FIG. 63 INTERFEROGRAMS OF SEVEN DIFFERENT OBLIQUE SHOCK-WAVE DIFFRACTIONS IN NITROGEN IN NONSTATIONARY FLOWS. PLATES (a) TO (g) CORRESPOND TO REGIONS (1) TO (7) ON FIG. 39

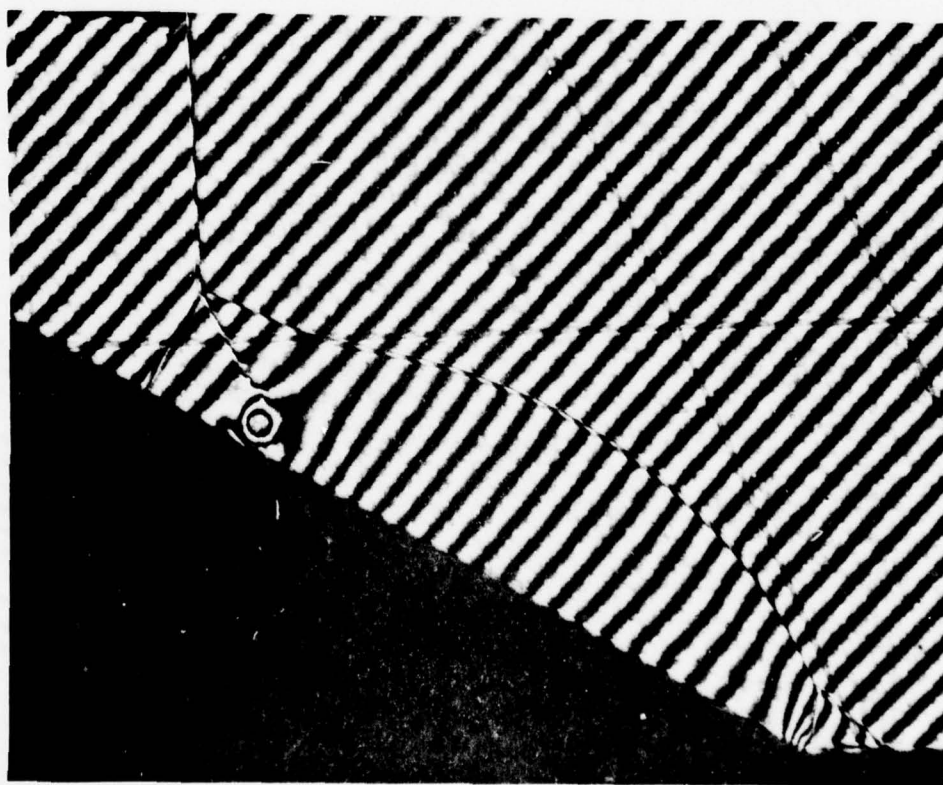
(a) $M_s = 4.68$, $\theta_w = 60.00^\circ$, $P_o = 15.31$ torr, $T_o = 298.1$ K.



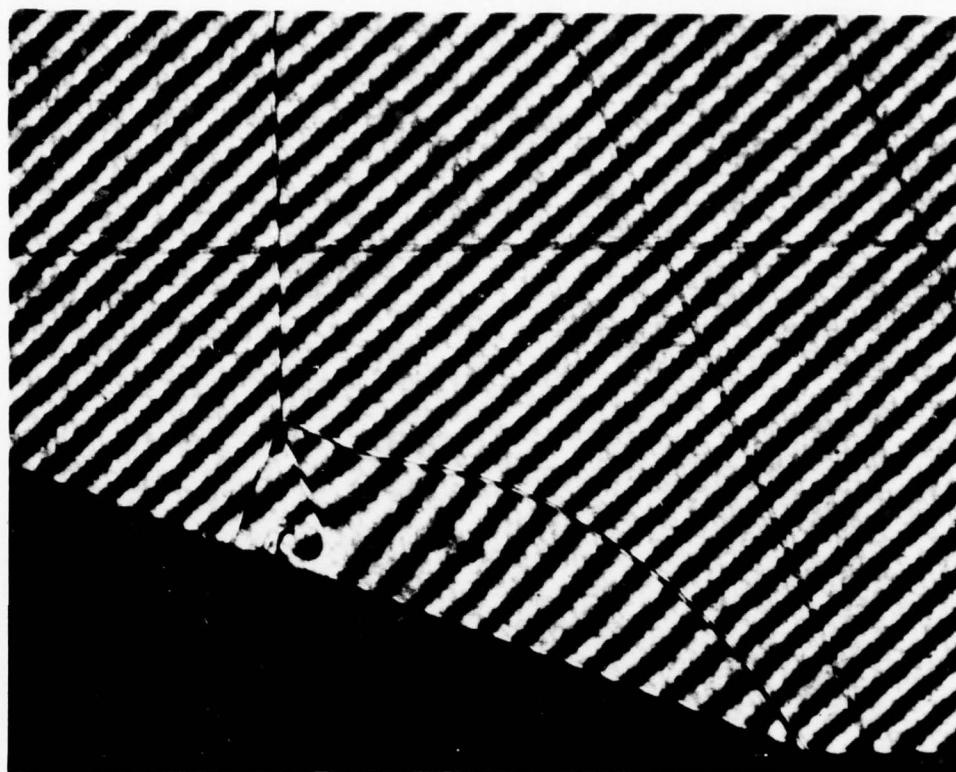
(b) $M_s = 2.61$, $\theta_w = 10.00^\circ$, $P_o = 37.00$ torr, $T_o = 297.8$ K.



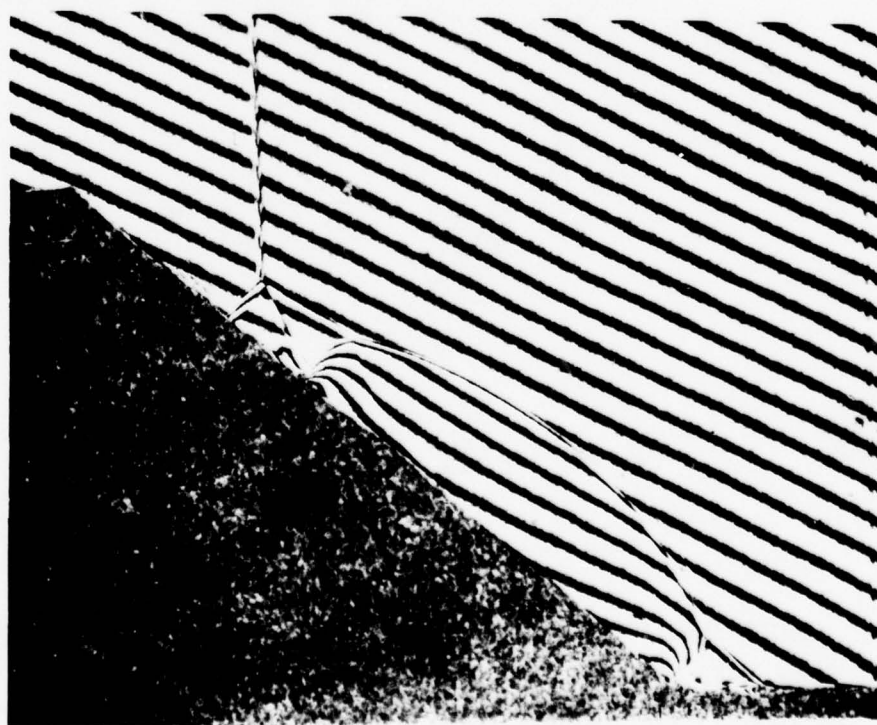
(c) $M_s = 4.72$, $\theta_w = 10.00^\circ$, $P_o = 15.00$ torr, $T_o = 295.0$ K.



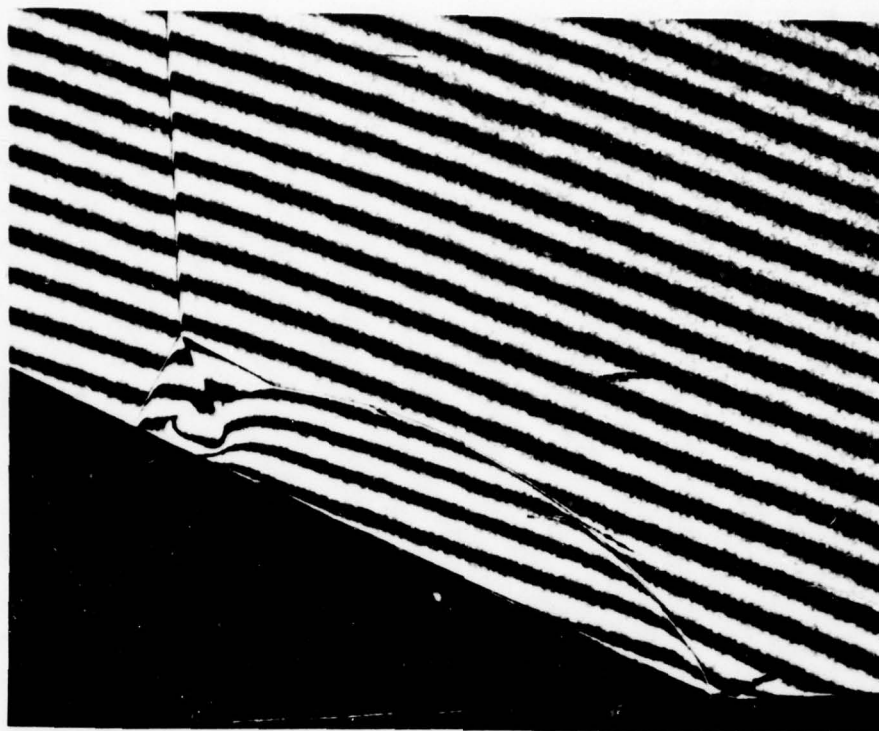
(d) $M_s = 3.74$, $\theta_w = 30.00^\circ$, $P_o = 15.27$ torr, $T_o = 297.3$ K.



(e) $M_S = 6.90$, $\theta_w = 20.00^\circ$, $P_o = 10.12$ torr, $T_o = 295.8$ K.



(f) $M_S = 3.74$, $\theta_w = 40.00^\circ$, $P_o = 15.34$ torr, $T_o = 297.4$ K.



(g) $M_s = 8.06$, $\theta_w = 26.56^\circ$, $P_o = 5.11$ torr, $T_o = 298.2$ K.

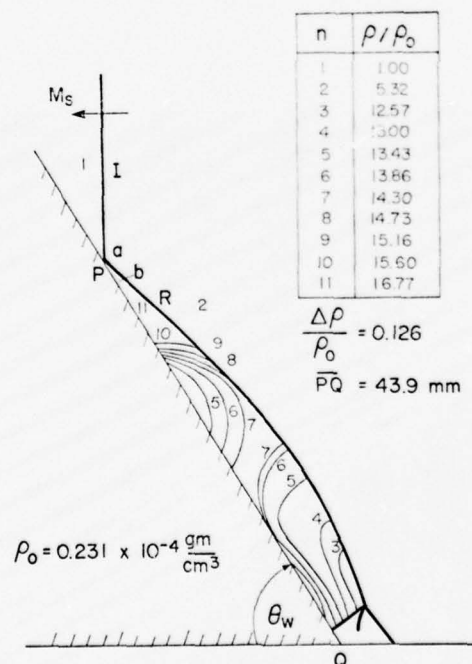
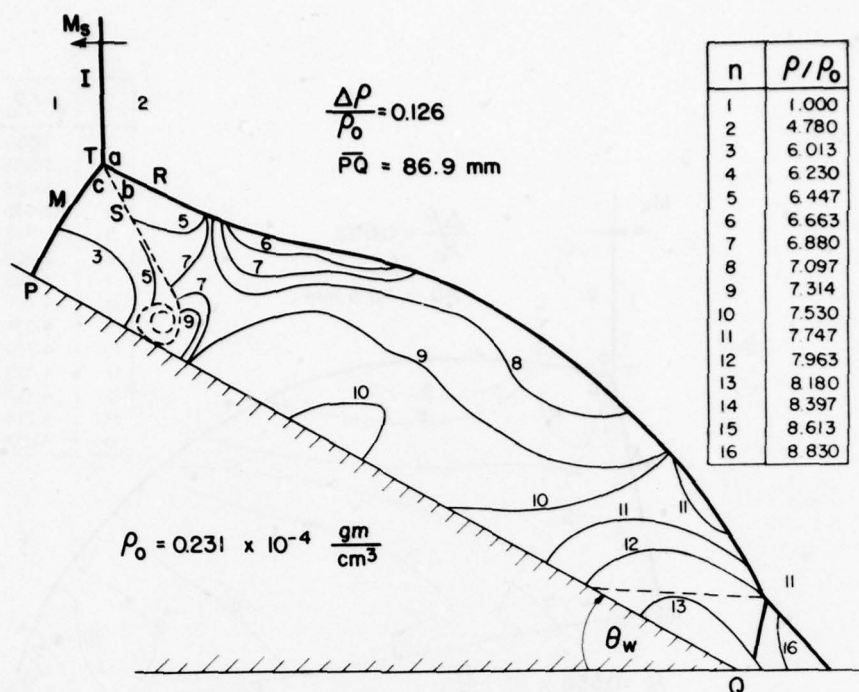
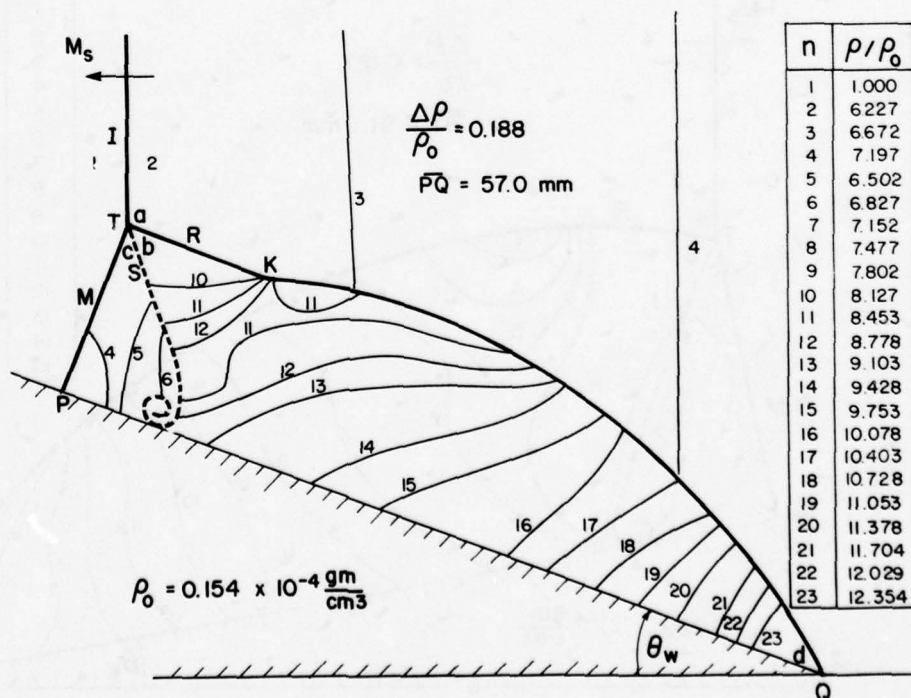


FIG. 64 ACTUAL FLOW ISOPYCNICS CORRESPONDING TO THE SEVEN DIFFERENT OBLIQUE SHOCK WAVE DIFFRACTIONS SHOWN IN FIG.63 (WITH IDENTICAL INITIAL CONDITIONS). THE IMPERFECT AND PERFECT (IN BRACKETS) DENSITY (ρ/ρ_o) VALUES ARE GIVEN FOR POINT a, b AND c AT THE VICINITY OF THE TRIPLE POINT OR THE REFLECTION POINT.

(a) a-5.32, b-17.66 (4.88, 14.48)



(d) a-4.580, b-6.489, c-5.282 (4.376, 6.066, 4.861)



(e) a-7.191, b-9.131, c-7.570 (6.148, 7.585, 6.300)

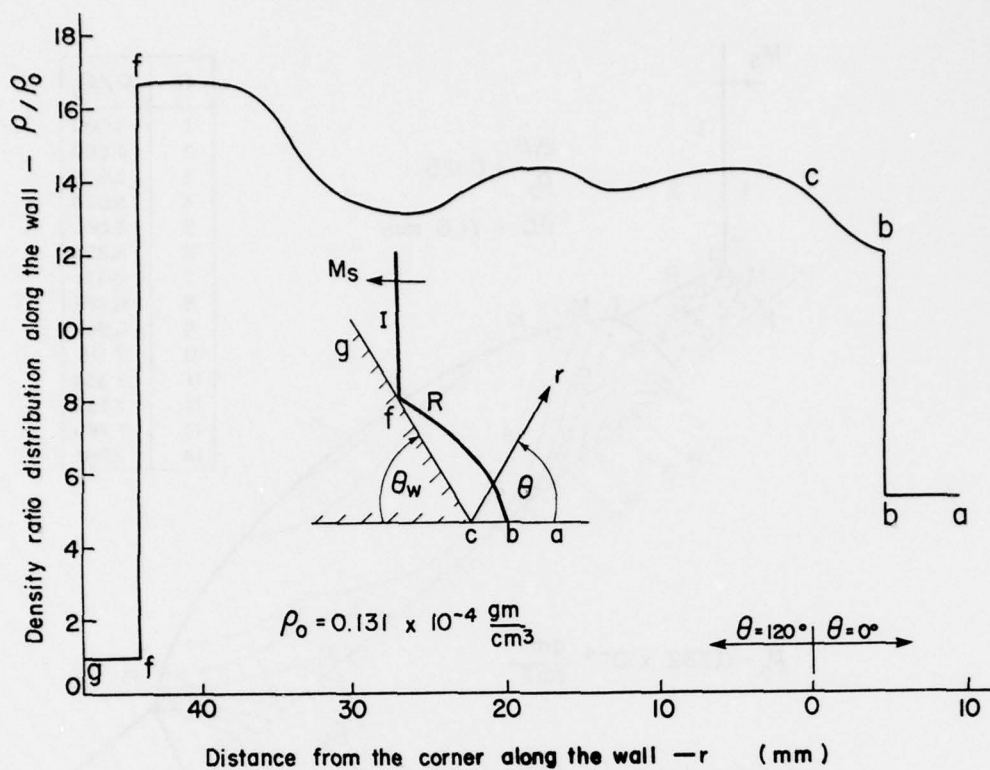


FIG. 65 (a) INTERFEROMETRIC DENSITY-RATIO DISTRIBUTION ALONG THE WALL FOR DIFFERENT OBLIQUE SHOCK-WAVE DIFFRACTIONS SHOWN IN FIG. 63 (WITH IDENTICAL INITIAL CONDITIONS)

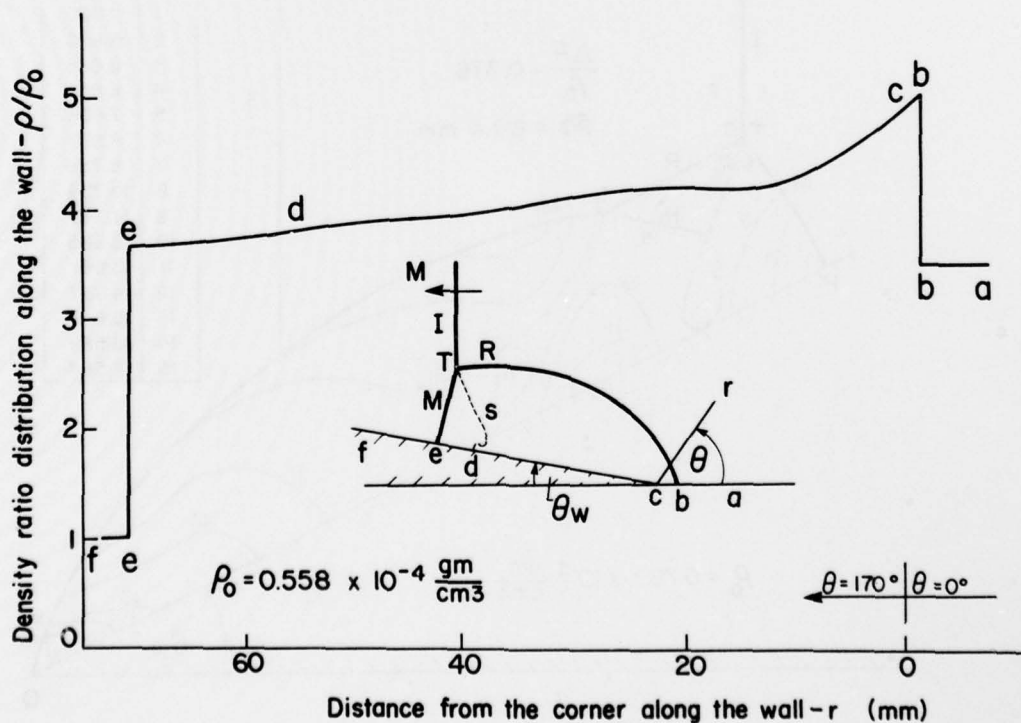


FIG.65 (b) CONT.

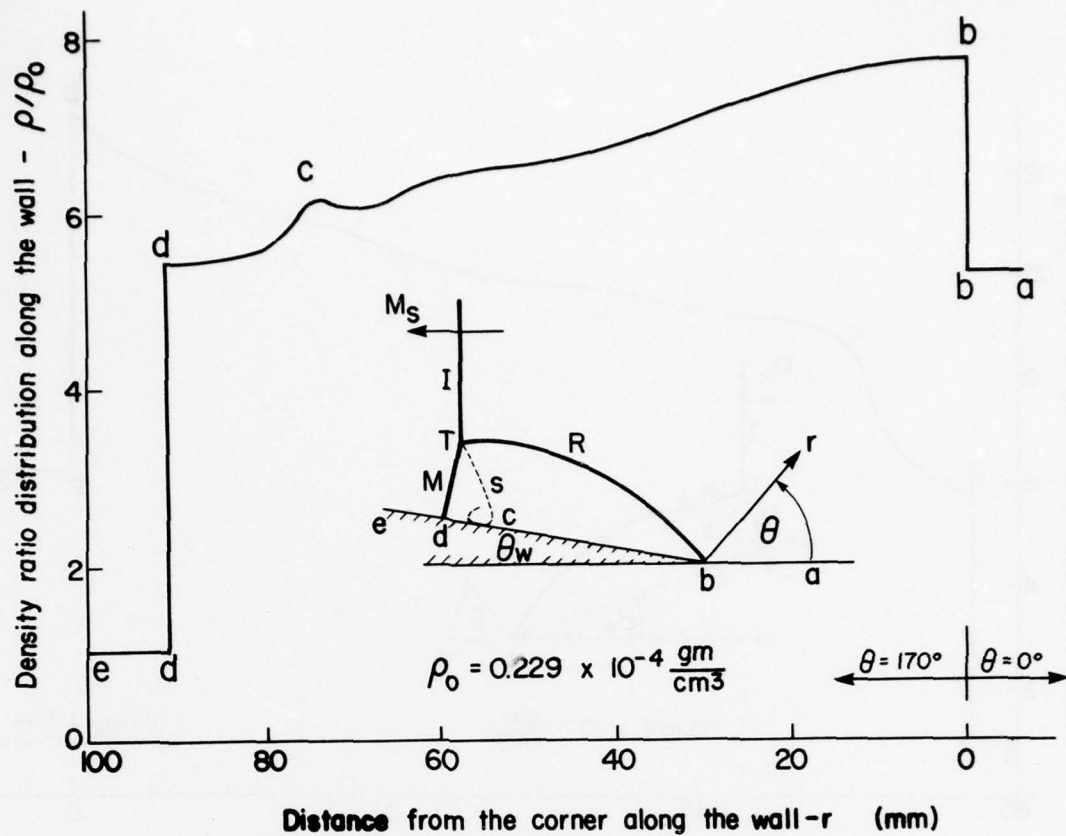


FIG. 65 (c) CONT.

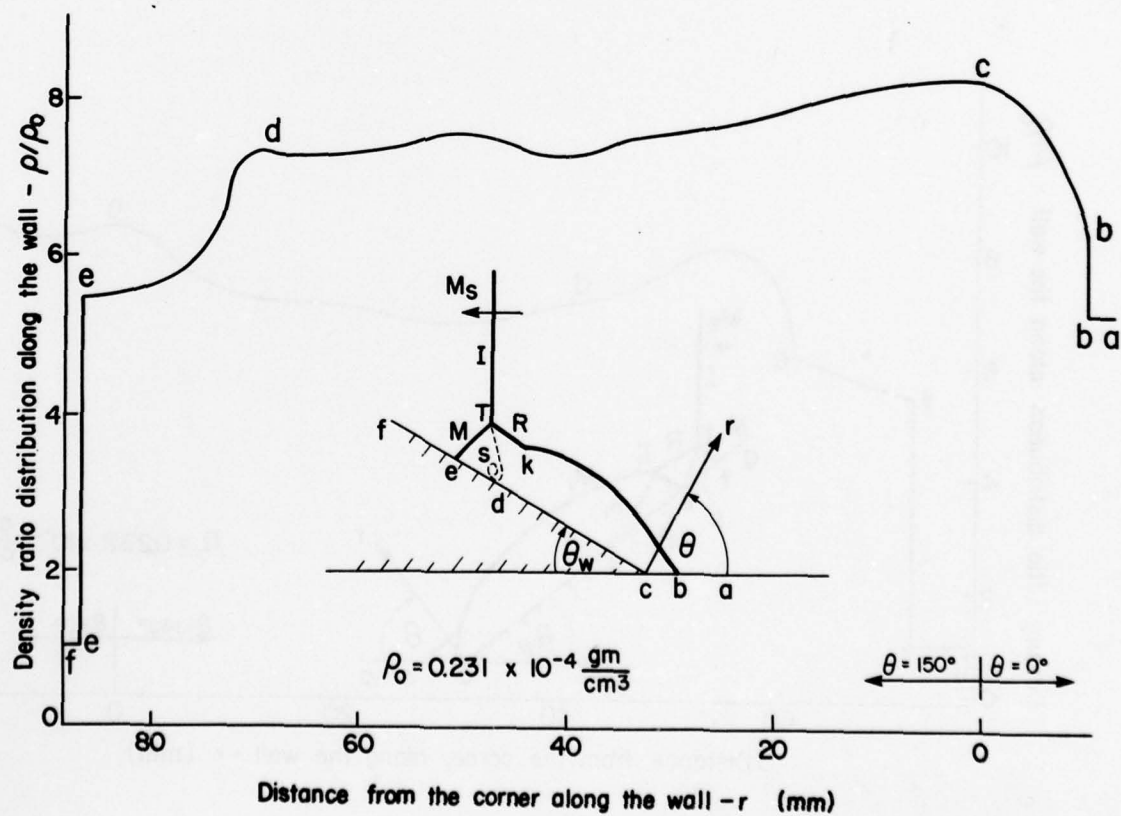


FIG. 65 (d) CONT.

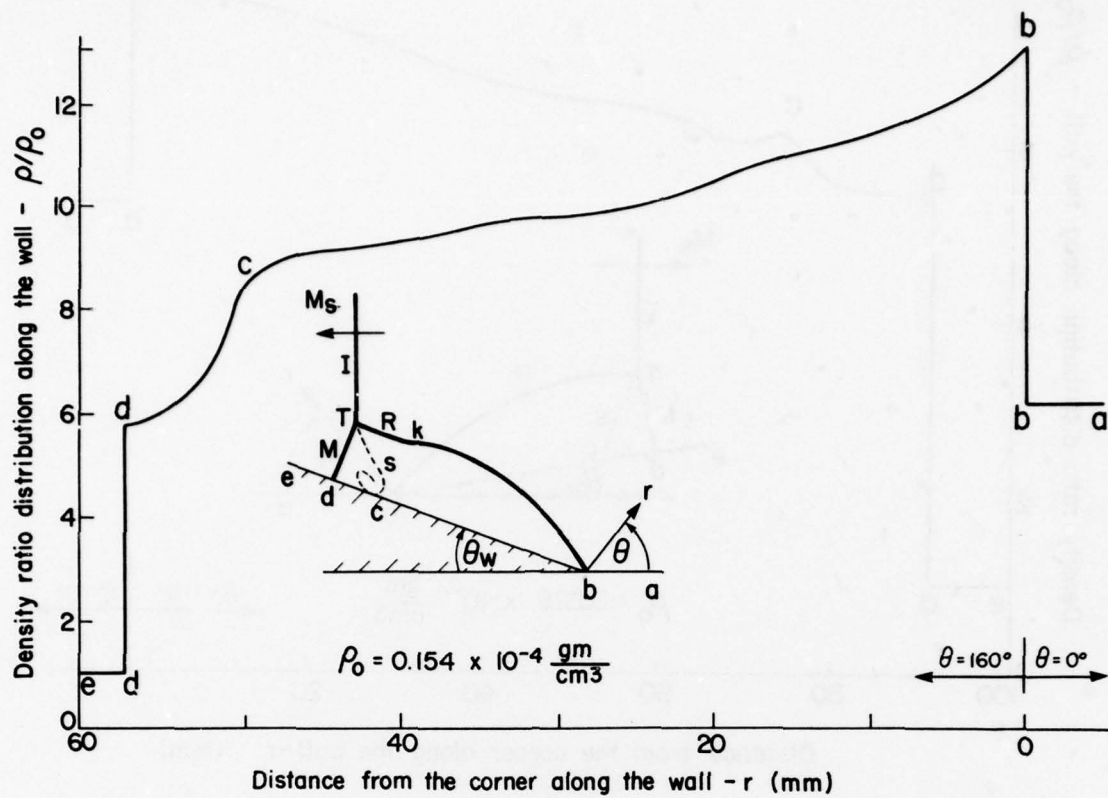


FIG. 65 (e) CONT.

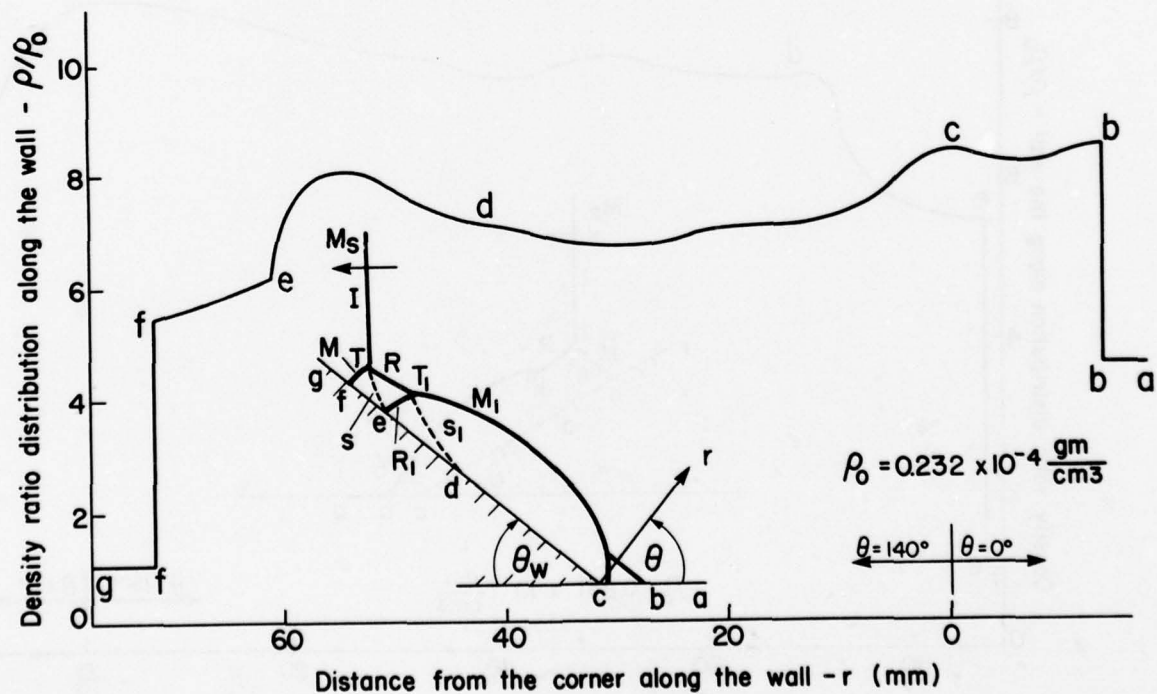


FIG. 65 (f) CONT.

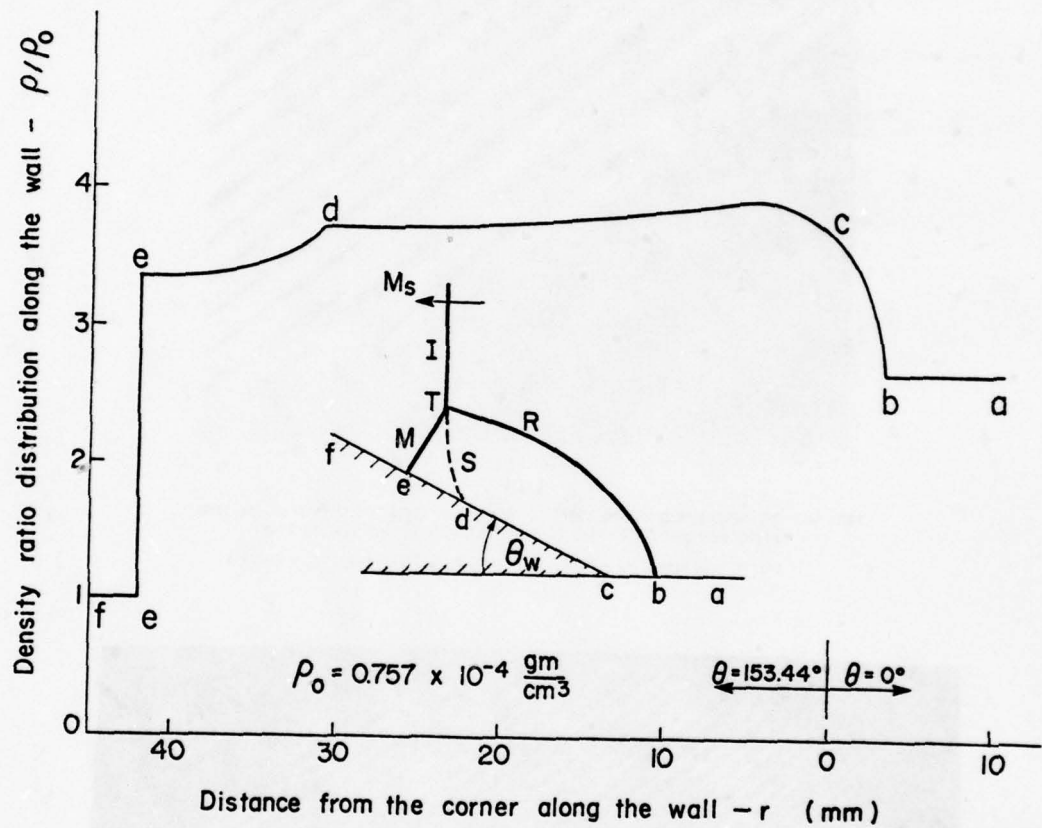
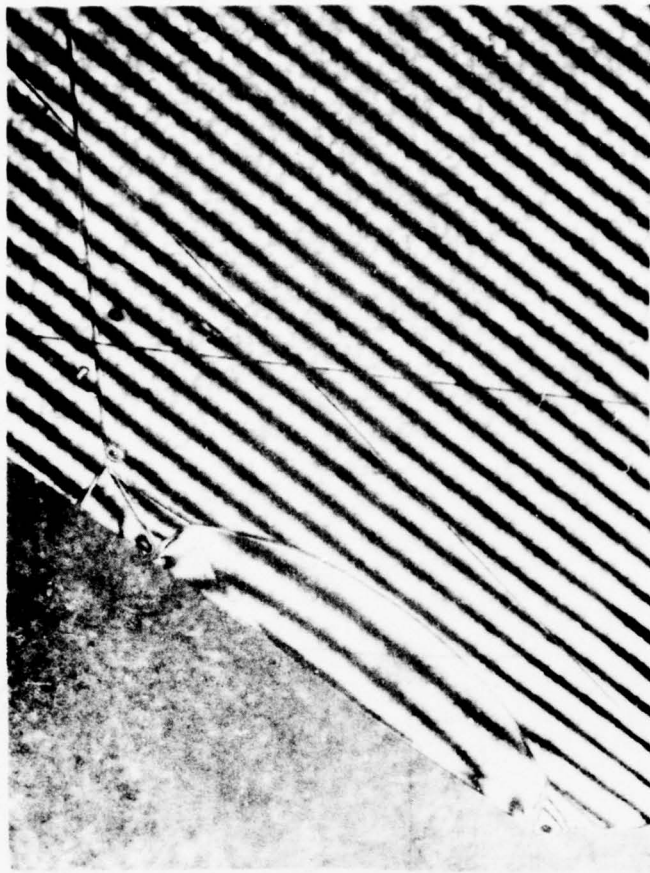


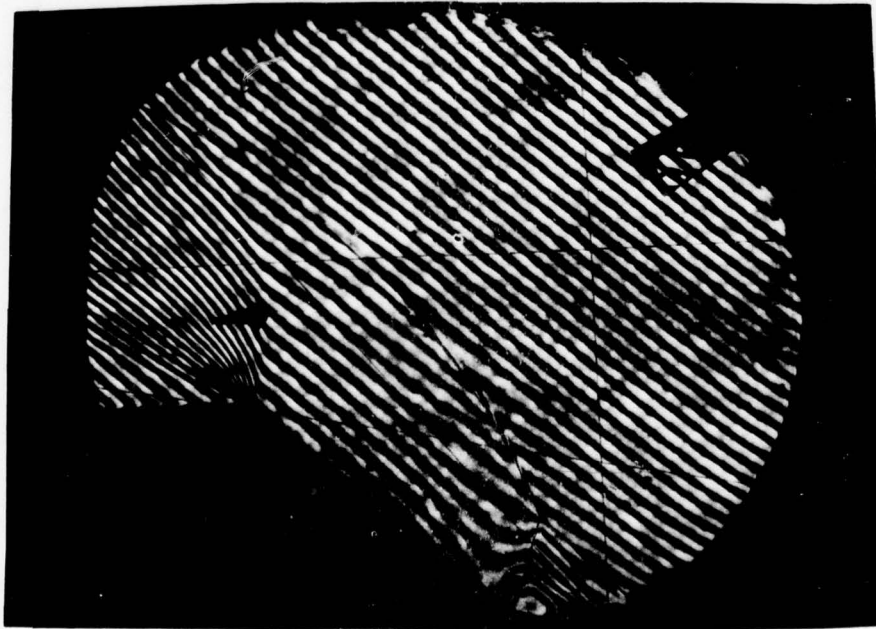
FIG.65 (g) CONT.



(a)

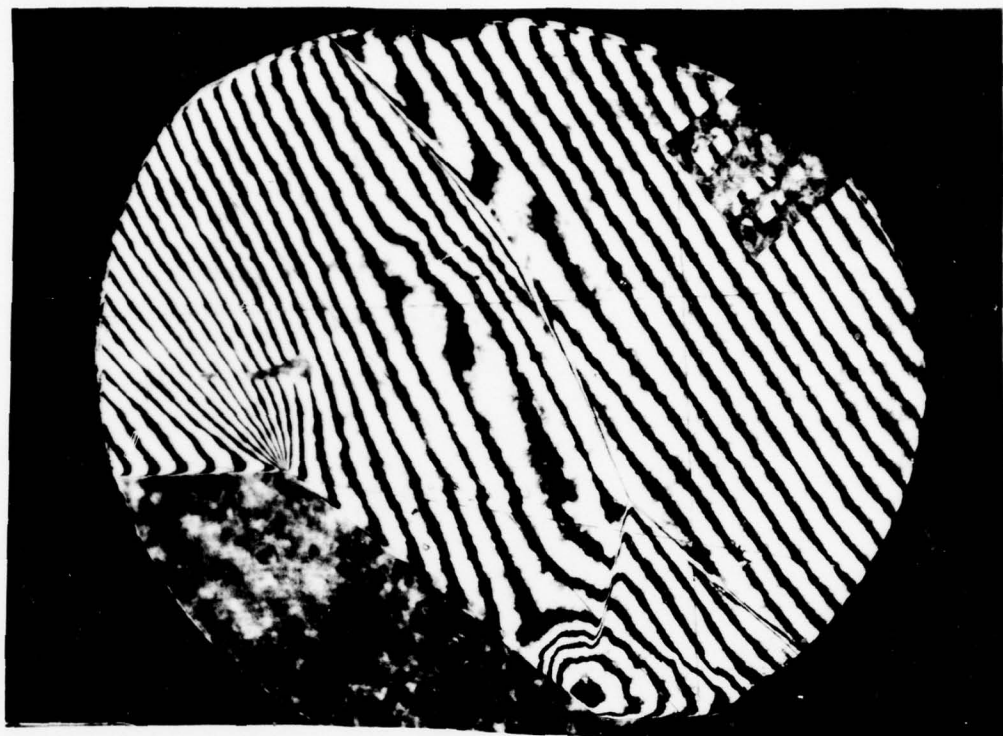
FIG. 66. THE DEVELOPMENT OF THE DETACHED SHOCK-WAVE BIFURCATION PROCESS, Δt -TIME AFTER INCIDENT SHOCK WAVE PASSED THE CENTRE OF THE TEST SECTION.

(a) $\Delta t = 26 \text{ } \mu\text{sec}$, $M_S = 4.64$, $\theta_W = 40^\circ$, $P_0 = 15.29 \text{ torr}$, $T_0 = 297.2 \text{ K}$.



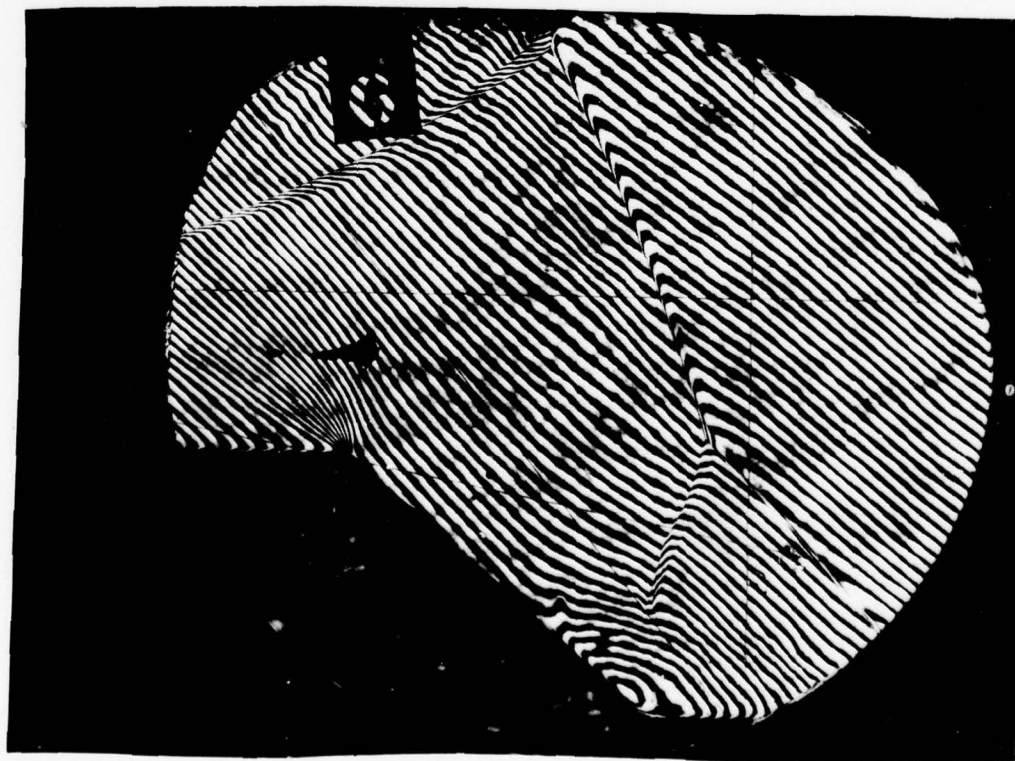
(b)

(b) $\Delta t = 126 \text{ } \mu\text{sec}$, $M_S = 4.59$, $\theta_W = 40^\circ$, $P_0 = 15.64 \text{ torr}$, $T_0 = 298.2 \text{ K}$.



(c)

(c) $\Delta t = 226 \mu\text{sec}$, $M_g = 4.60$, $\theta_w = 40^\circ$, $P_o = 15.15 \text{ torr}$, $T_o = 298.4 \text{ K}$.



(d)

(d) $\Delta t = 326 \mu\text{sec}$, $M_g = 4.72$, $\theta_w = 40^\circ$, $P_o = 13.21 \text{ torr}$, $T_o = 298.4 \text{ K}$.

n	p/p_0
1	1.000
2	1.015
3	1.079
4	1.070
5	1.061
6	1.052
7	1.043

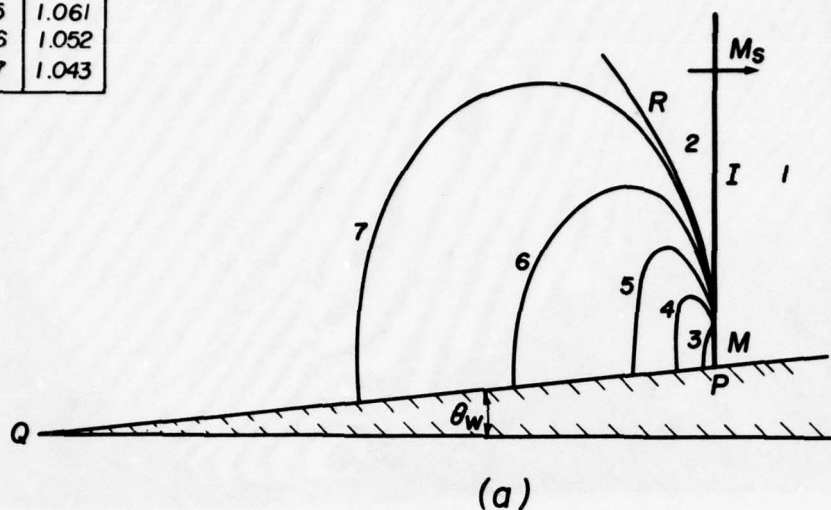
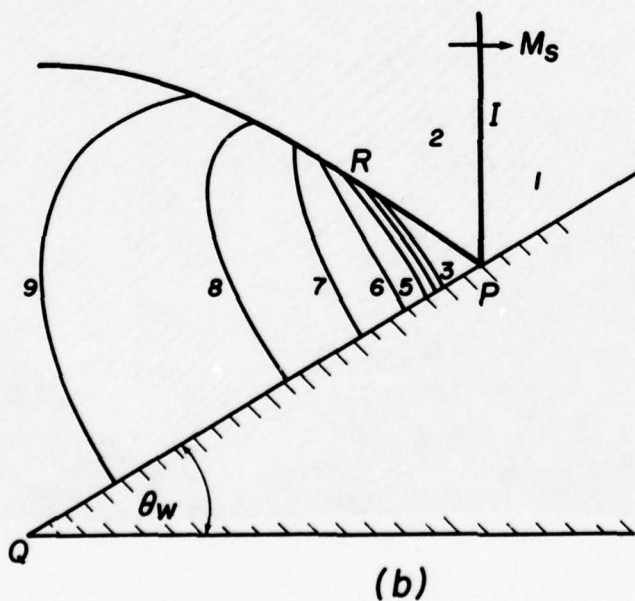


FIG. 67(a). SMR WITH SUBSONIC TURNING OVER THE CORNER (REGION 3, FIG. 39). REPRODUCTION OF FIG. 34 FROM REF. 17. $M_s = 1.010$, $\theta_w = 5.7^\circ$ (AIR).



n	p/p_0
1	1.000
2	1.029
3	1.057
4	1.054
5	1.050
6	1.046
7	1.043
8	1.039
9	1.035

FIG. 67(b). RR WITH SUBSONIC TURNING OVER THE CORNER (REGION 1, FIG. 39). REPRODUCTION OF FIG. 46 FROM REF. 17, $M_s = 1.018$, $\theta_w = 30^\circ$ (AIR).

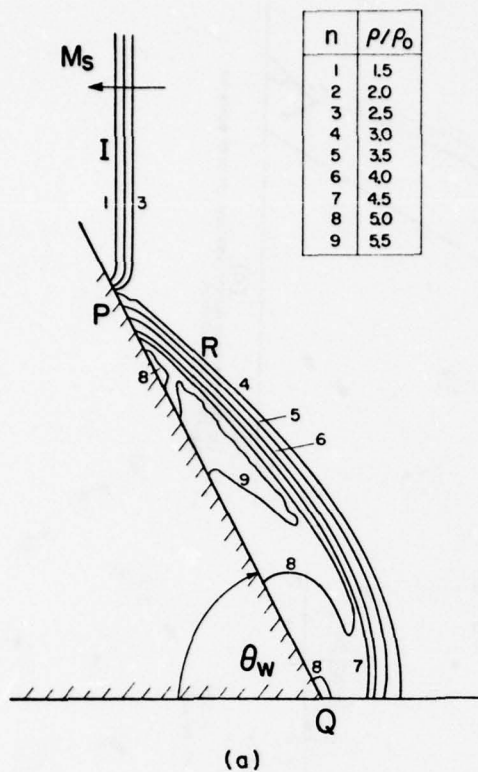
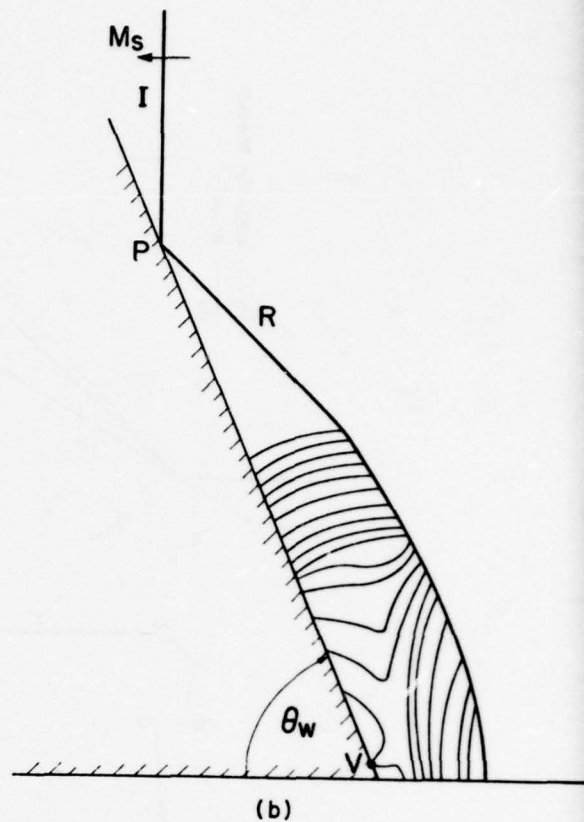
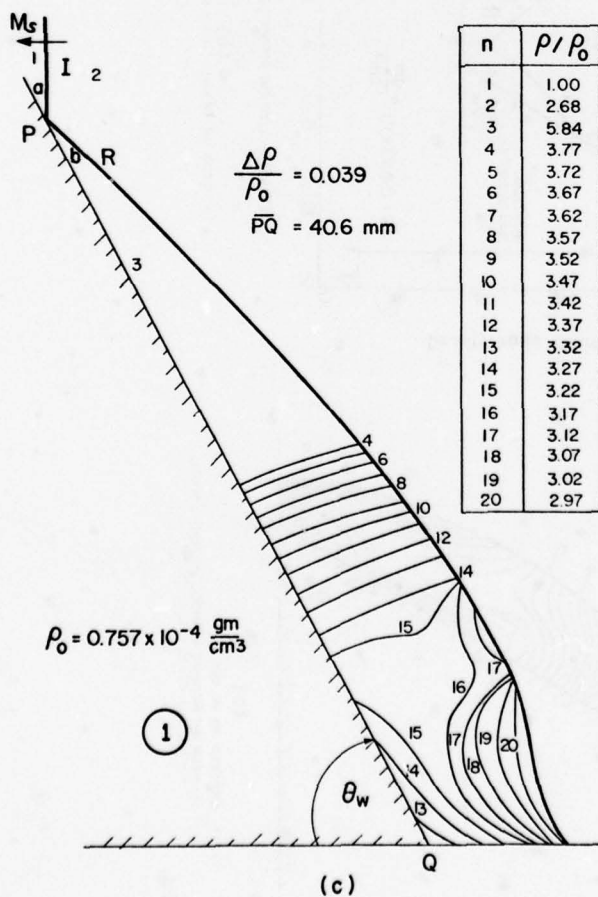


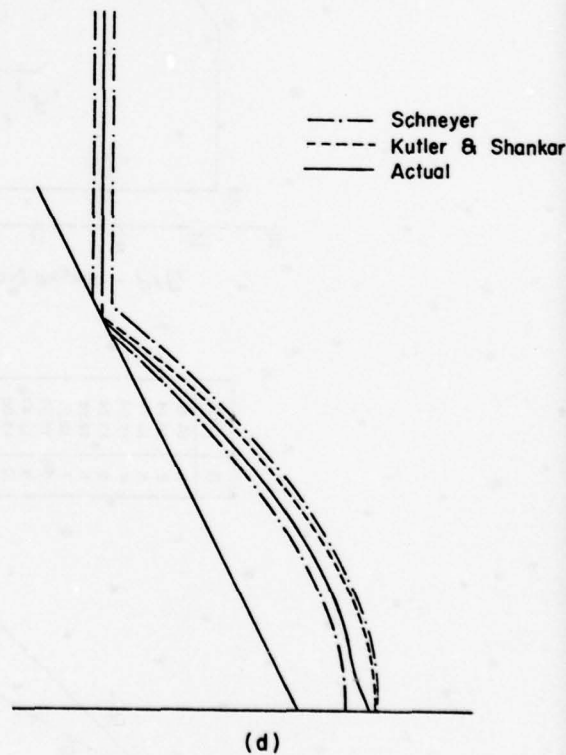
FIG. 68. ISOPYCNICS FOR RR, CASE 1.
(a) SCHNEYER'S NUMERICAL PREDICTIONS, $\gamma = 1.4$, $M_s = 2$, $\theta_w = 63.43^\circ$.



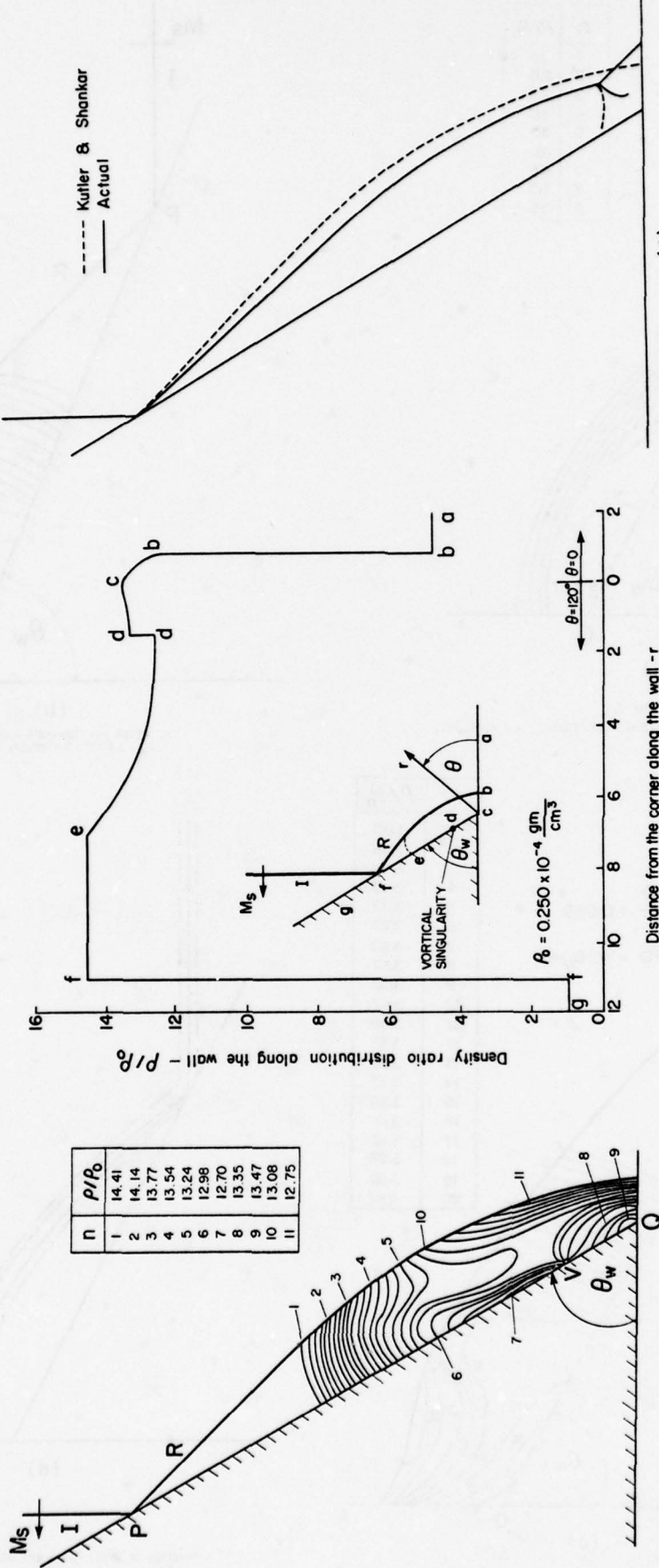
(b) KUTLER AND SHANKAR'S PREDICTIONS, $\gamma = 1.4$, $M_s = 2$, $\theta_w = 63.41^\circ$, V-VORTICAL SINGULARITY.



(c) ACTUAL FLOW ISOPYCNICS, NITROGEN, $M_s = 2.01$, $\theta_w = 63.43^\circ$.



(d) COMPARISON OF NORMALIZED SHOCK-WAVE SYSTEM OF SCHREYER AND KUTLER AND SHANKAR WITH EXPERIMENT.



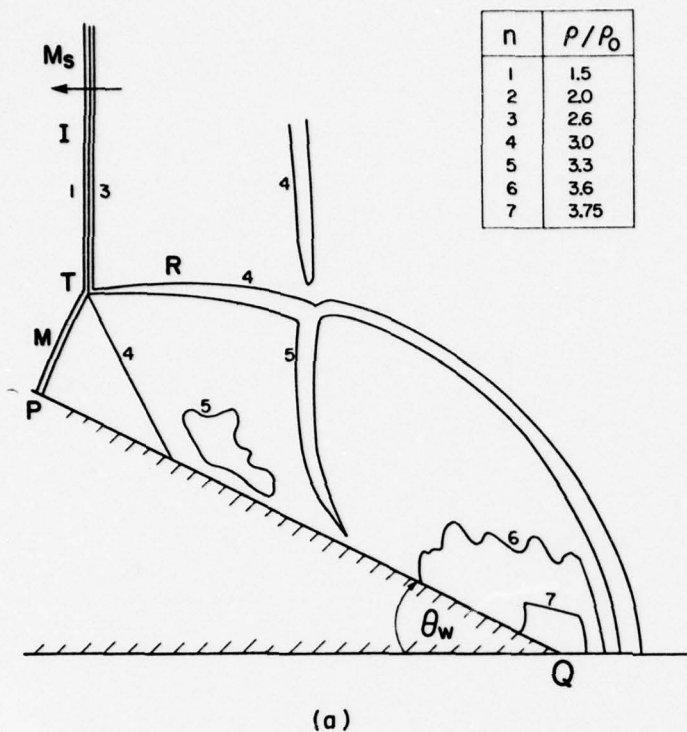
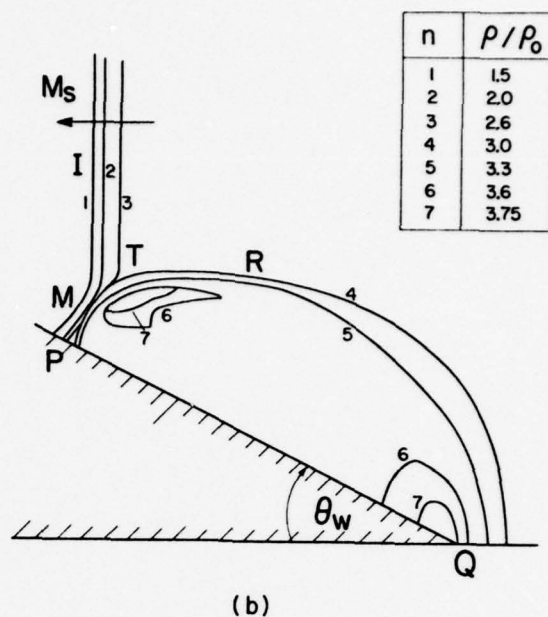
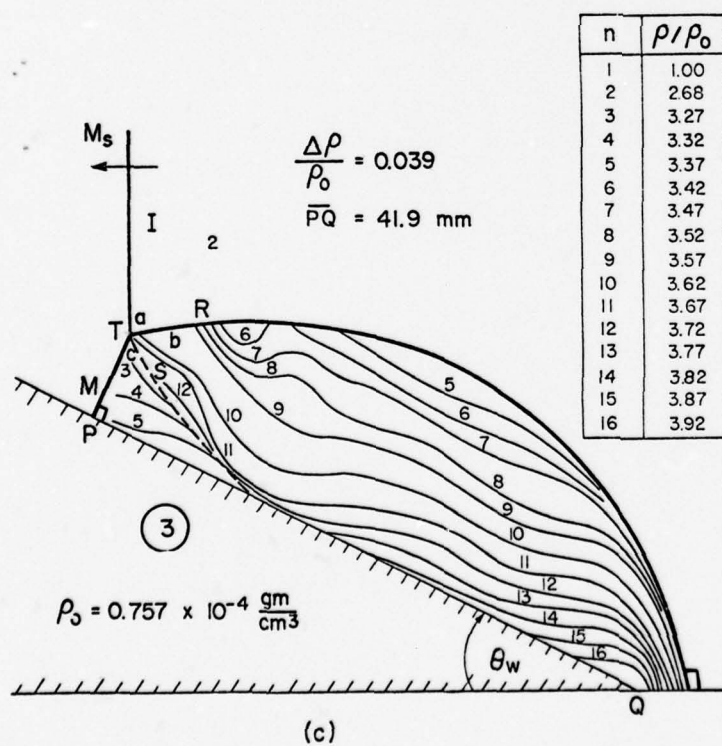


FIG. 70. ISOPYCNICS FOR SMR, CASE 3.

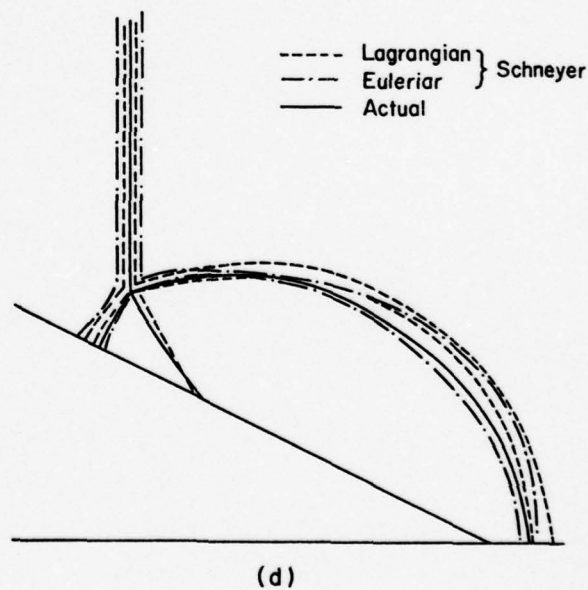
(a) SCHNEYER'S NUMERICAL PREDICTION USING A LAGRANGIAN CODE,
 $\gamma = 1.4$, $M_s = 2$, $\theta_w = 26.56^\circ$.



(b) SCHNEYER'S NUMERICAL PREDICTIONS USING AN EULERIAN CODE,
 $\gamma = 1.4$, $M_s = 2$, $\theta_w = 26.56^\circ$.



(c) ACTUAL FLOW ISOPYCNICS, NITROGEN, $M_s = 2.01$, $\theta_w = 26.56^\circ$.



(d) COMPARISON OF NORMALIZED SHOCK-WAVE SYSTEMS OF SCHNEYER WITH EXPERIMENT.

APPENDIX A

(P, θ)-SHOCK POLARS

The locus of all possible post-shock states that result from a given flow with pressure P , temperature T and Mach number M , when it passes through any oblique shock wave, is the shock polar (Fig. A.1).

Two important deflection angles, the sonic angle θ_s and the angle of maximum deflection (the detachment angle) θ_m , divide the shock polar (and the deflection process as well) into three different cases:

- (1) $0 < \theta < \theta_s$; the deflection is through a straight and attached shock wave (Fig. 5b) behind which the flow is supersonic.
- (2) $\theta_s < \theta < \theta_m$; the deflection is through a curved but attached shock wave behind which the flow is subsonic (Fig. 5c).
- (3) $\theta > \theta_m$, where the curved shock wave is detached (Fig. 5d).

The part of the shock polar below m is called the weak-shock solution portion and the remainder of the polar is for strong shocks. Consequently, for every deflection angle θ the pressure ratio is double valued. However, it is an experimental fact that in the case of sharp compressive corners the weak solution occurs. Note that in the presence of boundary layer or blunt bodies the strong solution can occur.

Each point on the shock polar corresponds to a state which could have been obtained by passing through an appropriate oblique shock wave. Consequently, there are two other points of interest in every shock polar, namely the limiting cases corresponding to a Mach wave ($\phi_0 = \mu = \sin^{-1} 1/M$) and a normal shock wave ($\phi_0 = 90^\circ$). The former represents no change in the flow properties, while the latter signifies the greatest changes in the flow properties. Note that the flow deflection for both cases is zero ($\theta = 0$).

It is well known (Ref. 27) that the higher the flow Mach number M_0 the greater the corresponding maximum deflection angle θ_m . This is illustrated in Fig. A.2 where the deflection angle increases from 43.2° to 49.0° as M_0 increases from 5 to 10. Consequently, a flow with $M_0 = 10$ would negotiate a wedge of 45° through an attached shock wave, while the deflection of a flow with $M_0 = 5$ would be through a detached shock wave. A detailed discussion of the influence of real-gas effects on the (P, θ) -polar is given in Refs. 48 and 51. A typical illustration is shown in Fig. A.3. It is seen that both the pressure ratio P/P_0 across the oblique shock wave and the angle of maximum deflection θ_m increase (see NSW points for example) as a result of real-gas effects. For this particular illustration of $M_0 = 10$, $P_0 = 15$ torr and $T_0 = 300$ K, $\theta_m = 42.7^\circ$ for a perfect diatomic gas and $\theta_m = 49.0^\circ$ for nitrogen in dissociation equilibrium.

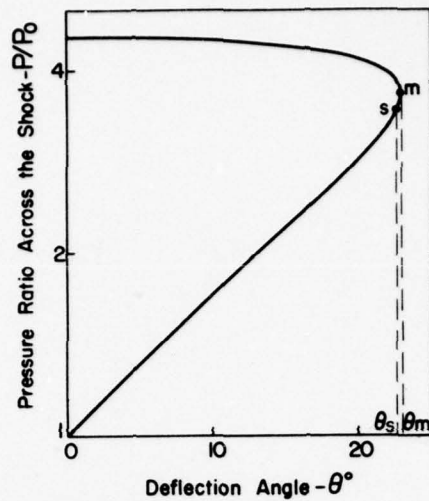


FIG. A-1. TYPICAL SHOCK POLAR, NITROGEN $M_0 = 2.00$, $P_0 = 15$ TORR, $T_0 = 298.6$

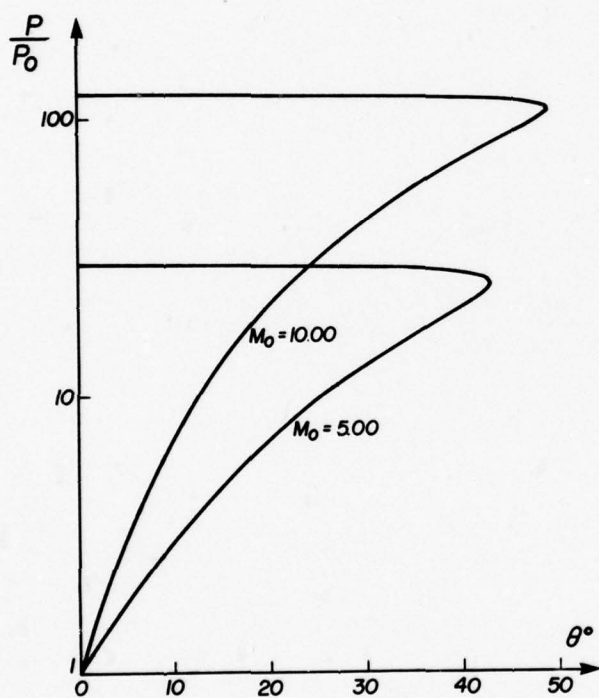


FIG. A-2. THE DEPENDENCE OF THE (P, θ) -SHOCK POLAR ON THE FLOW MACH NUMBER M_0 . NITROGEN, $P_0 = 15$ TORR, $T_0 = 300$ K.

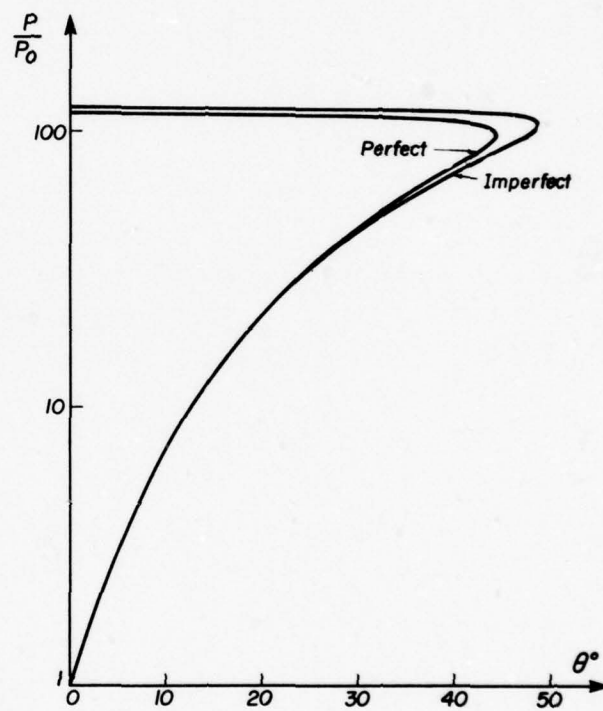


FIG. A-3. THE DEPENDENCE OF THE (P, θ) -SHOCK POLAR ON REAL GAS EFFECTS $M_0 = 10$, $P_0 = 15$ TORR, $T_0 = 300$ K.

APPENDIX B

ANALYTICAL SOLUTION OF THE EQUATIONS OF MOTION FOR RR

(Eqs. 2.1 to 2.9)

The following computer program follows the method discussed in Section 2.2.1.2 for solving Eqs. 2.1 to 2.9 with and without real-gas effects.

Although the following program is for nitrogen it could be modified very easily for any other gas by changing the following:

- (1) SUBROUTINE RGP that calculates the equilibrium thermodynamic properties of the gas under consideration for a given pressure and temperature.
- (2) SUBROUTINE GUESTP that supplies appropriate initial guesses of temperature and pressure ratios across a normal shock wave.

Two typical outputs follow the listing of the program for the two possible modes of operation (see comment statements in the following computer program for details). The CPU times of these two outputs were 0.19 and 0.06 sec, respectively, on an IBM 370 computer.

THIS PAGE IS BEST QUALITY PRACTICABLE
FROM COPY FURNISHED TO DDC

```

C-----THE FOLLOWING PROGRAM CALCULATES STATES (1) AND (2) OF A REGULAR
C REFLECTION FOR A SET OF INITIAL CONDITIONS: I-E** (TORR)
C P0=PRESSURE AHEAD OF THE INCIDENT SHOCK WAVE* (TORR)
C T0=TEMPERATURE AHEAD OF THE INCIDENT SHOCK WAVE* (K)
C TETAW=COMPRESSION WEDGE ANGLE* (DEGREE)
C MS=INCIDENT SHOCK WAVE MACH NUMBER.
C TWO OPERATION MODES ARE POSSIBLE:
C RRSOL=1: ONLY STATE (1) IS CALCULATED (STATE (2) IS GIVEN
C DUMMY VALUES)
C RRSOL=2: BOTH STATES (1) AND (2) ARE CALCULATED.
C-----
COMMON/ABC/ITYPE
COMMON/CDE/RRSOL
REAL M0,M1,M2,MS
INTEGER RRSOL,RRSOLV
C-----RRSOL=1 CALCULATE STATE (1) ONLY.
C-----RRSOL=2 CALCULATE STATES (1) AND (2).
C-----RRSOL=2
C-----CONVERTING FACTORS:
C-----FROM DEGREE TO RADIAN.
C Q=0.0174533
C-----FROM TORR TO DYN/CM**2
C QQ=980.665*1.36
C-----INITIAL CONDITIONS ARE AS FOLLOWS
C-----P0 IN TORR.
C P0=15.31
C-----T0 IN K.
C T0=300.
C-----TETAW IN DEGREE.
C TETAW=60.
C MS=4.68
C-----
WRITE(6,114)
114 FORMAT(1H1)
C-----ITYPE=1: IDEAL GAS SOLUTION.
C-----ITYPE=2: REAL GAS SOLUTION.
C DO 1 ITYPE=1,2
C WRITE(6,115)
115 FORMAT(1X,80(' '))
C-----CONVERT UNITS TO APPROPRIATE WORKING UNITS.
C TETAWR=TETAW*Q
C P0=P0*QQ
C-----
C-----MOVE FRAME OF REFERENCE TO THE REFLECTION POINT.
C M0=MS/COS(TETAWR)
C PHI0=90.-TETAW
C-----
C-----CALCULATE STATE (0) FROM THE GIVEN P0 AND T0
C CALL RGP(P0,T0,AL0,RO0,HO,AO)
C U0=AO*M0
C-----
C-----CALCULATE STATE (1).
C CALL OSW(P0,T0,AL0,RO0,HO,AO,M0,U0,P1,T1,AL1,RO1,M1,A1,M1,U1,PHI0,
C IDEL1D)
C-----
C-----GIVE DUMMY VALUES TO STATE (2).
C M2=0.
C P2=0.
C T2=0.
C RO2=0.
C PHI2=0.
C DEL2D=0.
C RSWAD=0.
C-----
C GO TO(2,3),RRSOL
C-----CALCULATE STATE (2)
C-----FIRST GUESS FOR PHI1D.
C 3 PHI1D=40.
C DO 11 I=1,30
C CALL OSW(P1,T1,AL1,RO1,M1,A1,M1,U1,P2,T2,AL2,RO2,M2,A2,M2,U2,PHI1D
C 1=DEL2D)
C F1=DEL2D/DEL1D-1.
C IF(ABS(F1).LE.1.E-05)GO TO 12
C PHI1D=1.01*PHI1D
C CALL OSW(P1,T1,AL1,RO1,M1,A1,M1,U1,P2,T2,AL2,RO2,M2,A2,M2,U2,PHI1D
C 1=DEL2D)
C F2=DEL2D/DEL1D-1.
C 11 PHI1D=PHI1D*(1.0+0.01*(F1/(F2-F1)))
C WRITE(6,999)
C 999 FORMAT(1X,'***** NO CONVERGENCE IN MAIN PROGRAM *****')
C STOP
C-----
C-----CALCULATE THE ANGLE BETWEEN THE REFLECTED SHOCK AND THE WEDGE SURFACE
C 12 RSWAD=PHI1D-DEL1D
C-----
C-----CHANGE PRESSURES BACK TO TORR.
C 2 P0=P0/QQ
C P1=P1/QQ
C P2=P2/QQ
C-----
C-----PRINT RESULTS.
C GO TO(4,5),ITYPE
C 4 WRITE(6,100)
C 100 FORMAT(25X,'REFLECT GAS SOLUTION')
C WRITE(6,101)
C 101 FORMAT(25X,20(' '))
C GO TO 6
C 5 WRITE(6,102)
C 102 FORMAT(25X,'IMPERFECT GAS SOLUTION')
C WRITE(6,103)
C 103 FORMAT(25X,22(' '))
C 6 WRITE(6,105)
C 105 FORMAT(10X,'REGION 0',7X,'REGION 1',7X,'REGION 2')
C WRITE(6,106)M0,M1,M2
C 106 FORMAT(1X,'MACH NUMBER',7X,3(F5.2,10X))
C WRITE(6,107)P0,P1,P2
C 107 FORMAT(1X,'PRESSURE',10X,3(F7.2,8X),6X,'TORR')
C WRITE(6,108)T0,T1,T2
C 108 FORMAT(1X,'TEMPERATURE',5X,3(F7.2,4X),5X,'K')
C WRITE(6,109)RO0,RO1,RO2
C 109 FORMAT(1X,'DENSITY',10X,3(E10.4,5X),7X,'G/CM**3')
C WRITE(6,110)
C 110 FORMAT(23X,'I',23X,'R')
C WRITE(6,111)PHI0,PHI1D
C 111 FORMAT(1X,'INCIDENT ANGLE',6X,F5.2,19X,F5.2,20X,'DEGREE')
C WRITE(6,112)DEL1D,DEL2D
C 112 FORMAT(1X,'DEFLECTION ANGLE',4X,F5.2,19X,F5.2,20X,'DEGREE')
C WRITE(6,113)RSWAD
C 113 FORMAT(1X,'ANGLE BETWEEN R AND WEDGE SURFACE IS',1X,F5.2,1X,'DEGRE
C 1E')
C 1 CONTINUE
C-----
C WRITE(6,115)
C WRITE(6,114)
C STOP
C END

```



```

SUBROUTINE OSW(IPA,TA,ALA,ROA,HA,AA,MA,UA,PB,TB,ALB,ROB,HB,AB,MB,UB
1,PHIAD,DELB)
C-----
C-----SUBROUTINE OSW CALCULATES THE CHANGES ACROSS AN OBLIQUE SHOCK
C WAVE (OSW). THE PARAMETERS ARE:
C PA-PRESSURE AHEAD
C TA-TEMPERATURE AHEAD
C ALA-DEGREE OF DISSOCIATION AHEAD
C ROA-DENSITY AHEAD
C HA-ENTHALPY AHEAD
C AA-SPEED OF SOUND AHEAD
C MA-MACH NUMBER AHEAD
C UA-FLOW VELOCITY AHEAD
C PB-PRESSURE BEHIND
C TB-TEMPERATURE BEHIND
C ALB-DEGREE OF DISSOCIATION BEHIND
C ROB-DENSITY BEHIND
C HB-ENTHALPY BEHIND
C AB-SPEED OF SOUND BEHIND
C MB-MACH NUMBER BEHIND
C UB-FLOW VELOCITY BEHIND
C PHIAD-INCIDENCE ANGLE BETWEEN SHOCK AND FLOW AHEAD
C DELB-FLOW DEFLECTION ACROSS.
C-----
C P1 IN DYN/CM**2
C REAL F(3),G(3),MA,MB,MAN
C-----
C CONVERT ANGLE TO RADIAN.
C Q=0.0174603 RAD/DEG
C PHIAR=PHIAD*Q
C-----
C CALCULATE NORMAL COMPONENTS OF VELOCITY AND MACH NUMBER.
C UAN=UA*SIN(PHIAR)
C MAN=UAN/AA
C-----
C DETERMINE CONSERVATION EQUATION CONSTANTS FROM INITIAL CONDITIONS
C C1=ROA*UAN
C C2=PA+ROA*UAN*UAN
C C3=HA+0.5*UAN*UAN
C-----
C BEGIN SOLVING THE SYSTEM USING NEWTONS METHOD
C CHOOSE STARTING VALUES FOR T AND P
C CALL GUEST(PMAN,PBA,TBA)
C ANEW=PBA/PA
C ANEW=TBA/TA
C-----
C BEGIN ITERATION PROCEDURE, MAX NO = 25
C DO 70 ITER=1,25
C DETERMINE NECESSARY PARTIAL DERIVATIVES TO SOLVE USING NEWTONS
C T=ANEW
C DEFINE STEP SIZE FOR P IN DETERMINING DERIVATIVES
C STEP=0.10*ANEW
C DO 60 K=1,2
C K=1 HOLD T CONSTANT, FIND F AND G FOR 3 VALUES OF P
C K=2 HOLD P CONSTANT, FIND F AND G FOR 2 VALUES OF T
C DO 50 J=1,3,K
C GO TO (32,34),K
C 32 P=ANEW+(J-2)*STEP
C GO TO 36
C 34 T=ANEW+(J-2)*STEP
C 36 PB=P
C TB=T
C CALL RGP(PB,TB,ALB,ROB,HB,AB)
C DETERMINE PARTICLE VELOCITY (SHOCK CO-ORDS) FROM CONTINUITY EQ
C U=C1/ROB
C MOMENTUM + ENERGY EQUATIONS DEFINE FUNCTIONS TO CHECK VALUES
C F(J)=(PB+C1*U-C2)/C2
C G(J)=(0.5*U*U+HB-C3)/C3
C IF F AND G MEET ACCURACY REQUIREMENTS, EXIT WITH SOLUTION
C 48 IF(ABS(F(J)))-1.E-5148+48.50
C 49 IF(ABS(G(J)))-1.E-5180+80.50
C 50 CONTINUE
C CALCULATE APPROPRIATE DERIVATIVES
C DFDT=(F(3)-F(1))/(STEP*STEP)
C DGDG=(G(3)-G(1))/(STEP*STEP)
C GO TO (54,60),K
C FOR K=1, DERIVATIVES ARE WITH RESPECT TO P
C 54 DFDP=DFDT
C DGDG=DGDG
C DEFINE STEP SIZE FOR T IN DETERMINING DERIVATIVES
C STEP=0.01*ANEW
C P=ANEW
C 60 CONTINUE
C DETERMINE NEW VALUES FOR P AND T USING NEWTONS METHOD
C WRONS=DFDP*DGDG-DFDT*DGDG
C ANEW=ANEW-(F(2)*DGDG-G(2)*DFDT)/WRONS
C ANEW=T- (G(2)*DFDP-F(2)*DGDG)/WRONS
C 70 CONTINUE
C GIVE ERROR MESSAGE IF NO CONVERGENCE
C WRITE(6,2)
C 2 FORMAT(' *NO CONVERGENCE*')
C-----
C CALCULATE DYNAMIC PROPERTIES.
C 80 IF(PHIAD-90.182+81.81
C 81 DELBR=0.
C GO TO 83
C 82 DELBR=PHIAR-ATAN(ROA/ROB*SIN(PHIAR)/COS(PHIAR))
C 83 UB=C1/SIN(PHIAR-DELBR)/ROB
C MB=UB/AB
C-----
C CONVERT ANGLES TO DEGREE.
C PHIAD=PHIAR/Q
C DELRD=DELBR/Q
C-----
C RETURN
C END

```

THIS PAGE IS BEST QUALITY PRACTICABLE
FROM COPY FURNISHED TO DOD

THIS PAGE IS BEST QUALITY PRACTICABLE
FROM COPY FURNISHED TO DDC

```

SUBROUTINE RGP(P,T,ALPHA,RO,MX)
COMMON/ABC/TYPE
REAL KO,M
DIMENSION EA(5),EM(4),GA(5),GM(4),BM(4),TETAM(4),GAMAM(4),QTZ(4),
1PXZ(4),PXZ(5)
C-----THE GAS CONSTANTS ARE AS FOLLOWS
C-----UNIVERSAL GAS CONSTANT
R=8.3143E 08
C-----M-ATOMIC WEIGHT
M=14.008
R=R/2/M
RT=R*T
C-----
GO TO(90,91),TYPE
C-----IDEAL GAS SECTION
90 GAMAM=1.4
ALPHA=0.
Z=1.
RO=P/RT
E=1./(GAMAM-1.)*RT
H=E*RT
A=SQRTE(GAMAM*RT)
RETURN
C-----REAL GAS SECTION
91 CONST=1.331E-9
CONST=M*(14.008/5.314)/(M**2/NA)**1.5
C-----K=0.138054E-15 BOLTZMAN CONSTANT
C-----H=0.69250E-26 PLANK CONSTANT
C-----NA=0.602252E+24 AVOGADRO NUMBER
C-----ATOMIC CONSTANTS
C-----LA=NUMBER OF ENERGY LEVELS GIVEN FOR THE ATOM
LA=9
GA(1)=0.
GA(2)=10.
GA(3)=10.
GA(4)=0.
GA(5)=0.
EA(1)=0.
EA(2)=27696.
EA(3)=27696.
EA(4)=4485.
EA(5)=4485.
C-----MOLECULAR CONSTANT
C-----LM=NUMBER OF ENERGY LEVELS GIVEN FOR THE MOLECULE
LM=2
GM(1)=1.
GM(2)=3.
EM(2)=71571.486
EM(1)=0.
BM(1)=2.861421
BM(2)=2.0619964
GAMAM(1)=8.165593E-06
GAMAM(2)=1.744261E-05
TETAM(1)=3350.7046
TETAM(2)=2060.4343
TETAD=113300.
TETAV=3340.
C-----CONST=CONST*(M)**1.5
PXZT=0.
DO 1 I=1,LM
IF(EM(I)/T-170.13+3.44
3 HBR=1/EXP(EM(I)/T)
GO TO 5
4 HBR=1/EXP(170.)
5 QTZ(1)=1/GAMAM(1)*T*HBR/(1-1/EXP(TETAM(1)/T))
PXZ(1)=GM(1)*QTZ(1)/BM(1)
PXZT=PXZT+PXZ(1)
1 CONTINUE
DO 2 I=1,LA
IF(EA(I)/T-170.16+6.7
6 CCC=1/EXP(EA(I)/T)
GO TO 8
7 CCC=1/EXP(170.)
8 PX(1)=GA(1)*CCC
PX(1)=PX(1)+PX(1)
2 CONTINUE
IF(T=0.0)T=9.9E+10
9 KD=0.
GO TO 11
10 AAA=EXP(TETAD/(4*T))
KD=CONST*T**1.5/AAA/AAA*PX(1)*PX(1)/PXZT/AAA/AAA
11 ALPHA=SQRTE(KD/(KD+0.0))
Z=1./ALPHA
RO=P/RT/Z
ZZ=TETAV/T
ZZZ=ZZ/(EXP(ZZ)-1.)
E=(2.5*RO+5*ALPHA+ALPHA*TETAD/T*(1.-ALPHA)*ZZZ)*RT
H=E*RT
CVIBR=EXP(ZZ)*ZZZ**2.
CVR=1.5*(1.+ALPHA)+(1.-ALPHA)*(1.+CVIBR)*ALPHA*(1.-ALPHA)/(2.-ALPH
1A)*TETAD/T+0.5*ZZZ**2.
CPR=2.5*(1.+ALPHA)+(1.-ALPHA)*(1.+CVIBR)*ALPHA*(1.-ALPHA)*2.1/2.4*
1TETAD/T+1.5*ZZZ**2.
GAMA=CPR/CVR
GAMAE=GAMA*2./(2.+ALPHA-ALPHA**2.)
GAMAF=(1.+5.*ALPHA)/(5.+ALPHA)
A=SQRTE(GAMAE*Z*RT)
RETURN
END

SUBROUTINE GUEST(P,MAN,PRA,TBA)
C-----SUBROUTINE GUEST GUESSES THE TEMPERATURE AND PRESSURE RATIO ACROSS
C-----A NORMAL SHOCK WAVE.
C-----THIS SUBROUTINE IS FOR NITROGEN.
C-----THE PARAMETERS ARE
C MAN=FLOW MACH NUMBER
C PBA=PRESSURE RATIO
C TBA=TEMPERATURE RATIO.
C-----
REAL MAN
COMMON/ABC/TYPE
C-----FIRST GUESS FOR PRESSURE RATIO ACROSS THE SHOCK
G1=1.4
N1=(G1-1.)/2./G1
ALFA1=(G1+1.)/G1-1.
PRA1=(MAN**2/81)**1./ALFA1
GO TO(909,11),TYPE
C-----FIRST GUESS FOR TEMPERATURE RATIO ACROSS THE SHOCK
1 IF(PRA1=0.0)GO TO 900
TRA=26.
RETURN
900 IF(PRA1<300.)GO TO 902
TRA=23.
RETURN
902 IF(PRA1<200.)GO TO 903
TRA=21.
RETURN
903 IF(PBA1<100.)GO TO 904
TRA=17.
RETURN
904 IF(PRA1<40.)GO TO 905
TRA=7.
RETURN
905 TRA=PRA1*(PRA1*ALFA1)/(1.+PRA1*ALFA1)
RETURN
END

```

PERFECT GAS SOLUTION

	REGION 0	REGION 1	REGION 2	
MACH NUMBER	9.36	3.58	0.0	
PRESSURE	15.31	388.95	0.0	TORR
TEMPERATURE	300.00	1560.00	0.0	K
DENSITY	0.2293E-04	0.1120E-03	0.0	G/CM**3
	I		R	
INCIDENT ANGLE	30.00		0.0	DEGREE
DEFLECTION ANGLE	23.26		0.0	DEGREE
ANGLE BETWEEN R AND WEDGE SURFACE IS	0.0			DEGREE

IMPERFECT GAS SOLUTION

	REGION 0	REGION 1	REGION 2	
MACH NUMBER	9.36	3.81	0.0	
PRESSURE	15.31	396.77	0.0	TORR
TEMPERATURE	300.00	1460.54	0.0	K
DENSITY	0.2293E-04	0.1221E-03	0.0	G/CM**3
	I		R	
INCIDENT ANGLE	30.00		0.0	DEGREE
DEFLECTION ANGLE	23.81		0.0	DEGREE
ANGLE BETWEEN R AND WEDGE SURFACE IS	0.0			DEGREE

PERFECT GAS SOLUTION

	REGION 0	REGION 1	REGION 2	
MACH NUMBER	9.36	3.58	2.13	
PRESSURE	15.31	388.95	2147.41	TORR
TEMPERATURE	300.00	1560.00	2907.71	K
DENSITY	0.2293E-04	0.1120E-03	0.3319E-03	G/CM**3
	I		R	
INCIDENT ANGLE	30.00		38.08	DEGREE
DEFLECTION ANGLE	23.26		23.26	DEGREE
ANGLE BETWEEN R AND WEDGE SURFACE IS	14.82			DEGREE

IMPERFECT GAS SOLUTION

	REGION 0	REGION 1	REGION 2	
MACH NUMBER	9.36	3.81	2.42	
PRESSURE	15.31	396.77	2253.20	TORR
TEMPERATURE	300.00	1460.54	2498.72	K
DENSITY	0.2293E-04	0.1221E-03	0.4052E-03	G/CM**3
	I		R	
INCIDENT ANGLE	30.00		36.28	DEGREE
DEFLECTION ANGLE	23.81		23.81	DEGREE
ANGLE BETWEEN R AND WEDGE SURFACE IS	12.47			DEGREE

THIS PAGE IS BEST QUALITY PRACTICABLE
FROM COPY FURNISHED TO DDC

APPENDIX C

ANALYTICAL SOLUTION OF THE EQUATIONS OF MOTION FOR SMR

(Eqs. 2.17 to 2.30)

The following computer program follows the method discussed in Section 2.3.1.3 for solving Eqs. 2.17 to 2.30 with and without real-gas effects.

Although the following program is for argon it could be modified very easily to fit any gas by changing the following:

- (1) SUBROUTINE RGP that calculates the equilibrium thermodynamic properties of the gas under consideration for a given pressure and temperature.
- (2) SUBROUTINE GUESTP that supplies some initial guesses of temperature and pressure ratios across a normal shock wave.

Note that unlike SUBROUTINE RGP of Appendix B where the thermodynamic properties are calculated from the partition function $P(T)$ itself, here, a fit of the form $P(T) = f(T)$ was used in order to reduce the computing time and hence operational cost.

A typical output follows the listing. The computing time for this typical output was 3.6 seconds. The author is indebted to Mr. B. T. Whitten, Research Assistant at UTIAS, for supplying him with subroutines RGP (for argon) and MCNPS.


```

C-----
C-----THE FOLLOWING PROGRAM CALCULATES STATES (2), (2) AND (3) OF A MACH
C REFLECTION, FOR A GIVEN SET OF INITIAL CONDITIONS: 144.
C P0=PRESSURE AHEAD OF THE INCIDENT SHOCK WAVE. (TORR)
C T0=TEMPERATURE AHEAD OF THE INCIDENT SHOCK WAVE. (K)
C PH0=INCIDENCE ANGLE BETWEEN THE INCIDENT SHOCK AND ONCOMING
C FLOW. DEGREE
C M0=FLOW MACH NUMBER AHEAD OF INCIDENT SHOCK WAVE.
C THE METHOD OF SOLUTION IS SENSITIVE TO THE INITIAL GUESSES.
C PH=INCIDENCE ANGLE BETWEEN FLOW AND REFLECTED SHOCK WAVE.
C TH=INCIDENCE ANGLE BETWEEN FLOW AND MACH STEM.
C THUS, IF THE SOLUTION DIVERGES CHANGE TH OR PH OR BOTH.
C-----
C REAL M0,M1,M2,M3,P1,P2,P3,Q1,Q2,Q3
C COMMON/ABC/ITYPE
C-----CONVERTING FACTOR
C-----FROM TORR TO DYN/CM**2
C Q0=1.36*980.65
C-----DEFINE KNOWN PROPERTIES OF STATE (0)
C P0=10.
C T0=300.
C PH0=58.
C M0=11.8
C-----
C WRITE(6,108)
C 108 FORMAT(1H1)
C DO 1 I=1,N2
C ITYPE=1=PERFECT GAS.
C ITYPE=2=IMPERFECT GAS.
C WRITE(6,109)
C 109 FORMAT(1X,100I'')
C-----CONVERT UNITS TO WORKING UNITS.
C-----CHANGE P0 TO DYN/CM**2
C P0=P0/Q0
C-----CALCULATE STATE (0)
C CALL RGP(P0,T0,AL0,RO0,MO,M0,U0,P1,T1,AL1,RO1,M1,AL1,M1,U1,PH1,Q1)
C U0=AD0*MO
C-----CALCULATE STATE (1)
C CALL OSW(P0,T0,AL0,RO0,MO,M0,U0,P1,T1,AL1,RO1,M1,AL1,M1,U1,PH1,Q1)
C 1=DEL1D1
C-----CALCULATE STATES (2) AND (3)
C-----BEGIN SOLVING THE SYSTEM USING NEWTONS METHOD
C-----CHOOSE STARTING VALUES FOR PH1D=PH0,PH1D=TH
C PH=58.
C TH=11.8
C-----BEGIN ITERATION PROCEDURE, MAX NO = 30
C DO 70 ITER=1,30
C-----DETERMINE NECESSARY PARTIAL DERIVATIVES TO SOLVE USING NEWTONS
C T=TH
C-----DEFINE STEP SIZE FOR P IN DETERMINING DERIVATIVES
C STEP=0.01*PH
C DO 80 K=1,2
C-----K=1 HOLD T CONSTANT, FIND F AND G FOR 3 VALUES OF P
C-----K=2 HOLD P CONSTANT, FIND F AND G FOR 2 VALUES OF T
C DO 30 J=1,3+K
C GO TO 132+3+K
C 32 P=PH+(J-2)*STEP
C GO TO 36
C 34 T=TH+(J-2)*STEP
C 36 PH=P
C PH2=T
C CALL OSW(P1,T1,AL1,RO1,M1,AL1,M1,U1,P2,T2,AL2,RO2,M2,AL2,M2,U2,PH1,Q1)
C 1=DEL1D1
C CALL OSW(P0,T0,AL0,RO0,MO,M0,U0,P3,T3,AL3,RO3,M3,AL3,M3,U3,PH2,Q2)
C 1=DEL3D1
C-----BOUNDARY CONDITIONS DEFINE FUNCTIONS TO CHECK VALUES
C F(1)=P2/P3-1.
C IF(M0*G(1)-1.74)GO TO 99
C G(1)=(DEL3D1-DEL2D1)/DEL1D1.
C GO TO 98
C 99 G(1)=(DEL3D1-DEL2D1)/DEL1D1.
C-----IF F AND G MEET ACCURACY REQUIREMENTS, EXIT WITH SOLUTION
C 98 IF(ABS(F(1))-1.E-5)48+8+50
C 48 IF(ABS(G(1))-1.E-5)80+80+50
C 50 CONTINUE
C-----CALCULATE APPROPRIATE DERIVATIVES
C DFD1=(F(1)-F(1))/(STEP*STEP)
C DGD1=(G(1)-G(1))/(STEP*STEP)
C GO TO 134+80+K
C-----FOR K=1,DERIVATIVES ARE WITH RESPECT TO P
C 54 DFDP=DFD1
C DGD=GD1
C-----DEFINE STEP SIZE FOR T IN DETERMINING DERIVATIVES
C STEP=0.01*TH
C P=PH
C 60 CONTINUE
C-----DETERMINE NEW VALUES FOR P AND T USING NEWTONS METHOD
C WRONS=DFDP*DDGT-DFDT*DDGP
C PH=PH+(F(1)*DDGT-G(1)*DFDT)/WRONS
C TH=TH+(G(1)*DDGP-F(1)*DDDP)/WRONS
C 70 CONTINUE
C-----GIVE ERROR MESSAGE IF NO CONVERGENCE
C WRITE(6,2)
C 2 FORMAT(1X,'***** NO CONVERGENCE IN MAIN PROGRAM *****')
C GO TO 3
C 80 PH1D=PH
C PH1D=TH
C-----CHANGE PRESSURES BACK TO TOPP
C P0=P0/Q0
C P1=P1/Q0
C P2=P2/Q0
C P3=P3/Q0
C-----PRINT RESULTS.
C GO TO(4,5),ITYPE
C 4 WRITE(6,110)
C 110 FORMAT(35X,'PERFECT GAS SOLUTION')
C WRITE(6,111)
C 111 FORMAT(35X,20I'')
C GO TO 6
C 5 WRITE(6,112)
C 112 FORMAT(35X,'IMPERFECT GAS SOLUTION')
C WRITE(6,113)
C 113 FORMAT(35X,22I'')
C 6 WRITE(6,100)
C 100 FORMAT(25X,'REGION 0','7X,'REGION 1','7X,'REGION 2','7X,'REGION 3')
C WRITE(6,106)MO,M1,M2,M3
C 106 FORMAT(3X,'MACH NUMBER',12X,4(F6.3,9X))
C WRITE(6,101)P0,P1,P2,P3
C 101 FORMAT(3X,'PRESSURE',15X,4(F6.1,9X),4X,'TORR')
C WRITE(6,102)T0,T1,T2,T3
C 102 FORMAT(3X,'TEMPERATURE',11X,4(F7.1,8X),4X,'K')
C WRITE(6,107)RO0,RO1,RO2,RO3
C 107 FORMAT(3X,'DENSITY',15X,4(E10.4,5X),5X,'G/CM**3')
C WRITE(6,103)
C 103 FORMAT(25X,'1'+24X,'R'+24X,'M')
C WRITE(6,104)PH1D,PH1D,PH1D,PH1D
C 104 FORMAT(3X,'INCIDENT ANGLE',16X,3(F6.2,19X))
C WRITE(6,105)DEL1D,DEL2D,DEL3D
C 105 FORMAT(3X,'DEFLECTION ANGLE',4X,3(F6.2,19X))
C 1 CONTINUE
C-----
C WRITE(6,109)
C 3 STOP
C END

```


SUBROUTINE OSW(PA,TA,ALA,ROA,HA,AA,MA,UA,PB,TB,ALB,ROB,HB,AB,MB,UB,
1,PHIAD,DELBQ)

```

C-----SUBROUTINE OSW CALCULATES THE CHANGES ACROSS AN OBLIQUE SHOCK
C WAVE (OSW). THE PARAMETERS ARE:
C PA-PRESSURE AHEAD
C TA-TEMPERATURE AHEAD
C ALA-DEGREE OF DISSOCIATION AHEAD
C ROA-DENSITY AHEAD
C HA-ENTHALPY AHEAD
C AA-SPEED OF SOUND AHEAD
C MA-MACH NUMBER AHEAD
C UA-FLOW VELOCITY AHEAD
C PB-PRESSURE BEHIND
C TB-TEMPERATURE BEHIND
C ALB-DEGREE OF DISSOCIATION BEHIND
C ROB-DENSITY BEHIND
C HB-ENTHALPY BEHIND
C AB-SPEED OF SOUND BEHIND
C MB-MACH NUMBER BEHIND
C UB-FLOW VELOCITY BEHIND
C PHIAD-INCIDENCE ANGLE BETWEEN SHOCK AND FLOW AHEAD
C DELBQ-FLOW DEFLECTION ACROSS.
C-----
C-----P1 IN DYN/CM**2
C REAL F(3),G(3),MA,MB,MAN
C Q=0.0174603 RAD/DEG
C PHIAR=PHIAD*Q
C UAN=UA*SIN(PHIAR)
C MAN=UAN/AA
C-----DETERMINE CONSERVATION EQUATION CONSTANTS FROM INITIAL CONDITIONS
C C1=ROA*UAN
C C2=PA+ROA*UAN*UAN
C C3=HA+0.5*UAN*UAN
C-----BEGIN SOLVING THE SYSTEM USING NEWTONS METHOD
C-----CHOOSE STARTING VALUES FOR T AND P
C CALL GUESTP(MAN,PBA,TBA)
C ANEWP=PBA*PA
C ANEWT=TBA*TA
C-----BEGIN ITERATION PROCEDURE, MAX NO = 25
C DO 70 ITER=1,25
C-----DETERMINE NECESSARY PARTIAL DERIVATIVES TO SOLVE USING NEWTONS
C T=ANEWT
C-----DEFINE STEP SIZE FOR P IN DETERMINING DERIVATIVES
C STEP=0.10*ANEWP
C DO 60 K=1,2
C-----K=1 HOLD T CONSTANT, FIND F AND G FOR 3 VALUES OF P
C-----K=2 HOLD P CONSTANT, FIND F AND G FOR 2 VALUES OF T
C DO 50 J=1,3,K
C GO TO (32,34),K
C 32 P=ANEWP+(J-2)*STEP
C GO TO 36
C 34 T=ANEWT+(J-2)*STEP
C 36 PB=P
C TB=T
C CALL RGP(PB,TB,ALB,ROB,HB,AB)
C-----DETERMINE PARTICLE VELOCITY (SHOCK CO-ORDS) FROM CONTINUITY EQ
C U=C1/ROB
C-----MOMENTUM + ENERGY EQUATIONS DEFINE FUNCTIONS TO CHECK VALUES
C F(J)=(PB+C1*U-C2)/C2
C G(J)=(0.5*U*U+HB-C3)/C3
C-----IF F AND G MEET ACCURACY REQUIREMENTS, EXIT WITH SOLUTION
C IF(ABS(F(J))-1.E-5)48,48,50
C 48 IF(ABS(G(J))-1.E-5)80,80,50
C 50 CONTINUE
C-----CALCULATE APPROPRIATE DERIVATIVES
C DFDT=(F(3)-F(1))/(STEP*STEP)
C DGDT=(G(3)-G(1))/(STEP*STEP)
C GO TO (54,60),K
C-----FOR K=1,DERIVATIVES ARE WITH RESPECT TO P
C 4 DFDP=DFDT
C DGDP=DGDT
C-----DEFINE STEP SIZE FOR T IN DETERMINING DERIVATIVES
C STEP=0.01*ANEWT
C P=ANEWP
C 60 CONTINUE
C-----DETERMINE NEW VALUES FOR P AND T USING NEWTONS METHOD
C WRONS=DFDP*DGDT-DFDT*DGDP
C ANEWP=ANEWP-(F(2)*DGDT-G(2)*DFDT)/WRONS
C ANEWT=ANEWT-(G(2)*DFDP-F(2)*DGDP)/WRONS
C 70 CONTINUE
C-----GIVE ERROR MESSAGE IF NO CONVERGENCE
C WRITE(6,2)
C 2 FORMAT(' *NO CONVERGENCE*')
C 80 IF(PHIAD-90.)82,81,81
C 81 DELBR=0.
C GO TO 83
C 82 DELBR=PHIAR-ATAN(ROA/ROB*SIN(PHIAR)/COS(PHIAR))
C 83 UB=C1/SIN(PHIAR-DELBR)/ROB
C MB=UB/AB
C PHIAD=PHIAR/Q
C DELBQ=DELBR/Q
C PBA=PB/PA
C TBA=TB/TA
C RETURN
C END

```

THIS PAGE IS BEST QUALITY PRACTICABLE
FROM COPY FURNISHED TO DDC

THIS PAGE IS BEST QUALITY PRACTICABLE
FROM COPY FURNISHED TO DDG

```

SUBROUTINE RGP(P,T,ALPHA,RO,MA)
REAL CA(14),CI(14),MA,NA,NE
COMMON/ABC/ITYPE
C-----
C-----ARGON GAS CONSTANTS
C-----DETERMINE EQUILIBRIUM PROPERTIES OF THE MONATOMIC GAS, GIVEN T AND P
C-----ENTER FITTING COEFFICIENTS OF PARTITION FUNCTS VS TEMP FOR ATOMS AND IONS
DATA CA /11., 0.101473E 01, 0.249931E-01, 0.147316E-01, AR
1 0.512245E-02, 0.980966E-04, -0.833330E-03, -0.200937E-03, AR
2 0.287563E-03, 0.327650E-03, 0.183605E-03, 0.682482E-04, AR
3 0.106382E-03, -0.131914E 01/
DATA CI /11., 0.557826E 01, 0.347500E 00, -0.133355E 00, AR+
1 0.966895E+01, -0.208018E-01, 0.867643E-02, -0.321914E-02, AR+
2 0.122572E-02, -0.467015E-03, 0.161615E-03, -0.577352E-04, AR+
3 0.106382E-03, -0.131914E 01/
C-----
MA=6.63349E-23
R=2.08129E6
TI=182890.
RT=R*T
GO TO(1,2),ITYPE
C-----
C-----IDEAL GAS CONSIDERATION
1 GAMA=5./3.
ALPHA=0.
Z=1.
RO=P/RT
E=1./(GAMA-1.)*RT
H=E+RT
A=SQRT(GAMA*RT)
RETURN
C-----
C-----REAL GAS CONSIDERATION
2 ZA=1.0
DZA=0.0
IF(T.GT.10000.)CALL MCNPS(ZA,DZA,T,CA)
CALL MCNPS(ZI,DZI,T,CI)
D=0.0
IF(T.GT.2500.)D=0.6667145*Z1*T**2.5/(ZA*P*EXP(T/T))
ALPHA=SQRT(D/(1.+D))
RO=P/(RT*(1.+ALPHA))
NE=RO*ALPHA/MA
NA=RO*(1.-ALPHA)/MA
H=R*(2.5*(1.0+ALPHA)*T+TI*ALPHA+T*(1.0-ALPHA)*DZA/ZA+ALPHA*DZI/
1ZII)
DALDT=0.5*(1.-ALPHA*ALPHA)*ALPHA*(2.5+TI/T+T*(DZI/ZI-DZA/ZA))/T
C-----NEGLECT EXCITED STATE CONTRIBUTION
CPR=R*(2.5+TI)*DALDT
CP=2.5*R*(1.0+ALPHA)+CPR
A=SQRT((5.+ALPHA*(1.-ALPHA)*(2.5+TI/T)**2)*R*T/(3.-1.5*ALPHA+
1ALPHA*(1.-ALPHA)/(1.+ALPHA)*(1.5+TI/T)**2))
CM/SEC
RETURN
C-----
END

```

```

SUBROUTINE MCNPS(Y,DY,X,C)
DIMENSION C(14)
Y=0.0
DY=0.0
N=C(1)
IF(N-113+2+1
1 ARG=C(N+2)*X*(N+3)
IF(ABS(ARG)-2.00016+6+3
2 Y=C(2)
3 RETURN
6 ARG=ARG+ARG
H1=0.0
H0=0.0
DH1=0.0
DH0=0.0
DO 7 I=1,N
K=N+1-I
H2=H1
H1=H0
DH2=DH1
DH1=DH0
DH0=ARG+DH1=DH2+2*H1
7 H0=ARG+H1=H2+C(K+1)
Y=0.5*(C(2)+H2+H0)
DY=0.5*(C(N+2)*(DH0-DH2)
RETURN
END

```

```

SUBROUTINE GUEST(MAN,PRA,TBA)
C-----SUBROUTINE GUEST GUESSES THE TEMPERATURE AND PRESSURE RATIO ACROSS
C-----A NORMAL SHOCK WAVE.
C-----THIS SUBROUTINE IS FOR ARGON.
C-----THE PARAMETERS ARE:
C      MAN=FLOW MACH NUMBER
C      PRA=PRESSURE RATIO
C      TBA=TEMPERATURE RATIO.
C-----
REAL MAN
COMMON/ABC/ITYPE
C-----FIRST GUESS FOR PRESSURE RATIO ACROSS THE SHOCK
G1=5./3.
B1=(G1-1.)/2./G1
ALFA1=(G1+1.)/(G1-1.)
PBA=(MAN**2/B1-1.)/ALFA1
GO TO(800,1),ITYPE
C-----FIRST GUESS FOR TEMPERATURE RATIO ACROSS THE SHOCK
1 IF(PBA-1.451800+800+801
800 TBA=PBA*(PBA+ALFA1)/(1.+PBA*ALFA1)
RETURN
801 TBA=PBA*(PBA+ALFA1)/(1.+PBA*ALFA1)*(3./(MAN+4.))
RETURN
END

```

PERFECT GAS SOLUTION

	REGION 0	REGION 1	REGION 2	REGION 3	
MACH NUMBER	11.800	1.192	1.001	0.688	
PRESSURE	10.0	1249.9	1600.5	1600.5	TORR
TEMPERATURE	300.0	9654.8	10663.7	12284.8	K
DENSITY	0.2136E-04	0.8296E-04	0.9618E-04	0.8349E-04	G/CM**2
INCIDENT ANGLE	I 58.00	R 68.20		M 73.65	
DEFLECTION ANGLE	35.60	3.07		32.52	

IMPERFECT GAS SOLUTION

	REGION 0	REGION 1	REGION 2	REGION 3	
MACH NUMBER	11.800	1.324	1.089	0.594	
PRESSURE	10.0	1275.9	1799.9	1799.9	TORR
TEMPERATURE	300.0	9200.7	9985.7	10801.1	K
DENSITY	0.2136E-04	0.8829E-04	0.1140E-03	0.1038E-03	G/CM**2
INCIDENT ANGLE	I 58.00	R 60.04		M 80.20	
DEFLECTION ANGLE	36.83	6.70		30.13	

THIS PAGE IS BEST QUALITY PRACTICABLE
FROM COPY FURNISHED TO DDC

APPENDIX D

RELATIVE MOTION OF THE SECOND TRIPLE POINT (OR KINK)

WRT THE FIRST TRIPLE POINT

The self-similarity (pseudo-steady) of the reflection phenomenon, i.e., the fact that any point on the wave configuration having a radius vector \bar{r} with the corner as origin is transformed to a new point $C\bar{r}$ where C is a scalar constant implies that the angles between the shock waves do not change. Consequently, the second triple point T_1 (or kink K) moves along a line formed by the straight portion of the reflected shock wave (i.e., the portion between T and T_1 or K) wrt the first triple point T .

Consider Fig. D.1a in which the triple point T moves with the velocity \bar{V}_{TL} along a line inclined at an angle χ to the wedge (wrt the laboratory frame of reference).

The second triple point T_1 moves along the line defined by the straight portion of the reflected shock wave R with the velocity \bar{V}_{iT} (i stands for T_1 or K , respectively) wrt the triple point T . In the laboratory frame of reference T_1 moves along a line inclined at an angle χ' to the wedge surface with a velocity \bar{V}_{iL} .

Simple vector analysis yields:

$$|\bar{V}_{TL}| = U_s \operatorname{cosec} \phi_0 \quad (D.1)$$

(Note $|\bar{V}_{TL}| \equiv U_0$ by definition.)

If the distance travelled by the incident shock wave I from the moment it collided with the wedge corner, $t = 0$ (the moment when the reflection started) is L_s , then the time passed is:

$$\Delta t = \frac{L_s}{U_s} \quad (D.2)$$

and the velocity of T_1 wrt T is:

$$|\bar{V}_{iT}| = \frac{L_i}{\Delta t} = \frac{L_i}{L_s} U_s = L U_s \quad (D.3)$$

where L_i is the length of the straight portion of the reflected shock wave R , and L is defined as L_i/L_s .

The velocity of T_1 in the laboratory frame of reference is then:

$$\bar{V}_{iL} = \bar{V}_{iT} + \bar{V}_{TL} \quad (D.4)$$

The x and y components of \bar{V}_{iL} can be expressed as follows:

$$V_{iL}^x = |\bar{V}_{TL}| \sin \phi_0 - |\bar{V}_{iT}| \sin \omega \quad (D.5)$$

$$V_{iL}^y = |\bar{V}_{TL}| \cos \phi_0 + |\bar{V}_{iT}| \cos \omega \quad (D.6)$$

where ω is the angle between the incident and reflected shock waves (I and R).

The velocity of T_1 in the laboratory frame of reference now becomes:

$$|\bar{V}_{iL}| = [(V_{iL}^x)^2 + (V_{iL}^y)^2]^{1/2}$$

With the help of Eqs. D.3 and D.4 the last equation can be rewritten as:

$$|\bar{V}_{iL}| = U_s [\operatorname{cosec}^2 \phi_0 + 2L \operatorname{cosec} \phi_0 \cos(\phi_0 + \omega) + L^2]^{1/2} \quad (D.7)$$

If the frame of reference is attached to T_1 the angle of incidence between the flow in state (0) and the incident shock wave $-\phi'_0$ is:

$$\phi'_0 = \tan^{-1} \frac{V_{iL}^x}{V_{iL}^y}$$

and again by inserting Eqs. D.3 and D.4 one obtains:

$$\phi'_0 = \tan^{-1} \left[\frac{1 - L \sin \omega}{\cot \phi_0 + L \cos \omega} \right] \quad (D.8)$$

The angle ω can be expressed using Fig. D.1b as follows:

$$\omega = 180^\circ - (\phi_1 + \phi_0 - \theta_1) \quad (D.9)$$

Thus Eqs. D.7 and D.8 can be rewritten in the form:

$$|\bar{V}_{iL}| = U_s [\operatorname{cosec}^2 \phi_0 + 2L \operatorname{cosec} \phi_0 \cos(\phi_1 - \theta_1) + L^2]^{1/2} \quad (D.10)$$

$$\phi'_0 = \tan^{-1} \left[\frac{1 - L \sin(\phi_1 + \phi_0 - \theta_1)}{\cot \phi_0 - L \cos(\phi_1 + \phi_0 - \theta_1)} \right] \quad (D.11)$$

It should be mentioned here that states (1), (2) and (3) are found by solving Eqs. 2.17 to 2.30 which holds here too. Consequently, all the parameters (except L which should be measured from an actual interferogram) are known. Note that one could measure (from an actual interferogram) the value of χ' [the second triple point (or kink) trajectory angle] rather than L ($=L_1/L_s$, Fig. D.1a) and perhaps simplify the above equations. However, the accuracy in measuring angles is in general much smaller than that of lengths, and hence the present method ensures a greater accuracy.

It is worthwhile mentioning that Law and Glass (see Ref. 51 for details) developed an analytical method by which the location of T_1 can be predicted in fairly good agreement with experiments in the range $\theta_w \leq 40^\circ$ (Ref. 62). Applying their method will result in:

$$L = \frac{\rho_0}{\rho_1} \operatorname{cosec}(\phi_1 + \phi_0 - \theta_1) \quad (D.12)$$

Inserting Eq. D.12 into Eqs. D.10 and D.11 yields:

$$|\bar{v}_{1L}| = U_s \left[\operatorname{cosec}^2 \phi_0 - 2 \frac{\rho_0}{\rho_1} \operatorname{cosec}(\phi_1 + \phi_0 - \theta_1) \operatorname{cosec} \phi_0 \cos(\phi_1 - \theta_1) + \left(\frac{\rho_0}{\rho_1} \right)^2 \operatorname{cosec}^2(\phi_1 + \phi_0 - \theta_1) \right]^{1/2} \quad (D.13)$$

and

$$\phi'_0 = \tan^{-1} \left[\frac{1 - \rho_0/\rho_1}{\cot \phi_0 - \frac{\rho_0}{\rho_1} \cot(\phi_1 + \phi_0 - \theta_1)} \right] \quad (D.14)$$

Equation D.13 can be rewritten in a slightly different form:

$$M'_0 = M_0 \left[1 - 2 \frac{\rho_0}{\rho_1} \frac{\sin \phi_0 \cos(\phi_1 - \theta_1)}{\sin(\phi_1 + \phi_0 - \theta_1)} + \left(\frac{\rho_0}{\rho_1} \right)^2 \frac{\sin^2 \phi_0}{\sin^2(\phi_1 + \phi_0 - \theta_1)} \right]^{1/2} \quad (D.15)$$

where M'_0 is the Mach number of the flow in state (0) wrt the triple point T_1 . The Mach number of this flow wrt the incident shock wave in a frame of reference attached to T_1 is:

$$M_0^+ = \frac{M_s}{\sin \phi'_0}$$

Using the relation $M_s = M_0 \sin \phi_0$ finally results in:

$$M_0^+ = M_0 \frac{\sin \phi_0}{\sin \phi'_0} \quad (D.16)$$

It is worth mentioning that all the variables involved in Eqs. D.13 to D.16 consist either of initial conditions U_s , M_0 , ϕ_0 and ρ_0 or variables that result from the solution of Eqs. 2.17 to 2.30, i.e., ϕ_1 , θ_1 , ρ_1 . Consequently $|\bar{V}_{iL}|$, ϕ'_0 , M'_0 and M_0^+ can all be calculated once the first triple point is solved.

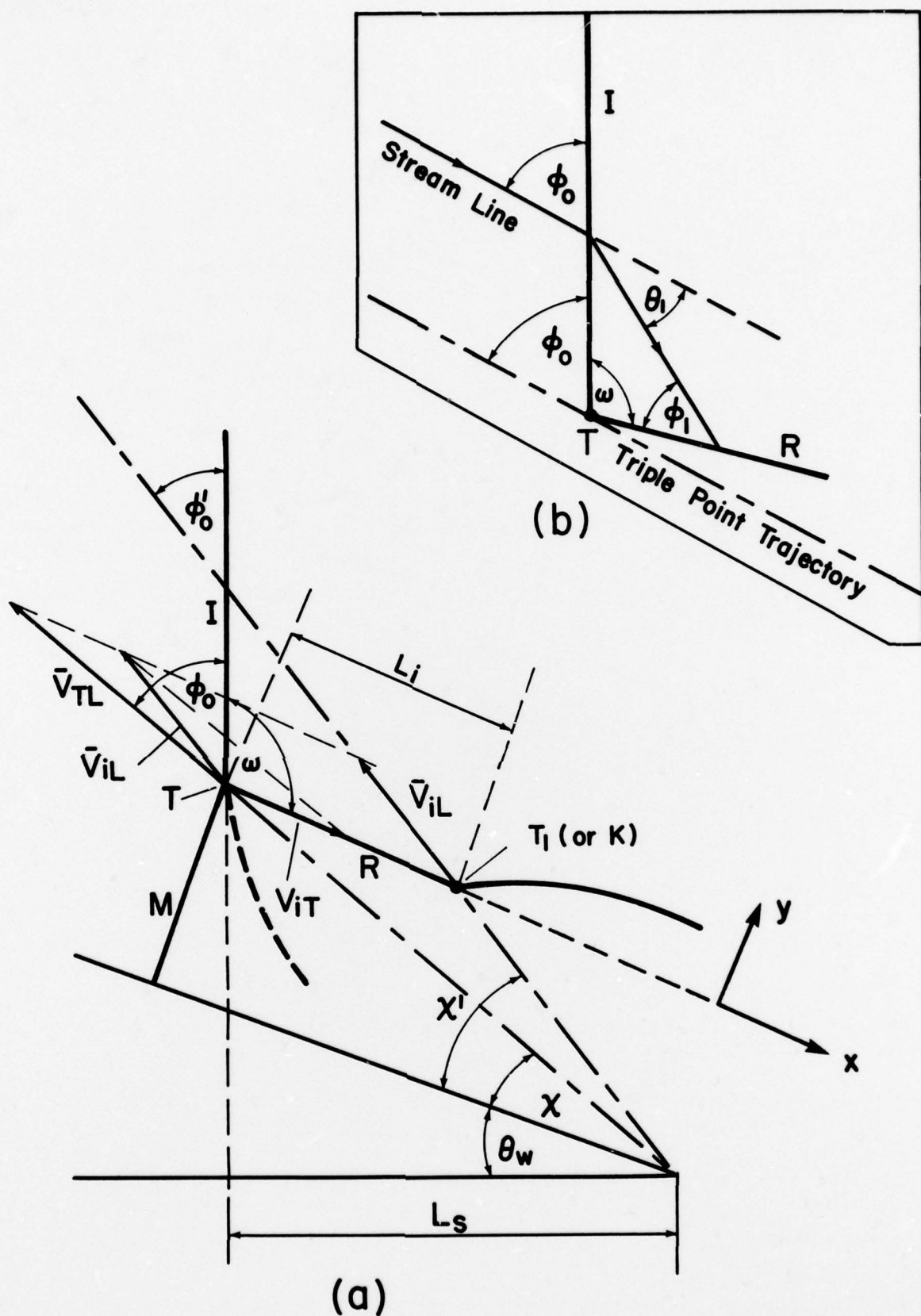


FIG. D-1. RELATIVE MOTION OF THE SECOND TRIPLE POINT (T_1) OR KINK (K) w.r.t. THE FIRST TRIPLE POINT (T).

APPENDIX E

METHOD OF REDUCING ISOPYCNICS FROM INTERFEROGRAMS

The present scheme for analyzing interferograms was developed by Whitten and reported in detail in Refs. 71 and 75. It requires the transformation of the fringe's location into digital form wrt a chosen reference point. The digitized results of two interferograms, flow and no-flow, are shown in Figs. E.1a and E.1b, respectively. The same physical point is chosen for all the interferograms (of one experiment) as the reference point and it is assigned to be the origin (0.0); see Figs. E.1a and E.1b. Each fringe can then be thought as a line [or locus of (x,y)-point] having the value of fringe number (interference order). With all four interferograms (1 flow and 1 no-flow for each wavelength) of one experiment digitized in this fashion wrt the same reference point (origin), the actual fringe shift, i.e., change in the value of the fringe, at any (x,y)-coordinate, can be easily determined.

To transform the fringes into digital form, a digitizer was used. First, it involved picking up a common reference point in all four interferograms (usually a cross hair that was put in the field of view prior to the experiment) and then a hand-held cursor was used to trace the fringes, and their location wrt the reference point were recorded on a magnetic tape. The recorded data were later transferred onto computer cards. An IBM 1800 plotter was then used to reproduce the digitized version of the interferograms (Figs. E.1a and E.1b). By comparing the digitized and original interferograms, all the points misaligned due to errors in the digitizing process were corrected and rechecked until a satisfactory reproduction was obtained. The original interferograms were enlarged to about four times their actual size in order to make the whole digitizing correction procedures much easier and more accurate.

Once the reproduction was satisfactory, all the points were linearly interpolated into uniform steps. Fringe numbers were also interpolated and assigned to each (x,y)-coordinate. With the flow and no-flow pictures of the two wavelengths digitized and fringe numbers assigned, fringe shift at any point could be calculated yielding in turn the changes in flow properties (density and degree of dissociation) at that point. Consequently, the entire density field was then known.

Once the above procedure was complete, the density distribution along lines of constant x or y was found. Typical density distributions (i.e., ρ/ρ_N vs y where ρ_N is a normalizing density) along two different constant-x lines, $x = 0.00$ and -5.00 (on Figs. E.1a and E.1b) are shown in Figs. E.2a and E.2b respectively. By changing x in small steps (0.5 - 2 mm usually) a set of these lines of density distribution was obtained. From these density-distribution figures, (x,y)-coordinates that correspond to the same ρ/ρ_N were deduced. For example, Figs. E.2a and E.2b suggest that $\rho/\rho_N = 0.9$ at $x = 0.00$, $y = -32.42$ and $x = -5.00$, $y = -31.12$. Sets of (x,y)-coordinates for different values of ρ/ρ_N were obtained from the set of density-distribution figures (Figs. E.2a and E.2b, for example) in a similar way and finally the isopycnics were drawn. Note that $\rho_N \neq \rho_0$ and hence ρ/ρ_N was multiplied by ρ_N/ρ_0 in order to get the isopycnics in the form ρ/ρ_0 .

In selecting the values of ρ/ρ_0 (i.e., ρ/ρ_N) for which sets of (x,y)-coordinates were obtained, care was taken that the step $\Delta\rho/\rho_0$ will be greater than the maximum possible error (Eqs. 8.1 and 8.2) associated with the reduction of density from interferograms.

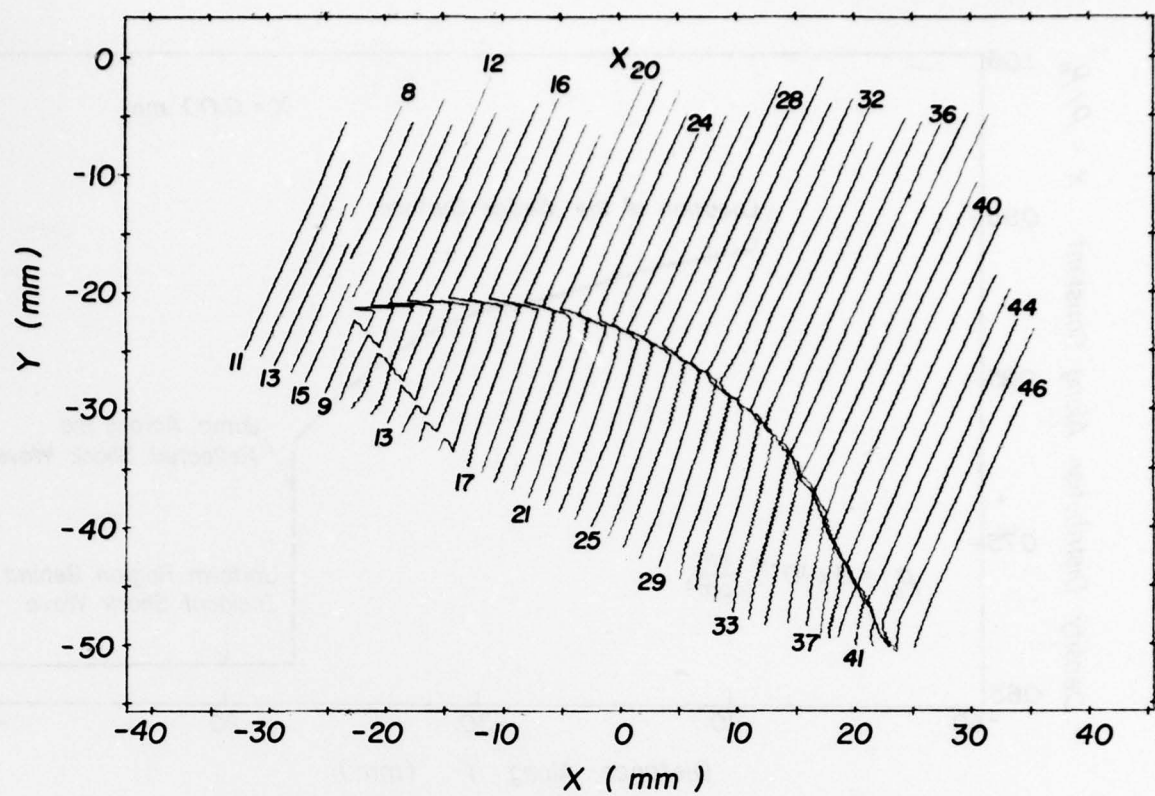


FIG. E-1(a). DIGITIZED REPRODUCTION OF A FLOW INTERFEROGRAM (SMR)

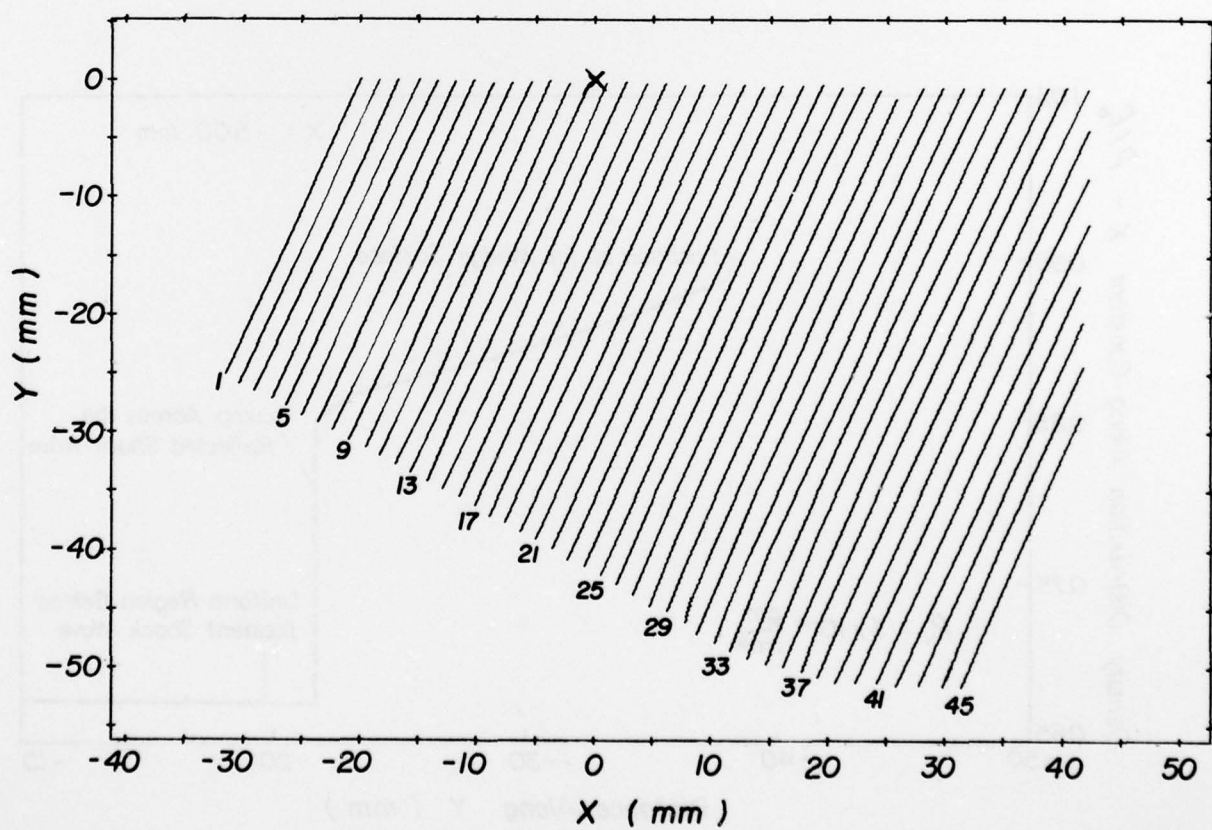


FIG. E-1(b). DIGITIZED REPRODUCTION OF A NO-FLOW INTERFEROGRAM.

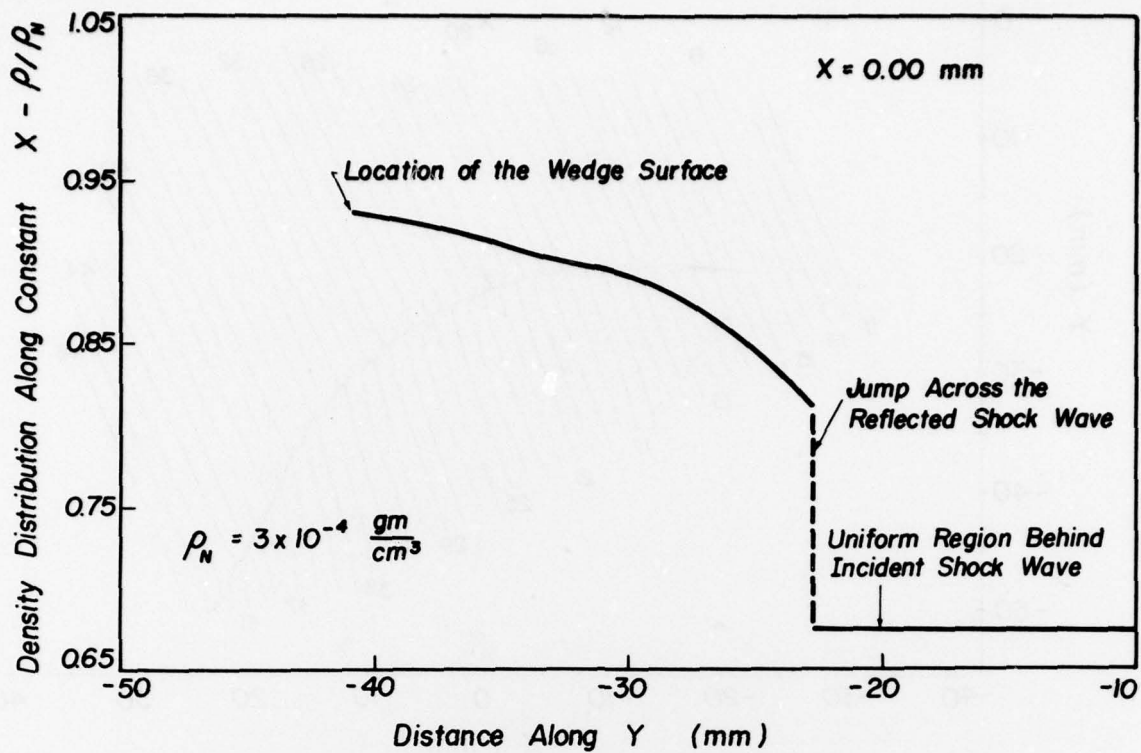


FIG. E-2(a). DENSITY DISTRIBUTION ALONG $X = 0.00$ OF FIG. E-1.

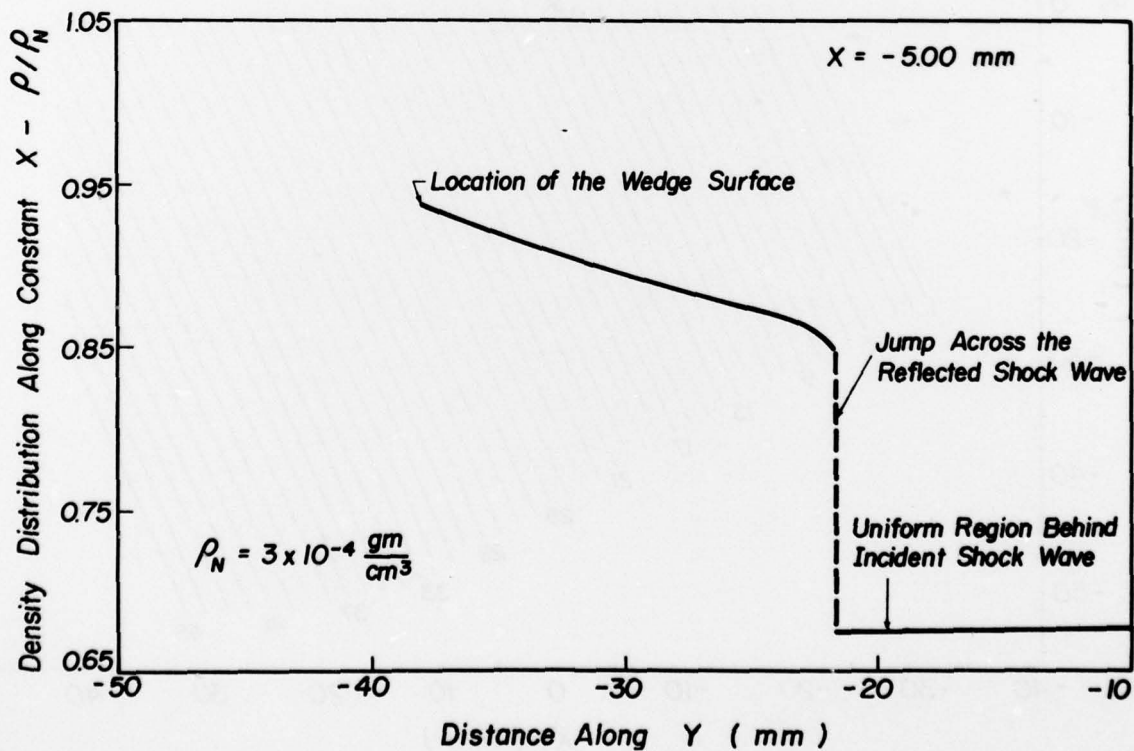


FIG. E-2(b). DENSITY DISTRIBUTION ALONG $X = -5.00$ OF FIG. E-1.



UTIAS REPORT NO. 232

Institute for Aerospace Studies, University of Toronto (UTIAS)
4925 Dufferin Street, Downsview, Ontario, Canada, M3H 5T6

REGIONS AND TRANSITIONS OF NONSTATIONARY OBLIQUE SHOCK-WAVE DIFFRACTIONS
IN PERFECT AND IMPERFECT GASES

Ben-Dor, G. 150 pages (approx) 75 figures 9 tables

1. Nonstationary oblique shock-wave reflections
2. Shock-tube flows
3. Imperfect-gas flows
4. Interferometric measurements

I. Ben-Dor, G.

II. UTIAS Report No. 232

The diffraction of shock waves ($2 \leq M_0 \leq 8$) in perfect and imperfect nitrogen and argon by sharp compressive corners ($2^\circ \leq \theta \leq 60^\circ$) were investigated analytically and experimentally. It is shown that seven shock-wave diffraction domains exist in nitrogen and six in argon in the ranges $1 \leq M_0 \leq 10$ and $0 \leq \theta \leq 90^\circ$. The domains consist of the four well-known shock wave reflections, i.e., regular reflection (RR), single-Mach (SMR), complex-Mach (CMR) and double-Mach (DMR) reflections. All the transition boundaries between these regions were established analytically and substantiated by the present experimental results as well as the data from other sources. Over 100 experiments were conducted in the UTIAS 10 x 18 cm Hypervelocity Shock Tube equipped with a 23-cm dia field of view Mach-Zehnder interferometer equipped with a dual-frequency laser light source. It is shown that real-gas effects have a significant influence on the size of the regions and their transition boundaries. Some comparison between steady and nonstationary reflections are made and discussed. Isopycnics (lines of constant density) as well as density distributions along the wedge surface are presented for the various diffraction processes and their differences and similarities are discussed.

Available copies of this report are limited. Return this card to UTIAS, if you require a copy.



UTIAS REPORT NO. 232

Institute for Aerospace Studies, University of Toronto (UTIAS)
4925 Dufferin Street, Downsview, Ontario, Canada, M3H 5T6

REGIONS AND TRANSITIONS OF NONSTATIONARY OBLIQUE SHOCK-WAVE DIFFRACTIONS
IN PERFECT AND IMPERFECT GASES

Ben-Dor, G. 150 pages (approx) 75 figures 9 tables

1. Nonstationary oblique shock-wave reflections
2. Shock-tube flows
3. Imperfect-gas flows
4. Interferometric measurements

I. Ben-Dor, G.

II. UTIAS Report No. 232

The diffraction of shock waves ($2 \leq M_0 \leq 8$) in perfect and imperfect nitrogen and argon by sharp compressive corners ($2^\circ \leq \theta \leq 60^\circ$) were investigated analytically and experimentally. It is shown that seven shock-wave diffraction domains exist in nitrogen and six in argon in the ranges $1 \leq M_0 \leq 10$ and $0 \leq \theta \leq 90^\circ$. The domains consist of the four well-known shock wave reflections, i.e., regular reflection (RR), single-Mach (SMR), complex-Mach (CMR) and double-Mach (DMR) reflections. All the transition boundaries between these regions were established analytically and substantiated by the present experimental results as well as the data from other sources. Over 100 experiments were conducted in the UTIAS 10 x 18 cm Hypervelocity Shock Tube equipped with a 23-cm dia field of view Mach-Zehnder interferometer equipped with a dual-frequency laser light source. It is shown that real-gas effects have a significant influence on the size of the regions and their transition boundaries. Some comparison between steady and nonstationary reflections are made and discussed. Isopycnics (lines of constant density) as well as density distributions along the wedge surface are presented for the various diffraction processes and their differences and similarities are discussed.

Available copies of this report are limited. Return this card to UTIAS, if you require a copy.



UTIAS REPORT NO. 232

Institute for Aerospace Studies, University of Toronto (UTIAS)
4925 Dufferin Street, Downsview, Ontario, Canada, M3H 5T6

REGIONS AND TRANSITIONS OF NONSTATIONARY OBLIQUE SHOCK-WAVE DIFFRACTIONS
IN PERFECT AND IMPERFECT GASES

Ben-Dor, G. 150 pages (approx) 75 figures 9 tables

1. Nonstationary oblique shock-wave reflections
2. Shock-tube flows
3. Imperfect-gas flows
4. Interferometric measurements

I. Ben-Dor, G.

II. UTIAS Report No. 232

The diffraction of shock waves ($2 \leq M_0 \leq 8$) in perfect and imperfect nitrogen and argon by sharp compressive corners ($2^\circ \leq \theta \leq 60^\circ$) were investigated analytically and experimentally. It is shown that seven shock-wave diffraction domains exist in nitrogen and six in argon in the ranges $1 \leq M_0 \leq 10$ and $0 \leq \theta \leq 90^\circ$. The domains consist of the four well-known shock wave reflections, i.e., regular reflection (RR), single-Mach (SMR), complex-Mach (CMR) and double-Mach (DMR) reflections. All the transition boundaries between these regions were established analytically and substantiated by the present experimental results as well as the data from other sources. Over 100 experiments were conducted in the UTIAS 10 x 18 cm Hypervelocity Shock Tube equipped with a 23-cm dia field of view Mach-Zehnder interferometer equipped with a dual-frequency laser light source. It is shown that real-gas effects have a significant influence on the size of the regions and their transition boundaries. Some comparison between steady and nonstationary reflections are made and discussed. Isopycnics (lines of constant density) as well as density distributions along the wedge surface are presented for the various diffraction processes and their differences and similarities are discussed.

Available copies of this report are limited. Return this card to UTIAS, if you require a copy.



UTIAS REPORT NO. 232

Institute for Aerospace Studies, University of Toronto (UTIAS)
4925 Dufferin Street, Downsview, Ontario, Canada, M3H 5T6

REGIONS AND TRANSITIONS OF NONSTATIONARY OBLIQUE SHOCK-WAVE DIFFRACTIONS
IN PERFECT AND IMPERFECT GASES

Ben-Dor, G. 150 pages (approx) 75 figures 9 tables

1. Nonstationary oblique shock-wave reflections
2. Shock-tube flows
3. Imperfect-gas flows
4. Interferometric measurements

I. Ben-Dor, G.

II. UTIAS Report No. 232

The diffraction of shock waves ($2 \leq M_0 \leq 8$) in perfect and imperfect nitrogen and argon by sharp compressive corners ($2^\circ \leq \theta \leq 60^\circ$) were investigated analytically and experimentally. It is shown that seven shock-wave diffraction domains exist in nitrogen and six in argon in the ranges $1 \leq M_0 \leq 10$ and $0 \leq \theta \leq 90^\circ$. The domains consist of the four well-known shock wave reflections, i.e., regular reflection (RR), single-Mach (SMR), complex-Mach (CMR) and double-Mach (DMR) reflections. All the transition boundaries between these regions were established analytically and substantiated by the present experimental results as well as the data from other sources. Over 100 experiments were conducted in the UTIAS 10 x 18 cm Hypervelocity Shock Tube equipped with a 23-cm dia field of view Mach-Zehnder interferometer equipped with a dual-frequency laser light source. It is shown that real-gas effects have a significant influence on the size of the regions and their transition boundaries. Some comparison between steady and nonstationary reflections are made and discussed. Isopycnics (lines of constant density) as well as density distributions along the wedge surface are presented for the various diffraction processes and their differences and similarities are discussed.

Available copies of this report are limited. Return this card to UTIAS, if you require a copy.



UTIAS REPORT NO. 232

Institute for Aerospace Studies, University of Toronto (UTIAS)
4925 Dufferin Street, Downsview, Ontario, Canada, M3H 5T6

REGIONS AND TRANSITIONS OF NONSTATIONARY OBLIQUE SHOCK-WAVE DIFFRACTIONS
IN PERFECT AND IMPERFECT GASES

- Ben-Dor, G. 150 pages (approx) 75 figures 9 tables
1. Nonstationary oblique shock-wave reflections 2. Shock-tube flows
3. Imperfect-gas flows 4. Interferometric measurements

I. Ben-Dor, G.

The diffraction of shock waves ($2 \leq M_0 \leq 8$) in perfect and imperfect nitrogen and argon by sharp compressive corners ($2^\circ \leq \theta \leq 60^\circ$) were investigated analytically and experimentally. It is shown that seven shock-wave diffraction domains exist in nitrogen and six in argon in the ranges $1 \leq M_0 \leq 10$ and $0 \leq \theta \leq 90^\circ$. The domains consist of the four well-known shock wave reflections, i.e., regular reflection (RR), single-Mach (SMR), complex-Mach (CMR) and double-Mach (DMR) reflections. All the transition boundaries between these regions were established analytically and substantiated by the present experimental results as well as the data from other sources. Over 100 experiments were conducted in the UTIAS 10 x 18 cm Hypervelocity Shock Tube equipped with a 23-cm dia field of view Mach-Zehnder interferometer equipped with a dual-frequency laser light source. It is shown that real-gas effects have a significant influence on the size of the regions and their transition boundaries. Some comparison between steady and nonstationary reflections are made and discussed. Isopycnics (lines of constant density) as well as density distributions along the wedge surface are presented for the various diffraction processes and their differences and similarities are discussed.

Available copies of this report are limited. Return this card to UTIAS, if you require a copy.



UTIAS REPORT NO. 232

Institute for Aerospace Studies, University of Toronto (UTIAS)
4925 Dufferin Street, Downsview, Ontario, Canada, M3H 5T6

REGIONS AND TRANSITIONS OF NONSTATIONARY OBLIQUE SHOCK-WAVE DIFFRACTIONS
IN PERFECT AND IMPERFECT GASES

- Ben-Dor, G. 150 pages (approx) 75 figures 9 tables
1. Nonstationary oblique shock-wave reflections 2. Shock-tube flows
3. Imperfect-gas flows 4. Interferometric measurements

I. Ben-Dor, G.

The diffraction of shock waves ($2 \leq M_0 \leq 8$) in perfect and imperfect nitrogen and argon by sharp compressive corners ($2^\circ \leq \theta \leq 60^\circ$) were investigated analytically and experimentally. It is shown that seven shock-wave diffraction domains exist in nitrogen and six in argon in the ranges $1 \leq M_0 \leq 10$ and $0 \leq \theta \leq 90^\circ$. The domains consist of the four well-known shock wave reflections, i.e., regular reflection (RR), single-Mach (SMR), complex-Mach (CMR) and double-Mach (DMR) reflections. All the transition boundaries between these regions were established analytically and substantiated by the present experimental results as well as the data from other sources. Over 100 experiments were conducted in the UTIAS 10 x 18 cm Hypervelocity Shock Tube equipped with a 23-cm dia field of view Mach-Zehnder interferometer equipped with a dual-frequency laser light source. It is shown that real-gas effects have a significant influence on the size of the regions and their transition boundaries. Some comparison between steady and nonstationary reflections are made and discussed. Isopycnics (lines of constant density) as well as density distributions along the wedge surface are presented for the various diffraction processes and their differences and similarities are discussed.

Available copies of this report are limited. Return this card to UTIAS, if you require a copy.



UTIAS REPORT NO. 232

Institute for Aerospace Studies, University of Toronto (UTIAS)
4925 Dufferin Street, Downsview, Ontario, Canada, M3H 5T6

REGIONS AND TRANSITIONS OF NONSTATIONARY OBLIQUE SHOCK-WAVE DIFFRACTIONS
IN PERFECT AND IMPERFECT GASES

- Ben-Dor, G. 150 pages (approx) 75 figures 9 tables
1. Nonstationary oblique shock-wave reflections 2. Shock-tube flows
3. Imperfect-gas flows 4. Interferometric measurements

I. Ben-Dor, G.

The diffraction of shock waves ($2 \leq M_0 \leq 8$) in perfect and imperfect nitrogen and argon by sharp compressive corners ($2^\circ \leq \theta \leq 60^\circ$) were investigated analytically and experimentally. It is shown that seven shock-wave diffraction domains exist in nitrogen and six in argon in the ranges $1 \leq M_0 \leq 10$ and $0 \leq \theta \leq 90^\circ$. The domains consist of the four well-known shock wave reflections, i.e., regular reflection (RR), single-Mach (SMR), complex-Mach (CMR) and double-Mach (DMR) reflections. All the transition boundaries between these regions were established analytically and substantiated by the present experimental results as well as the data from other sources. Over 100 experiments were conducted in the UTIAS 10 x 18 cm Hypervelocity Shock Tube equipped with a 23-cm dia field of view Mach-Zehnder interferometer equipped with a dual-frequency laser light source. It is shown that real-gas effects have a significant influence on the size of the regions and their transition boundaries. Some comparison between steady and nonstationary reflections are made and discussed. Isopycnics (lines of constant density) as well as density distributions along the wedge surface are presented for the various diffraction processes and their differences and similarities are discussed.

Available copies of this report are limited. Return this card to UTIAS, if you require a copy.



UTIAS REPORT NO. 232

Institute for Aerospace Studies, University of Toronto (UTIAS)
4925 Dufferin Street, Downsview, Ontario, Canada, M3H 5T6

REGIONS AND TRANSITIONS OF NONSTATIONARY OBLIQUE SHOCK-WAVE DIFFRACTIONS
IN PERFECT AND IMPERFECT GASES

- Ben-Dor, G. 150 pages (approx) 75 figures 9 tables
1. Nonstationary oblique shock-wave reflections 2. Shock-tube flows
3. Imperfect-gas flows 4. Interferometric measurements

I. Ben-Dor, G.

The diffraction of shock waves ($2 \leq M_0 \leq 8$) in perfect and imperfect nitrogen and argon by sharp compressive corners ($2^\circ \leq \theta \leq 60^\circ$) were investigated analytically and experimentally. It is shown that seven shock-wave diffraction domains exist in nitrogen and six in argon in the ranges $1 \leq M_0 \leq 10$ and $0 \leq \theta \leq 90^\circ$. The domains consist of the four well-known shock wave reflections, i.e., regular reflection (RR), single-Mach (SMR), complex-Mach (CMR) and double-Mach (DMR) reflections. All the transition boundaries between these regions were established analytically and substantiated by the present experimental results as well as the data from other sources. Over 100 experiments were conducted in the UTIAS 10 x 18 cm Hypervelocity Shock Tube equipped with a 23-cm dia field of view Mach-Zehnder interferometer equipped with a dual-frequency laser light source. It is shown that real-gas effects have a significant influence on the size of the regions and their transition boundaries. Some comparison between steady and nonstationary reflections are made and discussed. Isopycnics (lines of constant density) as well as density distributions along the wedge surface are presented for the various diffraction processes and their differences and similarities are discussed.

Available copies of this report are limited. Return this card to UTIAS, if you require a copy.